International Journal of Modern Physics A
Vol. 26, Nos. 10 & 11 (2011) v–vi

DOI: 10.1142/S0217751X11053079

World Scientific
www.worldscientific.com

PREFACE

Fueled by recent advances, electron, proton and heavy ion accelerators are playing increasingly important roles in science, technology, and medicine including accelerator-driven subcritical reactors, industrial irradiation, material science, neutrino production, and cancer therapy. The drive for higher beam power, high duty cycle, high reliability and precisely controlled beams at reasonable cost has generated world-wide interest in Fixed-field Alternating Gradient accelerators (FFAGs). Fixed-field accelerators have the automatic advantage, or potential, to realize all of these desirable features using inexpensive, DC power supplies and various modes of acceleration. FFAGs are unique in their high repetition rates and large acceptances characteristic of cyclotrons, yet they also embody the advantages of the synchrotron: focusing is predominately "strong," with low injection and extraction losses. With the best features of the cyclotron and synchrotron combined, the FFAG accelerators represent new directions in accelerator science and are presently under international development. Strong interest worldwide has emphasized FFAGs for hadron therapy [RACCAM in France and PAMELA in the U.K.], in the context of proton and carbon accelerators, but other areas are gaining momentum: high intensity proton FFAGs for Accelerator Driven Subcritical Reactors (ADSR) and compact electron FFAGs for inspection systems such as cargo scanning. The elimination of pulsed operation which complicates and increases the expense of machines and restricts the delivered rate or beam power, makes the FFAG an ideal machine for industry, medical, and commercial applications. Further, recent advances in design, such as isochronous operation, will give the FFAG a distinct advantage in many applications, notably for medical and high-intensity applications. The FFAG stands to compete with the cyclotron, which is the current industrial and commercial standard. Commercial FFAG versions are already under development in Japan at Mitsubishi Corp. and NHV Corp.

The novel dynamics and potential have been the subject of intensive study, development and simulation as documented in a series of workshops held alternately in Japan, the U.K., France, Canada, and the U.S. (FFAG'99–FFAG'10), with the next workshop, FFAG11 scheduled to be held at Oxford University, Sept. 12–17th.

FFAG09 boasted over 50 participants including a large international contingent of renowned accelerator physicists from the U.K., Japan, France, Germany, and Canada. In addition to universities, major large accelerator laboratories in the U.S. were also represented and included Brookhaven National Laboratory, Argonne National Laboratory, and Lawrence Berkeley National Laboratory. Industrial participation included Siemens, Passport Systems, IBA, and Sumitomo with a paper being submitted to the proceedings by Passport Systems.

Carol Johnstone, Martin Berz, and Pavel Snopok
Editors

International Journal of Modern Physics A
Vol. 26, Nos. 10 & 11 (2011) vii–viii

DOI: 10.1142/S0217751X11053080

World Scientific
www.worldscientific.com

MEMORIES OF ALESSANDRO G. RUGGIERO

On June 26, 2010 Sandro Ruggiero passed away, leaving a legacy of wonderful memories and knowledge. Our first meeting was in 1966 at CERN. We were almost kids just out of university: he was 26 and I a bit younger.

At that time, Andy Sessler, only 15 years older, but already a world-famous scientist, was at CERN on leave from Berkeley for the design of a new accelerator. I was assigned to him. After some time Andy told me, with an all-American look, totally unknown new to me, that I had to give a seminar on the results of our work.

In the evening, after the seminar, a young man of my age came up to me and, talking with a strong and not unpleasant Roman accent, introduced himself: "My name is Sandro," he said, omitting his surname. This accent he would keep for a lifetime, even in French and English. He said he had followed the seminar, he liked the subject and asked if he could collaborate with me on the studies that I had undertaken under the guidance of Andy. I was happy to accept.

We began to work together. It was a delightful time. Andy's suggestions took us to entirely new horizons. At first we worked amid general indifference. There was also a bit of impatience. CERN was very hierarchical at the time. The hierarchy barely tolerated these two noisy Italians arguing constantly, and who in addition dared to work autonomously on theoretical aspects of accelerator physics. Andy had left and we no longer had a reference point: we had to see for ourselves. Every step forward was achieved after endless discussions. We met Minerva, the goddess of knowledge, as Italo Calvino says. Well in advance of my contract's expiration I was informed that it would not be renewed. So it was for Sandro as well. We were very disappointed, but we always consoled each other by the recollection that we were in good company. In 1969 we left CERN.

We went our separate ways: I to Naples, he to Karlsrhue. It was a hard time for both of us, maybe even harder for him. The situation was discouraging, but he was not discouraged. He was always a fighter and he has never loosened his hold. He, volcanic, had his wife at his side, a woman with an unshakable serenity. Finally in 1970 he went to Fermilab. In this new and completely different environment, his qualities were acknowledged. During this period he became increasingly conscious

that the work done at CERN was of great significance. His contributions to accelerator physics have touched almost all areas of this discipline, and in each he has left his imprint.

Following this are some comments from those who knew him. They all emphasize his remarkable scientific output, but also give special emphasis to his human qualities.

Andy Sessler, in response to my announcement of Sandro's departure, wrote me: "We remember Sandro with many good memories. The enthusiasm, the many new ideas (some crazy, and probably he knew it also, but they were certainly stimulating and often a step towards a good idea), the interest in many things (often far beyond physics), and many other things. In short, a contagious love of life . . ."

And Mike Craddock (Triumf), as I have been told, commented: "That's very sad news. We shall all miss Sandro's never failing imagination and enthusiasm."

Whoever knew him keeps in his heart the memory of his human warmth, his affectionate and sincere attitude, sometimes even childlike. I remember his amusement when I was telling stories and jokes. One he particularly liked was "L'histoire de la petite grenouille verte," a story to be told in French, where the comic aspect was to narrate it with a strong English accent. His amusement was so great that at every opportunity, in the presence of someone who did not know this story, he urged me to tell it again: a bit as children do when they always want to hear the same tale. And he always laughed with relish as if it was the first time . . . Let us remember him with a smile too.

Vittorio G. Vaccaro

International Journal of Modern Physics A
Vol. 26, Nos. 10 & 11 (2011) ix

DOI: 10.1142/S0217751X11053092

World Scientific
www.worldscientific.com

ORGANIZING COMMITTEE

Carol Johnstone, FNAL, Co-Chair
Alessandro Ruggiero, BNL, Co-Chair
Rajendran Raja, FNAL
Roger Barlow, Manchester Univ., U.K.
Chris Prior, RAL, U.K.
Shane Koscielniak, TRIUMF, Canada
Pavel Snopok, IIT/FNAL
Andy Sessler, LBNL
Martin Berz, MSU
Yoshi Mori, Kyoto University
Francois Meot, CEA, France
Takeichiro Yokoi, JAI, U.K.
Francois Ostiguy, FNAL
Scott Berg, BNL
Chuck Ankenbrandt, Muons Inc.
Eberhard Keil, retired, CERN
Rob Edgecock, CERN

LOCAL ORGANIZING COMMITTEE

Cynthia Sazama, FNAL, Co-chair
Suzanne Weber, FNAL
Jean Guyer, FNAL
Shekhar Mishra, FNAL
George Coutrakon, NIU

International Journal of Modern Physics A
Vol. 26, Nos. 10 & 11 (2011) 1659–1689

DOI: 10.1142/S0217751X11053109

World Scientific
www.worldscientific.com

LITERATURE REVIEW ON LINACs AND FFAGs FOR HADRON THERAPY

SILVIA VERDÚ-ANDRÉS
TERA Foundation
Via Puccini 11, I-28100 Novara, Italy
Silvia.Verdu.Andres@cern.ch

Instituto de Física Corpuscular IFIC (CSIC-UV),
Ed. Institutos de Investigación, E-46071 Paterna, Valencia, Spain
Silvia.Verdu@ific.uv.es

UGO AMALDI
TERA Foundation
Via Puccini 11, I-28100 Novara, Italy
Ugo.Amaldi@cern.ch

ÁNGELES FAUS-GOLFE
Instituto de Física Corpuscular IFIC (CSIC-UV)
Ed. Institutos de Investigación, E-46071 Paterna, Valencia, Spain
Angeles.Faus-Golfe@uv.es

The document summarizes the recent papers, presentations and other public information on Radio-Frequency (RF) Linear Accelerators (linacs) and Fixed-Field Alternating-Gradient (FFAG) accelerators for hadron therapy. The main focus is on technical aspects of these accelerators. This report intends to provide a general overview of the state-of-the-art in those accelerators which could be used in short and middle-term for treating cancer.

Keywords: Hadron therapy; particle therapy; proton therapy; carbon ion therapy; medical accelerators; linacs; FFAG.

PACS numbers: 11.25.Hf, 123.1K

1. Introduction

Cancer is the second cause of death in developed countries.[1] Nowadays nearly 20000 patients in 10 million European inhabitants are treated with "conventional" radiotherapy alone or in combination with other kinds of treatment. The main goal of radiotherapy is to induce cell death or apoptosis in the tumor tissue with a minimum damage to surrounding healthy organs.

In 1946 R.R. Wilson suggested the use of charged particles in radiotherapy.[2] More than sixty years later, and thanks to many technical developments, hadron therapy has become the most suitable alternative to X-rays for treating deep-seated tumours and radioresistant tumours while producing less damage to the surrounding tissues due to the Bragg peak behaviour of hadrons.

At present, 25 facilities all around the world offer proton therapy and just 3 of them provide carbon therapy.[3] All these centers are cyclotron- or synchrotron-based facilities. However, neither cyclotrons nor synchrotrons present the optimal characteristics to be used for hadron therapy. Cyclotrons deliver a fixed energy beam, so absorbers are needed in order to vary the beam energy and consequently the tumour depth scanning. The use of absorbers needs a long and complicated energy selection system which causes neutron activation and carbon fragmentation. In the case of synchrotrons, the main disadvantage is in the beam timing. The beam is not always present and 1-2 seconds separate the successive "flat tops" during which the beam is extracted.

In this context, PARTNER is an "interdisciplinary, multi-national initiative, which has the primary goal of training researchers. These researchers will then help to improve the overall efficiency of hadron therapy in cancer treatment, and promote clinical, biological and technical developments at a pan-European level".[4]

One of the PARTNER Work Packages (WP25: "Novel Accelerator Concepts for Hadrontherapy") objectives is to compare two novel accelerator concepts for hadron therapy: linacs and FFAGs. Both types of accelerators present interesting features which make them good candidates for hadron therapy.

This work summarizes the recent papers, presentations and other public information on RF linacs and FFAGs for hadron therapy by concentrating on the technical aspects of these accelerators and intends to provide a general overview on the state-of-the-art in those accelerators which could be used in short and middle-term for treating cancer. This document is the first step of a much deeper study on the RF linacs and FFAGs for hadron therapy, where the performance features of both technologies will be presented and compared accordingly to the beam requirements provided by clinicians.

The information has been structured as follows. The first chapter deals with the medical requirements for hadron therapy accelerators. In this part the medical specifications for a therapeutic beam and the consequent technical specifications for an accelerator for hadron therapy are presented. The following chapter presents the main features of RF linacs and discusses their advantages and disadvantages. Then, the recent linac approaches for hadron therapy are described. The next chapter provides a brief introduction to FFAGs, followed by a discussion of their advantages and disadvantages. In the last part of this chapter, the FFAGs designed for hadron therapy are introduced. The last chapter presents the preliminary conclusions extracted from the previous chapters.

Table 1. Beam parameter limitations from clinical specifications.

Accelerator beam	**Treatment beam**	
Energy	Range	Good energy selection system to provide adequate penetration depths
Size, emittance	Dose distribution	Better dose distribution to reduce cancer recurrence
Shape, repetition rate	Organ motion	Possibility to apply multipainting technique
Current	Dose rate	Simple and efficient extraction to minimize neutrons production and maximize intensity for therapy
Position, orientation, size, shape, precision	Conformal dose delivery	Better dose delivery to reduce cancer recurrence
Timing	Radiobiological response, better patient experience	Higher beam availability leads to better results

2. Medical Requirements for Hadron Therapy Accelerators

There is a difference between what clinicians want and what technology can currently provide.[5] Experts in hadron therapy and related fields should look to the future and dream together of the ideal accelerator for hadron therapy. Different authors have already listed the characteristics which an ideal accelerator for hadron therapy should have.

Beam parameters of medical accelerators are determined by clinical specifications[6] (see Table 1) and may vary due to different tumour location and delivery modalities.[7,8] A proton beam energy between 60 and 230 MeV and a carbon beam energy between 110 and 430 MeV/u correspond to a 3 to 32 cm range in soft tissue. A good energy selection system, preferably without absorbers, is required to avoid beam quality degradation and activations. A small energy spread (0.3–0.4% FWHM — Full Width Half Maximum) is needed to profit from the rapid fall-off of the Bragg peak. Moreover, a possibly rapid variation of the energy corresponding to a ± 0.5 mm range precision is required to accurately cover the target. Beam position and orientation, shape and size play a decisive role to ensure a conformal delivery of the dose to the tumour, which may translate into lower cancer recurrences.[8,9] Magnet precision is a sensitive issue as it directly influences beam position and orientation.[7] If the beam is delivered with a repetition rate in the range of 100–200 Hz, the beam pulse can be synchronised with moving organs and "cold spots" can be corrected by the *multipainting technique*. Furthermore, a beam with enough current is desired to reduce the duration of the treatment. The minimum dose rate is equal to 2 Gy/min in a 1 liter target.[5] Finally, a low emittance beam would permit to use magnets with smaller apertures and therefore smaller sizes.[7]

The most significant beam performances for hadron therapy and their acceptable values have been presented by different authors.[10,11] Table 2 contains the clinical requirements which should be satisfied by an accelerator for hadron therapy.

Table 2. Clinical performance specifications for a therapeutical beam.

Beam parameter	**Value**
Min./Max. Extraction Energy[a] $[MeV/u]$	60/230 (protons) 110/430 (carbon ions)
Beam Energy Modulation Step[b] [MeV/u]	~ 1
Energy Resolution (FWHM) at Min./Max. Energy [%]	3.5/1.8
Min./Max. Average Dose Rate [Gy $\cdot$ min$^{-1} \cdot L^{-1}$]	2/10
Delivery Dose precision [%]	$\leq \pm 2.5$
Repetition Rate [Hz]	100-400
Beam Size – FWHM [cm]	0.4-1.0
Beam Size Step [cm]	0.1
Beam Size Accuracy [cm]	$\leq \pm 0.025$
Lateral Penumbra[c] (80%-20%) [cm]	< 0.2
Distal Dose Fall-off[d] (80%-20%) [cm]	< 0.2
Min./Max. Field Size [cm $\times$ cm]	$2 \times 2/20 \times 20$
Bunch Charge at Min./Max. Rep. Rate [pC]	16/4 (protons) 3/1 (carbon ions)
Bunch Charge Stability [%]	< 10

[a]Correspondent to ranges between 3 and around 32 cm in soft tissue.
[b]Equivalent to less than one millimeter in tissue-equivalent depth (0.1 g/cm^2).
[c]For each side, at the phantom entrance surface.
[d]In addition to intrinsic distal fall-off.

The therapeutical beam must be stable, accurate and clean of neutrons and other particles coming from scattering processes in absorbers.[8,12] The accelerator complex should incorporate a precise measurement system of the beam parameters (energy, size, position, intensity and emittance) as well as a reliable beam control system.[13] A versatile machine which provides fixed and movable beams, in different positions and orientations, and permits to use different delivery modalities would bring greatest benefit to patients. For safety reasons the beam must be decoupled from the patient and the accelerator must be perfectly shielded. A high extraction efficiency is required for low equipment activation and low exposure to personnel.[7] Power supply stability, stable performance of the machine, vacuum and cooling systems operation must be guaranteed. Power supply stability is especially critical in that it affects the energy, intensity and position stability of the therapeutic beam.[7] On the other hand, the complex has to be easy to operate, maintain and repair.[8,12] An accelerator complex divided in modules is one design consideration which would facilitate maintenance, reparation, upgrading and extension of the facility.

Socio-economical aspects are especially important. Accelerators for hadron therapy should have a relatively low price, require little plug power and have reduced dimensions.[8,12,13] Facilities based on accelerators which deliver beam to multiple rooms (multiple-room accelerators) are typically more economical than those based on single-room accelerators. Nevertheless, if there is a breakdown in a multiple-room accelerator, the treatment delivery has to be stopped in several rooms of the

facility.[14] On the other hand, the choice of an adequate patients' flow will lead to a rapid investment recovery and will allow to acquire statistically significant clinical data. Finally, hospital-based facilities present some advantages from the point of view of patient experience, beam time for therapy and availability of sanitary resources,[7] but laboratory-based facilities allow R&D necessaries for advancing in the field.

Other requirements are more related to routine operation of the facility. The availability of the accelerator complex should be higher than 99% of the time.[8] Therapy for patients in the third or forth week of treatment cannot be aborted: cancer recurrence probability increases dramatically in these cases, therefore, reliable operation is very important.

3. Linacs and Linac-Based Complexes for Hadron Therapy

In 1928 Rolf Widerøe proposed and tested the first linear accelerator. Some decades later, linacs are used for many industrial, scientific and medical applications.

In a linac, charged particles are accelerated in a straight line either by a steady electric field or by a time-varying field. The most successful way to accelerate charged particles is to use radio-frequency RF fields, as very high accelerating voltages can be achieved in resonant RF cavities compared to those obtainable in electrostatic accelerators of similar dimensions. Therefore most of the linear accelerators proposed for hadron therapy are based on acceleration by means of RF fields.

Another type of linear accelerator, the induction linac, makes use of the transformer principle: an electrical eddy field is excited along the particle path by means of a time-varying azimuthal magnetic field. This electric field serves to accelerate the beam. In practice, the transformer principle is applied repeatedly to several units which are lined up along a straight path and are triggered in synchronism with the particles. The interest on induction linacs for hadron therapy has increased in the last years. In particular, the Dielectric Wall Accelerator (DWA), a recently proposed new concept in induction accelerators, could achieve high gradients which would permit to reduce the accelerator length. This document will not go deeper in the concept as just very preliminary designs of such a machine for hadron therapy are available in the literature. A review on DWA was recently published (see Ref. 15).

In the following, the basis of particle acceleration by means of RF fields is introduced. A deeper approach to the topic can be found in many books (see Refs. 16–18).

3.1. *RF fields for particle acceleration*

Different types of RF accelerators have been developed in accordance with the input and output beam energy, the beam intensity and the kind of particle that has to be accelerated.

RF fields are alternating current electric fields in the frequency range between 10 MHz to 30 GHz. A linear accelerator consists of an array of RF cavities or cells

where electromagnetic fields are generated and timed such that a particle absorbs and accumulates energy from each section.

In a linac the RF field sign is reversed every half period $T/2$, where T is the period of the RF pulse. The motion of the particles must be synchronized with the RF field frequency f ($f = 1/T$) to ensure that the particles are exclusively exposed to accelerating RF fields and not to decelerating ones. Hence, a particle must run from an accelerating cavity to the next one during the time $T/2$ it takes the field to reverse sign. During this half period $T/2$, the particle has to be shielded from the field. Technically this requirement is realized by surrounding the beam path with metallic drift tubes. The distance d between the centers of two accelerating cavities has thus to be

$$d = \frac{1}{2} vT, \tag{1}$$

where v is the velocity of the particle. This is known as the *synchronicity condition* (see Fig. 1).

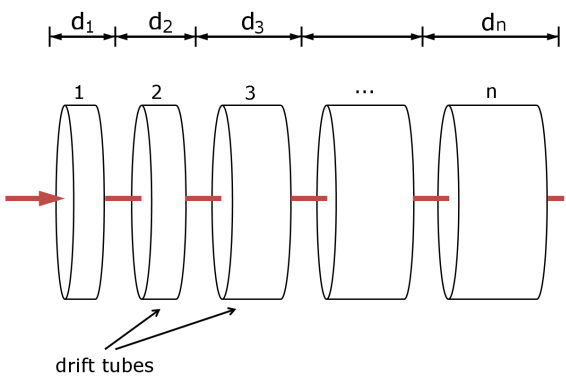

Fig. 1. *Synchronicity condition.* The distance d_i between two accelerating cavities has to be equal to half the velocity of the particle v_i times the period of the RF pulse T.

The RF fields excited in the structure must fill the cavities in such a way that only electromagnetic modes which exhibit electric field components in the direction of propagation of the particles (longitudinal components) can survive in the structure. Appropriate boundary conditions (cylindrical or rectangular tubes) have to be introduced to create such longitudinal electric field components. The wave equation for an accelerating field E_z in a cylindrical waveguide in cylindrical coordinates (r, θ, z) is

$$\frac{\partial^2 E_z}{\partial r^2} + \frac{1}{r}\frac{\partial E_z}{\partial r} + \left(k_c^2 - \frac{n^2}{c^2}\right) E_z = 0, \tag{2}$$

where r is the position vector, k_c is the cut-off wave vector separating propagating from evanescent solutions and c is the speed of light in vacuum. The solution of

Eq. (2) is a combination of Bessel functions J_n, and represents many modes n for the field component E_z consistent with the boundary conditions:

$$E_z = A\, J_n(k_c r). \tag{3}$$

There are two kinds of modes: the TE modes (just the Transversal components of the Electric field are different from zero) and the TM modes (just the Transversal components of the Magnetic field are different from zero). Hence, only TM modes can be useful for acceleration. The solutions $\mathrm{TM}_{r\theta z}$ are characterized by three indices: r and θ indicate the number of halfwaves for the electric field in the radial and azimuthal coordinates and z indicates the number of halfwaves for the electric field in the longitudinal direction. The selection of the appropriate mode permits a more efficient use of the field for acceleration. In Fig. 2 the simplest TM mode, the TM_{010}, is shown. TM_{010} means that the magnetic field has only transversal components and that the electric field has only radial component with a node in the cavity wall.

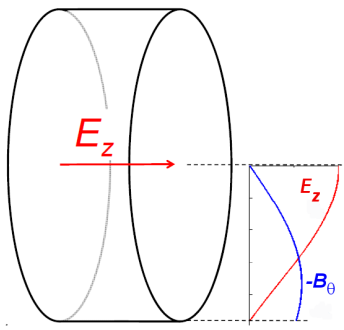

Fig. 2. Electric and magnetic fields of the TM_{010} mode in a cylindrical cavity.

Cavity geometry plays an important role on the field distribution, but it also influences important quantities such as the efficiency to use the energy stored in the cavity as electromagnetic field to accelerate the particles.

Another important parameter is the phase shift, which describes the field phase difference from one cavity to a nearby cavity. The electric field configurations for different phase shifts, also called structure modes, are represented in Fig. 3. Each mode presents advantages and disadvantages that will not be discussed in this document.

The RF power supply systems needed to excite an electromagnetic field in a cavity are commercialized for different frequencies. The resonance frequency determines not only the beam dynamics and cost of the machine but also the maximum accelerating gradient that can be achieved in the structure. The accelerating gradient is proportional to the electric field obtained in the direction of propagation of the particles in the accelerator and determines the total length of the machine

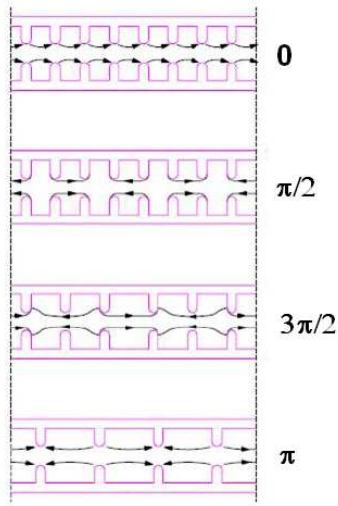

Fig. 3. Instantaneous electric field configurations for different structure modes.

needed to deliver a beam with determinate output energy. Single-pass machines like linacs present the drawback that high accelerating gradients, limited by breakdown phenomena, need to be achieved to keep a reasonable accelerator length.

In the 1950's Kilpatrick delimited the accelerating gradients at which reliable operation could be performed in function of the accelerator frequency. Higher accelerating gradients can be achieved for higher frequencies,[19] as the semi-empirical expression given by T.J. Boyd shows:

$$f[\mathrm{MHz}] = 1.64\,(E[\mathrm{MV/m}])^2 \cdot e^{-8.5/E[\mathrm{MV/m}]}, \tag{4}$$

where f is the accelerator frequency and E is the maximum accelerating gradient at which reliable operation can be obtained. Up to now, different experiments have shown that the breakdown model used by Kilpatrick does not apply, that the maximum surface field is not the proper parameter to look at, and that Kilpatrick's limitation was too conservative and thus higher accelerating gradients than those given as a threshold could be achieved. Nevertheless, high accelerating gradients are still a challenge for accelerating structures development. Recently a new quantity, the modified Poynting vector, has been found to determine the breakdown rate.[20] A collaboration between the CLIC RF structure group at CERN and TERA Foundation has been established to advance together in this field of knowledge.[21]

3.2. *Linear accelerators performance*

Linacs can provide high-energy and high-intensity pulsed beams of high quality, where quality means small beam size, small angular spread, small time spread of the beam pulses and small energy spread.

Single-pass linear structures have various advantages. Firstly, beams describe linear trajectories and therefore linear machines require much simpler lattices than circular machines. Then, beam injection and extraction pose no problem because of the inertia of the particles. Furthermore, strong focusing can easily be performed with quadrupoles to obtain high-current beams. Finally, the beam passes just once through the accelerating structure, so there is no possibility to accumulate repetitive lattice errors which would lead to destructive beam resonances. However, single-pass machines present the drawback that high accelerating gradients need to be achieved to shorten the length of the machine.

3.3. *Linacs for hadron therapy*

A complete overview on high-frequency linacs for hadron therapy has been recently published (see Ref. 21). The paper presents the main advantages of high frequency linacs and includes the designs of linac-based proton and carbon facilities. In the following a compilation of the latest linac designs for hadron therapy is presented. None of these linacs has been ever constructed. Just some parts or modules of some of them have been built and tested.

3.3.1. IDRA*, a cyclinac-based facility for proton therapy*

A cyclotron followed by a linac is known as *cyclinac*. The concept was proposed by U. Amaldi in 1993 and developed by TERA Foundation.

The first cyclinac design was based on LIBO (LInear BOoster), a 3 GHz standing wave side-coupled linac (often called CCL for Cell Coupled Linac) which accelerates protons from 62 to 200 MeV at 400 Hz repetition rate. The linac is divided into 36 tanks grouped into 9 modules. Each module is fed by its own klystron. In total, the length of the linac is 13.5 m. The beam energy is modulated by reducing or switching off the power that arrives to the modules. The lattice of LIBO is very simple: a series of thin permanent magnetic quadrupoles are used along the linac to focus the beam.

A collaboration between TERA, CERN, the University and INFN of Milan and the University and INFN of Naples was established to build and test a scale prototype of the first module of LIBO (see Fig. 4). This module, 1.3 meters-long, is designed for achieving an accelerating gradient of 15.8 MV/m. It has to accelerate protons from 62 to 74 MeV with an RF peak power of 4.4 MW. During the tests, an accelerating gradient of 28.5 MV/m was achieved, which means that shorter modules could still be designed.[22]

In 2001, TERA proposed a *cyclinac*-based facility for proton therapy called IDRA (Institute for Diagnostics and RAdiotherapy). A scheme of the facility is shown in Fig. 5. The facility uses a 30 MeV high-current commercial proton cyclotron as a pre-accelerator. The cyclotron is followed by a side-coupled linac, based on the LIBO design, which accelerates protons up to 230 MeV. The linac is 18 meters-long and works at high repetition rate (100–200 Hz). The pulse length is

Fig. 4. First module of LIBO.[22]

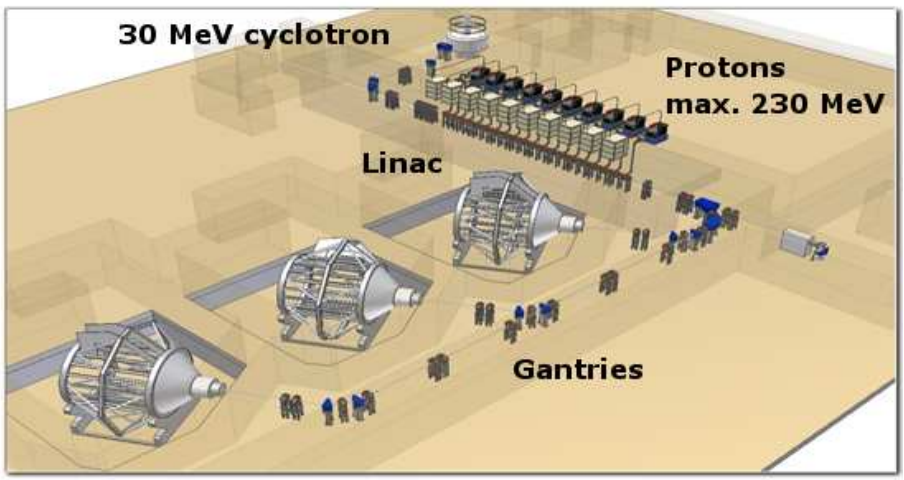

Fig. 5. The IDRA concept, a *cyclinac*-based facility for proton therapy.[21]

3.2 μs. The total peak RF power required by the linear machine is around 60 MW, which at 200 Hz corresponds to an average plug power of 150 kW. Commercial klystrons can be used to power the machine.

The ADAM (Application of Detectors and Accelerators to Medicine, S.A.) company, a CERN spin-off, will exploit the commercial possibilities of this kind of facility. Nowadays two prototype modules for accelerating protons from 30 to 41 MeV are being built and are being currently tested by the ADAM Accelerating Structure Department.[21]

3.3.2. ACLIP*, a booster for a 30 MeV cyclotron*

A collaboration which comprises the University Federico II of Naples, the INFN section of Naples, the University and the INFN section of Milan, the University and the INFN section of Bari, the University of Sannio, CERN and the e2v Technologies company has designed a 3 GHz proton standing wave CCL which differs from LIBO because the half-cells forming an accelerating tank are cut in such a way that the number of pieces to be machined is reduced by a factor of 2.[23] Based on this design, ACLIP receives the protons delivered by a 30 MeV cyclotron and accelerates them to 62 MeV. It will be followed by a LIBO to accelerate the protons from 62 to 200–230 MeV. ACLIP consists of 5 modules for a total length of 3.1 m. The first module, already built and tested, is divided into two tanks and should accelerate protons from 30 to 35 MeV (accelerating gradient of 16 MV/m). Acceleration tests has been performed at the Catania INFN cyclotron facility with success.

3.3.3. TOP *project, all-linac solution for proton therapy*

The TOP (Terapia Oncologica con Protoni) project proposes an all-linac solution for proton therapy. The project is followed by ENEA (Ente per le Nuove tecnologie, l'Energia e l'Ambiente) and ISS (Istituto Superiore di Sanità) at the oncological centre IFO in Rome. A Radio-Frequency Quadrupole (RFQ) followed by a Drift-Tube Linac (DTL) accelerates protons up to 7 MeV. Both accelerators operate at 425 MHz. Then, particles are injected into a 3 GHz Side-Coupled Drift-Tube Linac (SCDTL), which accelerates them up to 40 MeV. The length of the SCDTL is around 10 m. RF power required to feed it is around 8 MW. Finally, protons achieve the appropiate energy for therapy in a 3 GHz side-coupled linac of LIBO type.[24] The facility based on this accelerator complex is called TOP-IMPLART and is shown in Fig. 6.

3.3.4. *3 GHz* CABOTO *for hadron therapy*

CABOTO (CArbon BOoster for Therapy in Oncology) is a first solution proposed by the TERA Foundation for carbon therapy. An SC-EBIS (SuperConducting-Electron Beam Ion Source) source produced by DREEBIT GmbH (Dresden) will deliver about $5 \cdot 10^7$ fully stripped carbon ions in 1.5 μs at 400 Hz. The ions will be pre-accelerated up to 300 MeV/u in SCENT (Superconducting Cyclotron for Exotic Nuclei and Therapy), a superconducting cyclotron of 350 tons and 5 m diameter which has been designed in the INFN National Laboratory LNS in Catania.[21] Then the particles will be injected into a 3 GHz high-gradient Side-Coupled Linac (SCL) which will accelerate C^{6+} from 300 to 430 MeV/u in 22 meters (the accelerating gradient is about 25 MV/m). The linac is divided into 16 accelerating modules. Each module is fed by its own klystron of 7.5 MW peak power. The beam energy selection is done by switching off certain number of the modules for high energies and regulating the power that is feeding the last active module. The linac

Fig. 6. Artist's view of the projected TOP-IMPLART facility.[24]

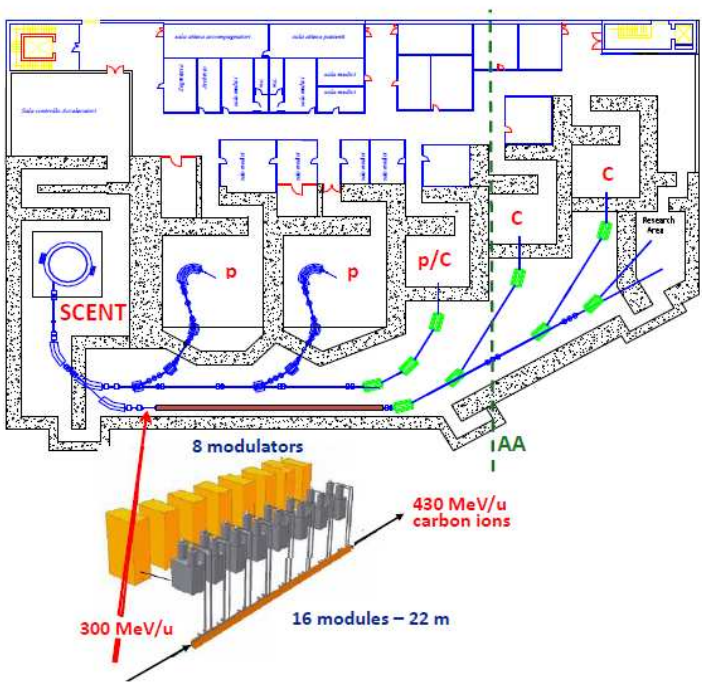

Fig. 7. hadron therapy facility based on the SCENT cyclotron and 3 GHz CABOTO.[21]

operates at high repetition rate ($\leq$ 400 Hz) and delivers short hadron pulses of 1.5 μs. An image of such a center is shown in Fig. 7.

3.3.5. *5.7 GHz* CABOTO *for hadron therapy*

Another design for CABOTO has been recently proposed by TERA Foundation. The main difference between this design and the one presented in the previous section is the frequency and consequently, the maximum accelerating gradient which can be achieved in the linac while ensuring reliable operation.

Three SC-EBIS sources provide a flux of 10^8 C^{6+} in 3 μs pulses at 300 Hz. The ions are pre-accelerated in a superconducting cyclotron up to 120 MeV/u before being injected into the side-coupled linac. The K480 superconducting cyclotron weighs 190 tons and has a 4 m diameter. The linac boosts carbon ions from 120 up to 400 MeV/m. It is being designed for operating at 5.7 GHz and achieving high accelerating gradients (around 40 MV/m), which will permit a reduction in the total length of the linac to about 24 m.[25]

Klystrons of 12 MW peak power with 2 μs pulse length and working at 200–300 Hz will feed the 18 modules which compose the linac. The accelerator complex is shown in Fig. 8. By switching on and off the last modules of the linac and by adjusting the amplitude and phase of the power delivered by the klystron to the last module in operation, one can adjust continuously the output energy, as in all linacs described in this chapter. Commercial compact solid-state modulators power the klystron. ADAM is testing the reproducibility in adjusting the power amplitude and the RF phase of such a device.

The linac will also permit the acceleration of H_2^+ molecules for proton therapy. Total average plug power for running the complex is 800 kW.[26]

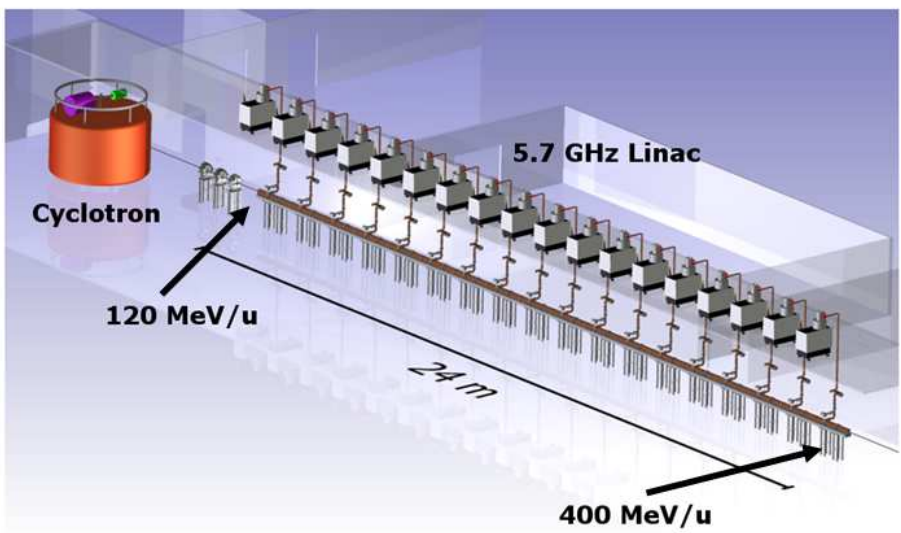

Fig. 8. Artist's view of 5.7 GHz CABOTO, TERA's proposal for hadron therapy.[25]

4. FFAGs for Hadron Therapy

The concept of FFAG accelerators was independently proposed in Japan, Russia and the USA in the 1950's. A comprehensive text where the basics of an FFAG accelerator are explained was published by Craddock and Symon in 2008 (see Ref. 27). Other books and papers also give a general overview of this subject (see Refs. 18, 28 and 29).

In the following discussion, the fundamentals of FFAGs are introduced.

4.1. *Basics on FFAGs*

FFAGs are circular accelerators that can provide high-intensity pulsed beams.

Circular machines are based on the use of magnetic fields to guide the charged particles along a closed orbit. The acceleration is usually performed in few accelerating cavities which are traversed by the particles many times during their circular motion. Compared with linacs, this greatly simplifies the RF system which provides the energy to the particles. Since the cavity fields are oscillating, acceleration is not possible at all times and a specific synchronism condition between the particles and the cavities is needed. Every turn, the particle gains some energy, which translates into a gain of momentum.

The radius of the orbit described by the particle is derived from the Lorentz equation and depends on both the particle momentum and the magnetic field of the machine:

$$r = \frac{p}{qB}, \tag{5}$$

where r is the radius of the orbit, p is the momentum, q is the charge of the particle and B is the magnetic field. The maximum orbit radius is determined by the maximum magnetic field that can be induced in the magnets and the output beam energy.

In circular machines, the beam sees the same magnet lattice several times. Such periodic lattices are greatly affected by the resonances. Small deviations in particle trajectory due to magnet misalignment or field imperfections occur periodically every turn. If these perturbations are synchronized with the oscillatory motion of the particles, there is a resonance, and their effect adds up. As a consequence, the beam can be lost, which implies structure activation, structure damage and lost time before the beam can run into the machine again.

*The Fixed-Field Alternating-Gradient (*FFAG*) accelerators*

FFAGs consist of a series of fixed field magnets distributed and shaped in such a way that the beam can be strongly focused.

The employment of fixed fields (i.e. the magnetic field B is static in time) avoids the appearance of eddy currents, allows high repetition rates and simplifies the machine operation. According to Eq. (5), the use of fixed fields has the consequence that particles follow, on average, spiral orbits of increasing radius, and thus the

machines require bigger beam pipes and magnets. FFAGs are high intensity accelerators as the radial and momentum acceptances are quite big.

Strong focusing is achieved by application of the alternating gradient (AG) principle. The chain of magnets which constitutes the accelerator alternates focusing and defocusing magnets. Following this, the particles are deflected inwards and outwards alternatively.

There are two ways for obtaining a net focusing effect of the lattice: if focusing magnets are stronger than defocusing magnets and/or if the particles which were previously deflected by the defocusing magnets arrive further from the center of the focusing magnet. The last trick benefits from the fact that the focusing force in a magnet is proportional to the trajectory displacement in respect to the magnet center.

The net focusing effect that can be achieved using the AG principle is greater than the one achieved in other circular machines like betatrons, which is the reason why it is commonly known as *strong focusing*. Strong focusing leads to a decrease of the beam oscillation amplitude and therefore smaller magnets apertures. It also allows a reduction in the spread suffered by equilibrium orbits in the radial coordinate which results in smaller magnets.

Additional focusing can be done by taking advantage of fringe fields at magnet edges and by choosing an appropriate magnet pole shaping.

The magnetic field B in the magnets of an FFAG can be written as

$$B(r) = B_0 \cdot \left(\frac{r}{R_0}\right)^k, \tag{6}$$

where B_0 is the reference magnetic field at the magnet center, r is the radial coordinate with origin at the accelerator center, R_0 is the distance between the accelerator center and the magnet center and k is the field index or field factor (see Fig. 9). One distinguishes two types of magnets: linear and non-linear magnets, depending on the variation of the magnetic field B with respect to the radial coordinate r. Linear magnets have $k = 1$; non-linear magnets present $k \neq 1$.

Resonance crossing is a problem in case of low acceleration rate. Beam stability can be severely compromised. In order to avoid slow resonance crossing, the orbit shape, beam optics and tunes are preserved during the acceleration process by keeping k constant. FFAGs which operate on this principle are called scaling FFAGs (S-FFAG). If rapid acceleration is possible, there is no time to damage beam quality while crossing resonances and consequently there is no point in keeping orbit shape, beam optics and tunes constant. Those FFAGs in which k is not constant are known as non-scaling FFAGs (NS-FFAG). In Fig. 10 the trajectories described in both scaling and non-scaling FFAG are shown.

4.2. *FFAGs performance*

FFAGs have interesting characteristics which would make them very attractive for hadron therapy. In principle, FFAGs can provide a high average current pulsed

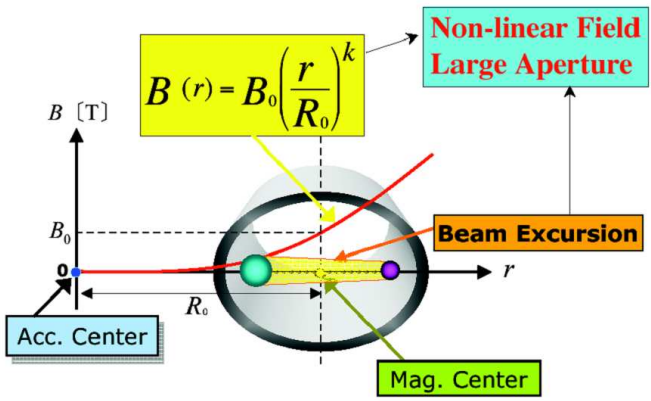

Fig. 9. Magnetic field variation with respect to the radial coordinate for an FFAG.[30]

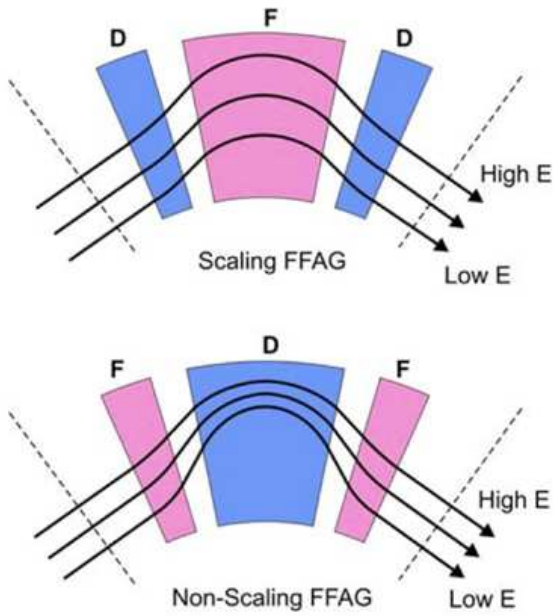

Fig. 10. Trajectories described by the particles in a scaling FFAG and in a non-scaling FFAG.

beam at high repetition rate.[11,14,31,32] Moreover, the beam can be extracted at different energies with appropriate magnetic and electric deflectors but without the need of absorbers.[11,31] The variable energy and the high repetition rate are interesting for the three-dimensional multipainting of tumours. However, only small

currents are needed for hadron therapy (of the order or less than 1 nA instead of the many mA of the other FFAG applications) and in this respect the FFAG solution is not particularly appropriate.

By definition, these compact machines use fixed fields. This yields some benefits: simple operation, simple and cheap power supplies and the absence of eddy-currents.[5]

In general, technical difficulties of FFAGs are related to magnets complexity, extraction techniques and the broad-band high-gradient RF cavities needed for acceleration. Broad-band cavities need more power than narrow-band cavities; high gradients in the operating frequency band used in FFAGs are limited by the Kilpatrick's criterion.

S-FFAGs are easy to operate and present less difficulties when resonances are crossed. Nevertheless, a chain of S-FFAGs is required for a medical facility and S-FFAGs need radially large and costly magnets.[28] On the contrary, NS-FFAGs magnets are smaller and simpler than those used in S-FFAGs and the special magnet configuration leads to a smaller machine circumference. So far, however, they have dense lattices, which makes the placement of RF cavities, injection and extraction lines complicated. Moreover, many resonances are crossed while accelerating the particles in a NS-FFAG, which compromises beam stability. Furthermore, operation of NS-FFAG must still be proven.

The next section contains the recent designs of FFAGs for hadron therapy. The different proposals have been organized taking into account if the machine is under design, construction or operation. The most advanced projects correspond to S-FFAGs. All the NS-FFAGs designed for hadron therapy are still in the design phase.

A very complete review on the present developments of FFAGs for hadron therapy has been recently published (see Ref. 28). The paper also includes a discussion on the advantages and disadvantages associated with each type of FFAG.

4.3. *FFAGs for hadron therapy*

4.3.1. *In operation*

Just one facility all over the world is currently running FFAGs. The facility is in Japan and is exclusively dedicated to research.

Cascade of three S-FFAGs at KURRI (Japan)

The FFAG complex at KURRI (Kyoto University Research Reactor Institute)[33] was conceived as a test facility to prove the feasibility of ADS (Accelerator Driven Sub-critical system). Nowadays it is dedicated to research on nuclear physics, chemistry, material science and cancer therapy. The facility consists of a cascade of three FFAGs and was successfully commissioned in February 2009 (see Fig. 11).

Fig. 11. Cascade of three S-FFAGs for proton acceleration at KURRI.[33]

The first accelerator is an eight spiral sector S-FFAG, with field factor $k = 2.5$ and spiral angle equal to 42°. It was designed to accelerate protons from 0.1 to 2.5 MeV at 120 Hz and has a maximum orbit radius of 0.99 m. The total length of the average orbit is about 5 meters.

The second accelerator is an eight radial sector S-FFAG, with field factor $k = 4.5$, which should accelerate the particles from 2.5 to 20 MeV at 60 Hz. The maximum orbit radius of this accelerator is 1.71 m. The total length of the average orbit is about 9 meters. Low Q cavities of 1 kV which work in the frequency range of 1 to 4 MHz are used for acceleration.

The third accelerator is a 12 radial sector FFAG, with $k = 7.5$, which is designed for accelerating protons from 20 up to 150 MeV at 60 Hz. Its maximum orbit radius is 5.12 m. The total length of the average orbit is about 30 meters.[33–36]

4.3.2. *In commissioning*

Another FFAG-based facility, also located in Japan, is in the commissioning phase. The beam provided by the accelerator complex will be used for nuclear, biological and medical research. It is not clear if it too will be used for proton therapy.

150 MeV S-FFAG, Kyushu University (Japan)

An S-FFAG was designed, constructed and commissioned at KEK (High Energy Accelerator Research Organization) in Japan.[37] It was built in order to prove the operation and possible application of this kind of accelerator to several fields, including proton therapy.

The radial sector S-FFAG, with field index k = 7.5, delivers protons from 10 up to 125 MeV at a repetition rate of 100 Hz. Beam extraction at this values was already proven in 2005. For acceleration, 2 RF cavities of 4 kV have been developed. The RF power output of each cavity is 200 kW. The lattice consists of 12 DFD (defocusing, focusing and defocusing magnets) cells. The peak magnetic field is 1.63 T for the focusing magnets and 0.78 T for the defocusing magnets. Vertical and horizontal tunes are, respectively, 1.45 and 3.62 (given in 2π radians). The diameter of the ring is around 11 meters. The total length of the average orbit is about 35 meters. A 12 MeV cyclotron is used as pre-accelerator.

The accelerator has been disassembled and transported from KEK to the Center for Accelerator and Beam Applied Science at Ito Campus in Kyushu University in 2008. In this facility, a cyclotron will accelerate the particles delivered by an internal PIG (Ion Source for Proton Acceleration) source up to 10 MeV. Then, the particles will be injected into the FFAG by using a septum magnet, an electrostatic septum and two bump magnets. The beam will be extracted from the FFAG by means of a fast kicker magnet and a septum magnet. The magnetic field and the length of these magnets are, respectively, 0.4 T and 0.5 m for the septum and 0.5 T and 0.6 m for the kicker.

During the first stage of the facility (from 2009 to 2013), the FFAG will incorporate some developments and will be commissioned again. Pilot research on nuclear, biological and medical research should also start in this period.[38,39]

4.3.3. *In design*

Several designs of FFAG-based accelerator complexes for hadron therapy have been presented in the last years. In the following those which have not been built yet are presented. The different designs are classified in two groups: those based on S-FFAGs and those based on NS-FFAGs.

Scaling FFAG*s:*

Two S-FFAG-based accelerator complexes for proton therapy and another two for carbon therapy are presented in this section.

RACCAM spiral sector S-FFAG

The RACCAM project (Research on ACCelerators and Applications in Medicine) involves some hospitals and laboratories in France.[40] In this framework a proton 10 spiral sector S-FFAG is under study. The machine will accelerate protons from 70 to 180 MeV. The RACCAM accelerator complex is shown in Fig. 12.

The S-FFAG is divided in 10 spiral sectors, with an angle of 53.7° each. The maximum orbit of the ring is at 3.46 m radius. The total length of the average orbit is about 22 meters. Vertical and horizontal tunes are around 1.60 and 2.76, respectively (given in 2π rad). Cavities of 6 kV with an RF frequency swing from 3

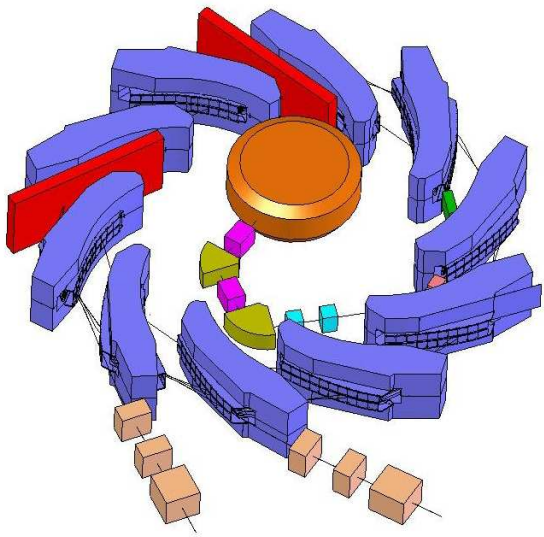

Fig. 12. Layout of the RACCAM accelerator complex. A variable energy cyclotron injects protons in a spiral sector S-FFAG ring.[42]

to 7.5 MHz have been chosen for acceleration.[41] A H^- variable energy cyclotron will inject the protons into the FFAG ring. The cyclotron delivers a beam of protons with an energy between 5.55 and 15 MeV.

Two methods are considered for beam extraction: (i) the horizontal plane single-turn extraction by using a kicker-septum system or (ii) a global variation of magnetic field with variable energy cyclotron injector.[42]

A magnet prototype of the FFAG ring has been already built and measured.[43]

230 MeV S-FFAG, Ibaraki Medical Facility (Japan)

The Ibaraki Medical Facility will obtain a proton beam at a maximum energy of 230 MeV from an eight spiral sector S-FFAG. The high current beam ($I = 0.1\mu$A) will be delivered at a repetition rate between 20 and 100 Hz. A cyclotron will inject the protons at 2.2 meters radius in the main accelerator. The fast extraction will take place for a radius of 4.1 m. The machine diameter will be around 8 m. The total length of the average orbit is about 25 meters.[28,35]

MEICo proton therapy S-FFAG

The company Mitsubishi Electric has initiated design studies of a spiral S-FFAG which will deliver a proton beam up to 230 MeV at a repetition rate of 2 kHz. Superconducting magnets will be used in order to build a very compact machine of 0.7 meters radius.[28,35]

MEICo carbon therapy S-FFAG

Mitsubishi Electric has also studied the design of an S-FFAG for carbon therapy. The accelerator will consist of 16 spiral sectors with a spiral angle of 64°. Warm magnets are used with a maximum magnetic field lower than 1.9 T. The field factor k is planned to be 12. C^{6+} ions will be accelerated from 7 to 400 MeV/u at 500 Hz repetition rate. The radius of the machine is between 7.0 and 7.5 m. The total length of the average orbit is about 40 meters.

Another accelerator with k equal to 0.7 will be used as the injector of the main accelerator. It will accelerate C^{4+} ions up to 7 MeV at the same repetition rate as the main accelerator. The radius of the injector is between 1.4 and 1.8 m. The total length of the average orbit is about 9 meters, so that the total length of the complex is about 50 meters.[28,35]

400 MeV concentric S-FFAGs, Chiba Medical Facility (Japan)

A design of three concentric S-FFAGs was presented as alternative for the Chiba Medical Facility (Japan) in 2004.[44] The very dense lattice of this design (see Fig. 13) makes it difficult to place a fast-extraction system. Finally, a synchrotron was selected for the medical facility and this solution of three concentric S-FFAGs was never implemented.[28,35]

The first FFAG, with $k = 6.5$, accelerates the C^{4+} ions provided by an Electron Cyclotron Resonance (ECR) source from 40 keV/u to 6 MeV/u. One RF cavity with accelerating voltage of 3.3 kV and operating at a frequency between 0.215 and

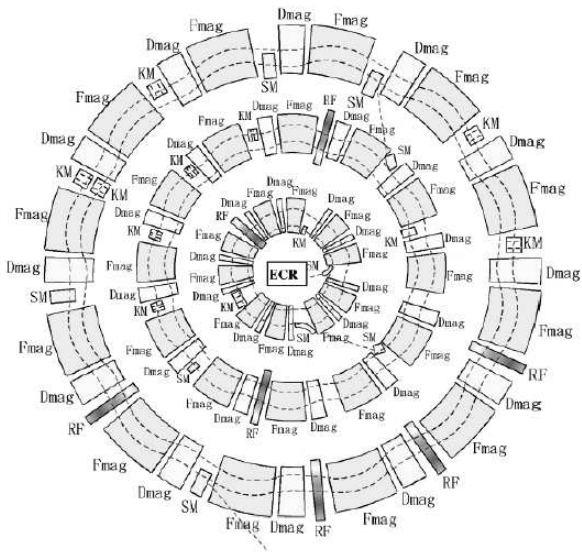

Fig. 13. The three concentric S-FFAGs' proposal for the Chiba Medical Facility.[44]

1.878 MHz is used for acceleration. It requires a power of 20 kW. The injection and extraction radii of this FFAGs are, respectively, 2.1 and 2.9 m. The total length of the average orbit is about 15 meters. The stripping technique is used for beam extraction, so the C^{4+} ions become C^{6+} ions.

The second FFAG, with $k = 5.7$, accelerates C^{6+} ions from 6 to 100 MeV/u. Acceleration is done by two RF cavities with accelerating voltage of 18.4 kV and operating in the frequency range of 0.894 to 3.002 MHz. 90 kW are needed to feed the cavities. The injection radius is 5.9 m and the extraction radius is 6.7 m. The total length of the average orbit is about 40 meters.

The third FFAG, with $k = 10.5$, accelerates C^{6+} ions from 100 up to 400 MeV/u. Four RF cavities with accelerating voltage of 45.5 kV and operating between 1.991 and 3.098 MHz are needed for acceleration. The power required is 180 kW. The injection is done at 10.1 m and the extraction is done at 10.8 m. The total diameter of the accelerator complex is around 22 m. The total length of the average orbit is about 60 meters. The repetition rate for all three accelerators is 200 Hz.

Non-Scaling FFAG*s:*

In the last years, some NS-FFAG-based accelerator complexes designs have been proposed for hadron therapy. Their characteristics are given in the next discussion.

Ion therapy with three concentric linear NS-FFAGs

In 2007 three concentric FFAGs were proposed in Ref. 45. In this design three linear NS-FFAG would accelerate either protons or carbon ions for therapy in a quite dense lattice (see Fig. 14). A radio-frequency quadrupole accelerator and a linear accelerator will inject the beam into the smallest FFAG. The first and the second FFAGs are used for accelerating protons; the second and the third FFAGs are used for accelerating carbon ions. The smallest FFAG, with a radius of 5.5 m, accelerates protons from 7.95 to 31 MeV. The total length of the average orbit is about 35 meters. The medium energy FFAG, with a radius of 6.87 m, receives the protons from the previous FFAG and accelerates them from 31 to 250 MeV. The total length of the average orbit is about 40 meters. This ring can also accelerate carbon ions from 7.9 to 69 MeV/u. The biggest FFAG, with a radius of 8.25 m, accelerates carbon ions which come from the central FFAG from 69 up to 400 MeV/u. The total length of the average orbit of this FFAG is about 50 meters, so that the total length of the three accelerators is about 120 meters. Extraction of the proton beam is performed with one kicker and one septum; extraction of the carbon beam needs two kickers.

Each ring has 48 periodic doublet cells. A cell consists of a focusing and a defocusing magnet followed by a 0.29 meter-long straight insertion where RF cavities and kickers are placed. The distance between magnets is 0.08 m. The maximum magnetic field is 1.69 T for the magnets in the two inner accelerators while it

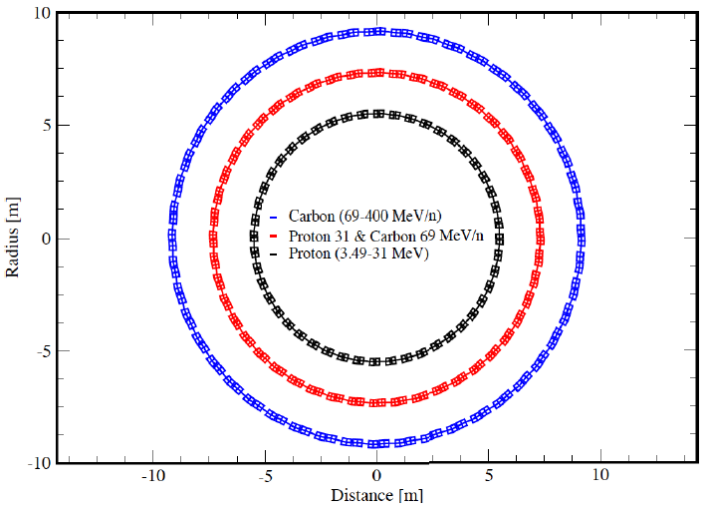

Fig. 14. Lattice of the three concentric linear NS-FFAGs for hadron therapy.[45]

reaches 3.35 T in the outer accelerator (superconducting technology). Focusing magnet lengths for the smallest, medium and biggest rings are 0.17, 0.26 and 0.35 m, respectively; defocusing magnet lengths are 0.18, 0.27 and 0.36 m.

In order to accelerate protons up to 250 MeV, 12 cavities of 19 kV each are needed, which requires a power of 1.2 MW. On the other hand, 37 RF cavities with an accelerating voltage of 19 kV are required in the last ring for accelerating carbon ions up to 400 MeV/u. The total power would be 3.7 MW. Acceleration is performed with frequency-modulated RF cavities whose frequency of operation is around 370 MHz.[28]

Some technical problems related to high accelerating voltages and huge, expensive RF cavities make the construction of this complex difficult.[46]

250 MeV proton therapy linear NS-FFAG

Based on the previous machine, another design for the medium energy ring has been presented.[28] The linear NS-FFAG will accelerate protons from 31 to 250 MeV. It is composed of 24 doublet cells, 1.12 meters-long each. The distance between cells is 0.38 m. Maximum magnetic field is 1.8 T for focusing magnets and 1.5 T for defocusing magnets. Focusing magnets, with an aperture of 0.24 m, have a length of 0.44 m; defocusing magnets, with an aperture of 0.15 m, have a length of 0.22 m. The lattice is shown in Fig. 15. The distance between magnets is 0.08 m. Twelve RF cavities are used for acceleration and beam extraction is performed by 3 kickers. The total radius of the machine is 4.28 m. The total length of the average orbit is about 25 meters. Vertical and horizontal tunes are 7.20 and 7.92 for injection and 1.20 and 3.36 for extraction (given in 2π rad).[47]

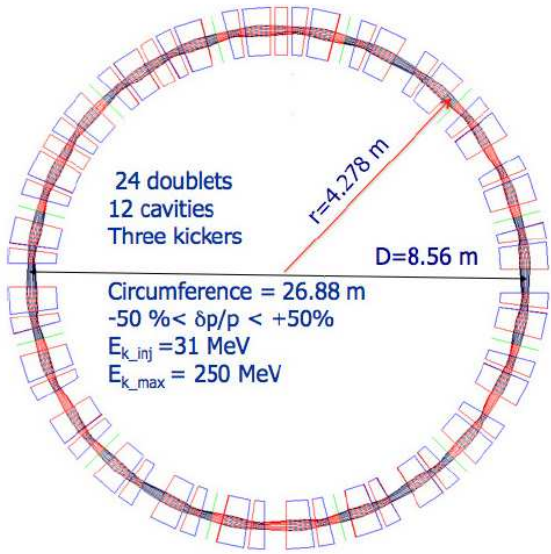

Fig. 15. Lattice of the linear NS-FFAG for proton therapy. The maximum beam energy is 250 MeV. The machine is divided in 24 doubled cells and has a maximum radius of 4.28 m.[28]

PAMELA ion therapy non linear NS-FFAG

The CONFORM project (COnstruction of a Non-scaling FFAG for Oncology, Research and Medicine) is a British collaboration which intends to prove the principle of operation of NS-FFAGs (EMMA, Electron Model for Many Applications) and to explore the possibilities of NS-FFAGs as accelerators for hadron therapy (PAMELA, Particle Accelerator for MEdicaL Applications).

Several preliminary lattices were proposed for PAMELA. The lattice which presented the most stable tune at that moment was selected (Machida's lattice, shown in Fig. 16). The design for PAMELA has been developed around this lattice.[48] PAMELA is a non-linear NS-FFAG that will accelerate protons from 30 to 250 MeV (field factor $k = 38$). The repetition rate of the machine is 1 kHz. Acceleration is provided by no more than 8 RF cavities of 15 kV operating between 1.94 and 4.62 MHz. The lattice is comprised of 12 non-scaling FDF (focusing, defocusing and focusing magnet) triplet cells. The maximum magnetic field in the focusing and defocusing magnets is, respectively, 1.67 and 2.25 T. Magnets are 0.31 meters long. The longest straight drift is 1.7 meters long; the shortest, 0.31 meters long. The maximum orbit radius is 6.25 m, so that total length of the average orbit is about 40 meters. Vertical extraction is used as energy selection system.[49] Protons will be injected to the FFAG by a 30 MeV cyclotron.[11]

The machine is quite big for accelerating protons up to 250 MeV and an extension to a carbon machine does not seem feasible. On the other hand, operation of NS-FFAGs must still be proven. An NS-FFAG for accelerating electrons,

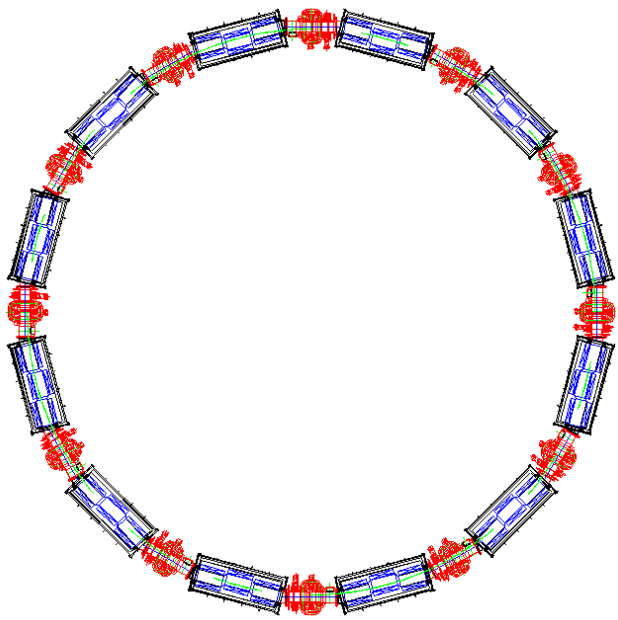

Fig. 16. Machida's lattice. The non linear NS-FFAG is divided in 12 cells and is designed for accelerating protons from 31 to 250 MeV.[11]

EMMA, will try to demonstrate the feasibility of this technology.[50] EMMA will be followed by PAMELA, which should demonstrate the feasibility of non-relativistic NS-FFAGs. It must be remarked that EMMA accelerates electrons and thus is a relativistic NS-FFAG, and is hence intrinsically simpler than a hadron FFAG like PAMELA.

Ion therapy non-linear NS-FFAG

The proposal of the American company Particle Accelerator Corporation is to use an NS-FFAG for accelerating protons up to 250 MeV. After an upgrade the machine could provide both proton and carbon ion beams.[47]

The accelerator will be divided into 8 sectors and will contain 24 superconducting magnets (see Fig. 17). Each sector contains an FDF triplet cell followed by a single, 1.2 meter-long straight insertion. Peak magnetic field will be 3.13 T in focusing magnets and 3.41 T in defocusing magnets. Focusing magnets length is between 0.65 and 0.80 m, with an aperture of 0.63 m, whereas defocusing magnets length is between 0.13 and 0.18 m, with an aperture of 0.55 m. Magnet edge shaping will increase focusing and therefore tune flatness, which will help to cross resonances. The extraction radius of the proton machine is 3.39 m, so that the total length of the average orbit is about 22 m. Vertical and horizontal tunes are 1.75 and 2.48 for injection and 1.55 and 2.48 for extraction (given in 2π rad).

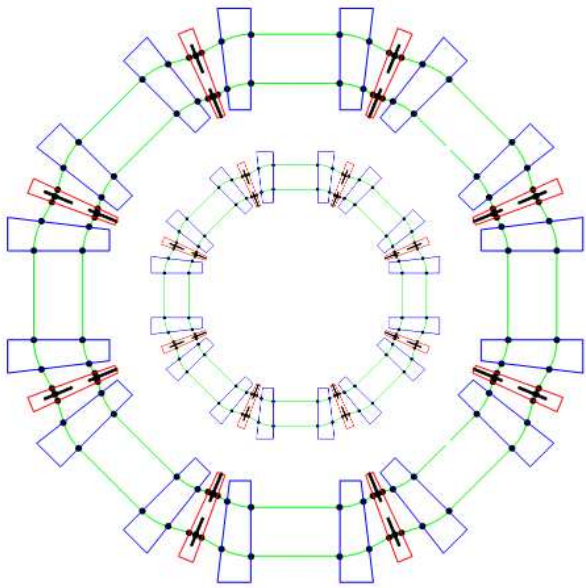

Fig. 17. Johnstone's lattice. An NS-FFAG will accelerate protons up to 250 MeV. The machine is divided in 8 sectors and contains 24 magnets.[47]

In this design, modest RF cavities are needed for particle acceleration. Beam is foreseen to be extracted with fast kickers or by resonance excitation. Simulation tools to describe the FFAG's complex magnetic fields and high-order dynamics have been developed. A preliminary magnet concept design has also been presented. The group reports progress in compactness and tune stability. Enough space is reserved for RF cavities (long straights of 1.17 m, inter-magnet distances between 0.25 and 0.30 m).[47]

The additional ring to accelerate carbon ions from 60 up to 400 MeV/u would also be divided in 8 sectors with an FDF triplet superconducting cell each, with a very large maximum magnetic field of 4 T. The radius is designed to be 6.9 m, so that the total length of the average orbit is about 40 m.[28]

Recently, isochronous orbits have been achieved in a proton FFAG new design. When a machine is isochronous, the magnetic field strength varies with the radial coordinate in such a way that it compensates the relativistic mass gain of the particles with acceleration, so particles take the same time to make one turn in the machine independently on their energy; consequently, the RF frequency of the cavities used for acceleration can be fixed. However, this isochronous approach requires to divide the FFAG into two rings to have reasonable magnet apertures. Further studies are ongoing.[48]

5. Conclusions

The field of research on accelerators for hadron therapy is fully active, which reflects the interest of the scientific community in the subject.

The medical requirements for hadron therapy accelerators were introduced. The information presented came from different papers. A document that establishes the medical requirements for hadron therapy accelerators and that is approved by all the hadron therapy community is still missing. The document should provide the common vocabulary which physicians, medical physicists and accelerator experts dedicated to hadron therapy have to employ to report on therapeutical beam features. It should also identify the beam parameters whose values determine in great manner the success of the treatment and then set the minimum acceptable specifications that any beam intended for hadron therapy must satisfy.

Table 3 tries to summarize the main characteristics of the presented accelerator complexes. In this table, the injection and extraction energy for each accelerator is given. In the case of FFAGs, the quantity Average Orbit Length (AOL) is provided.

Few solutions have been presented for carbon therapy. Efforts mainly focus on developing an appropriate acceleration system for proton therapy. For the moment, both technologies still deal with some challenges.

So far 3 GHz linac accelerating modules with gradients of about 20 MV/m have been proven to work. Moreover, a 15 m long proton therapy linac can be designed so that the output energy is adjusted in a couple of milliseconds by making use of 8–10 distributed modulator-klystron systems running at 100–200 Hz. This feature is not shared by cyclotrons or synchrotrons. However the stability—within 0.3–0.4%—of the 8–10 klystrons output when they run at power levels smaller than the maximum has yet to be checked.

For carbon ion therapy the overall average "voltage" applied by the linac to the particles has to be more than twice the one needed for proton therapy: about 500 MV instead of 200 MV. Reliable operation at accelerating gradients definitely larger than 30 MV/m has to be ensured if the linac has not to be too long. This is the present challenge in the application of linacs to hadron therapy. Frequencies larger than the standard 3 GHz could possibly help in this purpose. For the reason discussed above, the overall RF peak power has to be increased from about 50 MW (protons) to about 200 MW (carbon ions). 10–15 modulator-klystron systems running at 300–400 Hz could provide the power needed. At present 10–15 MW klystrons do not exist for frequencies larger than 6 GHz and this limits the possible RF frequency choice to the 3–6 GHz range.

Concerning FFAGs, more efficient broad-band RF cavities should be developed, further studies on beam extraction are needed and more efforts should be directed towards obtaining simpler and smaller magnets. In the particular case of NS-FFAGs, operation still needs to be proven. Very dense lattices have been presented, which represent a difficulty to place acceleration, injection and extraction systems. Beam losses while crossing resonances remain an issue.

Table 3. Summary of the main characteristics of linac- and FFAG-based complexes for hadron therapy.

ID	Type	Phase	Particle	Energy [MeV]	Rep.Rate [Hz]	Radius/ AOL [m]	
Linac-based complexes							
LIBO	Linac, 3 GHz SCL	Testing	Proton	$62-200$	400	13.5	Inj.: cyclotron
IDRA	Linac, 3 GHz SCL	Design	Proton	$30-230$	100-200	18	Inj.: cyclotron
ACLIP	Linac, 3 GHz CCL	Testing	Proton	$30-62$	-	3.1	Inj.: cyclotron; Booster: LIBO-type
TOP	Linac, 425 MHz RFQ Linac, 3 GHz SCDTL Linac, 3 GHz SCL	Design	Proton	-7 $7-40$ -	-	- 10 -	Booster: LIBO-type
CABOTO 3 GHz	Linac, 3 GHz SCL	Design	Carbon	$300-430$	≤ 400	22	Inj.: SCENT cyclotron
CABOTO 5.7 GHz	Linac, 5.7 GHz SCL	Design	Carbon	$120-400$	200-300	24	Inj.: 4 m radius K480 cyclotron
Scaling FFAG-based complexes							
KURRI	8 spiral sector S-FFAG, k = 2.5 8 radial sector S-FFAG, k = 4.5 12 radial sector S-FFAG, k = 7.5	Operation	Proton	$0.12-2.5$ $2.5-20$ $20-150$	120 60 60	0.99 / 5 1.71 / 9 5.12 / 30	
Kyushu	12 radial sector S-FFAG, k = 7.5, warm	Commiss.	Proton	-125	100	5.5 / 35	Inj.: 10 MeV cyclotron
RACCAM	10 spiral sector S-FFAG, warm	Testing	Proton	$70-180$	-	3.46 / 22	Inj.: 15 MeV cyclotron
Ibaraki	8 spiral sector S-FFAG	Design	Proton	-230	20-100	4.1 / 25	Designed to provide $I = 0.1\mu$A
MEICo-p	spiral sector S-FFAG, cold	Design	Proton	-230	2000	0.7 / 4	
MEICo-C	16 spiral sector S-FFAG, k=12	Design	Carbon	$7-400$	500	7 / 40	Inj.: k = 0.7, radius= 1.4 m
Chiba	S-FFAG, k=6.5, warm S-FFAG, k=10.5, warm S-FFAG, k=10.5, warm	Design	Carbon	-6 $6-100$ $100-400$	200	2.90 / 15 6.70 / 40 10.8 / 60	Never implemented
Non-scaling FFAG-based complexes							
3 NS-FFAG	Lin. NS-FFAG, warm Lin. NS-FFAG, warm Lin. NS-FFAG, cold	Design	Proton p \ C Carbon	$8-31$ $31-250\backslash 8-69$ $69-400$	-	5.5 / 35 6.87 / 40 8.25 / 50	Inj.: RFQ + linac; 48 doublet cells
250 MeV NS-FFAG	Lin. NS-FFAG, warm	Design	Proton	$31-250$	-	4.28 / 25	24 doublet cells
PAMELA	Non Lin. NS-FFAG	Design	Proton	$31-250$	1000	6.25 / 40	Inj.: cyclotron; FDF triplet cells
PAC	Non Lin. NS-FFAG, cold Non Lin. NS-FFAG, cold	Design	Proton Carbon	-250 $60-400$	-	3.4 / 22 6.9 / 40	8 FDF triplet cells

Acknowledgments

This work is the 1^{st} Deliverable of the PARTNER (PARticle Training Network for European Radiotherapy) Work Package 25 "Novel Accelerator Concepts for Hadrontherapy" within the Marie Curie Initial Training Fellowship of the European Community. The research leading to these results has received funding from the Seventh Framework Programme [FP7/2007-2013] under grant agreement number 215840-2.

References

1. E. Niederlaender, Causes of death in Europe, *Eurostat* KS-08-02-001-EN-C (2006).
2. R.R Wilson, Radiological Use of Fast Protons, *Radiology* **47**, 48791 (1946).
3. Particle Therapy Co-Operative Group Website: http://ptcog.web.psi.ch/ptcentres.html
4. PARticle Training Network for European Radiotherapy: http://partner.web.cern.ch/
5. K. Peach, Novel Technologies in Radiation Therapy, talk in workshop on "*Physics for Health in Europe*" (CERN, Geneva, Switzerland, 2010): http://indico.cern.ch/getFile.py/access?contribId=178&sessionId=3&resId=0&materialId=slides&confId=70767
6. J. Flanz, Beam Delivery Systems: Scattering, Scanning w/wo Gantries, talk in workshop on "*Hadron Beam Therapy of Cancer*" (Erice, Italy, 2009): http://erice2009.na.infn.it/TalkContributions/Flanz1.pdf
7. G. Coutrakon and J.M. Slater, Design Considerations for Medical Proton Accelerators, in *Proc. Particle Accelerators Conference* PAC99 (New York, USA, 1999), p. 11-15.
8. S. Peggs, T. Satogata and J. Flanz, A Survey of Hadron Therapy Accelerator Technologies, in *Proc. Particle Accelerators Conference* PAC07 (Albuquerque, New Mexico, USA, 2007), p. 115-119.
9. W. Wieszczycka and W.H. Scharf, *Proton Radiotherapy Accelerators*, 1st edn. (World Scientific Publishing Co., Singapore, 2001).
10. R. Orecchia, Health Economic Aspects, lecture in PARTNER course on "*Hadrontherapy: Today and Tomorrow*" (CERN, Geneva, Switzerland, 2010): http://indico.cern.ch/contributionDisplay.py?contribId=22&confId=84152
11. K. Peach, J. Cobb, S. Sheehy, H. Witte, T. Yokoi, R. Fenning, A. Khan, R. Seviour, C. Johnstone, B. Jones, B. Vojnovic, M. Aslaninejad, M. Easton, J. Pasternak, J.K. Pozimski, N. Bliss, C.D. Beard, P. McInstosh, S.L. Smith, S.I. Tzenov, T.R. Edgecock, J. Rochford, D. Kelliher, S. Machida, C. Rogers, R.J. Barlow, H. Owen and S. Tygier Robert, PAMELA Overview: Design Goals and Principles, in *Proc. Particle Accelerator Conference* PAC09 (Vancouver, Canada, 2009).
12. M. Goitein, Proton Medical Facilities: what next?, in *Proc. Particle Therapy Co-Operative Group* PTCOG39 (San Francisco, USA, 2003).
13. U. Linz, Ion Beam Facilities from a Medical Perspective, talk in workshop on "*Hadron Beam Therapy of Cancer*" (Erice, Italy, 2009): http://erice2009.na.infn.it/TalkContributions/Linz.pdf
14. A.R. Smith, Vision 20/20: Proton Therapy. *Med. Phys.* **36**, 556-568 (2009).
15. G. J. Caporaso, Y. J. Chen and S. E. Sampayan, The Dielectric Wall Accelerator, in *Reviews of Accelerator Science and Technology*, Vol. 2 (World Scientific Publishing Co., 2009), p. 253-263.

16. T.P. Wangler, *Principles of* RF *Linear Accelerators*, 2nd edn. (John Wiley & Sons Inc., Darmstadt, 2008).
17. H. Wiedemann, *Particle Accelerator Physics. Basic Principles and Linear Beam Dynamics*, 2nd edn. (Springer-Verlag, Heidelberg, 1993).
18. M. S. Livingstone and J. P. Blewet, *Particle Accelerators* (McGraw Hill Book Company Inc., New York, 1962).
19. W. P. Kilpatrick, Criterion for Vacuum Sparking Designed to Include Both RF and DC, VCRL-2321 (1953).
20. A. Grudiev and W. Wuensch, A New Local Field Quantity Describing the High Gradient Limit of Accelerating Structures, in *Proc. Linear Accelerators Conference* LINAC08 (British Columbia, Canada, 2008), p.936-938.
21. U. Amaldi, S. Braccini and P. Puggioni, High Frequency Linacs for Hadrontherapy, in *Reviews of Accelerator Science and Technology*, Vol.2 (World Scientific Publishing Co., 2009), p. 111-131.
22. U.Amaldi, P. Berra, K. Crandall, D. Toet, M. Weiss, R. Zennaro, E. Rosso, B. Szeless, M. Vretenar, C. Cicardi, C. De Martinis, D. Giove, D. Davino, M.R. Masullo and V. Vaccaro, LIBO- A Linac-Booster for Protontherapy: Construction and Tests of a Prototype, *Nucl. Instr. and Meth. A* **521**, 512-529 (2004).
23. V.G. Vaccaro, C. De Martinis, D. Giove, M.R. Masullo, S.J. Mathot, A.C. Raino, R.J. Rush and V. Variale, Design, Construction and Low Power RF Tests of the First Module of the ACLIP Linac, in *Proc. European Particle Accelerators Conference* EPAC08 (Genoa, Italy, 2008), p. 1836-1838.
24. L. Picardi, S. Frulliani and C. Ronsivalle, TOP-IMPLART *Schema Progettuale* (Italy, 2009).
25. U. Amaldi, R. Bonomi, S. Braccini, M. Crescenti, A. Degiovanni, M. Garlasché, A. Garonna, G. Magrin, C. Mellace, P. Pearce, G. Pittà, P. Puggioni, E. Rosso, S. Verdú-Andrés, R. Wegner, M. Weiss and R. Zennaro, Accelerators for Hadrontherapy: From Lawrence Cyclotrons to Linacs, to appear in *Nucl. Instr. and Meth. A*.
26. A. Degiovanni, U. Amaldi, R. Bonomi, M. Garlasché, A. Garonna, S. Verdú-Andrés and R. Wegner, A Cyclotron + Linac Complex for Carbon Ion Therapy, talk in workshop on "*Physics for Health in Europe*" (CERN, Geneva, Switzerland, 2010): http://indico.cern.ch/contributionDisplay.py?contribId=65&confId=70767
27. M.K. Craddock and K.R. Simon, Cyclotrons and Fixed-Field Alternating-Gradient Accelerators, in *Reviews of Accelerator Science and Technology*, Vol.1 (World Scientific Publishing Co., 2008), p. 65-97.
28. D. Trbojevic, FFAGs as Accelerators and Beam Delivery Devices for Ion Cancer Therapy, in *Reviews of Accelerator Science and Technology*, Vol.2, (World Scientific Publishing Co., 2009), p. 229-251 (2009).
29. M. S. Livingstone, *Development of High Energy Accelerators* (Dover Publications Inc., 1966).
30. C. Ohmori, *FFAG*, talk in the 8^{th} International Committee for Future Accelerators ICFA Seminar on "*Future Perspectives in High Energy Physics*" (Kyungpook National University, Daegu, Korea, 2005).
31. J. Pasternak, J. Fourrier, E. Froidefond, B. Autin, F. Méot, J.L. Lancelot, D. Neuvéglise and T. Planche, Spiral FFAG for Hadrontherapy, in *Proc. Cyclotrons and Their Applications* (Catania, Italy, 2007), p. 198-200.
32. M. Tanigaki, Y. Mori, M. Inoue, K. Mishima, S. Shiroya, Y. Ishi, S. Fukumoto and S. Machida, Present Status of FFAG Accelerators in KURRI for ADS Study, in *Proc. European Particle Accelerators Conference* EPAC06 (Edinburgh, UK, 2006), p. 2367-2369.

33. Kyoto University Research Reactor Institute Web Page: http://www.rri.kyoto-u.ac.jp/en/
34. *Operation and Development of Facilities*, KURRI Progress Report 2008: http://www.rri.kyoto-u.ac.jp/en/PUB/PR/ProgRep2008/V_Operation.pdf
35. R. Edgecock, Introduction to FFAGs and a Non-Scaling Model, lecture in John Adams Institute for Accelerator Science, Oxford, UK (2005): http://www.adams-institute.ac.uk/lectures/robert_edgecock_ffag-adams.pdf
36. Y. Mori, Development of a proton FFAG accelerator for ADS at KURRI, talk in FFAG08 (Manchester, UK, 2008): http://www.cockcroft.ac.uk/events/FFAG08/presentations/Mori/ADSR-KURRI-1@FFAG08.pdf
37. FFAG synchrotron Home Page: http://hadron.kek.jp/FFAG
38. Kyushu University Web Page (Center for Accelerator and Beam Applied Science): http://www.kyushu-u.ac.jp/english/university/information/ins.php#20
39. Y. Yonemura, H. Arima, N. Ikeda, K. Ishibashi, K. Maehata, T. Noro, T. Okai, K. Sagara, N. Shigyo, Y. Uozumi, G. Wakabayashi, H. Ishikawa, H. Nakayama, A. Takagi, S. Fukumoto, Y. Kimura, T. Tomimasu and Y. Mori, Status of Center For Accelerator And Beam Applied Science of Kyushu University, in *Proc. European Particle Accelerators Conference* EPAC08 (Genoa, Italy, 2008), p. 3521-3523.
40. The RACCAM project: http://lpsc.in2p3.fr/service_accelerateurs/raccam.htm
41. F. Méot, private communication, 2010.
42. S. Antoine, B. Autin, W. Beekman, J. Collot, M. Conjat, F. Forest, J. Fourrier, E. Froidefond, J.L. Lancelot, J. Mandrillon, P. Mandrillon, F. Méot, Y. Mori, D. Neuvéglise, C. Ohmori, J. Pasternak and T. Planche, Principle Design of a Proton-therapy, Rapid-Cycling, Variable Energy Spiral FFAG, *Nucl.Instr. and Meth. A* **602**, 293-305 (2009).
43. T. Planche, J. Fourrier, J.L. Lancelot, F. Méot, D. Neuvéglise and J. Pasternak, Design of a Prototype Gap Shaping Spiral Dipole for a Variable Energy Protontherapy FFAG, *Nucl.Instr. and Meth. A* **604**, 435-442 (2009).
44. T. Misu, Y. Iwata, A. Sugiura, S. Hojo, N. Miyahara, M. Kanazawa, T. Murakami and S. Yamada, Design Study of Compact Medical Fixed-Field Alternating-Gradient Accelerators, in *Physical Review Special Topics - Accelerators and Beams*, Vol. 7, 094701 (2004).
45. D. Trbojevic, A.G. Ruggiero, E. Keil, N. Neskovic and A. Sessler, Design of a Non-Scaling FFAG Accelerator for Proton Therapy, LBNL Paper LBNL-57177 (2005).
46. E. Keil, Are FFAG Rings for Hadron Therapy Competitive?, talk in FFAG08 (Manchester, UK, 2008): http://www.cockcroft.ac.uk/events/FFAG08/presentations/Keil/compete.pdf
47. C. Johnstone, S. Koscielniak, M. Berz, K. Makino, P. Snopok and F. Mills, Nonscaling FFAG Variants for HEP and Medical Applications, in *Proc. Particle Accelerator Conference* PAC09 (Vancouver, Canada, 2009), p. 1-3.
48. C. Johnstone, private communication (2010).
49. T. Yokoi, Overview of PAMELA: The UK Non-Scaling FFAG Medical Facility, talk in workshop on "*Hadron Beam Therapy of Cancer*" (Erice, Italy, 2009): http://erice2009.na.infn.it/TalkContributions/Yokoi.pdf
50. The EMMA project: http://www.astec.ac.uk/projects/emma.html

International Journal of Modern Physics A
Vol. 26, Nos. 10 & 11 (2011) 1690–1712

DOI: 10.1142/S0217751X11053110

World Scientific
www.worldscientific.com

ADVANCES IN NONLINEAR NON-SCALING FFAGs

C. JOHNSTONE
Fermilab, Batavia, IL 60510, USA
cjj@fnal.gov

M. BERZ and K. MAKINO
Michigan State University, East Lansing, MI 48824, USA

S. KOSCIELNIAK
TRIUMF, Vancouver, BC 60439, Canada

P. SNOPOK
Illinois Institute of Technology, Chicago, IL 60616, USA

Accelerators are playing increasingly important roles in basic science, technology, and medicine. Ultra high-intensity and high-energy (GeV) proton drivers are a critical technology for accelerator-driven sub-critical reactors (ADS) and many HEP programs (Muon Collider) but remain particularly challenging, encountering duty cycle and space-charge limits in the synchrotron and machine size concerns in the weaker-focusing cyclotrons; a 10–20 MW proton driver is not presently considered technically achievable with conventional re-circulating accelerators. One, as-yet, unexplored re-circulating accelerator, the Fixed-field Alternating Gradient or FFAG, is an attractive alternative to the other approaches to a high-power beam source. Its strong focusing optics can mitigate space charge effects and achieve higher bunch charges than are possible in a cyclotron, and a recent innovation in design has coupled stable tunes with isochronous orbits, making the FFAG capable of fixed-frequency, CW acceleration, as in the classical cyclotron but beyond their energy reach, well into the relativistic regime. This new concept has been advanced in non-scaling nonlinear FFAGs using powerful new methodologies developed for FFAG accelerator design and simulation. The machine described here has the high average current advantage and duty cycle of the cyclotron (without using broadband RF frequencies) in combination with the strong focusing, smaller losses, and energy variability that are more typical of the synchrotron. The current industrial and medical standard is a cyclotron, but a competing CW FFAG could promote a shift in this baseline. This paper reports on these new advances in FFAG accelerator technology and presents advanced modeling tools for fixed-field accelerators unique to the code COSY INFINITY.[1]

1. Introduction

Accelerators are playing increasingly important roles in basic science, technology, and medicine including accelerator-driven subcritical reactors, industrial irradiation, material science, neutrino production, and provide one of the most effective

treatments for many types of cancer. Multi-MW proton driver capability remains a challenging, critical technology for many core HEP programs, particularly the neutrino ones such as the Muon Collider and Neutrino Factory, and for high-profile energy applications such as Accelerator Driven Subcritical Reactors (ADS) and Accelerator Transmutation of Waste (ATW) for nuclear power and waste management.[2–4] Aggressive, coordinated and funded programs are underway in Europe[5] (Belgium,[6] the U.K.[7]), Asia (India, Japan,[8] South Korea,[9] recently China[10]), also Russia, the Ukraine, Belarus, and Brazil on proton driver technologies.

Such high-intensity, multi-GeV accelerators however encounter duty cycle and space-charge limits in synchrotrons and machine size concerns in the weaker-focusing cyclotrons. A 10–20 MW proton driver is challenging at best, if even technically feasible, with conventional accelerators. Only an SRF linac, which has the highest associated cost and footprint, is presently considered realizable. Work is focused almost exclusively on an SRF linac, as, to date, no re-circulating accelerator can attain the high intensities necessary for the nuclear applications. However, the ultra-high reliability issues required in the nuclear applications complicate the accelerator and dramatically impact the cost and drive the technology to the limits in the linac solution. The only unexplored, potential candidate for ultra-high intensity, high energy applications is the Fixed-Field Alternating Gradient accelerator (FFAG).[2]

This increasing demand for higher and higher beam power, duty cycle, and reliability at reasonable cost has thus focused world attention on fixed-field accelerators, notably a broad class of accelerators termed Fixed-field Alternating Gradient (FFAGs). (Cyclotrons can be considered a specific expression or sub-class of FFAGs which employ a predominately constant rather than gradient magnetic field.) The fixed magnetic fields, strong focusing (coupled to recent advances in tune stability), a large dynamic aperture, compact footprint, and, importantly, the capacity for isochronous or CW operation have attracted international attention.[11] These new breeds of FFAGs have been tagged by energy collaborations for serious study.[2,12]

Advanced FFAG designs, however, are not mature and their ultimate limits in performance are just beginning to be explored. Recently, the concept of isochronous orbits has been proposed and developed for the most general type of FFAG (termed non-scaling) using powerful new methodologies in fixed-field accelerator design], with the concept recently achieved in non-scaling nonlinear FFAG designs.[13,14] The property of isochronous orbits enables the simplicity of fixed RF and by inference, CW operation. By tailoring a nonlinear radial field profile, the FFAG can remain isochronous, well into the relativistic regime. Therefore one application is high-intensity, and, in particular, high-energy (GeV) proton drivers. (Continuous beam delivery and ultra-high reliability are required to avoid thermal shock to the reactor in the nuclear application, mandating CW operation capability.[2]) With isochronous orbits, the FFAG has the high average current and duty cycle advantages of a cyclotron in combination with the strong focusing, smaller losses, and energy variability that are more typical of a synchrotron.

FFAG accelerator technology has been recently transferred to industry, with electron scaling FFAGs rapidly becoming commercially available. NHV and Mitsuibishi Corporations in Japan are building compact high current electron FFAGs which have a proven size advantage over other industrial electron accelerators.[15] Although the cyclotron is the current industrial and medical standard, a competing CW FFAG would have a broad impact on medical accelerators, proton drivers for neutron production, accelerator-driven nuclear reactors, waste transmutation, the production of radiopharmaceuticals, and open up a range of as-yet unexplored industrial applications. A high-energy, high-intensity CW re-circulating proton accelerator would have specific impact on HEP facilities and nuclear power. This paper reports on new advances in FFAG accelerator technology, design, and simulation, and also presents advanced tools developed for all fixed-field accelerators recently added the high-order code COSY INFINITY.[1]

2. Background

The FFAG concept in acceleration was invented in the 1950s independently in Japan,[16] Russia[17] and the U.S[18] (T. Ohkawa[16] in Japan, H.S. Snyder[18] at Brookhaven, and A.A. Kolomenskij[17] in the Soviet Union). The field is weak at the inner radius and strong at the outer radius, thus accommodating all orbits from injection to final energy. Focusing is provided by an alternating gradient. An extensive discussion of the various FFAG configurations, including derivations of the formulas relating the various accelerator and orbit parameters can be found in the references.[19] The configuration initially proposed was called a radial sector FFAG accelerator.[20] A spiral sector configuration[21] was also invented consisting of magnets twisted in a spiral as the radius increases, such that a beam crossing the magnet edges experiences alternating gradients. With no reverse-bending magnets, the orbit circumference of the spiral-sector scaling FFAG is about twice that for a circular orbit in a uniform field. These machines are the so-called scaling FFAGs (either spiral or radial-sector FFAGs) and are characterized by geometrically similar orbits of increasing radius. Direct application of high-order magnetic fields and edge focusing maintains a constant tune and optical functions during the acceleration cycle and avoids low-order resonances. The magnetic field follows the law $B \propto r^k$, with r as the radius and k as the constant field index.

The non-scaling FFAG was invented in 1997 (C. Johnstone and F. Mills) and a working lattice published in 1999[22] as a solution for the rapid acceleration of muon beams. The non-scaling FFAG proposed for muon acceleration utilizes simple, combined function magnets like a synchrotron. However, it does not maintain a constant tune and is not suitable for an accelerator with a modest RF system and requiring many turns for acceleration.

Recently, innovative solutions were discovered (C. Johnstone, Particle Accelerator Corp.) for non-scaling FFAGs which approximated the constant tune feature of the scaling FFAG without applying the scaling principle. This new non-scaling

FFAG accelerator applied weak and alternating gradient focusing principles (both edge and field-gradient focusing) in a specific configuration to a fixed-field combined-function magnet to stabilize tunes.[23−25] Note that, stable tunes, however, do not imply isochronous orbits or CW operation.

Isochronous orbits are achievable only at relativistic energies in a synchrotron and predominately non-relativistic energies in a cyclotron. In a synchrotron, the magnetic field increases proportional to energy and therefore particles are confined about a laboratory-based reference trajectory independent of energy. Since the path-length is fixed independent of energy, a frequency change is required except at highly-relativistic energies, so swept-frequency RF is unavoidable even at GeV energies. In a fixed-field machine, such as a FFAG or cyclotron, the reference orbit moves outward transversely with energy. The orbital path length and the orbital frequency change with energy (at energies approximately $\geq \frac{1}{4}$ GeV in a cyclotron). The challenges faced in a fixed-field accelerator, a FFAG or a high-energy cyclotron, are therefore twofold: the RF frequency must change or "sweep" to match the beam revolution time and the large orbit swing implies a cavity design with a large transverse aperture.

Recently, the concept of isochronous orbits coupled with constant machine tunes has been researched and successfully developed for the non-scaling FFAG using powerful new methodologies in fixed-field accelerator design.[26] By tailoring a nonlinear radial field profile, the FFAG can remain isochronous with stable tune, well into the relativistic, multi-GeV regime for protons. Specifically, the problem of isochronous, or CW operation, has been solved for a non-scaling FFAG design in an energy regime of a GeV and higher. This property of isochronous orbits enables the simplicity of fixed-frequency RF and by inference, CW operation, as in the cyclotron, but with strong focusing. (More quasi-isochronous orbits permit more rapid, > 100 Hz, swept-frequency RF, operation, a rate not achievable in synchrotrons and synchro-cyclotrons.) Designing and demonstrating performance for the FFAGs with their complex field profiles and edge contours required new advances in accelerator modeling.[13,14] The strong focusing attribute, particularly in the vertical plane of the FFAG as compared to cyclotrons, further implies stronger vertical envelope control and some degree of mitigation of space-charge effects when compared to the cyclotron. These new innovations will be discussed in detail in later sections after broader concepts describing properties of fixed-field accelerators are presented.

3. Dynamics of Fixed-Field Accelerators

Tune is perhaps the most important optical indicator of stable particle motion, since it determines when particles in the beam, executing periodic motion around the accelerator, return to the same transverse position relative to a central, or reference orbit in the machine. In a fixed-field machine such as an FFAG or cyclotron, this reference orbit moves with energy so the tune is controlled through radial and azimuthal variations in the magnetic field as described below.

Three conventional techniques exist for controlling the beam envelope and corresponding tune, or phase advance, in a magnetic field. The first confinement technique is the weak focusing principle used in classical cyclotrons in which changes in path-length through the magnetic field as a function of transverse position focus the beam, but only in the bend plane (which is typically horizontal). Weak focusing by the dipole component of the field in the body of the magnet does not affect the vertical plane.

The second arises from the field falloff at the physical edge of a magnet. A vertically-oriented (horizontally-bending) dipole field presents either a horizontally focusing or defocusing effect or no effect depending on the on the angle through which the beam traverses the fringe field. This edge effect is essentially equivalent to a quadrupole-like element located at each magnet edge: it can be either focusing horizontally and defocusing vertically, or the reverse for a non-normal crossing angle. (A normal entrance angle has no focusing effect.) In a cyclotron, vertical control is established via edge focusing through deliberate radial shaping of the pole-tip combined with a non-normal edge-crossing angle. The use of an edge-crossing angle in a cyclotron for vertical envelope control is normally weaker than focusing from path-length differences in the horizontal plane.

The remaining technique used in synchrotrons involves application of strong-focusing, alternating gradients in consecutive ring magnets. Strong-focusing techniques are capable of focusing equally in both planes with much stronger strengths resulting in larger phase advances, shorter focal lengths, and corresponding higher machine tunes than achievable in weak-focusing machines, i.e. stronger and more versatile envelope control. Contrary to cyclotrons, edge focusing effects are kept deliberately small in large multi-cell synchrotron rings. This term becomes increasingly important for and often causes difficulties in the dynamics of small synchrotron rings.

All three principles are applied in FFAGs—scaling machines specifically require edges plus gradient fields in relatively constant strengths to achieve similar orbits and corresponding constant tunes. In the non-scaling FFAG, the different focusing principles are combined in different and generally varying composition through the acceleration cycle—the varying composition can be exploited to control the machine tune without applying the field scaling law.

In particular, and unlike a cyclotron, the strength of the edge focusing and centripetal terms can be enhanced in the presence of a gradient - importantly their strength can increase with radius and therefore with energy. Understanding the powerful interplay between gradient and the centripetal and edge focusing is critical to understanding the dynamics and potential of the FFAG accelerator.

3.1. *Thin lens formalism*

The application of the transverse focusing terms and their inter-dependence can be understood conceptually using the thin-lens approximation. This approximation

provides direct insight into the transverse dynamics of both FFAGs and traditional accelerators

The dynamics of most accelerators can be expressed and understood almost completely in terms of the three "conventional" transverse focusing principles outlined above. To understand the interplay between strong, weak and edge focusing, a simple linear, thin-lens matrix model serves as a guiding example. The approach is most easily rendered using a simple sector magnet matrix, adding a gradient term to the focusing, and then applying an edge angle to the entrance and exit. The following is the first order matrix for a horizontally-focusing sector magnet with a gradient and an edge angle, η.

$$M = \begin{bmatrix} 1 & 0 \\ -\frac{\tan\eta}{\rho_0} & 1 \end{bmatrix} \begin{bmatrix} \cos\Theta & \frac{1}{\sqrt{K}}\sin\Theta \\ -\sqrt{K}\sin\Theta & \cos\Theta \end{bmatrix}, \tag{1}$$

where $\Theta = \sqrt{K}l$ and $K = k_0 + \frac{1}{\rho_0^2}$ for a combined function sector magnet with a linear gradient. For the edge angle we adopt the sign convention to be: $\eta > 0$ is outward, or away from the body of the magnet and thus it increases the net horizontal focusing. Reducing to thin lens, the matrices from the center of the gradient magnet through the edge are:

$$\begin{aligned} &\begin{bmatrix} 1 & 0 \\ -\frac{\tan\eta}{\rho_0} & 1 \end{bmatrix} \begin{bmatrix} 1 & l \\ -Kl & 1 \end{bmatrix} \approx \begin{bmatrix} 1 & 0 \\ -\frac{\eta}{\rho_0} & 1 \end{bmatrix} \begin{bmatrix} 1 & l \\ -Kl & 1 \end{bmatrix} \\ &= \begin{bmatrix} 1 & l \\ -\left(k_F l + \frac{l}{\rho_F^2} + \frac{\eta}{\rho_F}\right) & -\frac{\eta l}{\rho_F} + 1 \end{bmatrix} \\ &\cong \begin{bmatrix} 1 & l \\ -\left(k_F l + \frac{l}{\rho_F^2} + \frac{\eta}{\rho_F}\right) & 1 \end{bmatrix} \\ &= \begin{bmatrix} 1 & l \\ -\left(k_F l + \frac{(\vartheta+\eta)}{\rho_F}\right) & 1 \end{bmatrix} = \begin{bmatrix} 1 & l \\ -\frac{1}{f_F} & 1 \end{bmatrix}, \end{aligned} \tag{2}$$

where $k_0 \to K_F$ and $\rho_0 \to \rho_F$ for a horizontally focusing gradient and $\frac{l}{\rho_F^2} \cong \frac{\vartheta}{\rho_F}$, where ϑ is the sector bend angle and the length l is the half-magnet length. The edge angle here has been assumed small to allow the tangent function to be approximated. Note that the gradient does not necessarily have to be linear; this thin lens derivation applies "locally" even in the presence of a nonlinear gradient. For the case of a nonlinear gradient, the local focusing strength (B') is simply evaluated at each orbital location.

From Eq. (3) for the thin-lens focal length, one can immediately see that the sector angle and edge angle term increase the focusing in the horizontal plane for a positive bend angle or dipole component. The choice of dipole component—which, in the presence of a gradient, changes at each reference orbit as a function of energy—has very important consequences. If the dipole component increases with radius, then focusing increases with energy relative to injection. Both the centripetal

and edge-angle term add constructively with the strong-focusing. The integrated strength of the strong-focusing term can also increase if

a) the edge angle increases the path length through the magnetic field, and/or
b) if the gradient itself increases with radius (for a non-constant gradient; i.e. higher or quadrupole).

When the integrated strong focusing strength increases as a function of energy, it serves to stabilize the tune. Both planes are not identical, however, for in the vertical only the strong focusing and edge-angle terms contribute to a change in focusing strength.

$$1/f_F = k_F l + \frac{\vartheta}{\rho_F} + \frac{\eta}{\rho_F}. \tag{3}$$

Therefore, in the vertical version of Eq. (3), only the gradient, $k_D l$, and the edge term η/ρ_D apply so two terms contribute to the vertical machine tune. The following summarizes tune and envelope control in conventional accelerators.

- Centripetal (Cyclotrons + FFAGs):
  - bend plane only, horizontally defocusing or focusing;
  - strength $\propto \theta/\rho$ (bend angle/bend radius of dipole field component on reference orbit);
- Edge focusing (Cyclotrons + FFAGs):
  - horizontally focusing / vertically defocusing, vice versa, or no focusing;
  - strength $\propto \tan\eta/\rho$, or $\sim \eta/\rho$ for a small edge-crossing angle (edge crossing angle/bend radius of dipole field component at entrance to magnet;
- Gradient focusing (Synchrotrons + FFAGs):
  - body field components > dipole: $B = a + bx + cx^2 + dx^3 + \ldots$; $B' = b + 2cx + 3dx^2 + \ldots$;
  - constant gradient: synchrotrons, linear-field non-scaling FFAGs (muon FFAGs);
  - scaled nonlinear field, gradient increases with r or energy: scaling FFAGs;
  - arbitrary nonlinear field, gradient increases with r or energy: nonlinear, non-scaling FFAGs.

4. FFAG Design Principles

In a scaling FFAG, the field-scaling law predetermines that the reference beam trajectories remain parallel implying that much of the optics remain constant with energy—in particular the tunes remain fixed. The non-scaling FFAG relaxes this condition and aims only for stable beam during acceleration. If the acceleration is quick, then tune variations can be tolerated. If the acceleration is slow the tune must be more controlled (although some tune variation can be accommodated or compensated for if the acceleration cycle is slow enough).

Non-scaling in its simplest terms implies nonparallel reference orbits in a FFAG. Although parallelism automatically implies constant tune (through fixed number of betatron oscillations), it is not a necessary condition. In the non-scaling FFAG, the different focusing terms can be varied independently to control tune and further optimize machine parameters. This last point is very important for FFAGs because it allows the field, orbit location, and important machine parameters such as tune, footprint, and aperture to be more independent and strongly controlled than in cyclotron.

The constant + linear-gradient field case serves as an instructive example. Interestingly, this case remains a valid "local" interpretation of FFAG dynamics even in the presence of a strongly nonlinear global field. The local "quadrupole" strength parameter, k, is simply the "local" derivative of the field profile evaluated at the reference orbit for a specific energy. Even in the case of only linear gradient field profiles, a sextupole component[27] arises when the quadrupole body field is combined with an edge angle. The presence of higher-order field components contributes still higher nonlinear terms in combination with an edge angle. Therefore, even in the linear case, the dynamics do not obey linear optics. However, a local interpretation in terms of linear optics and dynamics remains valid and is critical to designing and understanding compact FFAG accelerators.

4.1. *FFAG lattice design*

FFAG lattices are completely periodic, like a cyclotron. Periodicity permits closed geometry and repetitive, adiabatic optical solutions over a tremendous range in momentum. However, the strong-focusing does allow stable, "long" straights to be integrated into the base unit cell. (Specialized utility insertions are under development but are nontrivial to properly match over the large dynamical momentum range of the FFAG).

All lattices are simple, single lens structures based on the FODO cell. That is, the maximum and minimum beam envelopes alternate between opposing planes—even in the so-called doublet and triplet FFAGs. Single lens structures are optically stable over a large range in momentum; there are no telescope-based FFAGs with any significant dynamical range.

FFAGs utilize short cells to achieve short focal lengths. The stronger the focusing and the shorter the focal length; the more adiabatic the optical functions, and the larger the stable momentum range. FFAG designs exploit combined function magnets to minimize unit cell length and optimize dynamic range. Long straights are inserted at points of reflection symmetry in the lattice (at points where the derivatives of optics functions are zero) thereby causing little disruption to the periodic optics.

4.2. *Progression of non-scaling FFAG design*

Initial non-scaling FFAG lattices (EMMA project)[11] utilized a linear fields/constant gradient and rectangular magnets. However, it does not maintain a constant tune

and is not suitable for an accelerator with a modest RF system and therefore a slower acceleration cycle.

With tune the strongest indicator of stable particle motion, simply constraining the machine tune can be sufficient to design a stable machine. In all fixed-field accelerators, the FFAG or the cyclotron, the reference orbit moves with energy. Using this property, tune can be controlled in a linear or nonlinear gradient FFAG by shaping the edges of the magnets.

All three focusing terms are impacted by the edge contour and their interaction can be used to manipulate the machine tune in the horizontal. Two terms, gradient and edge focusing, are available for tune control in the vertical. For example, use of a gradient plus an edge angle on a linear-gradient magnet enhances not only the integrated strong-focusing strength, but also weak (centripetal), and edge focusing as a function of radius (and therefore energy). Further, in a non-scaling FFAG, contributions from the different strength terms can vary with radial position and can also be independent in the F and D magnets. In a non-scaling FFAG the edge crossing angle often changes with energy resulting in non-similar orbits. This increase in strength of all the terms tracks the increase in momentum and stabilizes the tune. The result is a dramatic increase in the momentum reach of the machine, from 2–3 to a factor of 6 utilizing a simple edge contour on a constant-gradient magnet. Figures 1 and 2 indicate the improvement in tune control in a constant-gradient non-scaling FFAG through application of a simple linear edge contour.

Completely stable tunes, and compact machines in footprint and aperture, however, required higher-order, field profiles tailored to reach the advanced specifications. An arbitrary field expansion has been exceptionally successful in controlling both tunes and physical attributes of a machine. An order of magnitude increase

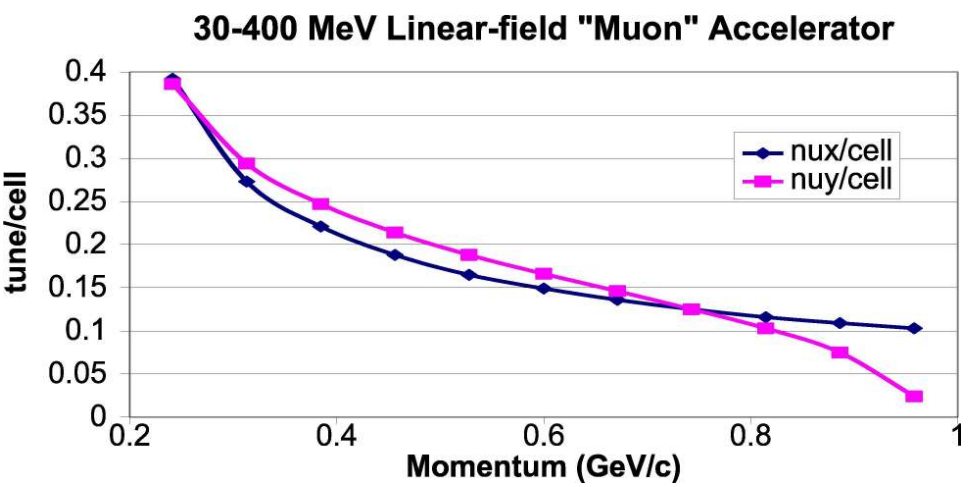

Fig. 1. Variation of tune in a linear gradient, large acceptance non-scaling FFAG for rapid acceleration.

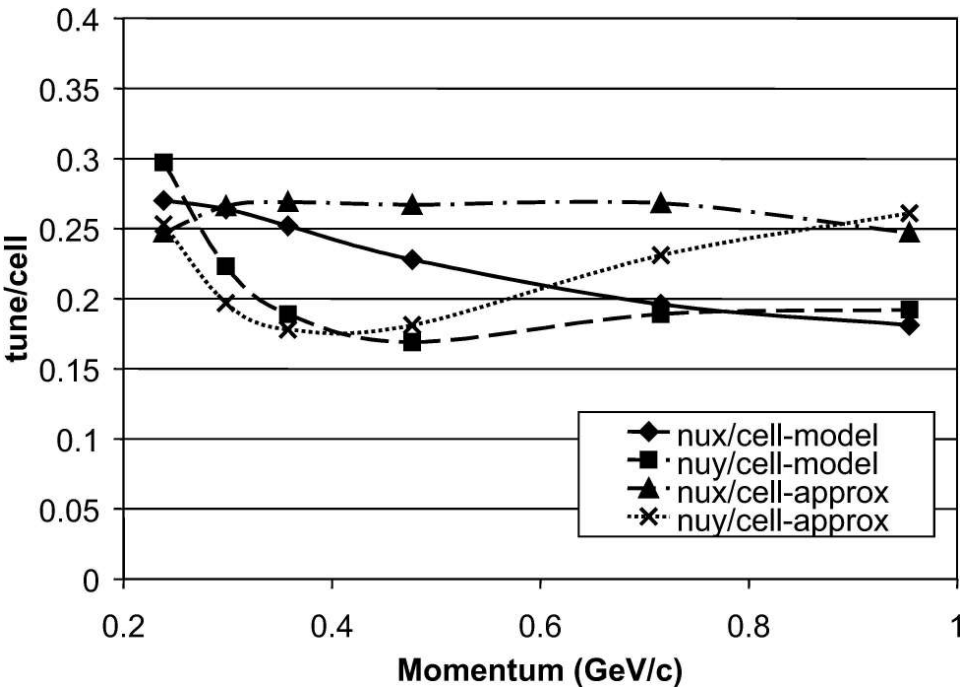

Fig. 2. A constant gradient non-scaling FFAG with an edge contour to stabilize tune. Approx curves indicate the results of a thin lens solution of linear dynamical equations and model curves give the results of a calculation in the accelerator code, MAD.[30]

has been achieved in momentum range relative to the initial non-scaling concept (an acceleration range of a factor of 44 has actually been achieved in one ultra-compact nonlinear design). Even in predominately nonlinear fields, the strong focusing permits adjustment of cell tunes to produce a large dynamic acceptance and surprisingly linear performance (elliptical phase space portraits).

Further, isochronous orbits have been achieved in a non-scaling FFAG by applying both a nonlinear gradient and edge contour. Isochronous implies CW operation and simple RF systems.

Isochronous orbit path lengths are proportional to velocity. However, the orbital path length of a particular momentum follows the B field and thus is not necessarily proportional to velocity. At relativistic energies, the momentum which defines the trajectory and ultimately the path length is an increasingly nonlinear function of velocity. Therefore, the integrated B field must be a nonlinear function of radius to keep it proportional to the relativistic velocity. A nonlinear field expansion combined with an appropriate edge angle can constrain the orbit at each momentum to be proportional to velocity and simultaneously control the tune. Unlike the cyclotron which relies on a dipole field and is therefore limited in adapting path length to match relativistic velocities, the non-scaling FFAG can maintain isochronous orbits well into strongly relativistic energy regimes as shown in Fig. 3.

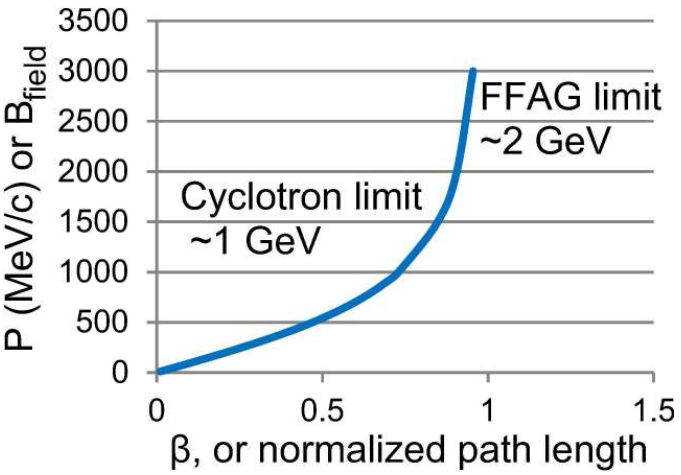

Fig. 3. Momentum dependence ($\propto \langle B \rangle$ field) on velocity (or path length) to maintain isochronous condition.

Further, the nonlinear gradient required to achieve this decreasing change in path length with increasing momentum at relativistic energies has the advantage of providing increasing focusing in both transverse planes as a function of energy.

5. Isochronous FFAG Design

In general, conventional accelerator codes provide too little flexibility in field description and are limited to low order in the dynamics; as such they cannot adequately formulate and predict FFAG accelerators, especially in the presence of the strong nonlinearities from edge contours and fields along with other high-order effects.

Powerful new methodologies in accelerator design and simulation have been pioneered using control theory and optimizers in advanced design scripts with final simulation in COSY INFINITY.[1] COSY INFINITY now has a full complement of sophisticated simulation tools to fully and accurately describe both conventional accelerators and the FFAG's complex electromagnetic fields. Specifically, new tools were developed for the study and analysis of synchrotron, cyclotron, and FFAG dynamics based on transfer map techniques unique to the code COSY INFINITY. With these new tools, closed orbits, transverse amplitude dependencies, and dynamic aperture are determined inclusive of full nonlinear fields and kinematics to arbitrary order. Various methods of describing complex fields and components are now supported including representation in radius-dependent Fourier modes, complex magnet edge contours, as well as the capability to interject calculated or measured 3D field data from a magnet design code or actual components, respectively. These new advanced tools fulfill a critical need in advanced accelerator design.

6. Design and Simulation Tools

A major prerequisite for advanced accelerator design is the existence of reliable, easy to use optimization and simulation tools. Such tools are different in nature for FFAGs than those used in other kinds of accelerators; the rapidly azimuthally varying fields entail significant fringe field effects and out-of-plane nonlinearities. Tracking of orbits for assessment of dynamic aperture needs to be carried out with careful consideration of the nonlinearities, with modern methods of symplectification to insure phase space volume conservation. Further, space charge effects inherent in the high-power operation of the devices produce very novel challenges due to the necessity to treat crosstalk with neighboring orbits. Optimization challenges are difficult since they always affect many orbits at the same time and hence need to be of a global nature.

The ability to model FFAGs—both scaling and non-scaling—with conventional codes is limited. Often new prototypes of accelerators including FFAGs are simulated with codes like MAD[29] and Optim[30] as the standard codes for modeling, but these codes do not provide much flexibility in the description of the available fields and are limited to low order. This limitation can be inadequate to fully demonstrate performance including dynamic aperture, where strong nonlinearities due to edge fields and other high-order effects appear. The significant size of the beam emittance nominally invalidates the paraxial representation (kinematical, or angle effects in the Hamiltonian are significant), which implies that codes that fully represent the kinematics are necessary.

The cyclotron code CYCLOPS[31] has been used to describe the FFAG, but has limited accuracy in this application primarily due to lack of out-of-plane expansion order, which specifically impacts the ability to describe dynamic aperture especially in the case of edge effects with rapid field fall-off—a condition that appears in the FFAG but is not normally present in cyclotrons. Field expansion codes such as ZGOUBI[32] can accurately track the kinematics of such machines, but they have limitations when field profiles become very complex and include significant nonlinear effects. Further, ZGOUBI requires dedicated effort and expertise in order to implement a FFAG design accurately, cannot easily deal with the large transverse emittances required, and lacks some modern analysis tools for symplectic tracking, global optimization, tune shifts and chromaticities, and resonance analysis. In particular, field map codes are difficult to use when one wants to study parameter dependencies, perform detailed study of dynamic aperture, extract advanced optical functions such as high-order resonances, or use optimization routines to study the most advantageous combination of multipole correction schemes, for example.

Modern extensions of the transfer map-based philosophy,[33] as implemented in the arbitrary order code COSY INFINITY,[1] can remedy the limitation in order and in the accuracy of the dynamics. It is particularly suitable for accurate, high-order descriptions of accelerators. Yet in their standard configuration based on pre-selected field elements like combined function magnets with edge angles, they

are still not sufficient to describe in full detail the richness of the nonlinearities that can arise in the fields.

Significant enhancements of the code COSY INFINITY for the particularly challenging case of FFAG accelerators have been implemented. Based on the Differential Algebra (DA) approach,[33] unconventional arbitrary-field elements comprising the machine can now be described in a conventional matrix formulation to any order, without any approximations in the dynamics. The following is a list of the powerful features developed for accelerators and native to COSY INFINITY.

Arbitrary Order Maps COSY allows the computation of all dynamics of the system to arbitrary order, including out-of-plane expansions of fields and any nonlinear terms in the Hamiltonian.

Arbitrary Fields There is no limitation in principle of the fields COSY can treat, as long as they can be modeled in a reasonable way. For efficient initial simulation and optimization, it is particularly useful to utilize very high order out-of-plane expansions of suitable mid-plane models.

Symplectic Tracking There are various methods to perform tracking in COSY that preserve the symplectic symmetry inherent in Hamiltonian systems, including methods that do so with minimal modifications based on the EXPO approach described in Ref. 34. These allow a very faithful estimation of dynamic aperture.

Nonlinear Analysis Tools In addition to the mere empirical study, there are various tools for analysis of nonlinear effects, including the normal form-based computation of high-order amplitude-dependent tune shifts and resonances.

Sophisticated Global Optimization COSY allows the automatic adjustment and optimization of arbitrary system parameters; and different from other tools, the search uses methods of global optimization with constraints over a prespecified search region, and not merely local optimization from a starting parameter setting.

In practice, different accelerators are described accurately by different orders in the matrix, or map. For design studies, often orders around 5 or 7 are sufficient; however, once a specific or optimal configuration is chosen, final tracking studies are usually pursued at the 11^{th}–15^{th} order for required accuracy in predicting performance.

6.1. *Examples: 6-fold symmetric FFAG*

To provide an illustrative example, a sample FFAG having six-fold symmetry was studied, with focusing supplied by an azimuthal field variation expressed as a single Fourier mode, as well as edge focusing. The system is studied to various orders of out-of-plane expansion, so that conclusions about dynamic aperture can be drawn. The results for orders three and five, which are typical for the situation of conventional out-of-plane expansion in codes like CYCLOPs, are shown. Since the method used in COSY is not based on divided differences, the necessary in-plane derivatives can actually be calculated to any order desired with an accuracy that is always close to machine precision.[33]

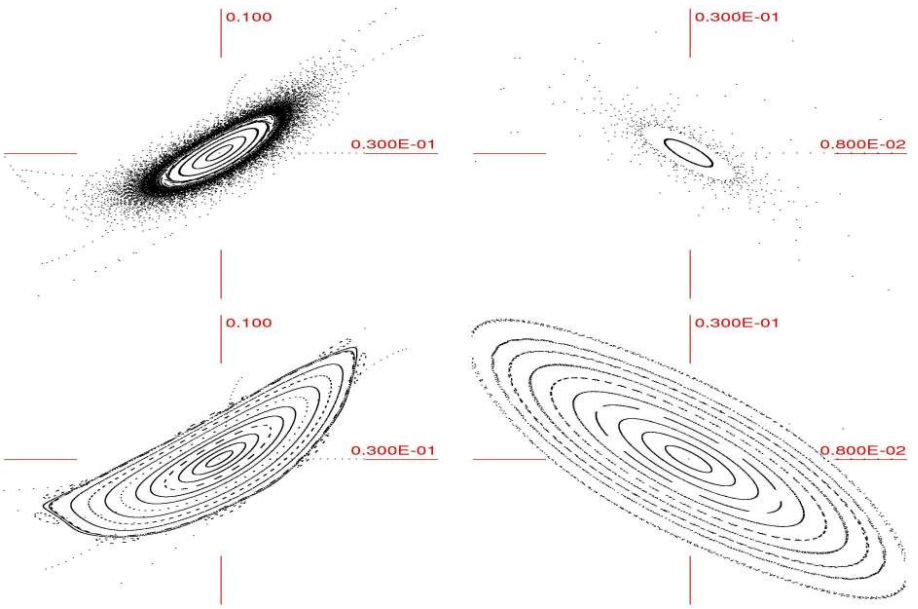

Fig. 4. Tracking in a model non-scaling FFAG with third-order out of plane expansion, without symplectification (top) and with symplectification (bottom).

The results of tracking without symplectification and with Expo symplectification are shown in Figs. 4–6. The Expo symplectification scheme is known to minimize the alterations to the non-symplectic tracking results compared to other symplectification methods. Still, symplectification greatly affects the inferred dynamic aperture of the system.

However, Fig. 6, which is based on order eleven out-of-plane expansion, shows significant additional effects and a different dynamic aperture, suggesting that the low order methods for out-of-plane expansion and dynamics are not sufficient to capture the details of the dynamics. It would in fact lead to an incorrect prediction of dynamic aperture, underestimating it in the horizontal direction and overestimating it in the vertical. Further increases in order beyond eleven do not significantly affect the details of the symplectic motion shown, but continue to influence the non-symplectic motion. A rough estimate reveals that in this particular case, the dynamics as seen in non-symplectic tracking seems to begin to stabilize around order 17, which is still rather easily obtained within the power of a modern workstation.

6.2. *FFAG and cyclotron design*

A powerful new methodology has been pioneered for all fixed-field accelerator optics design (FFAGs and cyclotrons), using control theory and optimizers to develop executable design scripts. These procedures allowed global exploration of all important machine parameters in a simplified lattice. With this methodology, the stable

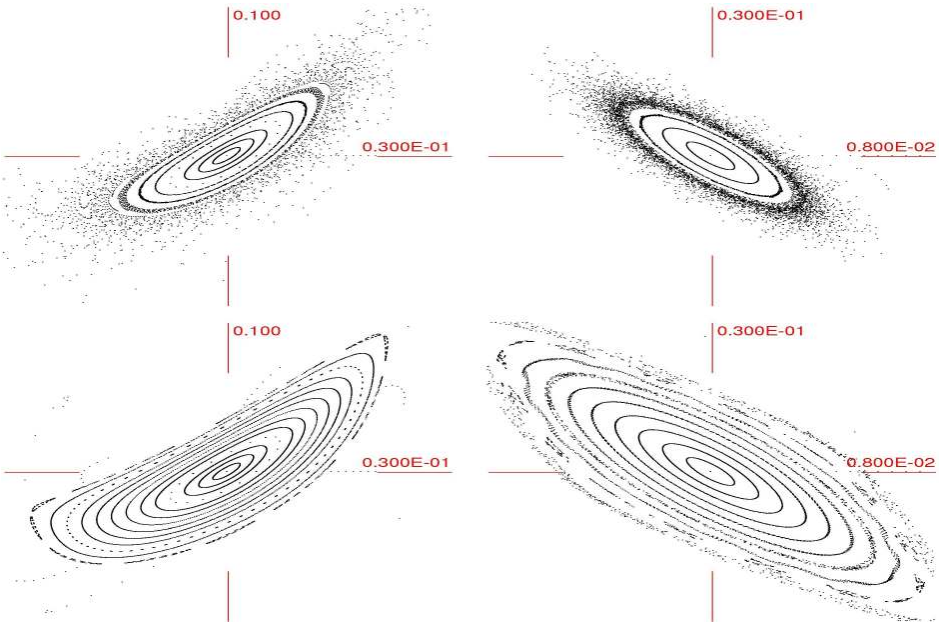

Fig. 5. Tracking in a model non-scaling FFAG with fifth-order out of plane expansion, without symplectification (top) and with symplectification (bottom).

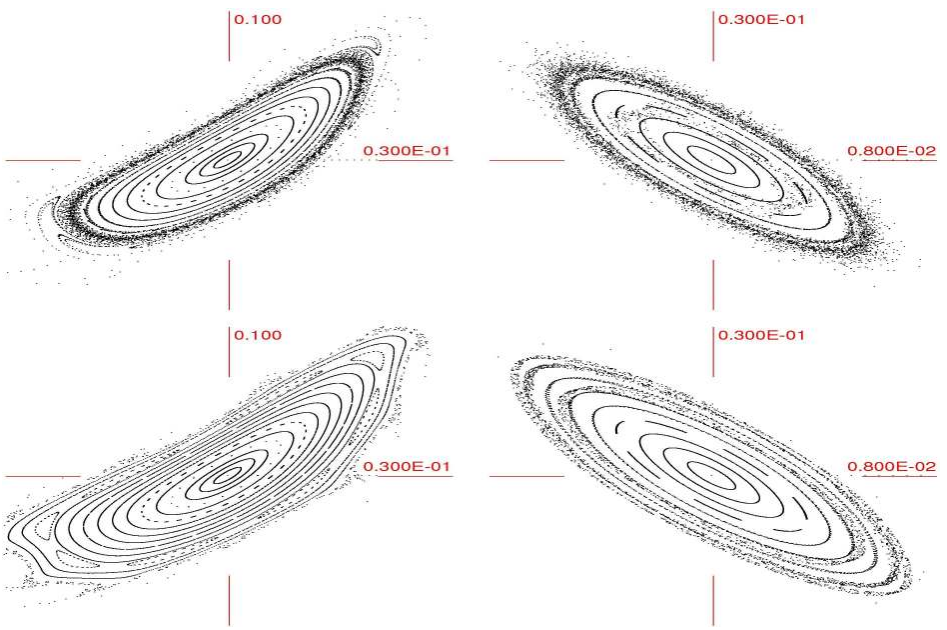

Fig. 6. Tracking in a model non-scaling FFAG with eleventh-order out of plane expansion, without symplectification (left) and with symplectification (right).

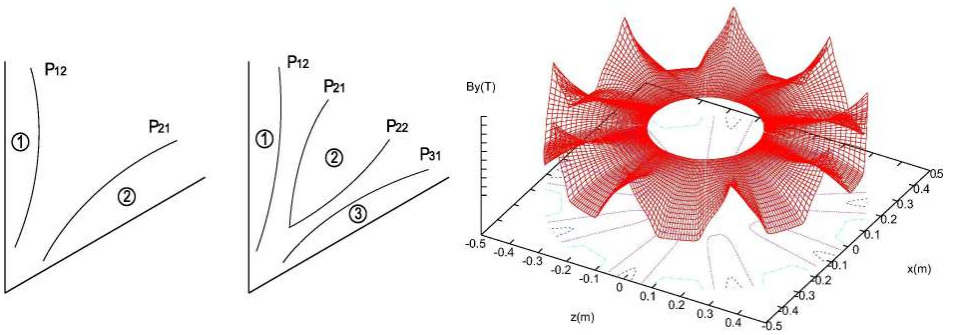

Fig. 7. Complex edge profiles supported in COSY (left) and realistic 3D field expansion output (right) by COSY in polar coordinates derived from simple starting design lattices.

machine tune for FFAGs, for example, was expanded over an acceleration range of 3 up to 6 in momentum with linear fields and a factor of 44 with nonlinear fields and included optimization of complex edge contours, footprint, and components. Full evaluation of the starting lattice, however, required the specific, new advanced simulation tools not existing in current accelerator codes. Such tools have been developed and implemented as an add-on to COSY INFINITY; the FACT (FFAG And Cyclotron Tools) accurately predict and optimize machine performance (Fig. 7). One output format from this add-on software is a 3D field expansion in polar coordinates which can be used by other codes (Fig. 7). In practice, the starting points describing the lattice as output from the design scripts are directly imported into and modeled in COSY INFINITY using FACT software.

Using this powerful methodology, scripts were implemented to design and optimize a FFAG and also for an equivalent cyclotron (low-energy, 4 MeV designs) shown in Fig. 8. The isochronous sector cyclotron employs a 5 kG field. The FFAG initiates injection at 5 kG, but the field rises to 1 T at extraction which allows longer straight sections between magnets thus improved extraction efficiency.

6.3. *High-energy isochronous FFAG example*

As discussed above, the concept of isochronous orbits has been invented for non-scaling FFAGs. This concept has been tested on a preliminary 0.25–1 GeV non-scaling FFAG designed using the new methodologies and optimizers described above. Two options are available to extend this initial effort to a complete accelerator system:

a) a two-ring system, both isochronous, with the lower energy one H^- or
b) a single ring with a high-order field profile which reaches 5T at extraction to increase compactness and energy range.

For the two-ring system use of H^- in the lower energy ring permits CW injection into the higher-energy ring through charge-changing or stripping methods.

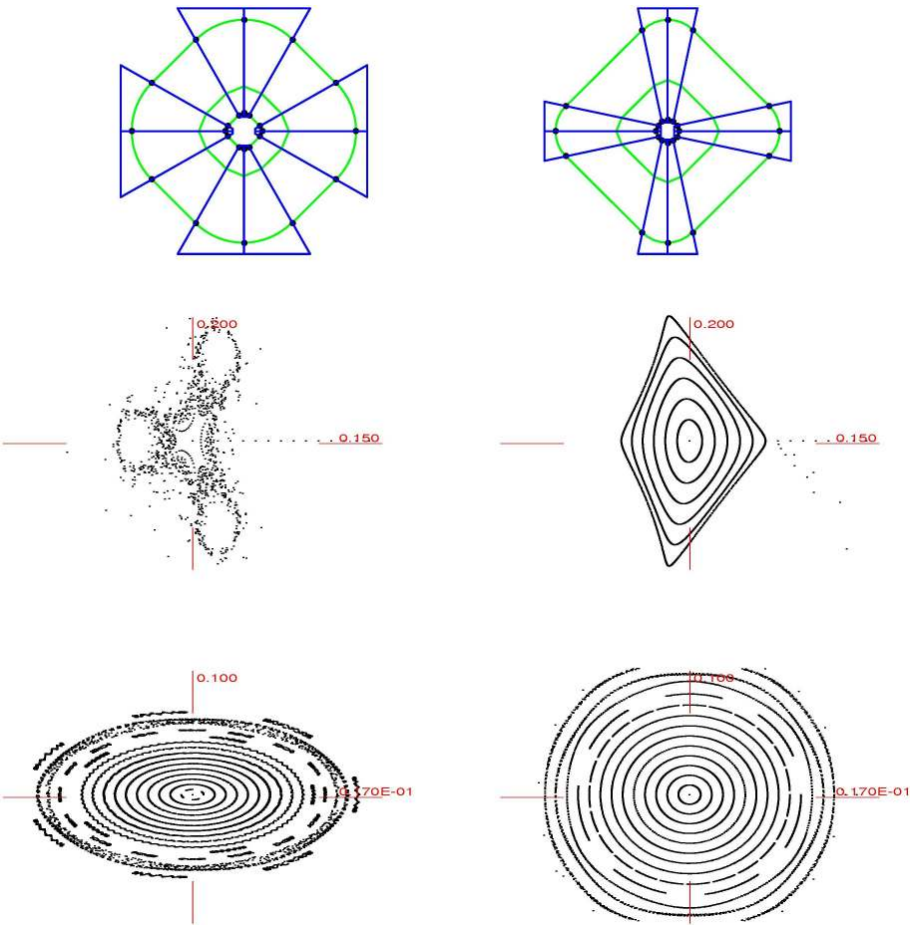

Fig. 8. Subtleties in the transverse dynamics of a cyclotron and an equivalent FFAG at 100 keV: horizontal cyclotron and FFAG (middle row) and vertical cyclotron and FFAG (bottom row) as observed in advanced tracking simulations in COSY.

Extraction can either be resonant, as in the cyclotron or synchrotron, or more likely through outer orbit field shaping as often used in the cyclotron. The advantage of the fixed-field accelerators is the orbit separation in energy. In a cyclotron (and a scaling FFAG), the higher the energy, the closer the orbit spacing as a function of energy, but this is not necessarily true for non-scaling FFAGs. A larger orbit separation can be maintained through appropriate field gradients in the FFAG, much more so than can be achieved with a strictly dipole field. Another advantage of the FFAG is that strong focusing in both planes permits insertion of long straight sections into the periodic cell structure, as in a synchrotron. Long straights promote low-loss extraction; there is room for an extended septum magnet. At high intensities, beam loss is a serious issue.

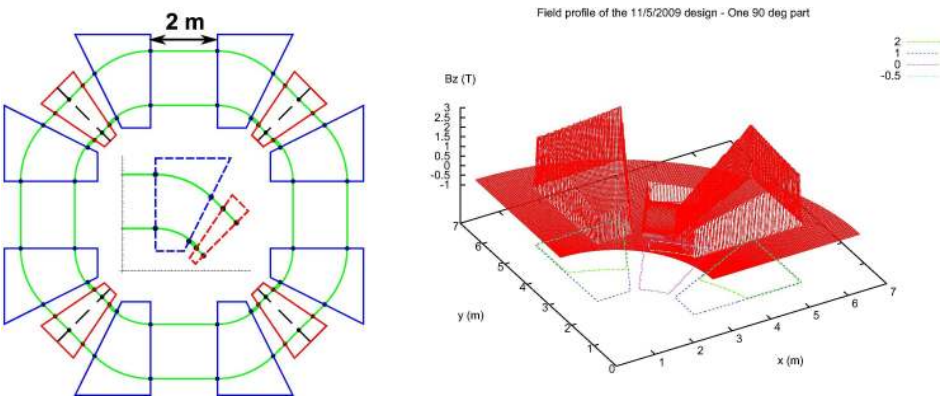

Fig. 9. Ring layout and 3D field profile from COSY. The 3D field profile of a quarter of the ring generated by the new tools in COSY INFINITY expanded from a simple hard-edge, radial field profile and azimuthal distribution.

As discussed above, the design is initiated and machine parameters explored using sophisticated scripts and powerful new methodologies in FFAG accelerator design (pioneered by Particle Accelerator Corporation). The approximate starting machine parameters generated by the scripts are then imported into the advanced accelerator simulation code, COSY INFINITY, which now has a full complement of sophisticated simulation tools (FACT) to fully and accurately describe the FFAG's complex electromagnetic fields—including realistic edge-field effects and high-order dynamics.[1,33] Performance and the isochronous condition can be accurately confirmed. Using this newly-developed design approach and advanced FFAG tools, a preliminary lattice has been discovered, and is discussed next.

6.4. *Lattice details*

As in the muon non-scaling FFAG, the ring must be completely periodic and a triplet cell structure containing a vertically defocusing D magnet positioned between two F magnets was chosen as the optimal base lattice unit. A minimum 0.3–0.5 m length has been imposed between magnets to prevent end-field overlap and cross talk between magnets. The long straight is 2 m to accommodate injection, extraction and the acceleration cavities, but may be increased in future designs. A 4-cell ring periodicity was found to be a strong initial starting point. The ring layout is shown in Fig. 9 derived from the simplistic design scripts. A simulation was then initiated in the code COSY INFINITY, with fully-described dynamics and realistic fringe fields, as the first test of the basic premise in a realistic computation. The 3D field profile generated by COSY INFINITY and subsequently tracked is also plotted in Fig. 9. General parameters of the ring are given in Table 1, the tracking results in Fig. 10 and the radius versus momentum in Fig. 11. The dynamic aperture is enormous—over ±20 cm in the horizontal and ±1 cm in the vertical.

Table 1. General Parameters of an initial 0.25–1 GeV non-scaling, isochronous FFAG lattice design.

Parameter	250 MeV	585 MeV	1000 MeV
Avg. Rad. (m)	3.419	4.307	5.030
Cell ν_x/ν_y (2π rad)	0.380/0.237	0.400/0.149	0.383/0.242
Ring ν_x/ν_y (2π rad)	1.520/0.948	1.600/0.596	1.532/0.968
Field F/D (T)	1.62/-0.14	2.06/-0.31	2.35/-0.42
Mag. length F/D (m)	1.17/0.38	1.59/0.79	1.94/1.14

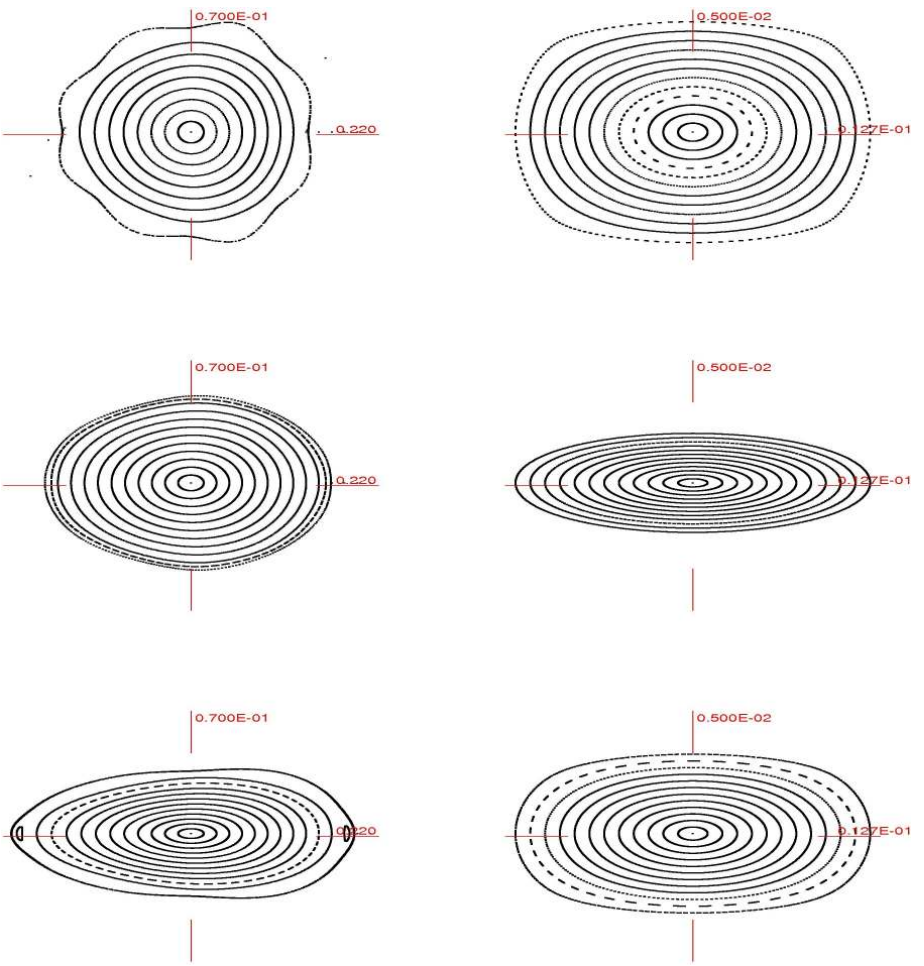

Fig. 10. Dynamic aperture at 250, 585, and 1000 MeV—step size is 15 mm in the horizontal (left) and 1 mm in the vertical (right).

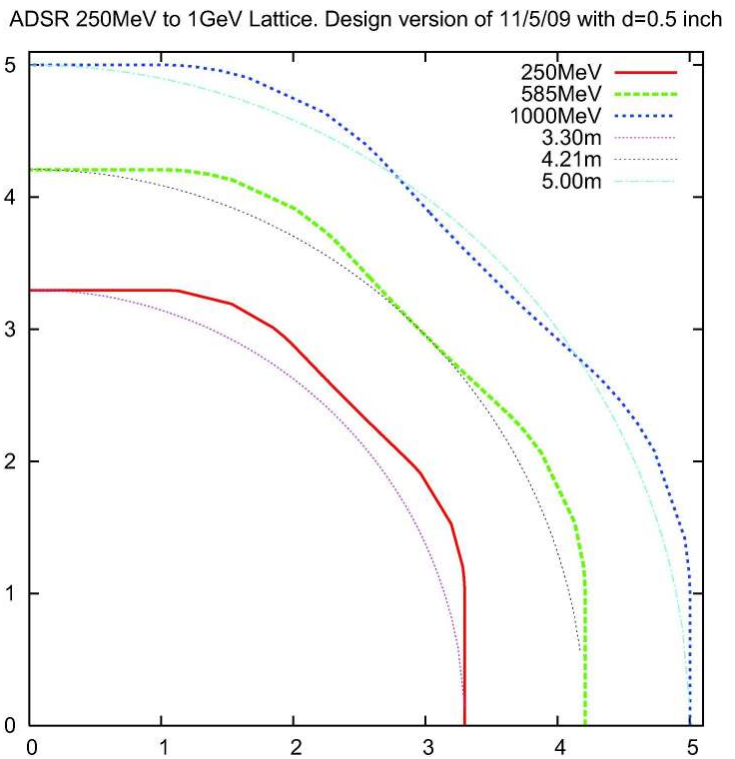

Fig. 11. Details of orbits at the 3 tracked energies over 1/4 of the ring.

Minor adjustment of the lattice parameters provides changes in the tunes in the horizontal and vertical, which can be set independently through relative changes in the F and D gradients. As stated above, this is the first iteration of the lattice design.

The first isochronous FFAG lattice has elicited international interest and further benchmarking is proceeding in alternative advanced codes by international accelerator experts. Fig. 12 and 13 show the corresponding results achieved by Craddock, et al.[35] using the cyclotron code, CYCLOPS using the 3D field map in Figure 9. The level of isochronous behavior is $\pm 3\%$ in this preliminary design.

The preliminary results of these initial studies indicate stable tunes and large dynamic apertures—additional optimization will establish desired machine tunes (tune shifts from the hard edge depend strongly on the vertical aperture due to fringe-field effects) and, more importantly, the results indicate a strong degree of isochronous operation. This lattice proves to be a viable starting point for development of an isochronous FFAG with either a fixed, or a rapidly modulated, RF system. It is anticipated this residual variation can be further reduced with optimization and extended development of the concept using more advanced optimizers available in COSY.

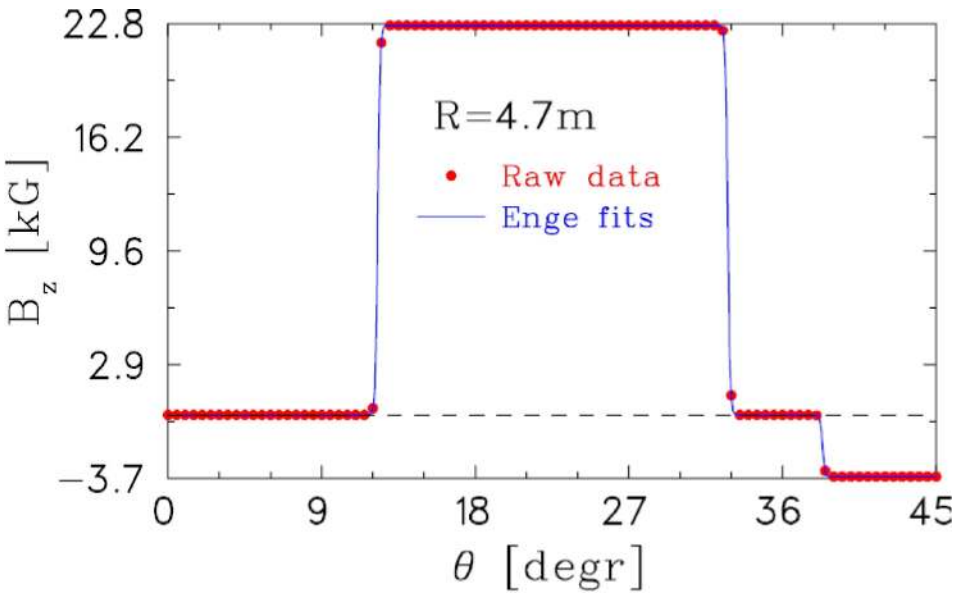

Fig. 12. Details of the B field implemented in CYCLOPS with Enge function fall off (fringe field) and a fine mesh.

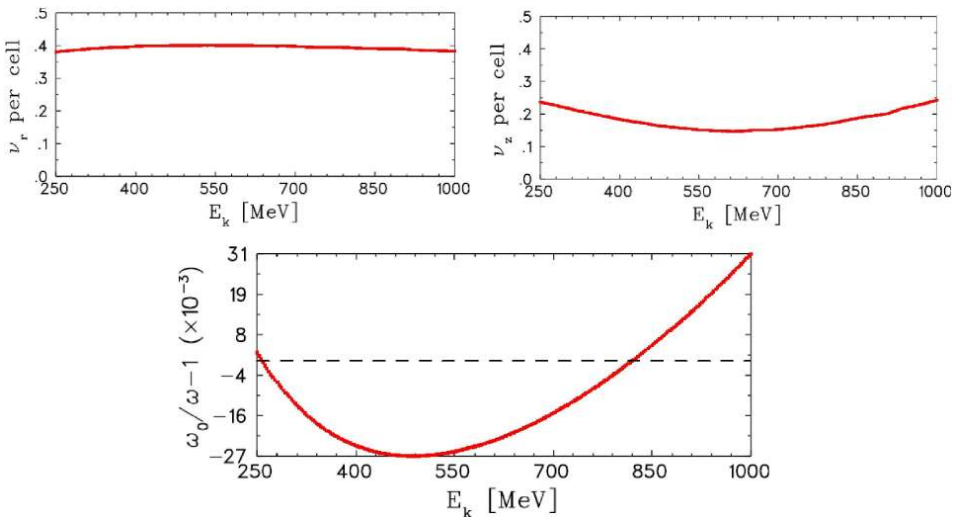

Fig. 13. Results using the cyclotron code CYCLOPs showing radial tune per cell (top, left), azimuthal tune per cell (top, right), and frequency change in percent (bottom).

7. Summary

Powerful new advanced accelerator design scripts have been developed using control theory and optimizers the results of which are directly imported into the advanced accelerator code COSY INFINITY. Various methods of describing complex fields

and components are now supported in COSY and include representation in radius-dependent Fourier modes, complex magnet edge contours, as well as the capability to interject calculated or measured field data from a magnet design code or actual components. With these new tools, a high-energy isochronous FFAG has been designed and the performance verified.

References

1. M. Berz, K. Makino, COSY INFINITY Version 9.0 beam physics manual. *Technical Report MSUHEP-060804,* Dept. of Physics and Astronomy, Michigan State University, 2006. See also `http://cosyinfinity.org.`
2. S. Henderson, *et al.*, Accelerator and Target Technology for Accelerator Driven Transmutation and Energy Production, `http://www.science.doe.gov/hep/files/pdfs/ADS/WhitePaperFinal.pdf.`
3. Accelerator Driven Systems and Fast Reactors in Advanced Nuclear Fuel Cycles, `www.nea.fr/ndd/reports/2002/nea3109.html.`
4. A. Mueller, Prospects for transmutation of nuclear waste and associated proton accelerator technology, *Eur. Phys J. Special Topics* 176, 179-191 (2009).
5. EUROTRANS, EUROpean Research Program for the TRANSmutation of high level waste, `http://www.enen-assoc.org/en/activities/for-universities/eurotrans.html` and `http://neutron.kth.se/research/projects/eurotrans/.`
6. The MYRRHA project, `http://myrrha.sckcen.be/.`
7. ThorEA, Capturing Thorium-fueled ADSR technology for Great Britain, `http://www.thorea.org/.`
8. TEF, Transmutation Experimental Facility, `http://j-parc.jp/Transmutation/en/ads.html.`
9. Korea Multipurpose Accelerator Complex, `http://komac.re.kr/NPET/new_proton/index.html.`
10. ADS International Workshop, Beijing, `http://english.cas.cn/Ne/ICN/201007/t20100719_56584.shtml.`
11. Thorium Energy Conference 2010, The Royal Institution of Great Britain, London, U.K., 2010.
12. R. Barlow, Thorium Energy Conference 2010, The Royal Institution of Great Britain, London, U.K., 2010.
13. C. Johnstone, *et al.*, Isochronous (CW) Non-Scaling FFAGs: Design and Simulation, to be published, *Proceedings AA2010,* Annapolis, MD, 2010.
14. C. Johnstone, *et al.*, Advances in Non-scaling FFAG Design, to be published, *Proc. Cyclotrons'10,* Lanzhou, China, 2010.
15. T. Baba, Industrial Applications of Electron Beam, FFAG'10, KURRI, Japan, 2010.
16. T. Ohkawa, FFAG Electron Cyclotron, *Phys. Rev.* 100, 1247 (1955).
17. A. A. Kolomenskij, A symmetric circular phasotron with oppositely directed beams, *Soviet Physics, JETP,* 6, pp. 231–233, 1958. (English version of 1957 paper in Russian.)
18. H. S. Synder, private communication.
19. K. R. Symon, D. W. Kerst, L. W. Jones, L. J. Laslett, and K. M. Terwilliger. Fixed-Field Alternating-Gradient Particle Accelerators. *Phys. Rev.* 103, pp. 1837–1859, 1956.
20. Keith R. Symon. A Strong Focussing Accelerator with a DC Ring Magnet. *MURA Notes,* 8/13/1954 and D.W. Kerst, K.R. Symon, L.J. Laslett, L.W. Jones, and K.M.

Terwilliger. Fixed field alternating particle accelerators, *CERN Symposium Proceedings,* v. I, p. 366, 1956.
21. D. W. Kerst, Properties of an Intersecting-Beam Accelerating System. *CERN Symposium Proceedings,* v. I, pp. 36–39, 1956.
22. C. Johnstone, *et al.*, Fixed Field Circular Accelerator Designs, PAC'99, New York, p. 3068.
23. C. Johnstone, *et al.*, A New Non-scaling FFAG for Medical Applications, *ICFA Beam Dynamics Newsletter* No. 43, July, 2007, `http://www-bd.fnal.gov/icfabd/Newsletter43.pdf,` pp. 125–132.
24. C. Johnstone, *et al.*, A New Non-scaling FFAG for Medical Applications, *Proc. of the Particle Accelerator Conference,* Albuquerque, NM, p. 2951, 2007.
25. C. Johnstone, *et al.*, Tune-stabilized Linear Field FFAG for Carbon Therapy, *Proc. of the 2006 European Particle Accelerator Conference,* Edinburgh, UK, pp. 2290–2292, 2006.
26. K. Makino, *et al.*, High-order Description of the Dynamics in FFAGs and Related Accelerators, *Int. Journal of Mod. Physics-A,* vol. 24, No. 5, pp.908–22 (2009).
27. S. Machida, *Proc. U.S. Particle Accelerator Conference PAC'07,* Albuquerque, NM, 2007.
28. S. Smith, *et al.*, to be published, *Proc. Cyclotrons'10,* Lanzhou, China, 2010.
29. MAD Version 9, `http://wwwslap.cern.ch/mad/.`
30. V. Lebedev, OptiM. `http://www-bdnew.fnal.gov/pbar/organizationalchart/lebedev/OptiM/optim.htm.`
31. R. Baartman, *et al.,* CYCLOPS.
32. F. Meot, The Ray-Tracing Code Zgoubi, *Nuclear Instruments and Methods A,* v. 427, pp. 353–356. 1999.
33. M. Berz, Modern Map Methods in Particle Beam Physics, *Academic Press,* San Diego, 1999. M. Berz, Differential Algebraic Description of Beam Dynamics to Very High Orders, *Particle Accelerators,* v. 24, p. 109, 1989.
34. B. Erdelyi, *et al.*, Optimal Symplectic Approximation of Hamiltonian Flows, *Phys. Rev. Lett.* 87(11) (2001) 114302. B. Erdleyi, *et al.*, Local Theory and Applications of Extended Generating Functions, *Int. J. Pure Appl. Math.* 11(3) (2004) 241-282.
35. M. Craddock, *et al.*, to be published, *Proc. Cyclotrons'10,* Lanzhou, China, 2010.

International Journal of Modern Physics A
Vol. 26, Nos. 10 & 11 (2011) 1713–1735

DOI: 10.1142/S0217751X11053122

World Scientific
www.worldscientific.com

ACCELERATORS FOR HOMELAND SECURITY

WILLIAM BERTOZZI, WILBUR FRANKLIN, STEVE KORBLY, ROBERT J. LEDOUX, RUSTAM NIYAZOV and DAVID R. SWENSON
Passport Systems, Inc., 70 Treble Cove Road, North Billerica, MA 01862

ALEXEI KLIMENKO
Los Alamos National Laboratory, Los Alamos, NM

1. Introduction

Viable concerns about Homeland Security provide many examples of terror inducing events and possible catastrophes. Some events might originate from the spread of biological organisms, some could involve the spread of toxic substances and others may involve the spread of radioactive materials via "dirty bombs"; many may involve great destruction caused by a variety of military and other explosives and maximally by nuclear weapons. The possibilities are legion and the scope of the terror involved, let alone the destruction, can be very destabilizing economically and politically to our country and to the world. The global community has already experienced some devastating examples yet none of these has reached the proportions that are imaginable. Some important dangers are listed below that indicate the important components that form the elemental and, where appropriate, the isotopic basis of the dangerous material.

- Explosives
  - Examples of extensive damage
    - Oklahoma, Lebanon, Lockerbie, Halifax (1917)
  - Important elements: N, O, Cl, Na, S, K, P (and fulminates)
- Toxic Substances
  - Examples of use
    - Sarin gas in Tokyo subway
  - Substances: Mustard Gas ($C_4H_8Cl_2S$), Sarin ($C_4H_{10}FO_2P$), Phosgene (CCl_2O)
- Dirty Bombs
  - ^{137}Cs, ^{60}Co (Unsafe and injurious disposal in Mexico of ^{60}Co)
  - Shielding Materials: Pb, W, Fe

- Special Nuclear Materials
  - ^{235}U, ^{239}Pu, ^{237}Np
- Weapons of Mass Destruction
  - ^{235}U, ^{239}Pu, ^{237}Np, Explosives, Tamper materials

One important means of mitigating future situations involves active examination of the contents of cargo containers being shipped by sea, rail, air and road transport. These containers, which number in the many millions, would be relatively inexpensive for terrorists to engage as accurate delivery systems. Without inspection, they would have a very high probability for successful delivery of large amounts of destructive materials. However, for an inspection procedure to be effective and accepted broadly the examination must be performed rapidly and minimize disruption on the commerce of the world. This means non-intrusive inspection must carry the largest burden of the task and will involve penetrating radiation in the form of neutrons and/or photons (often referred to as X-rays and or gamma rays) and requires particle accelerators of some form. Recent developments also attempt to use muons[1,2] from cosmic sources to locate special Nuclear Materials (SNM) such as ^{235}U and ^{239}Pu and heavy metal shields such as lead or tungsten via the difference in the angle of multiple scattering between high-Z and low-Z elements.[2] However, the technique does not identify specific isotopes and it does not appear to be universally adaptable to identify explosives and toxic substances, for example.

2. Nuclear Pathways in Non-Intrusive Inspection of Containers

The present use of accelerators in Homeland Security has been conditioned in large measure by what is commercially available and this has been driven by the copious use of X-ray machines for cancer therapy and non-destructive testing in industrial applications. This resulted historically in the use of linear electron accelerators (LINACS) and standard high voltage sources producing electron beams and X-rays or photons via bremsstrahlung to examine objects via transmission radiography in order to display shadowgraphs of the contents. The use of these accelerators for radiography has significant advantages in comparison with radioactive sources, such as ^{60}Co, which carry the additional burden of requiring heavy shielding when not in use and the possibility of being subverted via abrogation towards the very terrorist activity they were intended to help mitigate. These radiographic techniques have been largely limited to yielding information about variations in density in a two-dimensional projection of the object under inspection. Computed Tomography (CT) is useful with luggage and small containers and provides a three dimensional radiographic image. However, so far CT seems not to be a practical adjunct for radiographic imaging of the large containers commonly used in commercial transport. The involvement of neutrons generally makes use of commercially available generators employing the reaction ^{3}T(^{2}D,n)^{4}He. Neutron transmission profiles, nuclear activation and (n,γ) processes have been proposed for active and non-intrusive

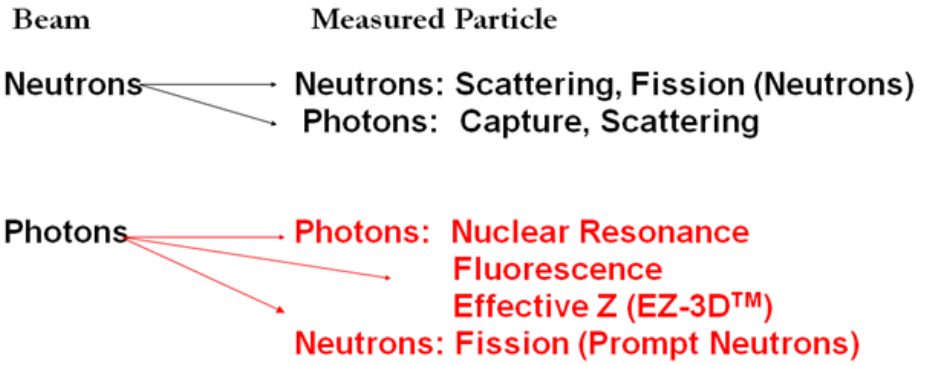

Fig. 1. Possible nuclear pathways.

inspection.[2] The accelerators anticipated or used in neutron generation have been generally electrostatic.

In Fig. 1 possible nuclear pathways are shown for penetrating radiation that is produced by using low energy (<∼20 MeV) electron accelerators to produce photon beams and low energy hadron accelerators (< a few MeV) to produce neutron beams. In each case the detected photons and/or neutrons involve different reaction channels or nuclear processes that distinguish the potential usefulness and specific advantages. Transmission radiography is possible with neutrons and photon beams, each technique involves different sensitivities and detection methods. The fission pathways with both beams are also different as to the specific reaction and nuclear sensitivities. Capture and scattering of neutrons produce photons in the detection channel that are characteristic of the nuclear target via resonance processes. Incident photons produce a variety of signatures in the detected photons that characterize the nuclear isotope by Nuclear Resonance Fluorescence (NRF) (Ref. 3) and the effective Z (Ref. 3) in a voxel (3D pixel) via the multiple processes involved in photon absorption and regeneration at back angles.

Possibilities for the production of neutrons are exhibited in Fig. 2. Shown are possible reactions and available intensities from one commercial vendor. Amplification with depleted uranium to very high intensities is illustrated. The use of stripping reactions is also a possibility with precise control of neutron energies and beam direction via the reaction dynamics. In all cases the neutron beams can be produced as both continuous streams (DC with electrostatic accelerators or continuous wave (CW) with radiofrequency accelerators) or as pulsed beams as short as a few nanoseconds in some cases.

3. Detection Processes that Use Photons

The remainder of this paper is focused on the detection of dangerous materials via the use of photon beams. These beams are produced by bremsstrahlung using

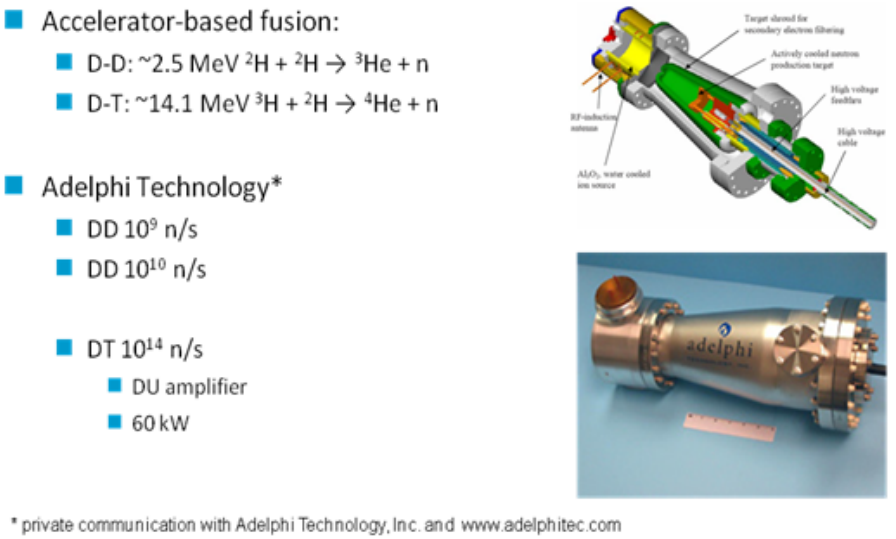

Fig. 2. Neutron generators.

electron beams. The character of the electron accelerators applied to such uses depends strongly on the processes used in detection. These processes are listed in Fig. 3 and presented in more detail in the following discussions that describes their use in the field. It is important to note that that all of these processes would benefit significantly from a high duty cycle electron accelerator and in the cases of Nuclear Resonance Fluorescence, Effective-Z determination and prompt neutrons from photon induced fission, a high duty factor accelerator is essential for practical non-intrusive scanners.

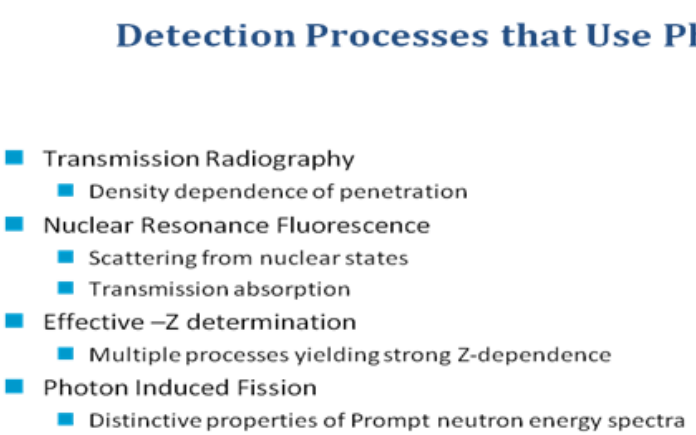

Fig. 3. Detection processes that use photon beams.

Transmission radiography measures the absorption of the beam and presents a two-dimensional shadowgraph of the density of materials along the photon beam path. As radiography is now practiced by most systems, the total energy of the beam deposited in a pixel is measured and represents the signal for absorption. The main reason to use total energy of deposition and not photon counting with explicit photon energy measurement is partly historical. It was always done that way with low energy beams used in medicine and the film used to detect transmitted intensity. Partly it results from the high cost of having many pixilated spectrometers. The duty cycle of the commercially available LINAC sets the pattern for higher energy photon beams that are needed for penetration of dense and large cargos. These LINACs have a duty cycle of approximately 1/1000, generated by a few microsecond electron beam pulsed at a roughly 300 Hz repetition rate. Given these conditions, counting individual photons, if not impossible it is very ineffective. This is particularly true if the energy of each photon is to be measured. Photon counting at high duty cycles makes possible several advantages such as the energy dependence of the transmission as well as improved dynamic range.

Fig. 4 is a schematic of a scanning system envisaged by Passport Systems, Inc. that has all the potential detection modalities described in Fig. 3 that are enabled

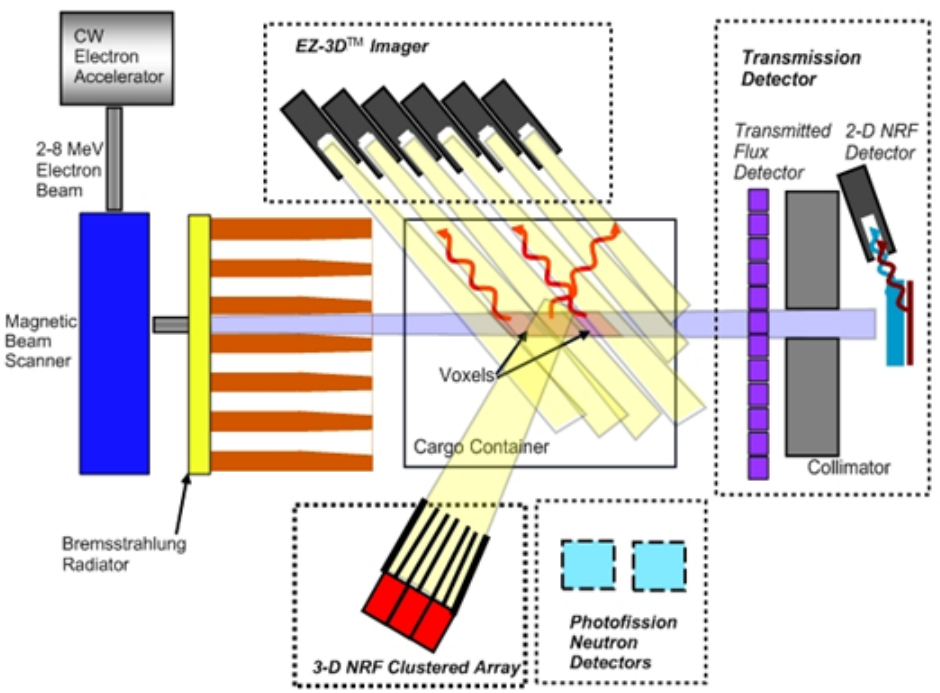

Fig. 4. NRF and EZ-3D^{TM} with 3D Voxels, 2-D NRF Transmission Detection and Prompt Photofission Neutrons.

by a high duty cycle accelerator. An electron beam of high duty cycle is scanned over a bremsstrahlung radiator. Collimators provide a collimated beam of photons for each position of the electron beam. Collimated NRF arrays and effective-Z (EZ-3D^{TM})[3] arrays have views that intersect the collimated photon beam and the common regions define a voxel of interrogation. Neutron detectors would measure the energy spectrum of neutrons produced in the container. The energy distribution of prompt neutrons from photon induced fission (PNPF)[3] determines the presence of actinides. After passing through the container the photon beam also impinges on a detector system to produce a transmission radiographic image of high resolution. This image can only be made by detectors that integrate energy deposition over a pixel or by detectors that count individual photons and measure their energy individually and hence the use of a high duty cycle accelerator is required.

The EZ-3D^{TM} technology is able to identify Regions of Interest (ROI) rapidly when the effective-Z in a region is unexpected. For example, inside doors of autos should be empty spaces and not contain a material of apparent density between 1 and 1.6 with an effective-Z in the neighborhood of nitrogen, such as is the case with C4. The same is true for the interior of pneumatic tires. Similarly, it can identify regions with effective-Z higher than tin, for example. If such regions are unexpected from the manifest it provides a ROI that can be explored with PNPF and/or NRF. The PNPF would rapidly clear the ROI for the presence of an actinide. If the ROI has an actinide then NRF will identify the existence of a SNM. Further, the existence of proximate tamper material and explosives would characterize a WMD.

In Fig. 5 a standard radiographic image of an automobile is shown. Dark and light portions may be an engine, transmission gears and other familiar components. However, there is no indication of the type or amount of metal that any dark region is composed of since only the total absorption results from radiography. NRF will inform about the specific isotopic content of any voxel or a region of interest (ROI) and cause the nature of this figure to change with information about the kind of steel the engine is made of and if it is harboring a part made of ^{235}U deep inside a cylinder, for example. It will also inform as to whether any dark shadow has the composition expected of the absorbing structure. For example, the palladium in the catalytic converter would be detected and an aluminum valve cover and aluminum pistons would be recognized. Finally, the transmission NRF detector provides a shadowgraph of the isotopic material in the container that is identical to the reference material in the transmission NRF assembly.

The PNPF technology is based on photon induced fission and will identify the existence of actinides unambiguously. It can serve as fast clear for the existence of SNM. Such an example could be a situation wherein EZ-3D^{TM} had identified a ROI with Z greater than that of tin. PNPF would be called upon to clear or demand further inspection with NRF because an actinide had been discovered.

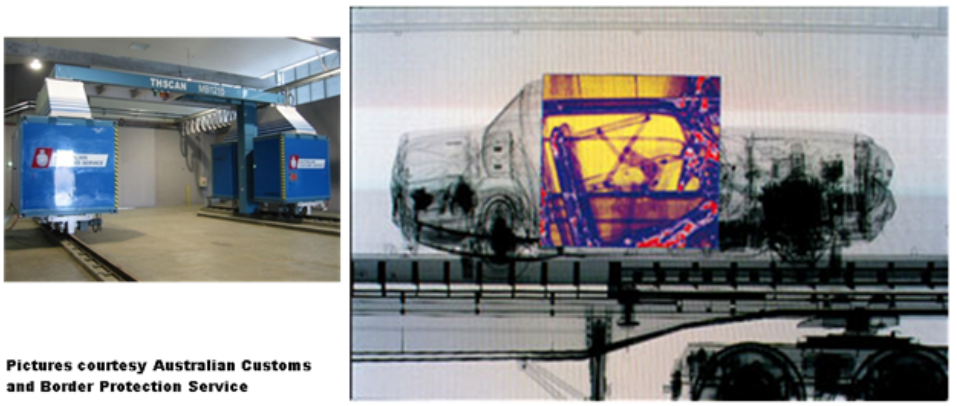

Fig. 5. Radiography with Photons.

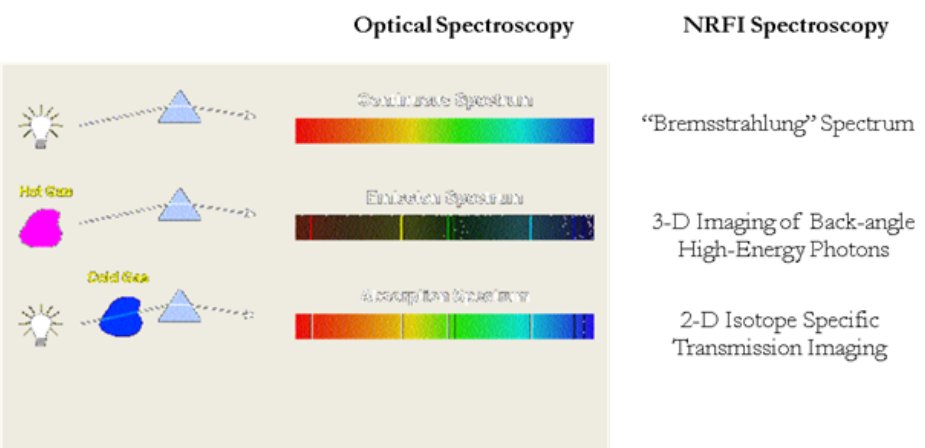

Fig. 6. Analogy between NRF and Optical Spectrometry.

4. Nuclear Resonance Fluorescence Physics

In Fig. 6 an optical analogy to NRF is displayed. The bremsstrahlung spectrum used with NRF is analogous to the white light of a lamp in that both have a continuously populated spectrum of photon energies. Replace the lamp with a glowing gas such as neon or sodium vapor lamp and distinct lines are apparent in the spectrum. If instead a white light is used and a cold gas is interposed between the lamp and the spectrometer, the incident continuous spectrum is found to have dark lines corresponding to the absorption lines of the gas. In the case of NRF the transmission detector employs a material identical to that of interest in the container. The intensity of the scattering of the characteristic lines indicates the presence of the same material as the reference scatterer in the container.

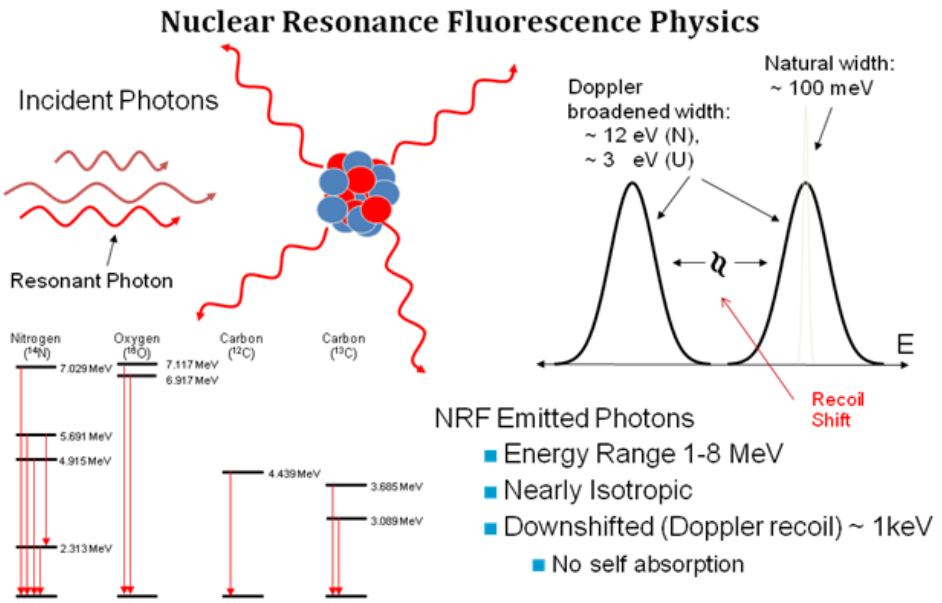

Fig. 7. Nuclear Resonance Fluorescence Physics.

In Fig. 7 the essential physics of NRF is presented. Incident photons (from bremsstrahlung for example) are incident upon a nucleus. Those that are resonant with exited states of the nucleus are absorbed (red) and excite the nucleus. The excited nucleus decays (typically in less than approximately 10^{-14} s) with the emission of photons of unique energy into all directions. The natural line width of a state of interested is generally larger than approximately 50 meV and less than a few eV. This width is broadened by the binding of the isotope to a crystalline lattice such as with a metal or to a molecule in the case of a gas or a liquid. In addition there is the thermal motion due to most systems being at approximately 300°K. However, the zero-point motion of binding is generally a larger contributor to the Doppler broadening. The recoil of the nucleus causes a Doppler shift in the emitted energy that is shown in Fig. 7. This Doppler shift is substantially larger than the Doppler width of the state and as a result the emitted photons are never resonant on the way out of a material. This is important since the cross section for NRF at the peak of the resonance is many times larger than the electromagnetic cross sections responsible for photon attenuation (photoelectric, Compton, Pair production) and severe attenuation would ensue otherwise. Note that the incident photon energy that is resonantly absorbed also must be of higher energy than the excited state energy because of a Doppler shift; that is, the absorbing nucleus is generally recoiling because it must conserve the photon momentum. The resulting nuclear kinetic energy is usually high enough to break crystalline and molecular bonds setting the nucleus free to recoil. This is in contrast to recoilless photon absorption and emis-

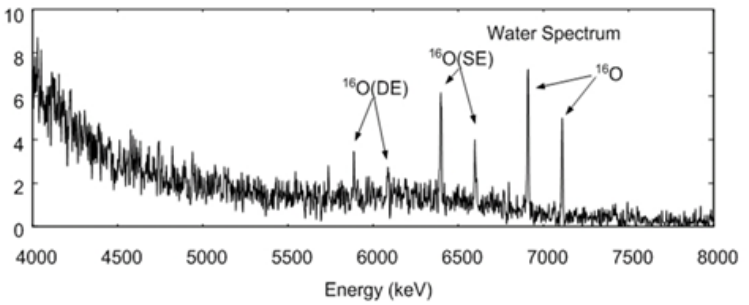

Fig. 8. The NRF Spectrum of ^{16}Oxygen.

sion when photon energies are much lower than those considered herein and leads to the well known Mössbauer effect.

Some excited states are shown in Fig. 7 for ^{12}N, ^{12}C, ^{13}C and ^{16}O. Notice that energies are in the MeV region, well above where recoilless radiation can be important.

In Fig. 8 the NRF spectrum from ^{16}O from water is presented. If a mixture of alcohol and water were to have been used, lines from ^{12}C and ^{13}C would be present as well as those from ^{16}O. It is clear that a mapping of the alcohol concentration is immediately available from primordial data about cross sections and the intensities of the lines from the isotopes of oxygen and carbon. In Fig. 9 the NRF spectrum from ^{235}U is exhibited. It can be detected through shielding and positively identified via this unique NRF spectrum and distinguished from ^{238}U and other actinides. This NRF spectrum was measured using the Van de Graff accelerator of the High Voltage Research Laboratory at MIT in collaboration with our colleagues at PNNL.[3] Note that these experiments used high purity germanium crystals with resolutions of approximately 3 keV at the MeV energies involved. The success of the NRF technique depends on high resolution photon spectroscopy. A high duty cycle accelerator is essential in such applications.

5. Effective-Z Determination — EZ–3D$^{\text{TM}}$

Effective-Z determination is easily demonstrated by the data in Fig. 10. It shows the photon spectra scattered at back angles from a target of ^{239}Pu encased in a steel container (Nitronic 40). It also shows the spectrum from an identical steel container without any ^{239}Pu enclosed. The NRF lines from ^{239}Pu (Ref. 4) are indicated and the decay to the ground state and the first excited rotational state are shown as pairs. This is expected since to first order the rotational state is identical to the ground state in intrinsic structure. Notice the additional lines from Mn, Cr and Al from the steel target holder. This is a good demonstration of the power of NRF to detect materials and specify elemental and isotopic composition. Different steels can be differentiated from this composition.

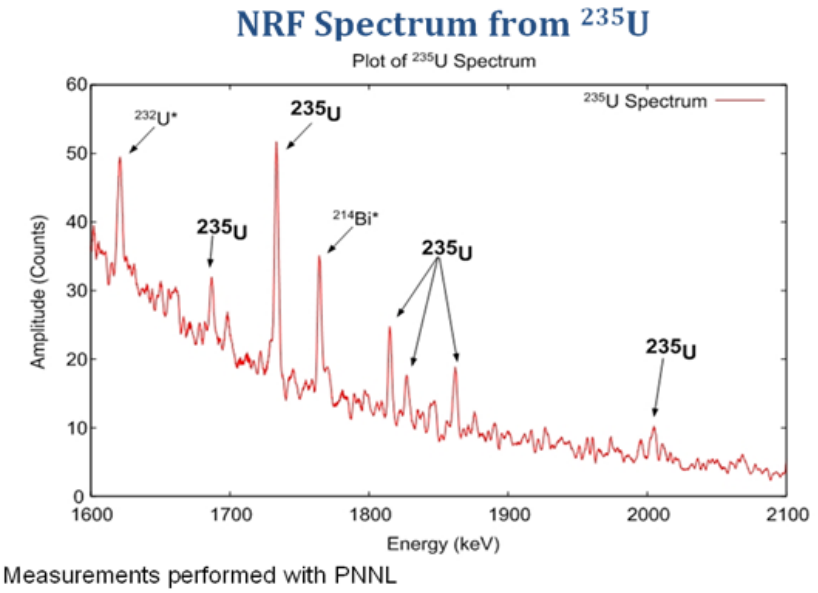

Fig. 9. The NRF Spectrum from ^{235}U.

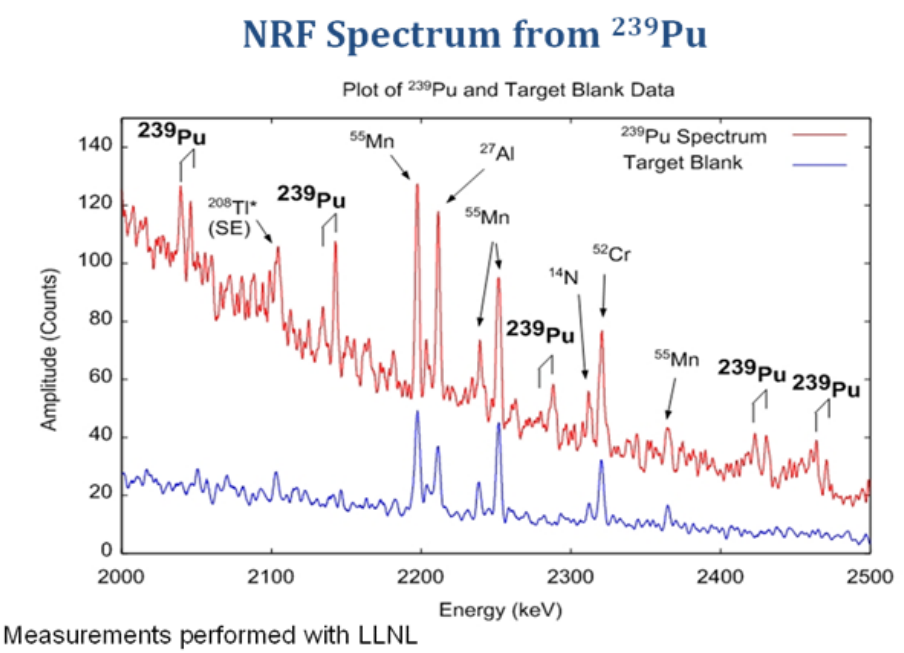

Fig. 10. Comparison Between a Steel Target and a ^{239}Pu target.

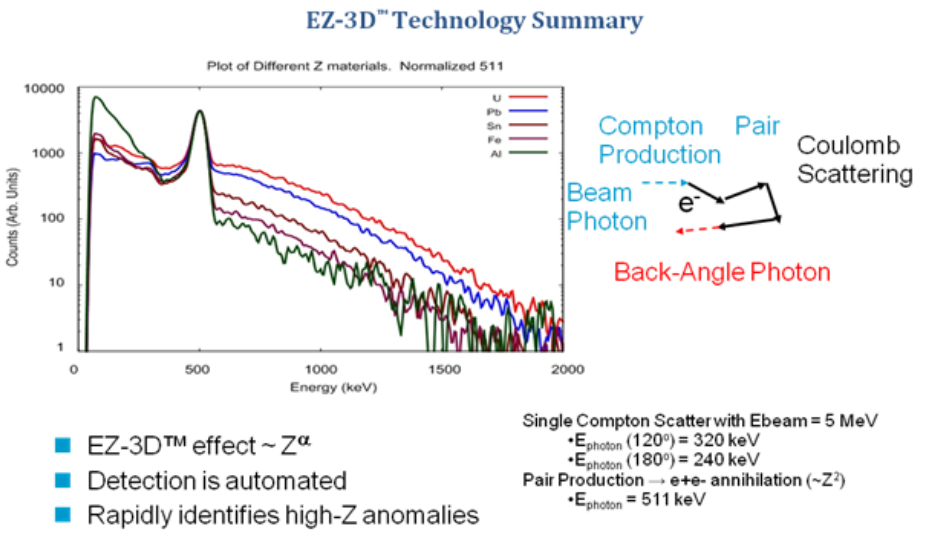

Fig. 11. A Summary of EZ-3D^{TM} Technology.

In addition to the NRF information in Fig. 10, it is useful to compare the smooth non-resonant background from the ^{239}Pu spectrum and that of the steel target. The content of ^{239}Pu (a few grams) is very much less than the mass of the steel container. Nevertheless, the background is much higher. This difference is an example of the EZ-3D^{TM} effect. In Fig. 11 this difference is developed further for many values of Z.

The spectra of photons scattered back of 90 degrees is shown for a variety of elements using a beam of photons from the bremsstrahlung of 2.8 MeV electrons. The spectra are normalized at the 0.511 MeV annihilation line. The comparison of these shapes allows a very accurate determination of the effective-Z of a region of space and the large differences provide an accurate indication of a heavy metal even when it is a minor part of the mass. The figure indicates how the single scatter of a 5 MeV photon at back angles cannot generate the high energy photons above 0.5 MeV. The photons above 0.5 MeV originate from multiple processes involving electron production, Coulomb Scattering and finally bremsstrahlung at back directions. For this reason the EZ-3D^{TM} effect is proportional to a high power of Z.

Fig. 12 demonstrates how materials of different Z can be detected even in the presence of a large amount of steel in the form of chain. A 2" cube of Pb is imbedded in a box of steel chain. On the left is displayed a standard transmission radiograph. The balk square moves through the circular aperture of sensitivity as the X-Ray beam is scanned. There is no way to distinguish the square object as far as it being Pb or just a long rectangular bar of steel, for example. However, reconstruction of the back scattering of 5 MeV Bremsstrahlung for density and effective-Z leads

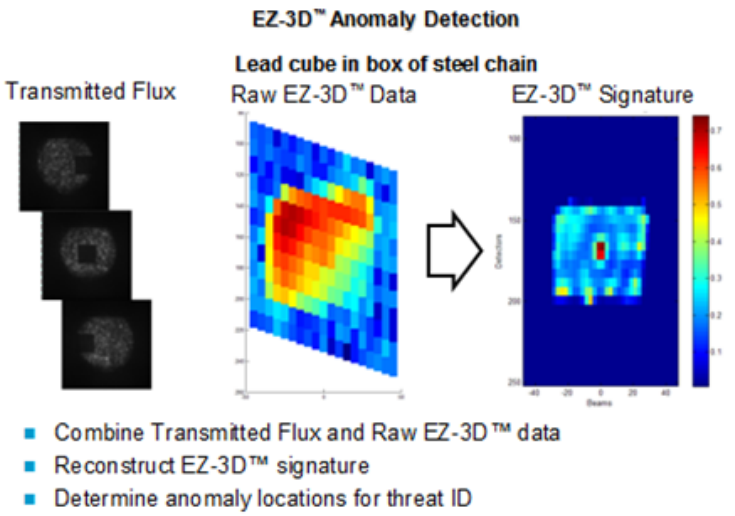

Fig. 12. A Demonstration of the Detection of Different-Z Materials.

to identification of a material with high effective-Z in the center (orange color). The comparison is with respect to the scattering from the iron of the chain that surrounds it (shades of blue-green). Such data can now lead to regions of interest for inspection with NRF or PNPF to further characterize the material composition. Because EZ-3D^{TM} uses almost all the photons in the Bremsstrahlung spectrum, it is a very fast method to detect regions of interest.

This work was performed with the assistance of the staff at the University of California at Santa Barbara free electron laser facility. The photon detectors used NaI scintillation crystals.

6. Prompt Neutrons from Photon Induced Fission

The energy spectrum of neutrons from photon induced fission at the lower photon energies provides us with an excellent discriminator for actinide nuclei. The physics follows from a measurement made in the early 1960's involving the determination of the energy spectra and angular distributions of neutrons from the photon induced fission from ^{232}Th.[5]

The conclusions of this experiment are:

- Less than 7% of prompt neutrons come from scission at separation.
- Prompt neutrons from photon induced fission result from fully accelerated fragments (velocity boost).
- Energy distribution of prompt neutrons extends past 8 MeV.
- Energy distribution of prompt neutrons is independent of photon energy below 10 MeV.

- Prompt, high energy neutrons provide unique signal for fissile material
- Neutron energy distribution independent of incident photon energy
- Minimal background contamination above threshold
- Significant neutron yield for E > 3 MeV → highly transmissive
- Relative to Prompt
  - Delayed Photons ~1/10
  - Delayed Neutrons ~1/200

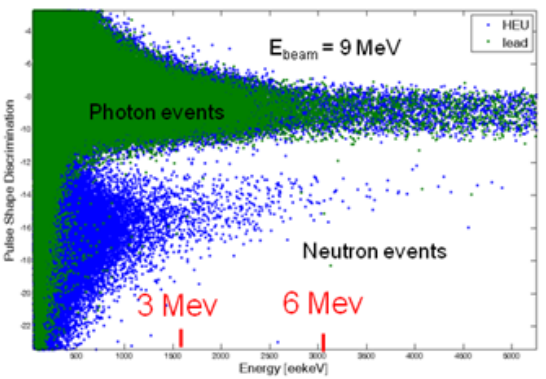

Fig. 13. Prompt Neutrons from Photon Induced Fission.

The fission fragments emit the prompt neutrons after they have reached most of their fully accelerated fragment velocities. The neutrons are thus boosted in energy and for bremstrahlung beams of 9 MeV for example, all neutrons above 2.5 MeV must be from fission. The one exception is Be and this can be differentiated by the yield above 5 MeV neutrons.

In Fig. 13 data are exhibited from experiments at the Technical University of Darmstadt wherein lead and HEU were exposed to 9 MeV bremsstrahlung and the energy spectrum of events was detected by liquid scintillation counters that use pulse shape discrimination to determine if the events are from electron recoils (photons) or proton recoils (neutrons) in the scintillant. Photons are clearly distinguished from neutrons. The neutrons from uranium are clearly distinguished from the events from lead wherein ^{207}Pb has a photo-neutron threshold of about 6.7 MeV. Prompt neutrons are ∼200 times more probable than delayed neutrons and are the particle of choice for the detection of actinides using photon induced fission. These features are common to all actinides.

7. Accelerators Needs for Homeland Security

It has been demonstrated in the above discussion that the duty cycle of a particle accelerator plays a dominant role in the types of technologies that are made possible in application for Homeland Security. Most of the novel technologies mentioned

require high duty cycle beams to be effective. Transmission radiography at higher energies (MeV and greater) has traditionally made use of low duty cycle LINACS using the technique of energy deposition in a detector. However, photon counting and spectral analysis would add considerably to the materials discrimination capabilities of transmission radiography, but again, high duty cycle beams would be required. A condensed version of criteria and benefits established in the discussion above is presented below for electron accelerators used for inspection applications, in particular, for homeland security with its special requirements.

Important criteria for electron accelerators in homeland security

- Energy: ∼3–9 MeV.
  3 MeV: NRF signatures for SNM is generally below this energy;
  6 MeV: Good yield for EZ-3D^{TM} and good penetration for radiography;
  9 MeV: NRF from oxygen; well above photofission thresholds for actinides, increased penetration; excellent yield EZ-3D^{TM}.
- Intensity: from zero to several mA.
  Needed for large dynamic range with different cargo loadings; adjustable to minimize dose.
- Duty cycle: As large as possible, 100% desirable.
  - Discrete event counting enhanced.
  - Improves detector performance.
  - Improves Signal to Noise, S/N.

Existing electron accelerator technology for these applications is very limited. In prevailing technology of RF LINACS, the duty cycle is typically limited to a value of approximately 10^{-3}. Higher duty cycle beams can be obtained from electrostatic machines, but these typically require a very large spatial profile and can only be used in select applications. Other commercially available high duty cycle machines, such as the IBA Rhodotron, require high initial and operating costs which are prohibitive for widespread deployment. There is a clear need for new technology providing high duty cycle beams at low cost, small spatial profile and portable design for widespread adoption

Passport Systems is developing a new type of compact, cost efficient electron accelerator which will provide electron beams of high duty cycle and variable intensity.

Perhaps the most promising technology that meets many of these conditions is the Fixed Field Alternating Gradient induction accelerator (FFAG). This concept was invented several decades ago by Donald Kerst and Keith Symon[6] during the Midwestern Universities Research Association (MURA) days but has not yet been articulated in a commercial device. The advantages of an electron accelerator utilizing a FFAG guide magnet and acceleration by induction are listed below:

- Simple concept of induction and simple acceleration process.
- Static guide magnetic fields.

- Simple power supply consideration.
  - Simple pulsed mode.
  - No radiofrequency power.
- Induction Core requirements are available commercially.
  - High permeability.
  - High saturation field.
  - Low losses.
- High duty cycle possible: to 50% (Kerst).
- Dynamic beam current modalities easily achieved: beam current rapidly variable and fast time structures programmable.

There are several types of FFAG electron accelerator designs that can be considered and these have differing characteristics that may be attractive to differing applications. They have not been explored thoroughly in this regard and considerations of cost, ease of operation, reliability and footprint will all play a role in matching accelerator type to application.

(1) Scaling Accelerators
- Radial sector
  - Inventors: Keith Symon, Andre Kolominsky, Andre Lebedev, Tihiro Ohkaiwa
- Spiral sector
  - Inventor: Donald W. Kerst

(2) Non-Scaling
- Linear field with edge modifications
  - Inventor: C. Johnstone
- Others to be invented

For the purpose of illustration in Fig. 14 a spiral ridge version of the scaling variety FFAG is shown. The mathematical expressions demonstrate radial scaling of the magnetic field. A transformation from the laboratory angle θ to the angle Ψ renders analytical treatment manageable. Parameters using the Fourier transformation of the fields lead to simple concepts such as flutter that define the first order characteristics of the design. All of this is discussed thoroughly in the MURA literature that is archived at the Fermi National Laboratory. In Fig. 15 is shown a photograph of a small scale test of the spiral design. It was constructed by Donald Kerst and collaborators as a test of the concept but it was only capable of accelerating electrons to 125 keV.

In Fig. 16 the theoretical model of the radial sector scaling FFAG is presented. Notice that the relationships are simpler than in the spiral sector design. The design inherently requires a larger footprint than the spiral sector design. The radial sector

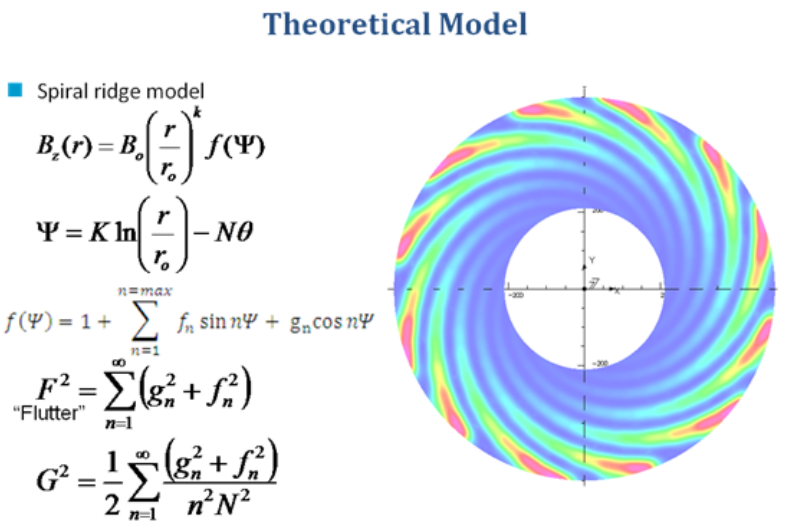

Fig. 14. Theoretical Model of a Spiral Ridge Version of a Scaling FFAG.

Fig. 15. The First Spiral Sector FFAG.

Theoretical Model

- Radial sector model

$$B_z(r) = B_o\left(\frac{r}{r_o}\right)^k f(\theta)$$

$$f(\theta) = 1 + \sum_{n=1}^{n=max} f_n \sin n\theta + g_n \cos n\theta$$

"Flutter"
$$F^2 = \sum_{n=1}^{\infty}\left(g_n^2 + f_n^2\right)$$

$$G^2 = \frac{1}{2}\sum_{n=1}^{\infty}\frac{\left(g_n^2 + f_n^2\right)}{n^2 N^2}$$

Fig. 16. A Radial Sector Scaling FFAG Theoretical Model.

A Radial Sector FFAG (~ 425 keV)

Inventors: Kieth Symon, Andre Kolominsky, Andre Lebedev, Tihiro Ohkaiwa

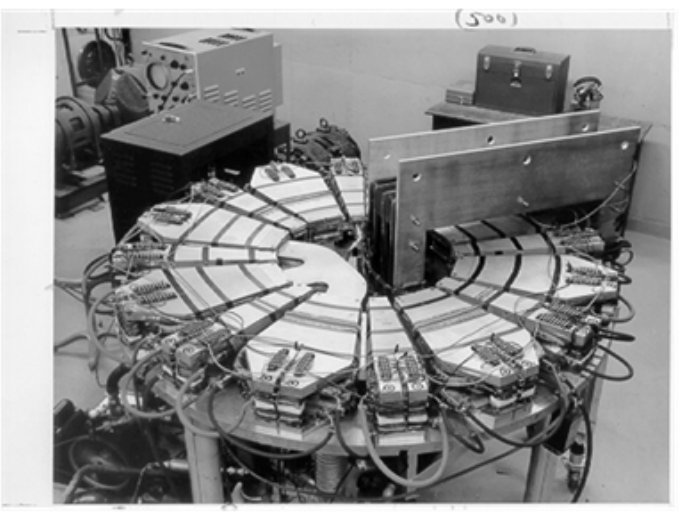

"Innovation Was Not Enough": Jones, Mills, Sessler, Symon and Young; World Scientific, Singapore, To be published

Fig. 17. A Successful Test of a Radial Sector Scaling FFAG at 425 keV.

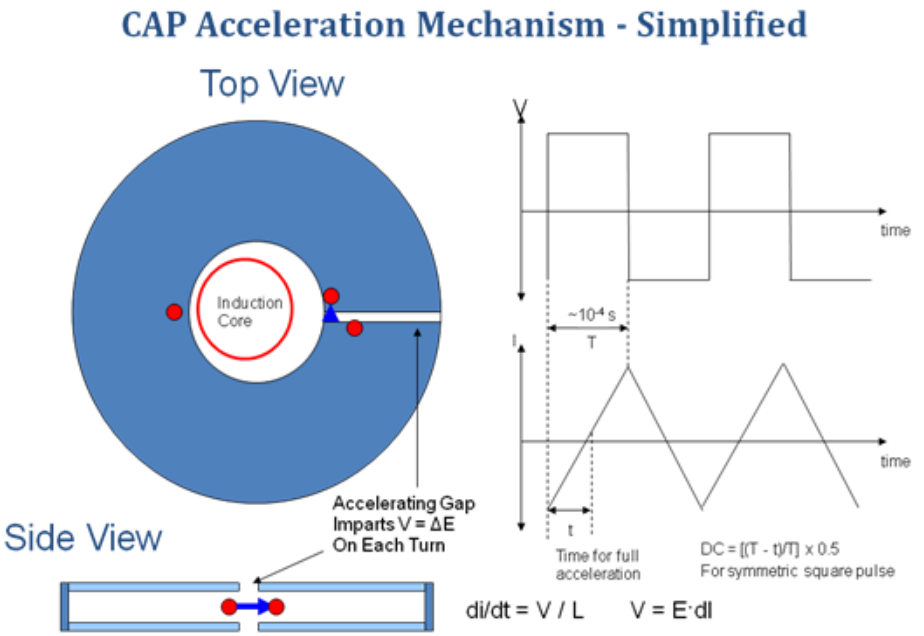

Fig. 18. The Compact Accelerator Project (CAP) at Passport.

design was tested with an electron accelerator that reached 425 keV and this is shown in Fig. 17. A successful 50 MeV radial design was also constructed by MURA in 1961 at the Stoughton site.

Fig. 18 shows a very simplified description of the acceleration mechanism of the Compact Accelerator Project (CAP) at Passport Systems, Inc. An induction core produces an inductance, L, which limits the current in a conducting vacuum chamber with a voltage, V, across an accelerating gap. The electrons (red dots) are accelerated by the amount V on each turn. The waveforms demonstrate how the duty cycle can reach as much as 50% for an ideal inductor.

The CAP design being developed by Passport has as its first articulation will be of a scaling design. It appears possible to construct a scaling machine with the standard tolerances available in commercial machining practice to accommodate a momentum range of 40, implying injection of approximately 50 keV and final energy of 9 MeV.

The tools used in the design are well known to those familiar with accelerator design. These are listed in Fig. 19 in tabular form for efficiency of presentation. One development of interest is the tracking turn by turn through the FFAG field by COSY accounting for each energy increase. This modification required extensive modification to COSY and it is very useful at tracking orbit by orbit at injection. In Fig. 20 the tracking of a beam of electrons in phase space is exhibited for four orbits showing how the beam can be displaced from the inflector at injection.

- Opera from Vector fields
  - FFAG Guide fields and relation to magnetic geometry
  - Electron gun and injection optics integrated to FFAG guide orbits
- Omnitrak
  - Electron gun and injector optics
    - Cathode parameters
    - Thermal effects
    - Electrode parameters
    - Emittance
- Cosy
  - Tracking orbits through fields
  - Establishing dynamic apertures
  - Extension for tracking each orbit with energy gain during each orbit
  - Establishing injection parameters to miss gun on first few turns
  - Establishing likely resonances
  - Establishing tunes

Fig. 19. Design Tools.

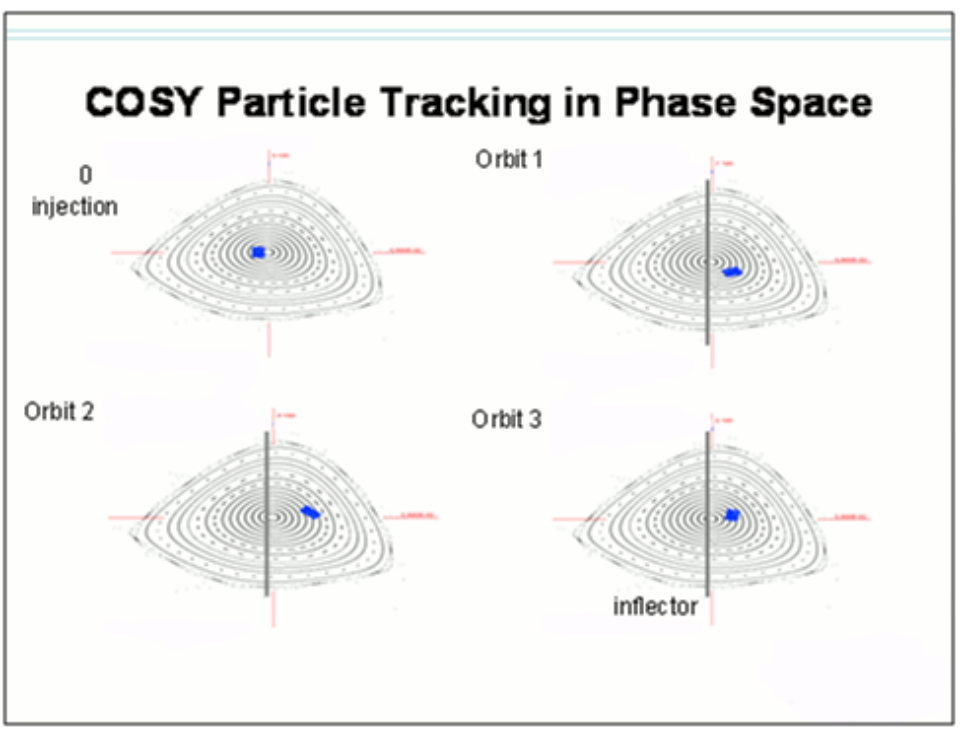

Fig. 20. First Four Turns Near Injection of the Beam: Tracking 1000 Particles.

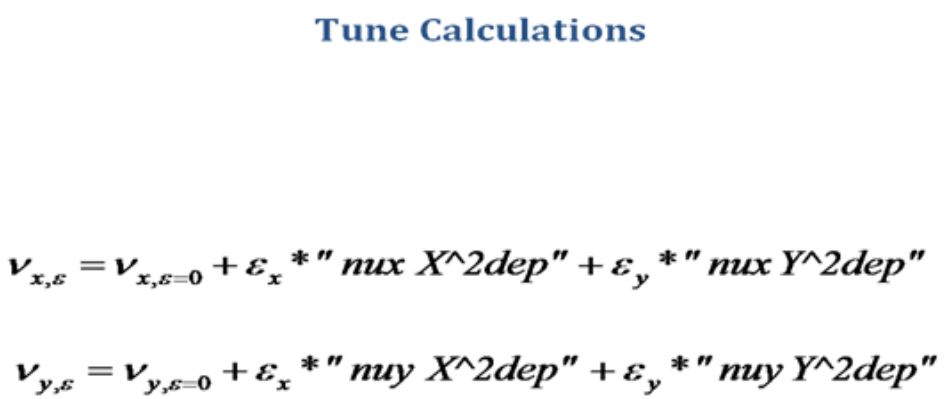

Fig. 21. Relations Between Tunes, Phase Space Amplitudes, and Emittances.

With the acceleration on each turn the beam is displaced to larger radii finally escaping from possible collisions with the inflector at injection.

Relationships relating the tunes to the closed orbit tunes (zero amplitude for betatron oscillation) and the dependencies on the X and Y emittances are shown in Fig. 21. These dependencies can be tracked turn by turn and the location of resonances established as well as the width of the resonances. Fig. 22 shows one example of a phase space diagram (left side) where the horizontal emittance is set to zero and the vertical amplitude dependency is allowed to develop. The islands show the presence of resonances with 4-fold and 5-fold symmetry located at specific amplitudes as calculated by COSY. The graph on the right shows a linear model for the amplitude dependent tune shift calculated by COSY and the islands from actual tracking particles through fields are manifested at the predicted amplitudes.

One example of the usefulness of tracking each turn after an impulsive acceleration is illustrated in Fig. 23. This figure shows the emittance in X and in Y (radial and vertical) as a function of beam energy for one specific magnetic field configuration. Of course, since energy and radius are strictly correlated the same plot can be made for emittance versus radius, indicating a closer tie to the exact magnetic field pattern. The emittance is seen to fall inversely as the momentum as expected over much of the energy region. The emittance growth near injection and 8 MeV shows the influence of resonances driven by the non-linear components of the field. The decrease starting just below 9 MeV is the result of the emittance growth being too large for a portion of the beam to navigate an aperture and it accounts for lost particles. The transmission of this specific design remains very good up to almost 9 MeV.

Non-scaling FFAG acceleration has been demonstrated to be a viable design alternative for high energy accelerators[7,8] such as for muons and cyclotrons. The non-linear behavior that is endemic to such a non-scaling design introduces

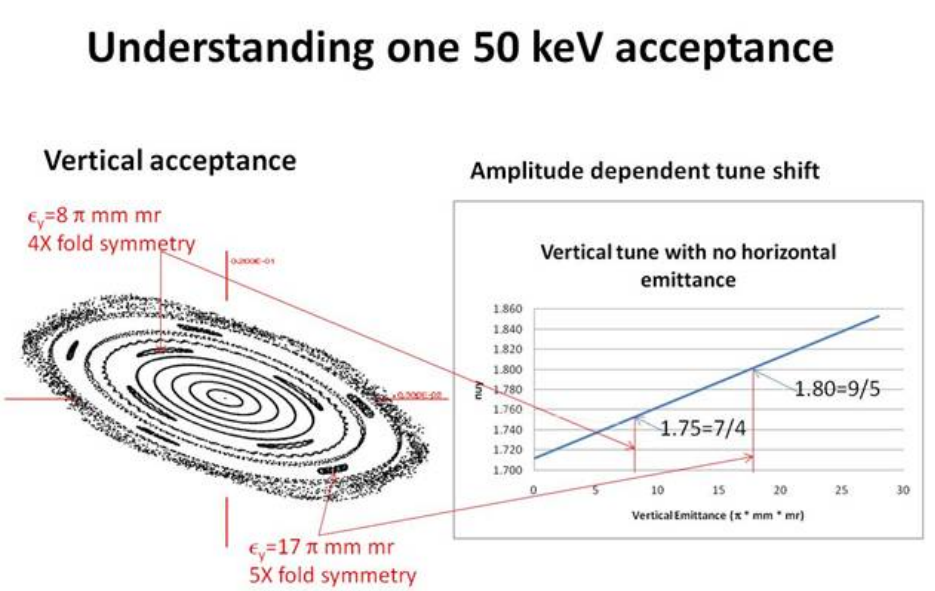

Fig. 22. One Example of Amplitude Dependent Tune Shift and Phase Space Patterns.

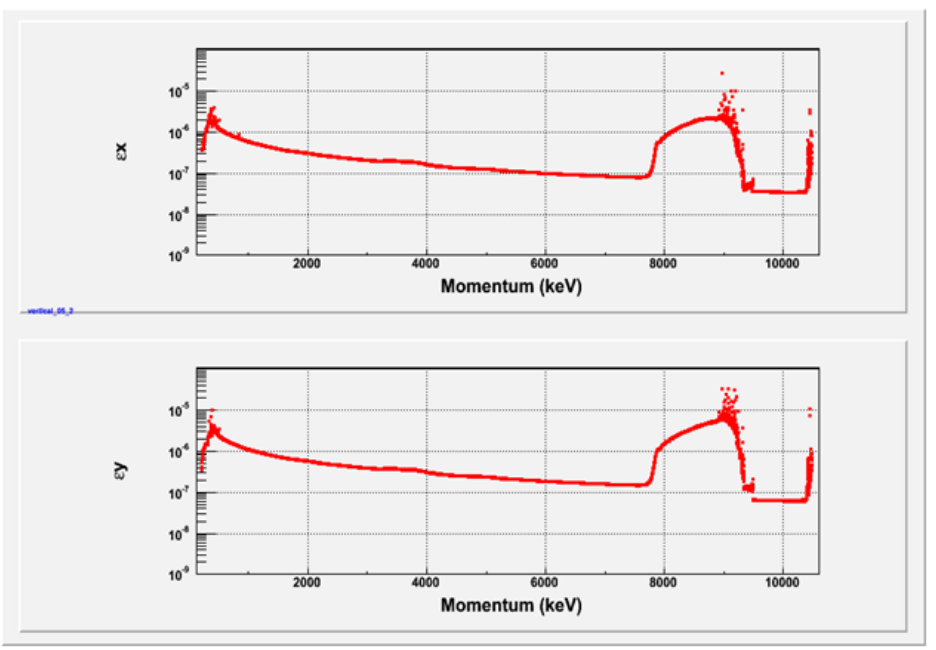

Fig. 23. Emittance in X and Y as a Function of Beam Energy.

resonances that can be a serious problem. Where rapid acceleration is possible resonances are surmounted by having only a few turns span the resonance width. At lower energies where induction is the accelerating mechanism the acceleration per turn is generally low and the presence of resonances must be avoided with greater care than with high energy machines. Some non-scaling designs have a variable tune with energy and this helps in avoiding resonances. The momentum gain for a 9 MeV accelerator starting with 50 keV injection is approximately a factor of 40. The designs discussed at higher energies for non-scaling FFAG machines have only reached a factor of 6 for this momentum range. Another problem is achieving the field patterns needed with the tight spacing imposed by an accelerator with small footprint. The separation of D and F magnets can become a serious challenge to maintaining field patterns as is the thickness of the magnets at small orbital radii. However, non-scaling versions of the FFAG concept for accelerators are under study for several applications[9] and the non-scaling FFAG may become one of the successful variants in homeland security.

8. Conclusions

The importance of high duty cycle has been demonstrated for applications to homeland security. It allows for a new set of important detection technologies to be employed and improves the performance of the older ones, notably radiography. The use of an induction FFAG electron accelerator modality provides:

- Large momentum range acceptance.
- Good transmission.
- Small footprint.
- High intensities.
- Dynamically variable currents over a wide range.
- Duty cycle approaching 50%.
- Lower costs.

References

1. *Muon Radiography; Detecting Nuclear Contraband*, Brian Fishbine, Los Alamos Research Quaterly, Spring 2003.
2. *Gamma-ray and Neutron Radiography as Part of a Pulsed Fast Neutron Analysis Inspection System*, J. Rynes, J. Bendahan, T. Gozani, R. Loveman, J. Stevenson and C. Bell; NIM A, **Volume 422:1-3,** 11 February 1999, pp. 895-899 and references therein.
3. *Imaging and Radiography with Nuclear Resonance Fluorescence and Effective-Z (EZ-3D™) Determination; SNM Detection Using Prompt Neutrons from Photon Induced Fission;* William Bertozzi, Richard Hasty, Alexei Klimenko, Stephen E. Korbly, Robert J. Ledoux and William Park; Application of Accelerators in Research and Industry: 20^{th} Int. Conf., edited by F. D. McDaniel and B. L. Doyle; AIP Conference Proceedings **1099.**

4. W.Bertozzi, J. A. Caggiano, W. K. Hensley, M. S. Johnson, S. E. Korbly, R. J. Ledoux, D. P. McNabb, E. B. Norman, W. H. Park, and G. A. Warren, Phys. Rev. C **78** 041601(C) (2008).
5. C. P. Sargent, W. Bertozzi, P. T. Demos, J. L. Matthews, and W. Turchinetz, *Prompt Neutrons from Thorium Photofission*, Phys. Rev. **137,** B89 - B101 (1965).
6. Donald W. Kerst and Keith R. Symon, *Imparting Energy to Charged Particles*, U. S. Patent 2,932,798, Apr. 12, 1960.
7. C. Johnstone, et al., *"Fixed Field Circular Accelerator Designs"*, PAC'99, New York, p. 3068.
8. *Nonscaling FFAG Variants for HEP and Medical Applications,* C. Johnstone et al., Proceedings of PAC09, Vancouver, BC, Canada.
9. C. Prior, Ed., ICFA Beam Dynamics Newsletter #43, August 2007, `http://www-bd-fnal.gov\icfabd\Newsletter43.pdf`.

International Journal of Modern Physics A
Vol. 26, Nos. 10 & 11 (2011) 1736–1743

DOI: 10.1142/S0217751X11053134

World Scientific
www.worldscientific.com

THE EMMA FFAG

ROB EDGECOCK
STFC Rutherford Appleton Laboratory, Chilton, Didcot, Oxon, OX11 0QX
rob.edgecock@rl.ac.uk

1. Introduction

As described previously,[1] non-scaling Fixed Field Alternating Gradient (ns-FFAG) accelerators have a significant potential for future applications, potentially replacing the currently used cyclotrons and synchrotrons. However, they, in particular linear ns-FFAGs, have a number of unique features and characteristics,[2] including:

- very large momentum compaction (Livingood definition, Ref. 3),
- large betatron tune variations and multiple resonance crossings,
- serpentine (bucketless) acceleration,
- the requirement for purpose-built tracking codes,
- the need for a highly symmetric lattice.

Due to these features and the need to benchmark the tracking codes employed with this type of accelerator, it was concluded that a proof-of-principle ns-FFAG needed to be built before this technology could be further developed for real applications. This machine is called EMMA (the Electron Model for Many Applications) and is currently (April 2010) under construction and testing at the STFC Daresbury Laboratory in the UK. Beam was first passed through the EMMA injection line on 26^{th} March 2010.

The following sections will describe the EMMA parameters and the resulting layout of the accelerator, the main components of the machine and the plans for commissioning and the experimental program.

2. EMMA Specifications

To prove the principle of ns-FFAGs and investigate the features listed above, it has been decided to design and build a linear machine, employing fixed frequency RF acceleration. To minimize cost, EMMA will accelerate electrons from 10 to 20 MeV and will use a beam provided by the existing ALICE accelerator[4] at Daresbury. The parameters of the machine have largely been determined by scaling down those for

Table 1. EMMA parameters.

Parameter	Value
Kinetic energy range	10 to 20 MeV
Cell	Doublet
Number of cells	42
RF	19 cavities; 1.3 GHz
Cell length	394.481 mm
Ring circumference	16.57 m

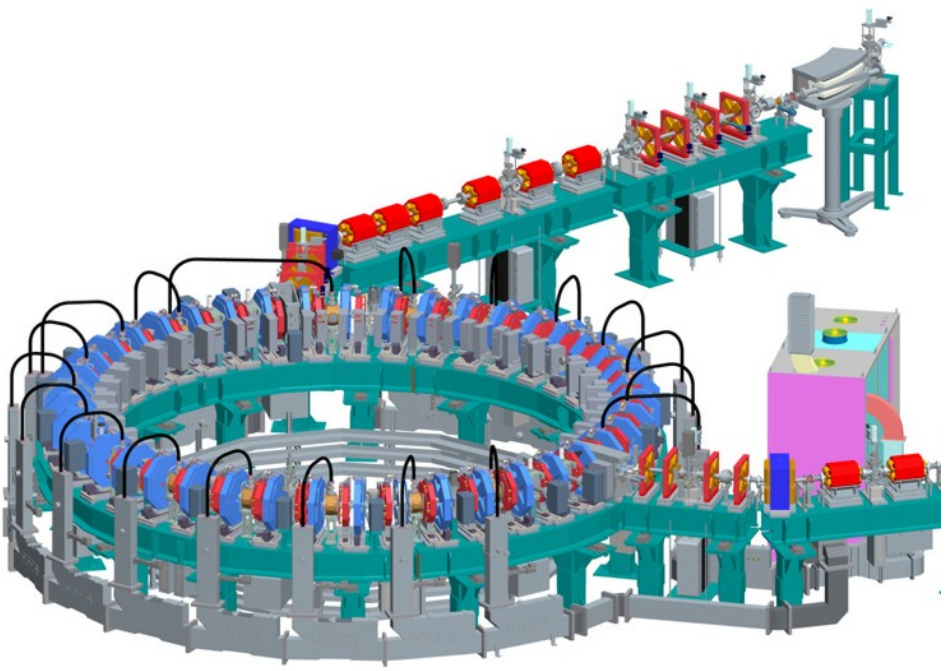

Fig. 1. Layout of EMMA, showing the last part of the injection line from ALICE (to the right), the EMMA ring and the extraction line, holding the diagnostic devices which will disrupt the beam.

a muon FFAG in the Neutrino Factory[5] and are listed in Table 1. A doublet lattice has been chosen, to minimize cost, and there will be 42 cells.

To deliver the aims of the project, 8 different lattice configurations have been designed,[6] which probe the longitudinal and transverse dynamics of the machine and different regions of the tune diagram. The specifications for EMMA have been determined by these lattices and the resulting machine layout is shown in Figure 1. The ring itself is built on 7 girders, with 6 cells per girder. Figure 2 shows a single cell, consisting of a magnet doublet and an RF cavity, and 4 of the girders in place next to the injection line from ALICE.

Fig. 2. An EMMA cell with a royal visitor (left) and 4 EMMA girders in place (right), with the end of the injection line at the bottom right of the photograph.

3. EMMA Hardware

The design and construction of the hardware for EMMA has been challenging for a number of different reasons. As this the first machine of its type, many problems have arisen that have required novel solutions. Further, the flexibility needed to provide the proof-of-principle for non-scaling optics and meet the requirements of the 8 lattices has created significant difficulties. Finally, as shown in Figure 1, the lattice is very compact and fitting everything into the machine has been a huge problem. The following subsections will outline the design of the three main components of the accelerator: the magnets, the RF and the diagnostics. All other parts are described elsewhere.[7]

3.1. *Magnets*

A number of different magnet types are required for EMMA and these are summarized in Table 2. The 84 main ring DC magnets require independently variable dipole and quadrupole components. They are implemented as quadrupoles and the dipole component is obtained by using them off-axis. This component is adjusted by mounting the magnets on precise, computer controlled sliders. As shown in Figure 2, each doublet is surrounded by clamp plates. These are to prevent field leakage into the iron of the kicker magnets, but are mounted on each doublet to minimise orbit errors from asymmetry. Almost all of the magnets will be powered from two power supplies, one for the Fs and one for the Ds. Two of each type of magnet will be powered using individual supplies, to allow the field strengths to be changed compared to the others to introduce artificial errors for resonance studies.

The pulsed magnets, the kicker magnets and septa, have proved to be the most difficult to design. The selected scheme is to use a septum and two kickers in adjacent cells for both injection and extraction. To avoid passing through the magnets in the neighboring cell, the entrance and exit angles are 65° and 71°, respectively. Further, the space available is limited to about 20 cm for each magnet and the fall (rise) time of the injection (extraction) kicker must be less than the revolution period of 55 ns. To be able to inject and extract and to probe the full acceptance

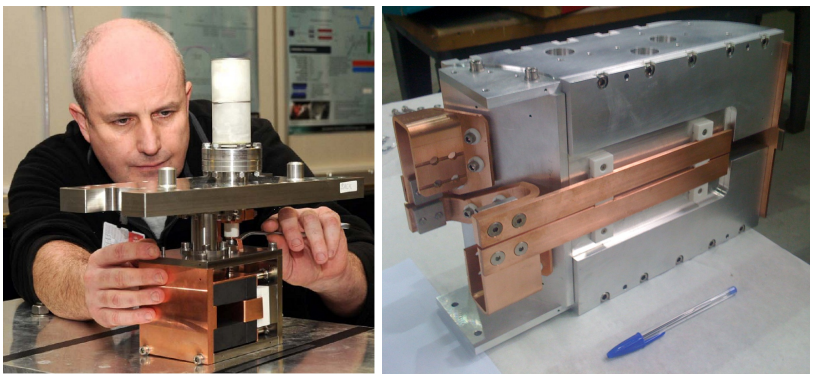

Fig. 3. EMMA kicker (left) and septum (right) magnets.

of the ring at all energies, it is also necessary to be able to move and rotate both septa. Examples of these magnets are shown in Figure 3.

Vertical steering and combined vertical and horizontal steering magnets are required in the injection line, the main ring and the diagnostics beam line. The combined steerers are used for orbit correction in the external lines, while the vertical steerers will be used to scan the full vertical acceptance of the ring. Horizontal scanning will be performed by the kicker magnets. The vertical steerers in the ring will be used for vertical orbit correction.

3.2. *RF system*

Rapid acceleration is obtained by placing accelerating cavities in every other cell around the EMMA ring, with two cavities omitted for injection and extraction of the electron beams. The RF system consists of 4 major sub-systems: a high power RF amplifier system, a RF distribution system, a low level RF (LLRF) control system and finally RF cavities that transfer energy to the beam. All 19 RF cavities are driven from the same RF source, with a complex distribution scheme providing equal power to each cavity. Synchronisation of the electron bunches to the RF cavity is also required to tight tolerances, to ensure that the accelerating field is present as the electron bunches pass each RF cavity. The RF operating parameters can be found in Table 3.

The high power RF amplifier system consists of a high voltage power supply, a 1 kW solid state amplifier and an Inductive Output Tube (IOT). This system will provide 90 kW of pulsed RF power at 1.3 GHz. The pulse length for the RF is 1.6 ms, with a pulse repetition frequency of up to 20 Hz required. Due to the R&D requirements for EMMA, a 5.5 MHz operational tuning range is specified. This puts additional strain on achieving stable operation as the master oscillator clock, which also synchronizes the RF to the ALICE RF, will be fixed at 1.3 GHz. For this reason, a full $360^{c}irc$ phase shifter is required prior to each cavity to allow local phasing of the RF.

Table 2. EMMA magnets.

Location	Type	Number
Injection line	Quadrupole	18
	Dipole	4
	Vertical steerer	2
	Combined steerer	4
Injection system	Septum	1
	Kicker	2
EMMA ring	Quadrupole – F	42
	Quadrupole – D	42
	Vertical steerer	16
Extraction system	Septum	1
	Kicker	2
Diagnostics line	Quadrupole	14
	Dipole	2
	Vertical steerers	2
	Combined steerers	4

Table 3. Specifications for the EMMA RF system.

Machine Parameters	Values	Units
Frequency	1.3	GHz
Frequency range	−4.0 to 1.5	MHz
Number of straights	21	
Number of cavities	19	
Total voltage per turn	2.3	MV
Upgrade voltage per turn	3.4	MV
Beam aperture	40	mm
RF pulse length	1.6	ms
RF repetition rate	1 to 20	Hz
Amplitude control	0.3	%
Phase control	0.3	°

The EMMA RF system is unique in that the 19 cavities are all fed from the same RF source distributed around a compact ring. A bespoke waveguide section that includes circulator, load, phase shifter, directional coupler and waveguide to coaxial transformer has been designed and built to achieve this.

As it is essential that the RF is synchronized with the beam in order to place the beam at the correct place in longitudinal phase space, a LLRF system is required to monitor signals from each cavity and provide the necessary phase or voltage adjustment to ensure the optimum RF settings are maintained. In order to maintain this stability during operation, feedback signals from the cavity fields are monitored in the LLRF system.

The ultimate performance on the accelerator will be the ability of the cavities to efficiently transfer energy to the beam. For EMMA, a normal conducting single cell re-entrant RF cavity design has been optimized for high shunt impedance, working within geometrical constraints of a 40 mm beam aperture and 110 mm flange to

Fig. 4. Design of an EMMA RF cavity (left) and a cavity under test (right).

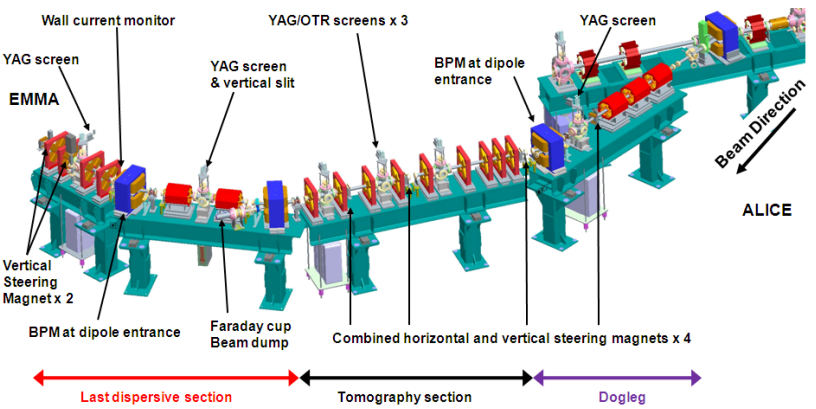

Fig. 5. EMMA injection line, showing the locations of the diagnostic devices.

flange length availability. The custom in-house design shown in Figure 4 meets the operation specification.

3.3. *Diagnostics*

As EMMA is a purely experimental machine, it is very important that it has sufficient diagnostic devices to make detailed measurements of the beam throughout the acceleration cycle. These are located in the injection line, to measure beam properties on injection into EMMA, and the ring itself. Destructive devices are located in an external diagnostics beamline. The extraction system into this is designed to allow extraction at all energies, so that measurements can be made at any energy. The devices employed are summarized in Table 4 and their locations in the machine are shown in Figures 5 and 6.

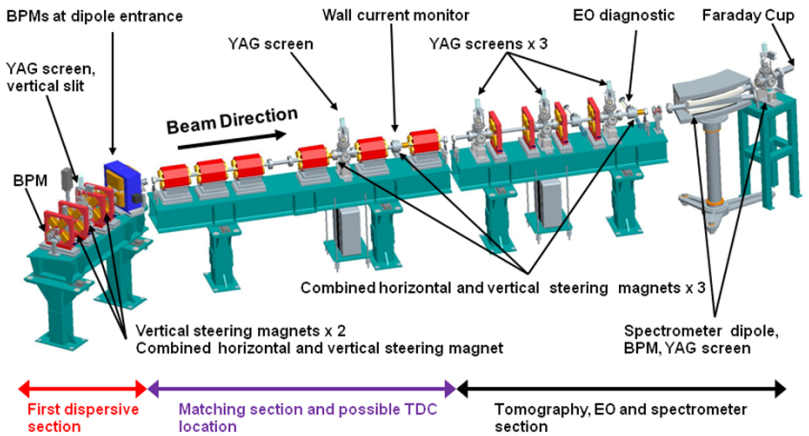

Fig. 6. EMMA diagnostics beam line, showing the locations of the diagnostic devices.

4. Experimental Program and Commissioning

An extensive experimental program is planned with EMMA. This will include, for each lattice:

- Demonstrating serpentine acceleration (see Figure 7).
- Demonstrating beam acceleration with multiple resonance crossings.
- Measuring the variation of the horizontal and vertical tune with energy.
- Measuring the variation of the time of flight with energy (see Figure 7).
- Scanning longitudinal phase space, including the variation of serpentine acceleration and beam emittance with the longitudinal parameters.
- Scanning the transverse phase space, including the variation of the dynamic aperture with energy and the time of flight and acceleration with beam amplitude.
- Studying resonance crossings with low acceleration.

These measurements will need to be repeated with each lattice and all the measurements made compared with the expectations from the tracking codes.

The commissioning phase of EMMA is being designed to make these measurements possible. It will include making beam measurements in ALICE, commissioning the injection line and injection system, placing the beam on the correct orbit, commissioning the diagnostic devices with beam, testing the extraction system and verifying the proposed methods for making the measurements listed above. The accelerator control system has been designed to allow a set of machine parameters to be tried out with an online model before and in conjunction with using them on the real machine, to enhance debugging and understanding the machine operation. It is expected that first results from EMMA will be available during the summer of 2010.

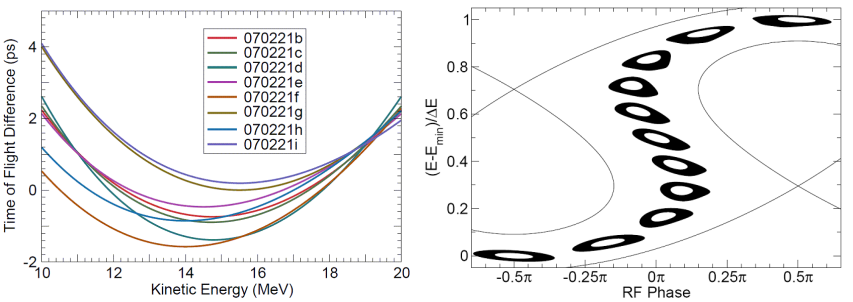

Fig. 7. Time of flight curves for the 8 EMMA lattices (left) and serpentine acceleration (right).

Table 4. The diagnostics devices to be used on EMMA. The location of the devices is shown in bold in the first column.

Measurement	Device	Number
Beam position **(Ring)**	4 button BPM	82
Beam position **(Injection)**	4 button BPM	7
Beam position **(Extraction)**	4 button BPM	5
Beam profile **(Ring)**	Screens	4
Beam profile **(Injection)**	Screens	5
Beam profile **(Extraction)**	Screens	6
Beam charge **(All)**	Wall current monitor	3
Phase wrt RF **(All)**	Wall current monitor	3
Transmission **(All)**	Wall current monitor	3
Transmission **(Extraction)**	Faraday cup	1
Beam loss **(Ring)**	Beam loss monitor	4
Emittance **(Inj/Ext)**	Screens	3
Momentum **(Ring)**	BPMs	
Momentum **(Extraction)**	Spectrometer	1
Long. Profile **(Extraction)**	Electro-optic monitor	1

References

1. C. R. Prior (ed), *ICFA Beam Dynamics Newsletter #43*, August 2007.
2. F. Mills. In *Proc. 4th Int. Conf. Physics Potential and Development of $\mu+\mu-$ Colliders*, 693–696, San Francisco, 1997; C. Johnstone. *Ibid.*, 696–698; A. Garren, C. Johnstone and W. Wan. In *Proc. 1999 Particle Accelerator Conf.*, pp. 3068–3070, New York, 1999.
3. J. J. Livingood, Principles of Cyclic Particle Accelerators, D. Van Nostrand, New York, 1961.
4. D. J. Holder et al. In *Proc. 11th European Particle Accelerator Conf.*, pp. 1001–1003, Genoa, Italy, 2008.
5. S. Machida, in *Proc. 22nd Particle Accelerator Conf.*, pp. 2614–2618, Albuquerque, USA, 2007.
6. J. S. Berg, The EMMA Main Ring Lattice, *Nucl. Instrum. Methods A*, 596:276–284, 2008.
7. C. Beard et al. EMMA—The World's First Non-Scaling FFAG, to be submitted to *Nucl. Instrum. Methods A*.

International Journal of Modern Physics A
Vol. 26, Nos. 10 & 11 (2011) 1744–1752

DOI: 10.1142/S0217751X11053146

World Scientific
www.worldscientific.com

ADVANCEMENT OF THE SCALING FFAG ACCELERATOR FOR ADSR, PULSED-SNS AND MUON ACCELERATION

YOSHIHARU MORI

Kyoto University,Research Rector Institute, Kumatori, Osaka 590-0494, Japan
mori@rri.kyoto-u.ac.jp

Progress in the study of beam optics and acceleration of the scaling FFAG accelerator has been presented in this paper.

Keywords: FFAG; zero-chromaiticiy.

PACS numbers: 11.25.Hf, 123.1K

1. Introduction

Production of intense neutrons is essential for accelerator driven sub-critical reactors (ADSR) and pulse spallation neutron sources (SNS). The neutron yield increases very abruptly up to the proton energy of about 1 GeV. Compared with the neutron yield at 100 MeV, more than two orders of magnitude increase in neutrons can be generated at 1 GeV. It should be also noted that in such a high energy region, nuclear cascade interaction (hadron shower reaction) is a dominant process and the mean free path for heavy target material such as Ta in this reaction is about 15 cm, which means a target thickness of about 50 cm is sufficient. Thus, from the point of view of neutron yield, the higher energy is better.

One beam specification requested of the proton beam for ADSR and pulsed SNS is its time structure. The pulsed SNS requires a short pulse (< 0.5 μsec) and a relatively low repetition proton beam. On the other hand, the beam time structure for the ADSR is rather modest and a relatively higher repetition rate (< 100 Hz) is favored to avoid thermal shock on the target. The types of accelerator which could satisfy both these requirements simultaneously are a proton linear accelerator (LINAC)/proton storage ring(PSR) complex, or a fixed field alternating gradient(FFAG) accelerator. Neither a cyclotron or synchrotron can be used. A LINAC/PSR complex is a straightforward solution but very expensive. On the other hand, a high intensity FFAG accelerator needs more research and development.

In muon acceleration, the FFAG accelerator is useful because of its capability for strong focusing and very fast acceleration, however, it requires more studies especially on advanced schemes for fast beam acceleration and beam manipulation for injection/extraction in the presence of relatively large beam emittances.

In this paper, advancement of the FFAG accelerator which could demonstrate the feasibility and capability of the FFAG accelerator for ADSR and pulsed SNS, and also for muon acceleration are discussed.

2. Beam Focusing and Acceleration in FFAG Accelerator

The idea of the FFAG accelerator was originally by Ohkawa in 1953[1] and by Symon and Kolomenskii, independently. Electron models of the FFAG accelerator were built by Kerst, Cole and Symon at MURA in the early 1960s.[2] However, since then, no FFAG proton accelerator has been built until recently. A proton FFAG accelerator, in particular, has significant technical difficulties such as its complicated configuration of magnetic field and more difficult rf acceleration. In 2000, the world's first proton FFAG accelerator (POP-FFAG) was demonstrated using a novel broad-band RF cavity with high permeability MA(magnetic alloy) cores at KEK.[3] Following this success, it has been recognized that FFAGs have large advantages in rapid acceleration with large momentum acceptance, which are useful both for muon accelerators and for high power proton drivers. Since then, intensive studies and discussions have been carried out, and various projects for the development of FFAGs have been started for many applications at many institutes.

The FFAG accelerator has distinctive features compared with other types of accelerators in beam focusing and acceleration. In transverse beam focusing, two types of beam focusing can be categorized: scaling and non-scaling. The scaling type of FFAG accelerator has non-chromatic beam optics in which a large amount of nonlinear field is essential. Fields were initially linear in the non-scaling type of FFAG accelerator. However, a number of betatron resonances have to be crossed during acceleration. As for beam acceleration, various schemes with new ideas such as a broad-band MA rf cavity, stationary bucket acceleration, serpentine acceleration and harmonic number jump acceleration have been studied intensively and some of them have been realized.

2.1. *Beam focusing*

2.1.1. *Scaling*

In the scaling type of FFAG accelerator, orbits for different beam momenta are geometrically similar in shape (curvature), thus insuring zero chromaticity in the beam optics. Thus, the betatron tunes for both horizontal and vertical directions remain constant during beam acceleration and do not experience problems caused by resonance crossing. The transverse linearized betatron equation of motion can be expressed by the following equation:

$$\frac{d^2X}{ds^2} + K(s)X = 0, \tag{1}$$

where X is the transverse displacement of the particle and s is the distance along the reference trajectory, and $K(s)$ can be given for horizontal (x) and vertical (z)

directions by

$$K_x = \frac{1 - n(s)}{\rho^2(s)}, \tag{2}$$

$$K_z = -\frac{n(s)}{\rho^2(s)}, \tag{3}$$

respectively. Here ρ is a orbit curvature and n is a field index defined with magnetic field strength as

$$n = -\frac{\rho}{B}\left(\frac{dB}{dX}\right). \tag{4}$$

The scaling condition requires that the equation of motion of Eq. 1 is independent of momentum both for horizontal and vertical directions.

In cylindrical coordinates, it can be shown analytically that the configuration of the magnetic field at the median plane can be expressed with a geometrical field index k and a reference orbit radius r_0 in the following equation including azimuthal direction:[4]

$$B(r,\theta) = B_0\left(\frac{r}{r_0}\right)^k \mathcal{F}\left(\theta - \zeta \ln\frac{r}{r_0}\right), \tag{5}$$

where $\zeta = \tan\xi$, and ξ is a spiral angle of the magnet in the azimuth plane. Accordingly, two schemes for beam focusing are invoked by this magnetic field configuration: one is radial sector focusing and the other spiral sector focusing. Radial sector focusing uses a combination of positive and negative bending magnets to make strong beam focusing with a FODO lattice configuration. In spiral sector focusing, strong edge focusing is exploited.

2.1.2. *Non-scaling*

The non-scaling linear-field type of FFAG accelerator has a basically simple structure composed of linear optical elements; i.e. dipole and quadrupole magnets. With only linear fields and rectangular (parallel-face) magnets, however, the transverse betatron tune is not constant during acceleration and fast acceleration is essential in this type of non-scaling FFAG accelerator to avoid beam losses caused by resonance crossing. To ensure this, the RF cavity phases are fixed for beam acceleration and the range of times-of-flight over the energy range of the accelerator is minimized when the path length difference has a parabolic dependence on beam momentum.[5] Based on the concept of linear non-scaling FFAG accelerators, some variations such as isochronous or semi-achromatic lattice[6,7] including small nonlinear elements (semi-scaling) have also been proposed.

2.1.3. *Advances in scaling FFAG optics*

The scaling law of the FFAG accelerator as required to satisfy the zero-chromaticity condition is applied to circular accelerator as described above, and each cell con-

tributes the same bending angle to complete the ring. A scaling FFAG unit cell can be designed with a straight section such that the total bending angle of zero is created, then with proper insertion/matching optics these "straight sections" can be incorporated into a conventional scaling FFAG ring. The scaling condition for the straight section unit cell, i.e. the same phase advance per cell at every energy, leads to a different field law:

$$\frac{d(\frac{1}{\rho^2})}{dp} = 0, \tag{6}$$

$$\frac{d(K\rho^2)}{dp} = 0. \tag{7}$$

Geometrical similarity is given by $\rho = \text{const}$, and it leads to a solution for the magnetic field configuration[8]

$$B = B_0 e^{m(X-X_0)} \mathcal{F}(Y - X\tan\xi_s). \tag{8}$$

Here

$$m = \frac{1}{B}\frac{dB}{dX}. \tag{9}$$

This scaling field law has been applied to the FFAG straight section, and insertion/matching optics added to the scaling FFAG rings have been examined for various applications.[9,10] Figure 1 shows an example of the scaling FFAG insertion with a straight section and dispersion suppression.[10] A schematic diagram of a scaling FFAG ring with dispersion suppressors and straight sections is presented in Fig. 2.

2.2. *Acceleration*

One of the most distinctive features of FFAG accelerators compared with ordinary strong focusing synchrotrons is that very fast acceleration is possible because the magnetic field is static. Accordingly, various new RF acceleration schemes, which are adequate both for scaling and non-scaling FFAG accelerators, have been proposed for fast acceleration, and some of them have already been realized.

2.2.1. *Broad-band RF cavity with MA cores*

Broad-band RF cavities with high permeability magnetic alloy (MA) cores have been used mostly in the scaling type of proton FFAG accelerators such as the POP-FFAG developed at KEK. No frequency tuning synchronized with beam revolution is needed and a very rapid acceleration cycle of several 100 Hz to 1 kHz becomes possible. However, above that rate, the required rf voltage becomes rather high, which is difficult to obtain with this type of rf cavity.

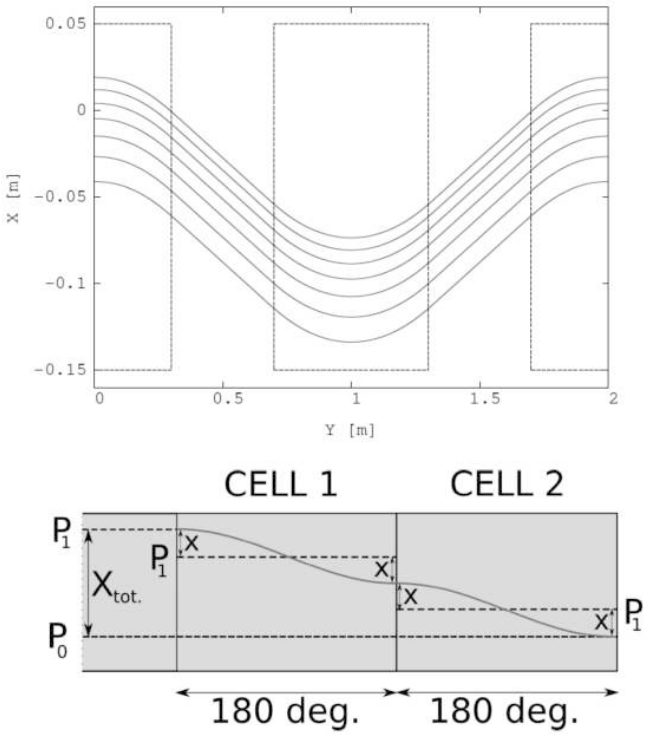

Fig. 1. Scaling FFAG straight line and the dispersion suppressing insertion.

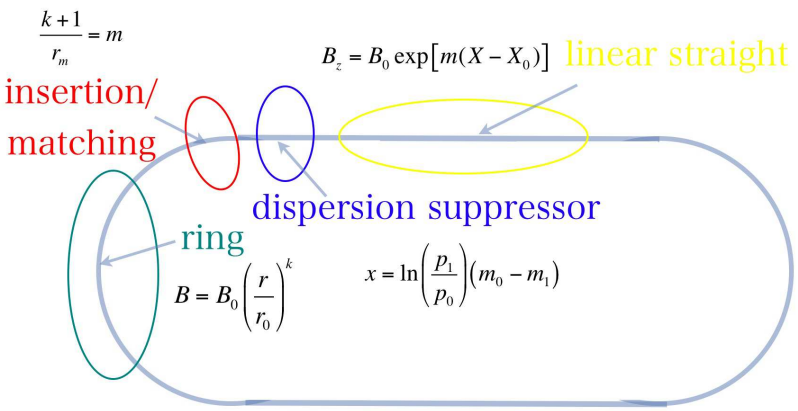

Fig. 2. Schematic diagram of scaling FFAG ring with linear straight section and the dispersion suppressing insertion.

2.2.2. *Stationary RF bucket acceleration*

In longitudinal phase space, the RF bucket of the scaling type of FFAG accelerator for relativistic particles such as high energy muons is not distorted for large momentum range because the momentum compaction is a constant and is independent of momentum. If the RF voltage is large enough, the particles can be accelerated in a stationary RF bucket corresponding to a half period of a synchrotron oscillation.[11]

2.2.3. *Serpentine acceleration*

In the non-scaling FFAG accelerator, a fixed frequency RF system is installed and acceleration out of longitudinal buckets is possible for relativistic particles when the path length difference has a parabolic dependence on momentum as described above. The revolution time (time-of-flight per turn) changes and has a minimum during beam acceleration.[12]

In the scaling FFAG accelerator, a similar acceleration scheme with a fixed frequency RF is also possible. The beam is accelerated by passing through the transition energy where the time-of-flight per turn is at a minimum. The longitudinal Hamiltonian in the case of scaling FFAG accelerator is analytically obtained as

$$\frac{H}{m_0c^2 f_s} = 2\pi \left[-\frac{A}{2(1-\lambda)}(\gamma^2 - 1)^{1-\lambda} + \gamma \right] + \frac{eVh}{m_0c^2}\cos\phi. \tag{10}$$

Here,

$$\lambda = \frac{k}{2(k+1)}, \tag{11}$$

$$A = \frac{(\gamma_s^2 - 1)^{\lambda}}{\gamma_s}. \tag{12}$$

Figure 3 shows an example of the phase space contour for the longitudinal motion of the scaling FFAG accelerator.[13] As can be seen from this figure, a serpentine path through the transition energy exists and beam acceleration for non-relativistic particles is possible with this scheme in the scaling FFAG accelerator.

2.2.4. *Harmonic number jump*

In FFAG accelerators, the transverse position of the beam changes during acceleration. If the energy gain varies with transverse position to achieve an integer change in the harmonic number with each turn, then the beam can be accelerated with a fixed frequency RF system.[14] The difficulty of this scheme is how to vary the energy gain properly and ideas such as a position-dependent RF voltage configuration have been proposed to overcome this difficulty.

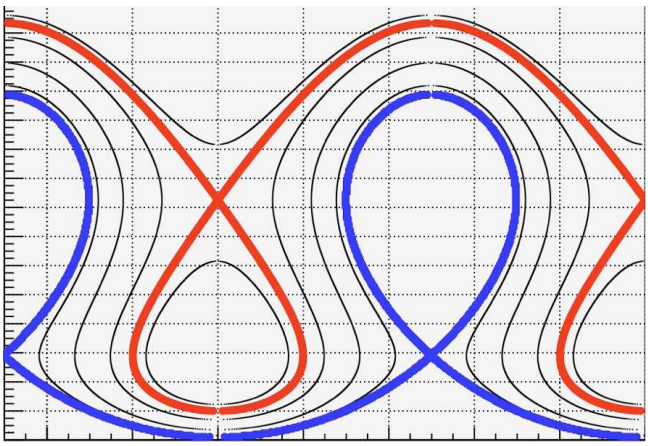

Fig. 3. Longitudinal Hamiltonian contour for serpentine acceleration in a scaling FFAG accelerator.

3. FFAG for High Intensity Proton Accelerator

A proton driver for producing an order of magnitude more intense secondary particles such as neutrons, muons, mesons etc. compared with the present high intensity proton accelerators (HIPA), such as J-PARC, SNS and ISIS, requires the next generation of HIPAs. The beam energy of this next generation of HIPAs needs to be more than 1 GeV because the nuclear interactions that generate hadron showers are more efficient at higher energy. This increased efficiency is required to achieve beam powers more than 10 MW—the power level presently being discussed. Requirements for the time structure of the beam from next generation HIPAs, however, have many variations which depend on application. The neutrino factory/muon collider requires a very short beam bunch (nsec) and low repetition rate operation (10 Hz). On the other hand, the ADSR requires a very large repetition rate of more than kHz or even cw operation. The next generation HIPAs should address these various requirements as much as possible.

The types of accelerator suitable for next generation of HIPA, from this point of view, are limited. Ordinary synchrotron and cyclotron can be excluded. The former is unsuited for high repetition operation and the latter for short bunched and high peak intensity pulse operation. Two candidates for the next-generation HIPA could be a superconducting LINAC/PSR complex, and a FFAG proton accelerator. The FFAG accelerator can be operated in various repetition pulsed modes and even in cw mode as described in the previous section. When the beam repetition is less than 1 kHz, the broad-band RF system as described in the previous section can be used for either scaling or non-scaling FFAGs. However, in order to realize cw operation, a fixed-frequency RF acceleration scheme is essential and, in particular, for the proton driver where the particle velocity is still non-relativistic, a scaling FFAG accelerator with serpentine acceleration seems to be a good candidate. Table 1

Table 1. Parameters of an example of proton driver based on scaling FFAGs with serpentine acceleration

Item	Value
Average radius(m)	15
Field index	3
Injection energy	300 MeV
Extraction energy	2.2 GeV
RF voltage per turn ($h = 1$)	38 MV

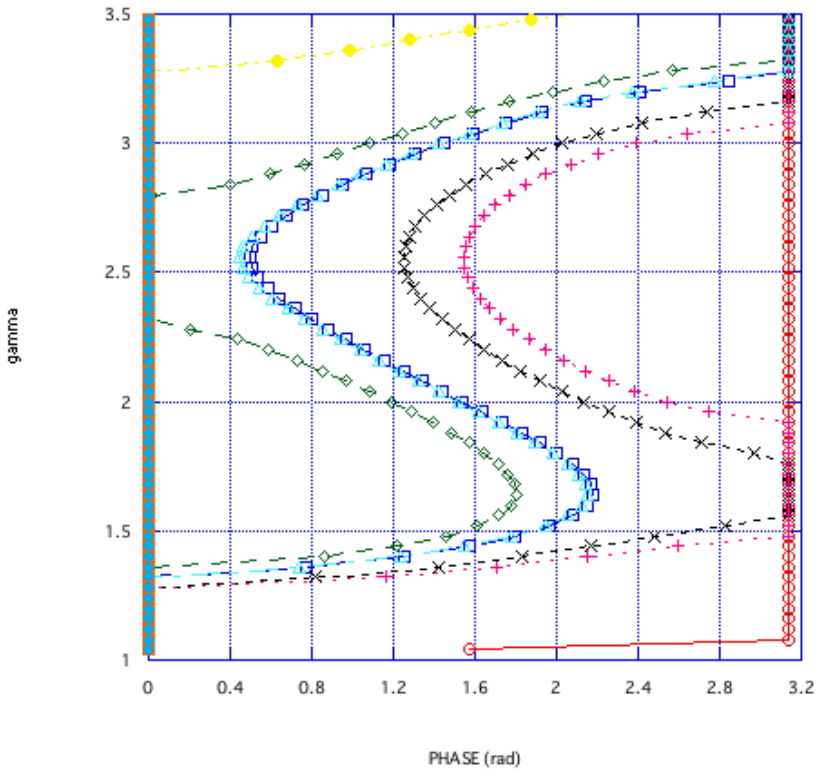

Fig. 4. Serpentine acceleration for HIPA(0.3–2.2 GeV) with scaling FFAG accelerator.

presents an example of the parameters of a proton driver based on a scaling FFAG accelerator using serpentine beam acceleration shown in Fig. 4.

In KURRI, the present 150 MeV proton FFAG accelerator is used for a basic experimental study of ADSR with Kyoto University Critical Assembly(KUCA). The machine will be upgraded soon to a the beam intensity of up to 5–10 μA with a repetition rate of 30 Hz using a H^- proton linac which exists already. The beam energy energy upgrade could be realized with an additional spiral FFAG having a diameter of about 16 m. For the high power ADSR experiment, the beam repetition

is to be increased to more than 300 Hz with additional RF acceleration systems for both 150 MeV and 700 MeV rings, and the thermal output power of the ADSR could become more than 5 MW.

4. Summary

Beam focusing and acceleration in the Fixed Field Alternating Gradient Accelerator (FFAG) have been briefly described and a possible concept of FFAG accelerator for next generation High Intensity Proton Accelerator for ADSR and pulsed SNS discussed. The future upgrade scenario and design of the FFAG upgrade at KURRI for ADSR and pulsed SNS, where the beam energy will be more than 700 MeV and the beam power will be 5 kW with 30 Hz repetition rate for pulsed SNS and 50 kW with 300 Hz rate for high power ADSR, have also been described.

References

1. T. Ohkawa, *Proc. annual meeting of JPS* (1953).
2. K. R. Symon et al., *Phys. Rev.* **103**, 1837 (1956).
3. Y. Mori, *Proc. EPAC'98*, 289 (2000).
4. A. A. Kolomenski, *"Theory of Circular Accelerators"*, 340 (1966).
5. D. Trbojevic, *Proc. of the International Workshop on FFAG Accelerators (FFAG'05)*, KURRI, Osaka, Japan(2005).
6. G. Rees, *Proc. of the International Workshop on FFAG Accelerators (FFAG'04)*, KEK, Tsukuba, Japan, 77 (2004).
7. A. G. Ruggeiero, *Proc. of the International Workshop on FFAG Accelerators (FFAG'05)*, KURRI, Osaka, Japan, 47(2005).
8. JB. Lagrange, T. Planche and Y. Mori, *Proc. of FFAG'09*, FNAL, Chicago, USA (2009).
9. Y. Mori, *International Workshop on FFAG Accelerators (FFAG'09)*, FNAL, Chicago, USA (2009).
10. T. Planche and Y. Mori, *Proc. of PAC09*, Vancouver, FR5PFP003 (2009).
11. Y. Mori, *International Workshop on FFAG Accelerators (FFAG'06)*, FNAL, Chicago, USA (2006).
12. S. Machida, *Proc. of the International Workshop on FFAG Accelerators (FFAG'05)*, KURRI, Osaka, Japan, 68 (2005).
13. E. Yamakawa, T. Uesugi and Y. Mori, *International Workshop on FFAG Accelerators (FFAG'09)*, FNAL, Chicago, USA (2009).
14. S. Berg, *International Workshop on FFAG Accelerators (FFAG'05)*, KURRI, Osaka, Japan, 93 (2005).

International Journal of Modern Physics A
Vol. 26, Nos. 10 & 11 (2011) 1753–1760

DOI: 10.1142/S0217751X11053158

World Scientific
www.worldscientific.com

STUDIES OF BREAKDOWN IN A PRESSURIZED RF CAVITY

M. BASTANINEJAD and A. A. ELMUSTAFA
ODU, Norfolk, VA

C. M. ANKENBRANDT, A. MORETTI, M. POPOVIC and K. YONEHARA
Fermilab, Batavia, IL

D. M. KAPLAN
IIT, Chicago, IL

M. ALSHARO'A, P. M. HANLET, R. P. JOHNSON, M. KUCHNIR and D. NEWSHAM
Muons Inc, Batavia, IL

D. V. ROSE, C. THOMA and D. R. WELCH
Voss Scientific, LLC, Albuquerque, NM

Microscopic images of the surfaces of metallic electrodes used in high-pressure gas-filled 805 MHz RF cavity experiments[1] have been used to investigate the mechanism of RF breakdown.[2] The images show evidence for melting and boiling in small regions of ∼10 micron diameter on tungsten, molybdenum, and beryllium electrode surfaces. In these experiments, the dense hydrogen gas in the cavity prevents electrons or ions from being accelerated to high enough energy to participate in the breakdown process so that the only important variables are the fields and the metallic surfaces. The distributions of breakdown remnants on the electrode surfaces are compared to the maximum surface gradient E predicted by an ANSYS model of the cavity. The local surface density of spark remnants, proportional to the probability of breakdown, shows a strong exponential dependence on the maximum gradient, which is reminiscent of Fowler-Nordheim behavior of electron emission from a cold cathode. New simulation results have shown good agreement with the breakdown behavior of the hydrogen gas in the Paschen region and have suggested improved behavior with the addition of trace dopants such as SF_6.[3] Present efforts are to extend the computer model to include electrode breakdown phenomena and to use scanning tunneling microscopy to search for work function differences between the conditioned and unconditioned parts of the electrodes.

1. Introduction

RF cavities pressurized with hydrogen gas are being developed to produce low emittance, high intensity muon beams for muon colliders, neutrino factories, and other applications. The high-pressure gas suppresses dark currents, multipacting, and other effects that are complicating factors in the study of breakdown in the usual RF cavities that operate in vacuum.

In the studies reported here, various metals were tested in a pressurized cavity where RF breakdown is expected to be due only to the interaction of the metallic surfaces with the electromagnetic fields. After exposure to the RF fields, metallic Be, Mo, Cu, and W samples were examined using a Hirox microscope and a scanning electron microscope (SEM) to measure the distribution of breakdown events on the electrode surfaces.

1.1. *Apparatus*

A schematic of the 805 MHz Test Cell (TC) geometry is shown in Figure 1. The TC is a cylindrical stainless steel pressure vessel. RF power is fed into the chamber via a coaxial line. A solenoid magnet (not shown in the figure) provides an axial magnetic field of up to 3 T, which is used in some of the data sets. Replaceable hemispherical electrodes of various materials (Cu, Mo, Be, W) are separated by a 2 cm gap.

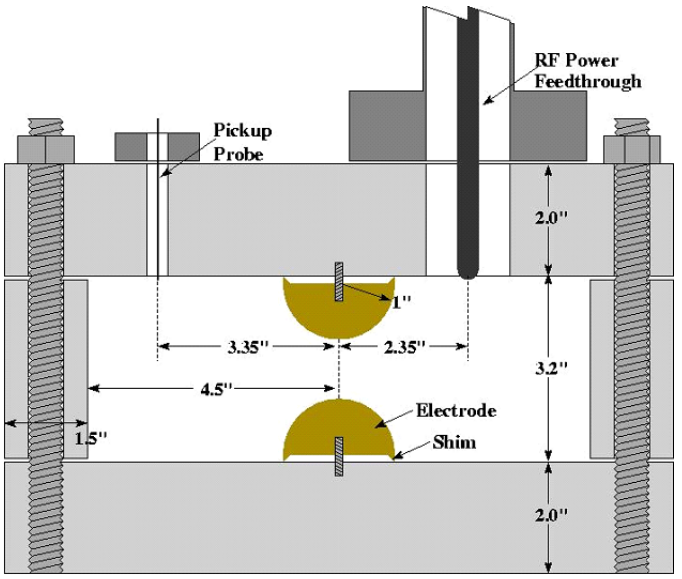

Fig. 1. Cross section of the test cell showing the replaceable one inch radius Cu, Mo, W, or Be hemispherical electrodes. The top and bottom plates and the cylinder are copper-plated stainless steel (the gas input/exhaust port is not shown in the figure).

2. Experimental Results

2.1. *RF breakdown*

Increasing gas density reduces the mean free collision path for ions giving them less chance to accelerate to energies sufficient to initiate showers and avalanches.

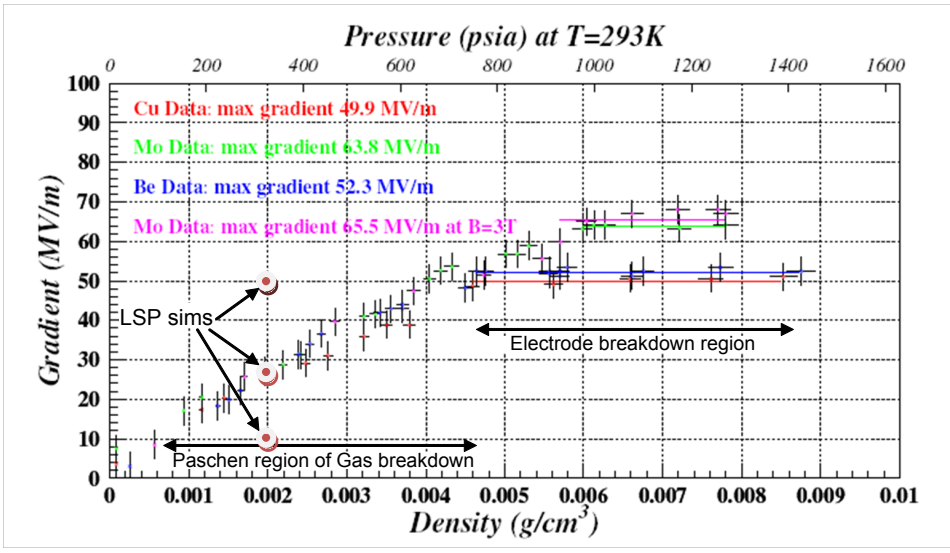

Fig. 2. Maximum stable TC gradient as a function of hydrogen gas density or pressure for Cu, Be, and Mo with no external magnetic field and Mo with 3 T. The three points labeled "Lsp sims" correspond to simulation results discussed below.

As shown in Figure 2, it is found that Cu and Be electrodes operated stably with surface gradients near 50 MV/m, Mo near 65 MV/m, while W achieved values near 75 MV/m.

2.2. *Electrode Analysis*

After the exposure of the electrodes to acquire the data shown in Figure 2, each electrode was examined using secondary and Hirox microscopes. The local surface density of breakdown remnants was recorded as a function of the zenith angle (zero angle corresponds to the axis of the TC). On Be, the breakdown remnants mostly look like boiled melted areas in a tadpole shape with head and tail (Figure 3).

For Mo the breakdown remnants look like overlapped circular melted regions and some splashed areas. Small holes in the melted region may be vents of metallic vapor due to boiling (Figure 4).

Tungsten breakdown remnants are furrow-shaped melted areas extended on the surface ending in a series of overlapped circles (Figure 5). Cracks that are seen on the breakdown areas are assumed to have occurred subsequent to breakdowns because they are seen on the last ending circle of the set of repeated circles.

3. Experimental Data Analysis

To investigate the correlation of breakdown and the electric field, the local surface density of breakdown remnants was compared with the maximum expected electric

Fig. 3. Beryllium breakdown remnants.

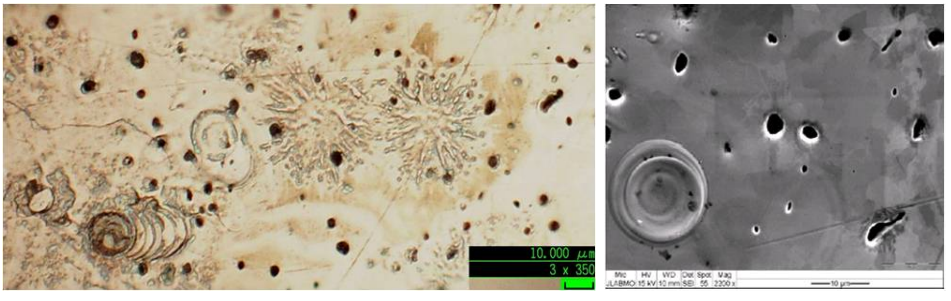

Fig. 4. Molybdenum remnants.

field using an ANSYS model. Least squares fits of the data to a power of the predicted maximum electric gradient at the surfaces of the electrodes show good agreement for high values of the exponent. Figure 6 shows the predicted maximum surface gradient (dashed), the data (black with error bars) as described above, and the best least squares fit (red) to the data $y=0.34E^7$ versus zenith angle for Be. Figures 7 and 8 show the experimental data, the ANSYS model data, and best fits for Mo and W respectively.

The plots also show that the breakdown data correlates with a high power of electric field: 7 for Be, 11.5 for Mo and 10 for W. This suggests that the breakdown is a quantum mechanical effect described by the Fowler-Nordheim theory of

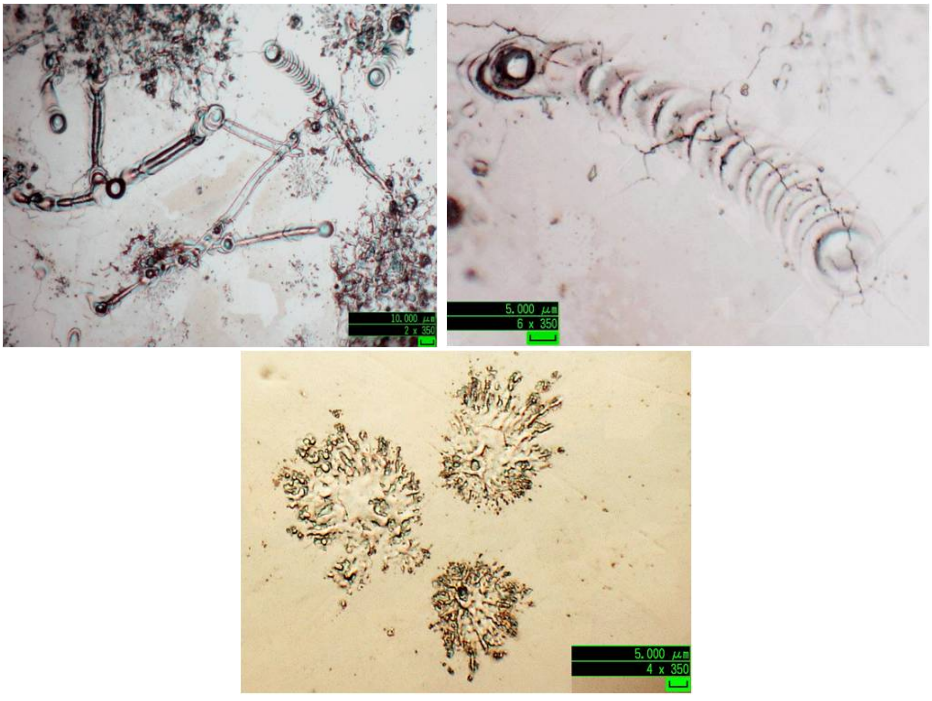

Fig. 5. Tungsten Breakdown.

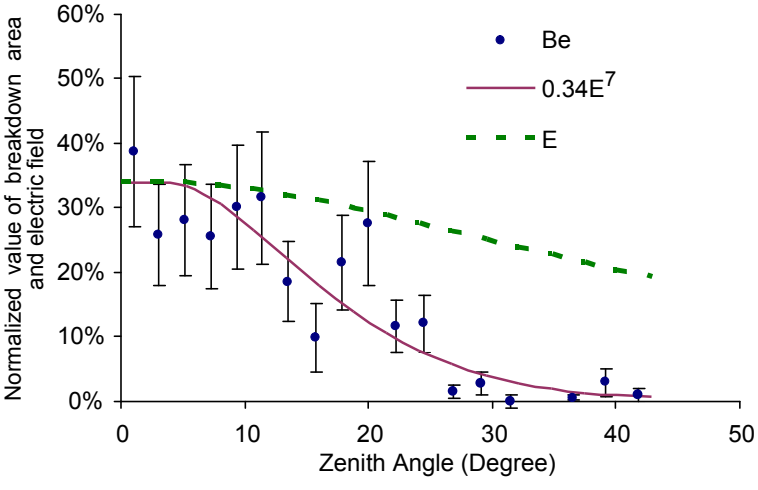

Fig. 6. Be breakdown area fraction vs. zenith angle.

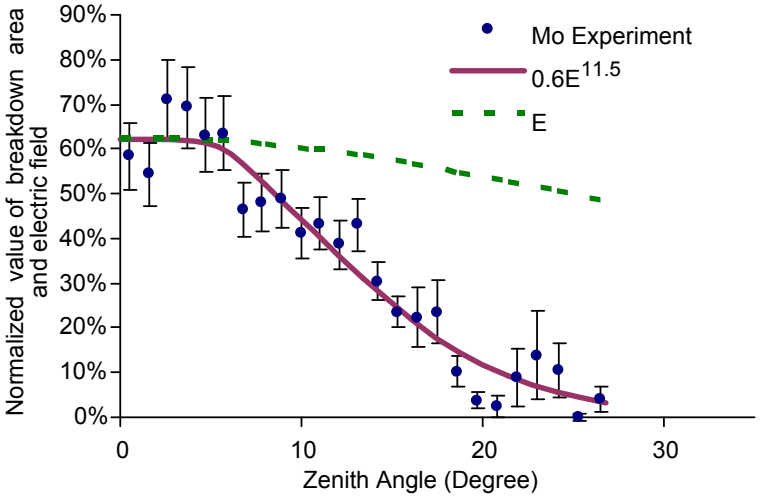

Fig. 7. Mo breakdown area fraction vs. zenith angle.

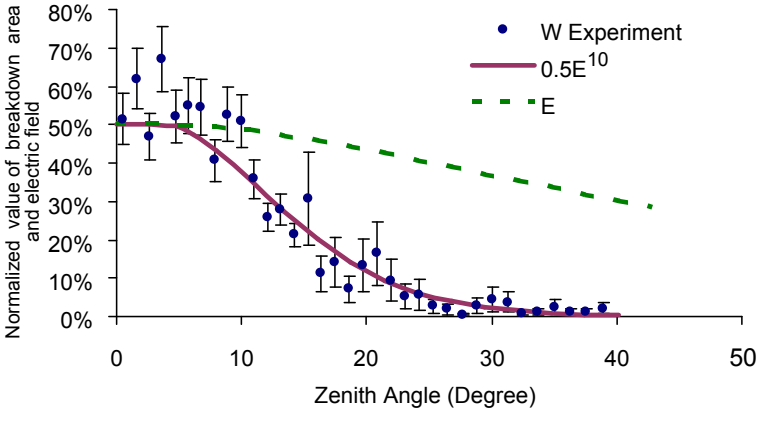

Fig. 8. W breakdown area fraction vs. zenith angle.

field emission by tunneling of electrons through a barrier in the presence of a high electric field.

4. First Computer Simulations

Computer calculations to simulate the behavior of breakdown in helium-filled spark-gap switches[4] have been extended to use hydrogen in the Muons, Inc. Test Cell.[5] Three values of electric field were used for the calculations in the conditions of Figure 2 at a density of 0.002 g/cm^3 as indicated by the three red and blue dots.

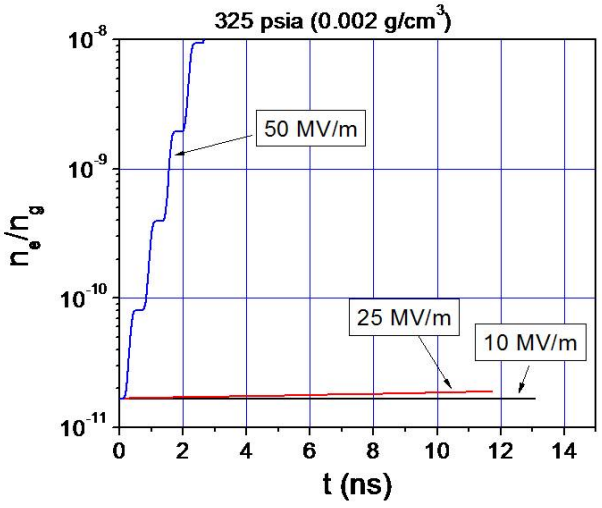

Fig. 9. Electron density as a function of time at 805 MHz and gas density 0.002 g·cm^{-3}.

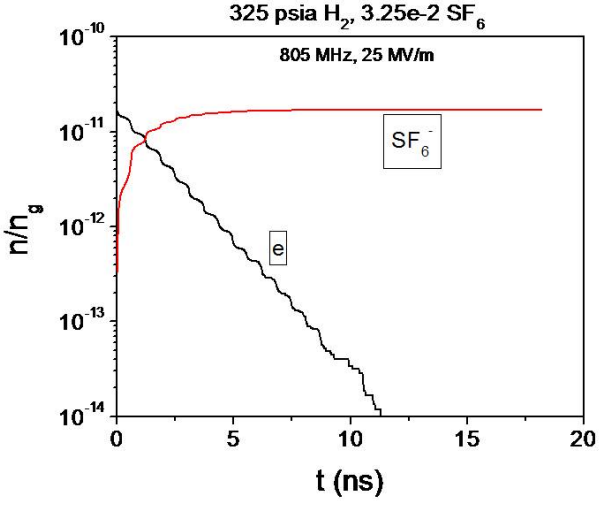

Fig. 10. Electron density depletion and SF_6 ion density growth as a function of time at H_2 density $6 \cdot 10^{20}$ cm^{-3} and SF_6 density $6 \cdot 10^{16}$ cm^{-3}.

Figure 9 shows the simulation results for the three electric filed strengths, where the electron density is stable below the Paschen curve (10 MV/m), slightly unstable at the curve (25 MV/m), and very unstable for values above the curve (50 MV/m).

The temporal evolution of these curves is consistent with the results of the experiment; for $E_0 = 10$ MV/m, the electron population does not grow because the field is too low to induce ionization of the neutral H_2. At 25 MV/m, the electron

density is slowly growing, consistent with this value of E_0 being at the edge of the Paschen law breakdown limit in Figure 2. At 50 MV/m, the electric field drives electrons in the tail of the distribution to high enough energies to efficiently ionize the gas. It is interesting that the 805 MHz period is seen in the growth of the electron density.

One proposed method to increase the effective breakdown threshold for the gas at a given pressure is to introduce a low concentration of electro-negative gas to the H_2. A very low ratio mixture of SF_6 is used to examine this effect. Three additional particle species of neutral SF_6, SF_6^+, and SF_6^- are added to the calculation. The results of a calculation at $E_0 = 25$ MV/m are shown in Figure 10, which plots the electron and negative ion density as a function of time. The initial electron population rapidly decreases, as the negative ion density increases. This demonstrates the desired effect of increasing the Paschen limit for breakdown in pure H_2.

5. Conclusions

The breakdown data shown in Figures 6, 7 and 8 show good agreement with high powers of electric field. This strong electric field dependence of the breakdown in pressurized gas is so similar to the dark current dependence predicted by Fowler and Nordheim that breakdown of a metal in a strong electromagnetic field is very likely also a quantum mechanical effect. The fact that the conditioned surfaces of the electrodes are rougher than the unconditioned areas implies the surface enhancement factor in the Fowler-Nordheim expression is not the dominant effect. Thus the work function is a likely factor in the ultimate breakdown limit of metallic structures. This has inspired the study of the distributions of work functions in the electrodes using scanning tunneling microscopy. On another front, computer simulations of the Paschen region of the breakdown data of the Test Cell show good agreement. The next steps to extend the model to include the metallic electrodes may give more insight to the mechanism of RF breakdown.

References

1. P. Hanlet, M. Alsharo'a, R. E. Hartle, R. P. Johnson, M. Kuchnir, K. Paul, C. M. Ankenbrandt, A. Moretti, M. Popovic, D. M. Kaplan, et al., in Proceedings of EPAC06, Edinburgh, Scotland (2006), p. 1364.
2. M. BastaniNejad et al., in Proceedings of PAC07, Albuquerque, New Mexico (2007), p. 2499.
3. Lsp is a software product developed by ATK Mission Research, Albuquerque, NM 87110.
4. C. Thoma, et al. IEEE Trans. Plasma Sci. 34, 910 (2006)].
5. D. V. Rose, C. Thoma, D. R. Welch, and R. E. Clark, Low Emittance Muon Collider Workshop, Fermilab, 2008.

International Journal of Modern Physics A
Vol. 26, Nos. 10 & 11 (2011) 1761–1774

DOI: 10.1142/S0217751X1105316X

World Scientific
www.worldscientific.com

ON SOME ERRORS AND BIAS IN PROTON COMPUTED TOMOGRAPHY

BELA ERDELYI

Department of Physics, Northern Illinois University, DeKalb, IL 60115
and
Physics Division, Argonne National Laboratory, Argonne, IL 60439
berdelyi@niu.edu

Novel accelerator technology, including Fixed Field Alternating Gradient Accelerators (FFAG) coupled with medical imaging devices, hold significant promise for enhanced proton therapy. The accuracy and efficiency of proton therapy treatments will see improvements with the implementation of proton computed tomography (pCT), currently under development. Here, we analyze the robustness of the image reconstruction method in pCT with respect to three different error sources and conclude that pCT is inherently resilient with respect to errors in mean ionization potential, discrete sampling of proton trajectories and bias in the limit of large radiation doses.

Keywords: Proton computed tomography; electron density resolution; most likely path.

PACS number: 87.57.Q-

1. Introduction

Imaging in general and medical imaging in particular are very important scientific endeavors. Their importance has been recognized by several Nobel prizes. Proton Computed Tomography (pCT) is such an example, having its roots in the works of a Nobel prize laureate (Allan Cormack, 1979). After a period of stagnation, the revival of the pCT idea is mainly due to the proliferation of proton therapy centers. The drivers of these proton therapy centers today are cyclotrons and synchrotrons. Future proton treatment centers entertain the possibility of using fixed-field alternating gradient (FFAG) accelerators for providing the proton beam necessary for treatment and potentially for imaging. For proton treatments, pCT promises better dose accuracy and more effective outcomes. To this end, a collaboration between Northern Illinois University, Loma Linda University Medical Center and the Santa Cruz Institute for Particle Physics embarked in a modeling, designing, building and testing program that will result in the world's first pCT prototype capable of imaging head-sized objects. Using the resulting system in conjunction with FFAG accelerators is a distinct possibility.

After a long history,[1–5] the revival of the pCT idea,[6] due to the proliferation of proton therapy centers,[7] allowed researchers to study by modeling and simulations a variety of effects necessary to gain a firm footing on the peculiarities of the method. Milestones in this endeavour are the development of the most likely path formalism,[8–10] several algebraic image reconstruction methods,[11,12] and estimating the achievable electron density resolution by filtered back-projection[13] and algebraic reconstruction methods.[14]

In this paper, we explore and analyze three different sources of errors and uncertainties in pCT and evaluate their impact on the expected performance of the system. These error sources are the uncertainties in the mean ionization potential of the medium, the discrete sampling of the proton paths in the image reconstruction process, and the possibility of bias of the algebraic reconstruction methods utilized to reconstruct the electron density maps from experimentally available data.

As detailed in Ref. 14, starting form the Bethe-Bloch equation, we can set up a system of linear equations

$$A\vec{\eta} = \vec{b} \tag{1}$$

that determines the pCT image reconstruction problem. The vector $\vec{\eta}$ represents the electron densities in each voxel rendered into a 1D array. The constant matrix $A \in \mathbb{R}^m \times \mathbb{R}^n$, $m \gg n$, is determined by the proton paths used for the image reconstruction and it is assumed to be known exactly; m denotes the number of protons used to reconstruct the image and n is the total number of voxels after image space digitization. Its "inverse" is denoted by A^+. It is given by the chosen solution method, which are typically iterative projection-based linear solvers.[12] The random vector $\vec{b} \in \mathbb{R}^m$ is the result of a numerical integration and represents the integrated electron densities along the proton paths. Explicitly, its components are given by

$$b_j = -\int_{E_0}^{E_j} \frac{\mathrm{d}E}{F(E)}, \tag{2}$$

where E_0 is a constant denoting the fixed initial energy of all protons and E_j is the actual exit energy of proton j that includes the energy loss straggling, and $F(E)$ is the medium's stopping power. Hence, the randomness of b_j comes from the upper limit of the integral (2).

We form the "solution" $\vec{\eta} \in \mathbb{R}^n$ to (1) by assuming $\operatorname{rank}(A) = n$. Then,

$$\eta_i = \sum_{j=1}^{m} A_{ij}^{+} b_j \tag{3}$$

for all $i = 1, 2, 3, \ldots, n$, where n represents the number of image voxels and m the total number of protons used for image reconstruction. The statistical properties of $\vec{b}$ transfer to statistical properties of $\vec{\eta}$, and we use this to define the electron density resolution of pCT.[14] It can be shown that the final result of these computations is

the following expression for the electron density resolution:[14]

$$\sigma_{\vec{\eta}} = \frac{g}{\sqrt{\sqrt{2}\text{arccoth}\left(\sqrt{2}\right)}} \frac{\sigma_{E_a}}{|F\left(E_a\right)|} \frac{\kappa\left(A\right)}{\sqrt{Ra}} \sqrt{\frac{n}{m}}. \tag{4}$$

The following notations have been used: g is a geometric form factor determined by the system geometry and object composition, σ_{E_a} is the energy loss straggling standard deviation of the average proton beam exit energy E_a, R is the radius of the smallest cylindrical object that encloses the object to be imaged, a is the voxel size assumed to have the same dimensions in all directions, and $\kappa\left(A\right)$ is an effective generalized matrix condition number defined by

$$\kappa\left(A\right) = \frac{\|A\|_F \|A^+\|_F}{n} \geq 1, \tag{5}$$

where $\|\cdot\|_F$ denotes the Frobenius matrix norm. This form of the result is valid in both two and three dimensions. Notice that the number of protons per pixel/voxel is constant for a given setup and fixed resolution.

2. Convergence of the image reconstruction in the limit of very large doses

Equation (4) gives a very useful estimate for the noise level that is present in pCT reconstructed images based on system parameters. Hence, the parameter dependencies and scaling laws are readily available. For example, it can be used to obtain estimates for the necessary dose to achieve a certain resolution for a fixed system and solution method. However, the question arises whether the solution converges in some sense to the actual, real solution in the limit of large doses.

Assume that a given setup is fixed: the incoming proton beam energy and geometry, the object to be imaged, the level of imaging space discretization; and a solution method is successfully used to reconstruct the image. The question posed can be answered mathematically in the sense of taking the limit of the number of protons going to infinity, $m \to \infty$. Therefore, if we make the reasonable assumption that the condition number is independent of the number of protons (or at least growing slower than $\sqrt{m}$ with m), we obtain from (4) that

$$\lim_{m\to\infty} \sigma_{\vec{\eta}} = 0. \tag{6}$$

In other words, in the limit of very large doses the noise should be removed from the images. According to a well-known theorem from statistics, if the variance of a random variable tends to zero, then its value tends to a constant, i.e. its expectation value. Under these conditions, the value of the random vector $\vec{\eta}$ will tend to its average value. This is given by averaging (3)

$$\eta_{i,\infty} = \lim_{m\to\infty} \langle \eta_i \rangle = \lim_{m\to\infty} \sum_{j=1}^{m} A_{ij}^{+} \langle b_j \rangle . \tag{7}$$

From (2) we can calculate $\langle b_j \rangle$. Since the random variable is E_j, we use the Taylor expansion for the moments of operatornametions of random variables to obtain the average of b_j. According to this propagation of uncertainty, if E_j is a random variable and $b_j\left(E_j\right)$ is a twice differentiable operatornametion of E_j, then

$$\langle b_j\left(E_j\right)\rangle \approx b_j\left(\langle E_j\rangle\right) + \frac{b_j^{''}\left(\langle E_j\rangle\right)}{2}\sigma_{E_j}^2. \tag{8}$$

Since

$$b_j^{''}\left(\langle E_j\rangle\right) = \frac{F'\left(\langle E_j\rangle\right)}{F^2\left(\langle E_j\rangle\right)}, \tag{9}$$

we obtain

$$\eta_{i,\infty} = \lim_{m\to\infty}\sum_{j=1}^{m} A_{ij}^{+}\left[b_j\left(\langle E_j\rangle\right) + \frac{F'\left(\langle E_j\rangle\right)}{2F^2\left(\langle E_j\rangle\right)}\sigma_{E_j}^2\right]. \tag{10}$$

The exact result is

$$\eta_{i,e} = \lim_{m\to\infty}\sum_{j=1}^{m} A_{ij}^{+} b_j\left(\langle E_j\rangle\right), \tag{11}$$

which entails the difference between the asymptotic and exact solutions to be

$$\Delta\eta_i = \eta_{i,\infty} - \eta_{i,e} = \lim_{m\to\infty}\sum_{j=1}^{m} A_{ij}^{+}\frac{F'\left(\langle E_j\rangle\right)}{2F^2\left(\langle E_j\rangle\right)}\sigma_{E_j}^2 = \text{const}. \tag{12}$$

From (11) we can conclude that since $\eta_{i,e}$ and $b_j\left(\langle E_j\rangle\right)$ are all positive quantities and A^{+} is independent of $\vec{b}$ (in principle the protons could see arbitrary electron densities along their path) the sum (12) has a chance of converging to zero only if $F'\left(E\right)$ is not sign definite. Indeed, if we define a vector $\vec{f} = (f_1, f_2, \ldots, f_m)$ with

$$f_j = \frac{F'\left(\langle E_j\rangle\right)}{2F^2\left(\langle E_j\rangle\right)}\sigma_{E_j}^2, \tag{13}$$

(12) can be written as

$$\Delta\vec{\eta} = A^{+}\vec{f}. \tag{14}$$

It follows by comparison with (11) that if $\vec{f} \lesseqgtr 0$ then $\Delta\vec{\eta} \lesseqgtr 0$. Unfortunately, $F'\left(E\right) < 0$ for any E, as shown in Figure 1. This entails that

$$\Delta\vec{\eta} < 0 \tag{15}$$

and const $\neq 0$, i.e. the estimator is biased. For practice it means that in the limit of very large dose the images become less and less noisy, but the tendency is to underestimate the real electron densities.

To estimate the magnitude of this effect the following relative error is defined:

$$\varepsilon_{\Delta\vec{\eta}} = \left\langle \frac{\lim_{m\to\infty}\sum_{j=1}^{m} A_{ij}^{+}\frac{F'\left(\langle E_j\rangle\right)}{2F^2\left(\langle E_j\rangle\right)}\sigma_{E_j}^2}{\lim_{m\to\infty}\sum_{j=1}^{m} A_{ij}^{+} b_j\left(\langle E_j\rangle\right)} \right\rangle, \tag{16}$$

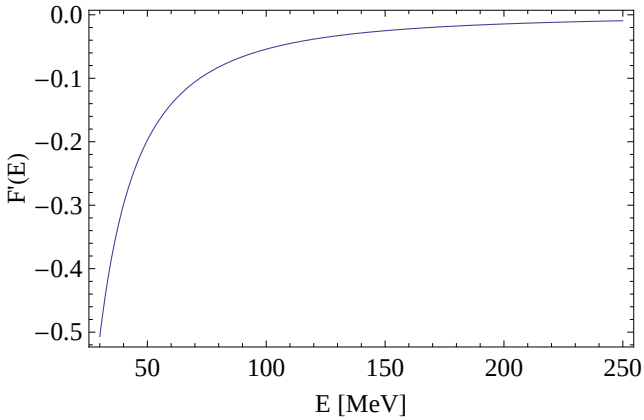

Fig. 1. The derivative of the stopping power with respect to energy as a operatornametion of energy, $F'(E)$. Note the negative definiteness.

where the average is taken over i. A good approximation of this is

$$\varepsilon_{\Delta\vec{\eta}} \lesssim \frac{\frac{F'(E_a)}{2F^2(E_a)}\sigma^2_{E_a}}{b\,(E_a)}. \tag{17}$$

Figure 2 illustrates the magnitude of $\varepsilon_{\Delta\vec{\eta}}$ for different energy ranges. For all energies of interest in pCT the errors are negligible, as they barely reach 10^{-4}. In conclusion, the pCT image reconstruction procedure is biased in theory, but for all practical purposes it is unbiased.

3. The effect of the uncertainties in the mean ionization potential

In the derivation of (1) it is typically assumed that the mean ionization of the potential of the medium is equal to the mean ionization potential of the water, $I_w = 75\,\text{eV}$. Qualitatively, this is a good approximation because the range of ionization potentials in typical tissues is limited and the potential appears as the argument of a logarithmic operatornametion, which is well-known to have a slow variation in this limited range. The purpose of this section is to evaluate the corresponding errors quantitatively.

Let us assume that the range of possible values is $I\,(\vec{r}) \in [50, 100]\,\text{eV}$. This includes adipose tissues ($I = 63\,\text{eV}$), muscle ($I = 75\,\text{eV}$) and compact bone ($I = 92\,\text{eV}$).[15] We can calculate errors in electron density due to errors in I values by first examining how these I value errors contribute to relative errors in the integrated electron densities (IED) (2). From there, the effect of this IED error on the error of the electron density resolution $\sigma_{\vec{\eta}}$ (4), can be calculated. The latter depends on the ratio of the standard deviation of the energy loss straggling and stopping power as shown in (4). The results depend on the initial proton energy and the length of the proton trajectory.

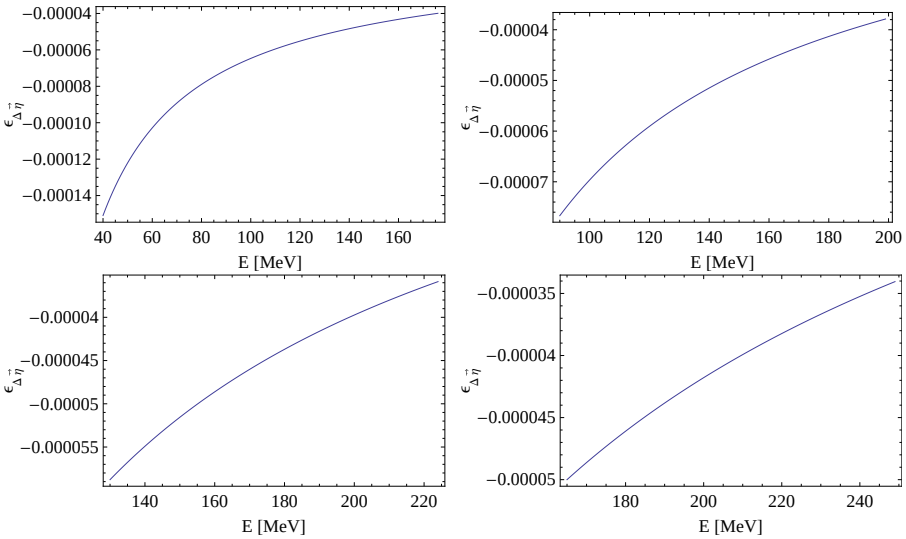

Fig. 2. The expected relative errors of the reconstructed electron density values in the limit of large doses with respect to the actual values. From upper left to bottom right, the initial proton energies are 177, 200, 225, and 250 MeV, respectively, and the object size is assumed to be up to 20 cm.

The results are summarized in Figures 3 and 4. For the boundaries of the interval containing all possible values of the mean ionization potential we plotted the relative error in IED (Figure 3) and electron density resolution (Figure 4) for various initial proton energies in the range $[177, 250]$ MeV and length of trajectories between $s \in [0, 20]$ cm, relevant for typical proton treatment centers and head-sized objects.

As shown in Figure 3, the error in IED is insensitive to the initial proton energy and total track length. The quantity that determines almost completely the error is the mean ionization potential. At the extremes of the interval $[50, 100]$ the relative error in the potential is 33%. However, this error is damped by at least a factor of 7 in the associated IED error; it never exceeds 5%. It is equally important to note that according to Figure 4 the relative electron density resolution error never exceeds 10%, even in extreme cases. However, in this case it is noticeable that higher initial proton energies result in smaller errors and the smaller the object is the smaller the errors are. Moreover, all error curves, independent of energy, tend to a common non-vanishing point in the limit $s \to 0$; the different energies determine different slopes at the origin. Finally, the errors are not symmetric with respect to the error in the ionization potential; for example an error of $\delta_I = -33\%$ results in larger IED and resolution errors than a corresponding $\delta_I = +33\%$.

4. Effective average chord length

It was shown in Ref. 14 that in a pCT geometry where the imaging space is digitized into pixels or voxels, and which is fixed with respect to a rotating parallel proton

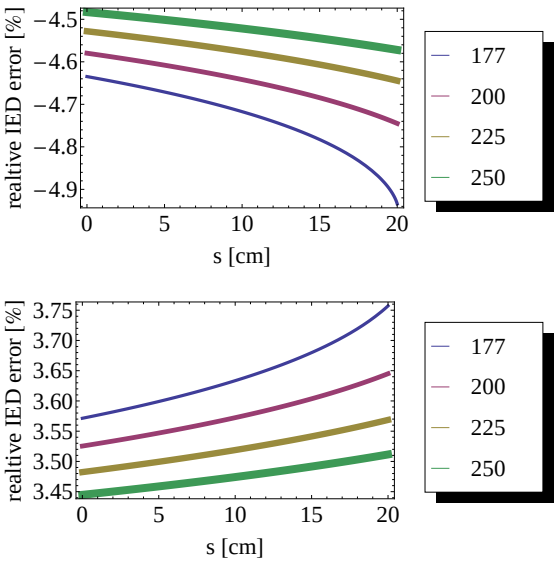

Fig. 3. The relative error with respect to water in the integrated electron density for protons of different initial energies and track length for a) $I = 50$eV and b) $I = 100$eV. Thicker lines correspond to larger initial energy.

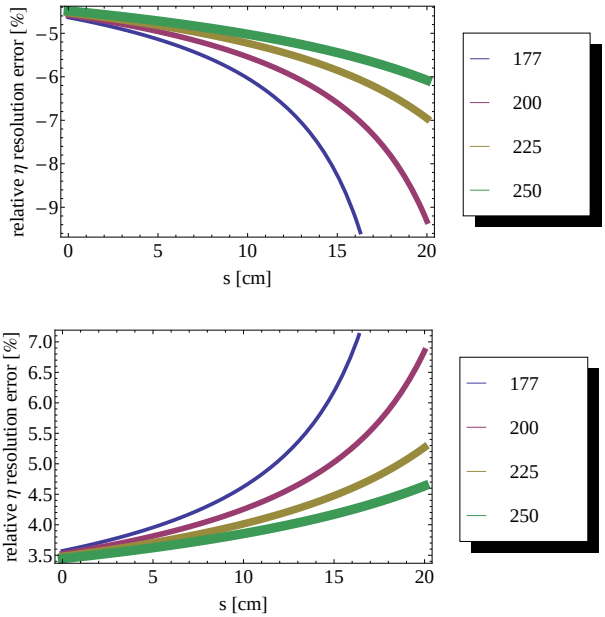

Fig. 4. The relative error with respect to water in the electron density resolution for protons of different initial energies and track length for a) $I = 50$eV and b) $I = 100$eV. Thicker lines correspond to larger initial energy.

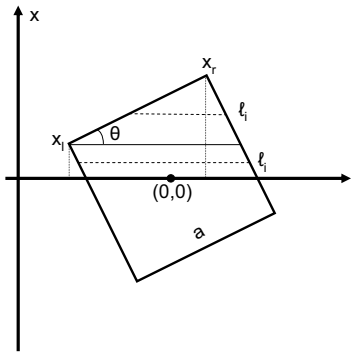

Fig. 5. The figure shows the quantities in the expression of the effective average chord length (20).

beam, one can attach an average chord length to each projection by calculating the average length of the trajectory per pixel of a proton, in the approximation of large number of pixels crossed. We also showed that for practically relevant setups, these asymptotic values are reached quite fast, inducing only a very small relative error. However, there is a larger effect that we did not consider yet. When setting up the system matrix in pCT, the most likely paths are sampled at regularly spaced intervals along the beam axis. The net effect of the discrete sampling is that some pixels are missed by the sampling. In order to recover the total length of the trajectory, essential for a quantitatively accurate reconstruction of electron density values, an effective average chord length $\langle L_{eff} \rangle$ can be defined according to

$$L_{tot} = N \langle L_{true} \rangle = N_d \langle L_{eff} \rangle , \tag{18}$$

where L_{tot} is the actual proton track length across the entire target volume, N is the total number of pixels crossed (or the number of protons crossing a pixel), $\langle L_{true} \rangle$ is the average chord length per pixel averaged over all paths traversing the pixel, and N_d is the number of pixels detected by the sampling. Therefore, we can compute an effective average chord length from

$$\langle L_{eff} \rangle = \frac{N}{N_d} \langle L_{true} \rangle . \tag{19}$$

It is known that[14]

$$\langle L_{true} \rangle = \frac{a}{|\cos\theta| + |\sin\theta|}, \tag{20}$$

where a is the pixel size and θ is the projection angle. See Figure 5 for an illustration of the quantities appearing in (20).

If we denote the fraction of the pixels detected by $p_d = N_d/N$, we have

$$\langle L_{eff} \rangle = \frac{\langle L_{true} \rangle}{p_d}. \tag{21}$$

Equivalently, we could have introduced the fraction of pixels undetected $p_u = 1 - p_d$ to obtain

$$\langle L_{eff} \rangle = \frac{\langle L_{true} \rangle}{1 - p_u}. \tag{22}$$

Assume that the most likely paths are sampled in equidistant steps $s \in (0, a)$. If the proton i has track length $l_i \in \left[0, \sqrt{2}a\right]$ in the pixel, the probability to detect the corresponding pixel is

$$p_i = \begin{cases} 1, & \text{if } l_i \geq s; \\ \frac{l_i}{s}, & \text{if } l_i < s. \end{cases} \tag{23}$$

If we sum up the detection probabilities for all the N protons and divide by the total number of protons we obtain

$$p_d = \frac{1}{N} \sum_{i=1}^{N} p_i. \tag{24}$$

From Ref. 14 we know that the track length of each proton i is

$$l_i = \begin{cases} \frac{a}{\cos\theta}, & \text{if } 0 \leq i \leq Nk(\theta); \\ \frac{a}{2} \frac{1+\cot\theta}{\cos\theta} \left(1 - \frac{i}{N}\right), & \text{if } Nk(\theta) < i \leq N; \end{cases} \tag{25}$$

where

$$k(\theta) = \frac{1 - \tan\theta}{1 + \tan\theta} \tag{26}$$

and $\theta \in [0, \pi/4]$. Therefore, the probability is less then 1, $p_i < 1$, for

$$i_l > \left[N \left(1 - \frac{2s}{a} \frac{\cos\theta}{1 + \cot\theta} \right) \right]. \tag{27}$$

It follows that

$$p_d = \frac{1}{N} \left(\sum_{i=0}^{i_l} 1 + \sum_{i=i_l+1}^{N} \frac{a}{2s} \frac{1 + \cot\theta}{\cos\theta} \left(1 - \frac{i}{N}\right) \right) \tag{28}$$

$$= \frac{1}{2N} + 1 - \frac{s \sin 2\theta}{2a(\cos\theta + \sin\theta)}. \tag{29}$$

Taking the limit $N \to \infty$, extending the angular range to $\theta \in [0, 2\pi]$ by symmetry and dividing by (20) gives

$$\langle L_{eff} \rangle = \frac{a}{|\cos\theta| + |\sin\theta| - \frac{s}{2a} |\sin 2\theta|}. \tag{30}$$

Notice that the convergence speed scales as $1/(2N)$ as expected. Hence, the average effective chord length approximation is also well justified. Figure 6 shows the result for $a = 1$ and $s = 1/2$ over the full angular range (in radians).

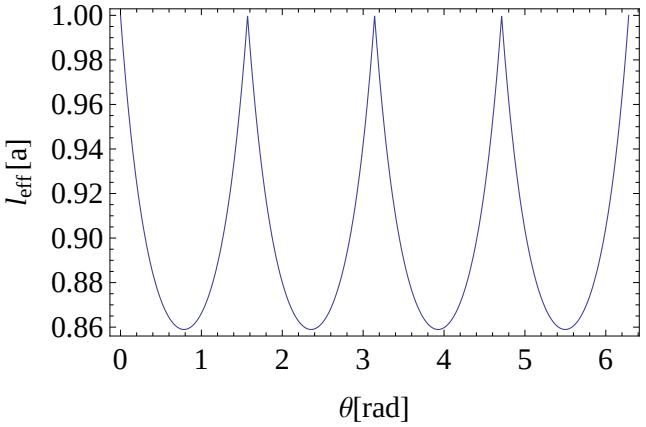

Fig. 6. The effective average chord length as a operatornametion of projection angle, evaluated for a step size equal to half the pixel side length.

4.1. *Comparison with previous results*

Another effective average chord length has already been derived for the purpose of more accurate pCT reconstructions. See Ref. 16. Here, we compare our result with that of Ref. 16. Augmenting the definitions above, we can also define an average detected and undetected chord length by

$$\langle L_d \rangle = \frac{1}{N_d} \sum_{i=1}^{N_d} L_d(i), \tag{31}$$

$$\langle L_u \rangle = \frac{1}{N_u} \sum_{i=1}^{N_u} L_u(i). \tag{32}$$

Together with

$$L_{tot} = \sum_{i=1}^{N_d} L_d(i) + \sum_{i=1}^{N_u} L_u(i) \tag{33}$$

$$= N_d \langle L_d \rangle + N_u \langle L_u \rangle, \tag{34}$$

the average effective chord length then can be defined as

$$\langle L_{eff} \rangle = \frac{L_{tot}}{N_d} \tag{35}$$

$$= \frac{N_d \langle L_d \rangle + N_u \langle L_u \rangle}{N_d} \tag{36}$$

$$= \langle L_d \rangle + \frac{N_u}{N_d} \langle L_u \rangle. \tag{37}$$

Expressed in terms of probabilities, we obtain

$$\langle L_{eff} \rangle = \langle L_d \rangle + \frac{p_u}{1 - p_u} \langle L_u \rangle. \tag{38}$$

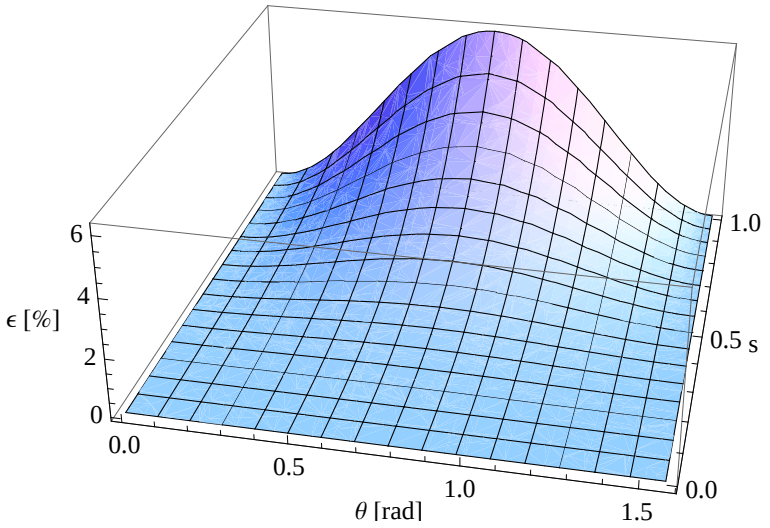

Fig. 7. The relative difference between the two formulae for the effective average chord length as a operatornametion of projection angle and step size as a fraction of pixel side length.

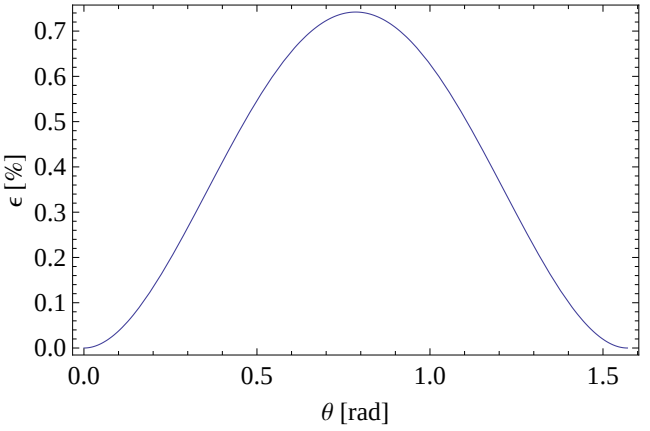

Fig. 8. The 2D projection of the relative difference shown in Figure 7 for $s = a/2$.

However, the expression in Ref. 16 is

$$\langle L_{eff} \rangle = \langle L_d \rangle + p_u \langle L_u \rangle , \tag{39}$$

which implies that it is a first order approximation of (38) in p_u, and therefore they are equivalent only in the case of small p_u. Fortunately, this seems to be the case, as the maximum difference in $\langle L_{eff} \rangle$ between (38) and (39) is less then 1% for $s = a/2$ and reaches only about 6% when $s \to a$. Figure 7 shows the relative difference ε between the two results as a operatornametion of step size and projection angle, while Figure 8 is a 2D projection for the practically relevant case of $s = a/2$.

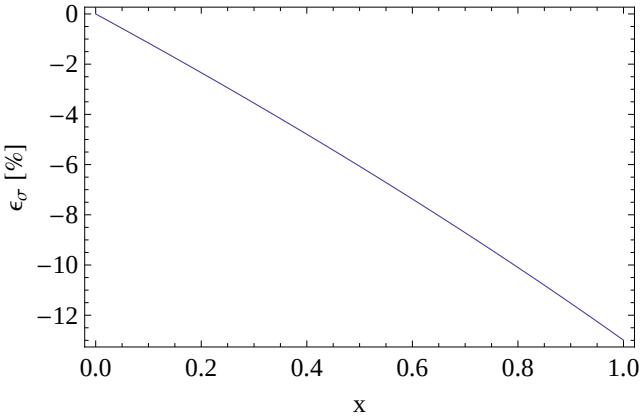

Fig. 9. The relative difference in the electron density resolution induced by the discrete sampling of the most likely paths. The horizontal axis quantifies the roughness of the sampling between $x = 0$ being the theoretical limit of no sampling errors and $x = 1$ being the voxel size.

4.2. *Effect on the electron density resolution*

The electron density resolution of pCT depends on the average chord length.[14] If $\langle L_{true} \rangle$ is written as

$$\langle L_{true} \rangle = ac\,(\theta)\,, \tag{40}$$

the resolution $\sigma_{\vec{\eta}}$ will depend on $\langle c\,(\theta) \rangle$, where the average is taken over θ. However, if the MLPs are sampled discretely with step size s the resolution will depend on the slightly different effective average chord length (30), $\langle L_{eff} \rangle = ac_{eff}\,(\theta, x)$, where we denoted by $x = s/a \in (0, 1)$. The electron density resolution then will be inversely proportional to $\sqrt{\langle c_{eff}\,(\theta, x) \rangle}$.[14] Hence, we can define the relative difference in the resolutions by

$$\varepsilon_\sigma\,(x) = \sqrt{\frac{\langle c\,(\theta) \rangle}{\langle c_{eff}\,(\theta, x) \rangle}} - 1. \tag{41}$$

Figure 9 shows the result as a operatornametion of x obtained from the numerical integration of (41). Therefore, the electron density resolution improves by 6–8% for practically relevant cases ($x \approx 1/2$). However, this improvement needs to be balanced by the increased errors in the system matrix A, which have not been taken into account yet. Nevertheless, our results seem to suggest that sampling with larger step sizes improves electron density resolution at the detriment of spatial resolution. Similar results have been reported previously.[17] A more detailed analysis will be the subject of future work.

5. Summary and conclusions

We investigated three potential error sources in proton computed tomography. The image reconstruction problem based on algebraic reconstruction methods has been

studied in the limit of very large doses. We found that while in theory the resulting estimator for the actual electron densities is biased, it turns out that from a practical point of view the tiny bias is completely negligible. Furthermore, we studied quantitatively the effects on the electron density resolution of the uncertainties in the mean ionization potentials. We found that even in extreme cases large errors in the potentials are damped by at least a factor of 3–4 in the resolution, resulting in maximum 10% error levels. Of course, for realistic anatomical objects, we expect much smaller errors (1–2%) since most of the pixels will have I values much closer to the assumed water value (75 eV) than what was modeled here. The influence on the integrated electron densities is even smaller in general. Finally, the discrete sampling of the proton trajectories during the image reconstruction seems to benefit the electron density resolution by a few percent. However, this positive result needs to be balanced by an associated negative result due to increased errors in the system matrix. These will be the main thrust of future work. In conclusion, proton computed tomography appears to be a robust medical imaging method, with image reconstruction methods benefiting from resilience with respect to a variety of errors and uncertainties.

References

1. A.M. Cormack. Representation of a function by its line integrals, with some radiological applications. *J. Appl. Phys.*, 34:2722–2727, 1963.
2. A.M. Cormack. Representation of a function by its line integrals, with some radiological applications. II. *J. Appl. Phys.*, 35:2908–2913, 1964.
3. A.M. Cormack and A.M. Koehler. Quantitative proton tomography: preliminary experiments. *Phys. Med. Biol.*, 21:560–569, 1976.
4. K.M. Hanson, J.N. Bradbury, R.A. Koeppe, R.J. Macek, D.R. Machen, R. Morgado, M.A. Paciotti, S.A. Sandford, and V.W. Steward. Computed tomography using proton energy loss. *Phys. Med. Biol.*, 26:965–983, 1981.
5. K.M. Hanson, J.N. Bradbury, R.A. Koeppe, R.J. Macek, D.R. Machen, R. Morgado, M.A. Paciotti, S.A. Sandford, and V.W. Steward. Proton computed tomography of human specimens. *Phys. Med. Biol.*, 27:25–36, 1982.
6. R.W. Schulte, V. Bashkirov, T. Li, Z. Liang, K. Mueller, J. Heimann, L.R. Johnson, B. Keeney, H.F.-W. Sadrozinski, A. Seiden, D.C. Williams, L. Zhang, Z. Li, S. Peggs, T.J. Satogata, and C. Woody. Conceptual design of a proton computed tomography system for applications in proton radiation therapy. *IEEE Trans. Nucl. Sci.*, 51:866–872, 2004.
7. A.R. Smith. Vision 20/20: Proton therapy. *Med. Phys.*, 36(2):556–568, 2009.
8. D.C. Williams. The most likely path of an energetic charged particle through a uniform medium. *Phys. Med. Biol.*, 49:2899–2911, 2004.
9. R.W. Schulte, S.N. Penfold, J.F. Tafas, and K.E. Schubert. A maximum likelihood proton path formalism for application in proton computed tomography. *Med. Phys.*, 35(11):4849–4856, 2008.
10. B. Erdelyi. A comrehensive study of the most likely path formalism for proton computed tomography. *Phys. Med. Biol.*, 54:6095–6122, 2009.
11. T. Li, Z. Liang, J.V. Singanallur, T.J. Satogata, D.C. Williams, and R.W. Schulte. Reconstruction for proton computed tomography by tracing proton trajectories, a Monte Carlo study. *Med. Phys.*, 33:699–706, 2006.

12. S.N. Penfold, R.W. Schulte, Y. Censor, V. Bashkirov, S. McAllister, K.E. Schubert, and A.B. Rosenfeld. Block-iterative and string averaging projection algorithms in proton computed tomography image reconstruction. In *Biomedical Mathematics: Promising Directions in Imaging, Therapy Planning and Inverse Problems*, Medical Physics Publishing, Madision, WI, USA, 2009.
13. R.W. Schulte, B. Bashkirov, M.C. Loss Klock, T. Li, A.J. Wroe, I. Evseev, D.C. Williams, and T. Satogata. Density resolution of proton computed tomography. *Med. Phys.*, 32(4):1035–1046, 2005.
14. B. Erdelyi. Electron density uncertainties in proton computed tomography. *Phys. Med. Biol.*, page submitted, 2010.
15. International Commission on Radiation Units and Measurements. Tissue Substitutes in Radiation Dosimetry and Measurements. Technical Report ICRU Report No. 44, ICRU, Bethseda, MD, 1989.
16. S.N. Penfold, R.W. Schulte, K.E. Schubert, and A.B. Rosenfeld. A more accurate reconstruction system matrix for quantitative proton computed tomography. *Med. Phys.*, 36:4511–4518, 2009.
17. S.N. Penfold, R.W. Schulte, Y. Censor, V. Bashkirov, and A.B. Rosenfeld. Characteristics of proton ct images reconstructed with filtered backprojection and iterative projection algorithms. In *Conference Record of The 2009 IEEE Nuclear Science Symposium and Medical Imaging Conference (2009 IEEE-NSS-MIC)*, Orlando, Florida, USA, October 25-31, 2009.

International Journal of Modern Physics A
Vol. 26, Nos. 10 & 11 (2011) 1775–1784

DOI: 10.1142/S0217751X11053171

World Scientific
www.worldscientific.com

INJECTION AND EXTRACTION SYSTEMS FOR THE MUON FFAG RING IN THE NEUTRINO FACTORY

DAVID KELLIHER and SHINJI MACHIDA

ASTeC, STFC Rutherford Appleton Laboratory,
Chilton, Didcot,Oxfordshire, OX11 0QX, UK
David.Kelliher@stfc.ac.uk

M. ASLANINEJAD

Imperial College London, UK

J. PASTERNAK

Imperial College London, UK
STFC Rutherford Appleton Laboratory,
Chilton, Didcot,Oxfordshire, OX11 0QX, UK

J. SCOTT BERG

BNL, Upton, Long Island, New York, USA

H. WITTE

Oxford University, John Adams Institute of Accelerator Science,
Denys Wilkinson Building, Keble Road, Oxford, OX1 3RH, UK

Non-scaling FFAG (NS-FFAG) rings have been proposed as a solution for muon acceleration in the Neutrino Factory. In order to achieve small orbit excursion and small time of flight variation, lattices with a very compact cell structure and consequent short straight sections are required. The resulting geometry, combined with the large transverse emittance of the muon bunch, places very challenging constraints on the injection/extraction systems. The injection/extraction system requires a set of distributed kickers, a superconducting septum and increased aperture in some of the main ring magnets. A scheme for both injection and extraction for a FFAG with triplet geometry is presented. In addition, a solution for the required kicker magnets is proposed.

Keywords: FFAG; muon; kicker.

PACS numbers: 29.27.Ac, 41.75.Lx

1. Introduction

An important area which is being addressed by the International Design Study for the Neutrino Factory (IDS-NF)[1] (which aims to produce a reference design report by 2012), is to design a chain of accelerators to accelerate the μ^+ and μ^-

beams to 25 GeV. Following a linac, which accelerates muons from 0.2 to 0.9 GeV, two recirculating linacs continue the acceleration on to 12.6 GeV and a FFAG on to 25 GeV.

The use of a FFAG ring is motivated by a higher efficiency of acceleration than in an RLA, since in the latter the number of turns is limited by the complications of the switchyard design.[2] A non-scaling FFAG is chosen due to its small aperture magnets and, since it is quasi-isochronous, it is possible to use high-frequency RF frequency (201 MHz) that is fixed during the acceleration cycle.[3] Furthermore, the use of only linear magnetic field components in the NS-FFAG results in a very high dynamical acceptance, which is needed for muon acceleration. Despite these advantages, there are two major challenges presented by the NS-FFAG:

- dependence of time of flight on transverse amplitude leading to longitudinal emittance blow-up;
- difficulty in injection and extraction due to the short drift lengths.

In this paper we address the problem of injection and extraction.

2. NS-FFAG Candidate Lattices

The present IDS reference design of NS-FFAG for muon acceleration consists of three candidate lattices which have either FODO or triplet cell geometry and either one or two cavity cells per available drift. The FFAG is made up of combined function magnets with both dipole and quadrupole components. These lattices evolved from an earlier set.[4] Since then, lattices with doublet cell geometry were rejected since they preclude the use of a single injection or extraction system for both muon signs. Additional drifts have been allocated for the distributed injection/extraction kickers and, for symmetry purposes, it is preferred that the number of cells be a multiple of four.[5] The cell tunes of the updated lattices are shown in Fig. 1 and are

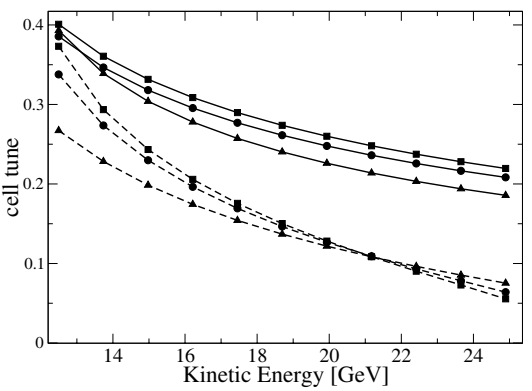

Fig. 1. Cell tunes as a function of energy in the candidate FFAG lattices—the triplet with one cavity cell per drift (circle) and two cavity cells per drift (square) and the FODO with one cavity cell per drift (triangle). Solid lines correspond to the horizontal tune and dashed to the vertical.

Table 1. Parameters of NS-FFAG triplet.

Number of cells	64
Cavity cells	88
Circumference	546 m
RF voltage	1.119 GV
Turns	11.8
F magnet field	3.6 T
D magnet field	6.5 T
F magnet gradient	16.3 T/m
D magnet gradient	-16.5 T/m
Drift length	3 m
Injection energy	12.6 GeV
Extractin energy	25 GeV

obtained by the ray-tracing code Zgoubi[6] which is used for calculations throughout this paper.

In this paper we study injection and extraction in the triplet lattice with two cavity cells in each available drift. This lattice was chosen in favor of the other two since the drift length in each cell is 1m longer, allowing a correspondingly longer kicker and septum length and hence lower peak fields. The parameters for this triplet are shown in Table 1.

3. Injection/Extraction Schemes

The non-scaling FFAG lattices for muon acceleration at the Neutrino Factory have very strong focusing optics in order to minimize the orbit excursion and accordingly the size of the superconducting magnets. This is achieved by designing a ring with a large number of cells, which leads to relatively short drift lengths and strong quadrupole magnets. This, in turn, results in low betatron values in the 3 m drifts, which together with the large transverse emittance (the required normalized transverse acceptance is 30 π mm rad) of the muon beam makes injection and extraction difficult.

The beam offset x_o at the observation point after passing through the kicker magnet with deflection θ_k can be approximated by the following formula:

$$x_o = \theta_k \sqrt{\beta_k \beta_o} \sin\Delta\phi + x_k \sqrt{\frac{\beta_o}{\beta_k}} \cos\Delta\phi \tag{1}$$

where β_k and β_o are betatron functions at the kicker and observation points respectively, and $\Delta\phi$ is the difference in phase advance between the two points. Note that the horizontal coordinate at the kicker x_k is non-zero in the case of a FFAG. The transverse plane in which it is more efficient to inject or extract is established by comparing the betatron function at the kicker and septum locations i.e. in the long drifts. From Fig. 2 it is clear that horizontal injection and vertical extraction are favored.

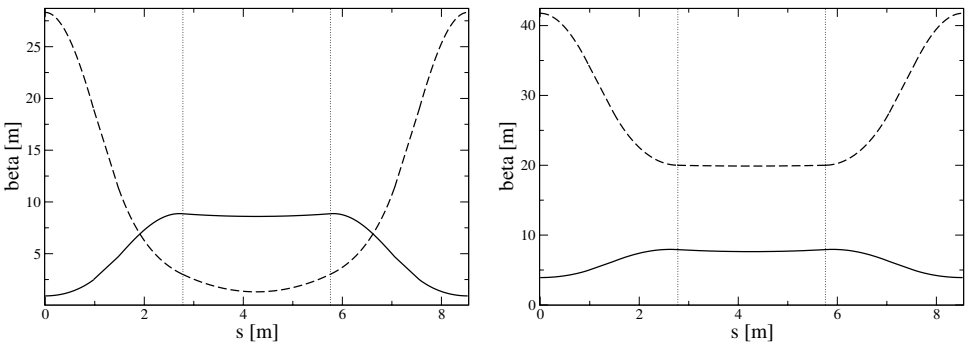

Fig. 2. Horizontal (solid) and vertical (dashed) betatron functions at injection energy (left) and at extraction energy (right) in the triplet FFAG ring. The extent of the long drift is indicated by the dotted vertical lines. The origin corresponds to the centre of the triplet.

Distributed kickers are required to achieve sufficient orbit separation at the septa, where the beta values are ∼10 m at injection and ∼20 m at extraction. The kickers and septum are placed in consecutive cells to minimize the size of the system. Furthermore, a septum placed at either end of this symmetrical distribution of kickers allows both muon species to use the same set of kickers. For simplicity it assumed that each kicker has the same peak field. Each kicker and septum is assumed to be 60 cm shorter than the long drift, i.e. 2.4 m in the case of this triplet lattice.

It is assumed that a 2 cm clearance between the kicked and circulating beam at the septum entrance is sufficient. In order to estimate the clearance needed so that the extracted or injected beam avoids the magnet immediately following the septum, the dimensions of the superconducting combined function magnet (SCFM) in the J-PARC neutrino beam line is used. Although in that case the dipole field is lower, it has a comparable field gradient. The width of the J-PARC SCFM from the inner radius of the coils to the outer radius of the cold mass is 19.8 cm.[7] This distance is used, together with the size of the muon beam, in calculating the septum field required.

The injection scheme, in the horizontal plane, employing 3 kickers is shown in Fig. 3. The kicker peak field is 0.09 T (with the polarity reversing in each successive kicker) and the septum field is 2.5 T. The extraction scheme, this time in the vertical plane, is shown in figure 4. Since the vertical phase advance per cell is low at extraction energy (Fig. 1), all kickers have the same polarity. The higher rigidity of the beam at extraction leads to a 4 T septum requirement. The parameters for injection and extraction are summarized in Table 2. They compare favorably with the equivalent parameters of an alternative lattice (a FODO lattice with 1m shorter drift length) in which six kickers were required for both injection and extraction.[8]

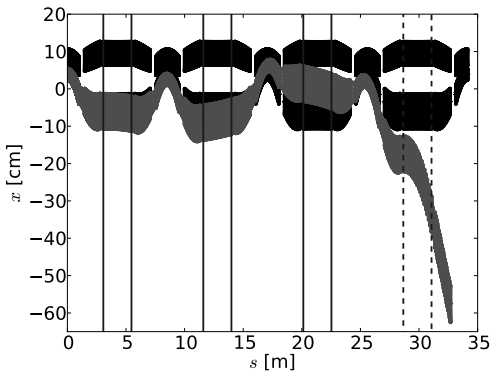

Fig. 3. Horizontal injection scheme into the triplet FFAG ring using 3 kicker magnets. The circulating beam at injection and extraction is shown in black and the injected beam (from right to left) in gray. The vertical lines represent the location of the kicker magnets (solid) and septum (dashed).

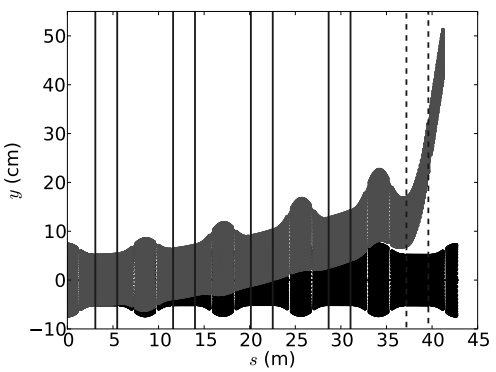

Fig. 4. Vertical extraction scheme from the triplet FFAG ring using 4 kicker magnets. The circulating beam is shown in black and the extracted beam in gray. The vertical lines represent the location of the kicker magnets (solid) and septum (dashed).

4. Kicker Magnet Design

In this section we outline a potential solution for an injection/extraction kicker meeting the requirements outlined in Table 2. We concentrate on the kicker for injection. The final bunch spacing is still being discussed, but in this paper we consider the scenario presented in Figure 5(a). As shown in the figure, three pulses are required with a spacing of about 100 μs. The rise, fall and flat-top time of each pulse should be about 1.5 μs.

To evaluate the requirements on the pulse forming network we study a conceptual design of a potential kicker magnet. The required kicker aperture is $0.3 \times 0.3\,\mathrm{m}^2$;

Table 2. Injection/Extraction parameters.

Scheme	Injection	Extraction
Plane	Horizontal	Vertical
Number of kickers	3	4
Kicker peak field	0.09 T	0.08 T
Septum field	2.5 T	4 T
Kicker/Septum length	2.4 m	2.4 m
Mirror Symmetry	Yes	Yes

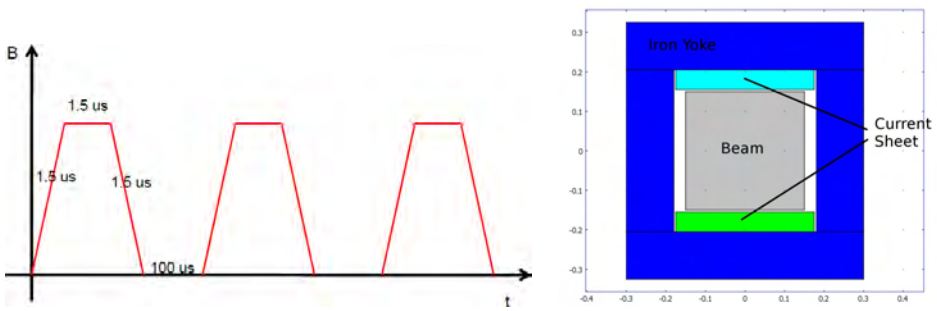

(a) (b)

Fig. 5. Figure (a) shows schematically the required kicker pulses; the rise and fall time should be less than about 1.5 μs with a flat top of more than 1.5 μs. Required are three consecutive pulses with a delay of about 100 μs. Figure (b) shows a conceptual design of a kicker magnet for vertical extraction.

the available length is 2.4 m. The required field over this length is about 90 mT. The magnetic energy of such a kicker can readily be calculated using a 2D FEA approach. We assume a classical window frame layout, which is shown in Fig. 5(b). The kicker magnet assumes a ferrite yoke (thickness 120 mm) made of 8C11 from Ferroxcube. The magnetic flux density at peak field is below 150 mT, which is well below saturation.

To generate 100 mT a peak current I_{peak} of 29 kA is required; the total magnetic energy W_{mag} of the kicker is 500 J. The inductance can be evaluated using $L = 2W_{\text{mag}}/I_{\text{peak}}$; assuming the kicker is made of a single turn, the inductance is 2.8 μH.

Due to the short time in between each pulse we envisage one designated pulse forming network (PFN) per pulse, which is shown in Fig. 6(a). It is essential that any reflections in the PFN are minimized in between pulses to ensure no unwanted fields from the kicker. To achieve this we require each PFN to be terminated appropriately.

The PFN needs to be of low impedance to deliver the required peak current at a reasonable voltage; we chose an impedance of 1 Ω, which at a peak voltage of 60 kV can provide about 30 kA.

To reduce the current each PFN is subdivided into three parallel PFNs with an impedance of 3 Ω each; each sub-PFN provides a peak current of 10 kA. Each sub-

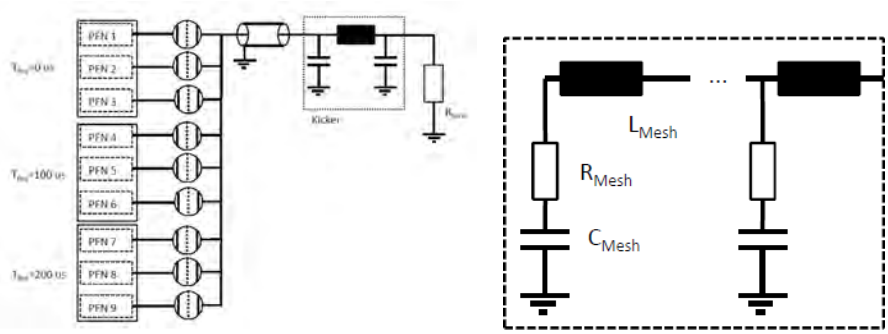

(a) (b)

Fig. 6. Figure (a) shows the general layout of the proposed kicker system. In total 9 PFNs are required, three for each pulse. Each PFN is a standard Raleigh-type PFN, which is shown in Fig. (b).

PFN is of type Rayleigh (shown in Fig. 6 (b)). Assuming 10 meshes, the required mesh capacitance and inductance are 66.67 nF and 600 nH, respectively. The PFNs are connected with coax-wire to the kicker magnet, which in practise could be facilitated by using 50 coax wires of type RG220 in parallel. Each sub-PFN is switched by a thyratron, for instance of type CX1936X from e2v. The thyratron is suitable up to a voltage of 80 kV and a peak current of 10 kA with a repetition rate of up to 5 kHz.

The kicker magnet is realized as a travelling wave kicker to match the impedances. This implies that the kicker is subdivided into at least 10 sections with added capacitance.

Due to the low impedance of the PFN and the large inductance of the kicker magnet substantial amounts of capacitance need to be added to match the impedance of 1 Ω. To estimate the feasibility of this we assume a plate capacitor with a cross-sectional area of 1 m^2 and a distance of 1 mm between the plates. The capacitance of such a capacitor would be about 1×10^{-8} F. For a kicker with 10 subdivisions we require added capacitance of about 1×10^{-7} F, which is equivalent to 10 plate capacitors over a length of 240 mm. This simple calculation illustrates that adding the required capacitance is not trivial but potentially achievable.

Fig. 7 shows the expected average current of all sections of the kicker magnet. The figure shows that the rise time is around 1.4 μs with a flat top length of about 1.5 μs. The fall time is about 2 μs. The figure shows the calculated current for a kicker which is subdivided into 10 and 20 sections. As shown the current is more uniform for 20 subdivisions (field homogeneity about 1.25% in comparison to about 2.7% for 10 subdivisions).

This section has outlined a potential solution for the IDS injection kicker. Further efforts will concentrate on identifying suitable components for the capacitors and thyratrons. It should also be investigated if the number of capacitors can be de-

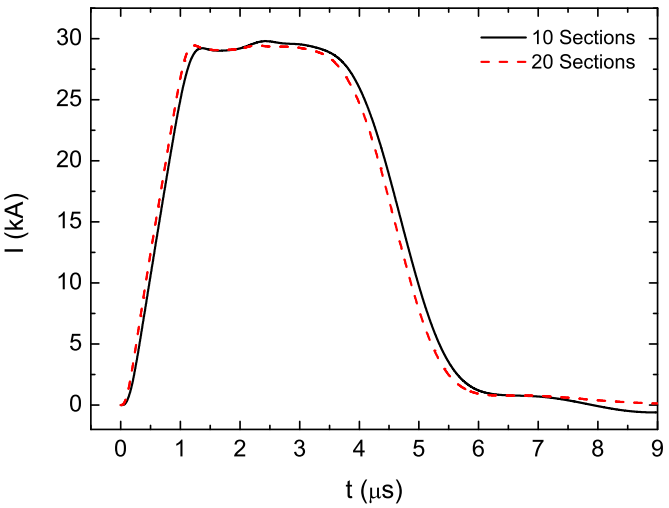

Fig. 7. Average current in the kicker magnet. The current is shown assuming the kicker is subdivided into 10 and 20 smaller kickers.

creased by employing PFNs with five meshes. Furthermore, we intend to investigate a preliminary engineering design of the described travelling wave kicker.

5. Effect of Special Magnets

One disadvantage of using distributed kickers is the need for special large aperture magnets to accommodate the resulting betatron oscillations. As can be seen in Fig 3 and 4, for injection at least one large aperture magnet is required in the focusing magnet neighboring the septum. In the case of extraction a larger aperture may be required in all of the magnets between the final kicker and the septum. These 'special' magnets will have a longer fringe field extent and their introduction will break the symmetry of the FFAG—leading to closed orbit and optics distortion in the circulating beam.

In order to study these effects, it is first necessary to establish the aperture of both the normal and special magnets. Assuming the magnet aperture is circular, we make use of an algorithm that finds the center and radius of the smallest circle that encloses the set of ellipses that define the beam size over the momentum range.[9] Following Zgoubi tracking studies, it is found that for injection the aperture increases from 23.5 cm to 34.2 cm in the case of the F magnet neighboring the septum and, for extraction, from 17.7 cm to 46.5 cm in the case of the D magnet closest to the septum.

The longer fringe fields of the special magnets result in a difference in the integrated field experienced by the beam. This is equivalent to a dipole kick and leads to orbit distortion. The orbit distortion during acceleration is calculated by introducing cavities in every drift and tracking over the 12.6–25 GeV energy range. In

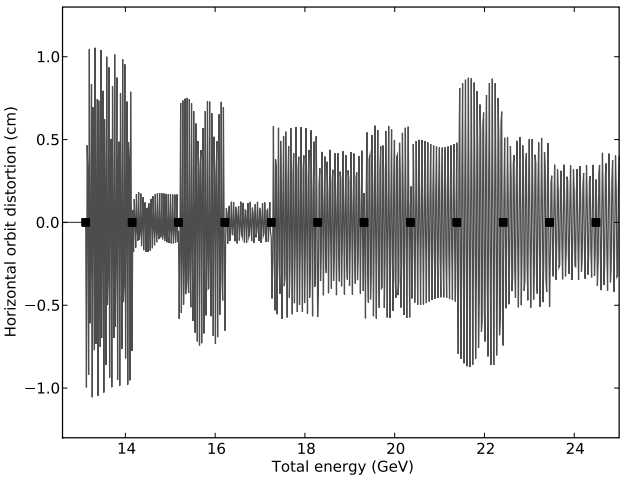

Fig. 8. Distortion of the accelerated orbit measured due to the presence of special magnets (locations given by squares). The distortion is measured at the middle of each long drift.

this simulation, just one set of large aperture triplet magnets required for extraction is included, using the apertures given above. For simplicity, a constant acceleration rate is assumed. Acceleration is completed in 12 turns, i.e. close to the design value for this lattice (Table 1). A single particle is tracked starting at the phase space coordinates given by the closed orbit at the injection energy. The difference in the horizontal coordinate in the middle of each long drift with and without special magnets gives the orbit distortion shown in Fig. 8. The maximum orbit distortion in acceleration is just over 1 cm. This orbit distortion can be reduced significantly by shifting the special magnet to compensate for the dipole kick introduced by the longer fringe field. Assuming the magnets are linear this shift should not affect the optics of the machine. It is calculated that the maximum orbit distortion in acceleration due to one special D magnet is reduced from 1 cm to 0.35 cm by shifting the magnet in question by 1.25 mm. Levels of orbit distortion at this level can tolerated in the large aperture magnets of the muon FFAG.

6. Summary

The injection and extraction systems in the non-scaling FFAG for muon acceleration in the Neutrino Factory are studied for the case of the triplet lattice with two cavities per cell. Based on the optics of this lattice, it is found to be advantageous to inject in the horizontal plane and extract in the vertical. Due to the restricted drift space in the NS-FFAG it is necessary to have a distributed set of kickers. The injection/extraction schemes are mirror-symmetric schemes so that the kickers can be reused for both signs of muons. The disadvantage of these solutions is a need for special magnets with large aperture in the injection/extraction region due to

the large kicked beam oscillations. However, it appears that the orbit distortion introduced by the longer fringe field extent of these magnets can be reduced to tolerable levels by introducing a horizontal shift. The strength and size of the required kickers pose a significant engineering challenge and the field in the septum magnets dictates the need for a superconducting design. A potential solution for the design of the kicker magnet system is presented.

References

1. http://www.ids-nf.org/
2. S. A. Bogatz and R. P. Johnson, in *Proc. EPAC08, Genoa, Italy, 2008*, (EPAC, EPS-AG, 2008) p. 2629.
3. J. S. Berg *et al.*, *Phys. Rev. ST Accel. Beams* **9**, 011001
4. J. Scott Berg, FFAG designs for the International Design Study for the Neutrino Factory, to appear in the proceedings of the 23rd Particle Accelerator Conference, (May 48, 2009, Vancouver, Canada)
5. J. Scott Berg, private communication (2009)
6. F. Méot, *Nucl. Instr. Meth. A* **427**, p. 353 (1999)
7. T. Ogitsu *et al*, *IEEE Trans. Appl. Supercond.*, vol. 19, no. **3**, pp. 1081 ¯1086, (1993)
8. J. Pasternak *et al*, Feasibility of Injection/Extraction Systems for Muon Rings in the Neutrino Factory, to appear in the proceedings of the 23rd Particle Accelerator Conference, (May 4–8, 2009, Vancouver, Canada)
9. J. S. Berg, in *Proc. EPAC08, Genoa, Italy, 2008*, (EPAC, EPS-AG, 2008) p. 2858

International Journal of Modern Physics A
Vol. 26, Nos. 10 & 11 (2011) 1785–1793

DOI: 10.1142/S0217751X11053183

World Scientific
www.worldscientific.com

ZERO-CHROMATIC FFAG STRAIGHT SECTION

J.-B. LAGRANGE

Graduate School of Engineering, Kyoto University Katsura, Nishikyo-ku, Kyoto, 615-8530, Japan
lagrange@rri.kyoto-u.ac.jp

T. PLANCHE

Graduate School of Engineering, Kyoto University Katsura, Nishikyo-ku, Kyoto, 615-8530, Japan

Y. MORI

Kyoto University Research Reactor Institute, Department of Nuclear Science and Engineering, 2, Asashiro-Nishi, Kumatori-cho, Sennan-gun, Osaka, 590-0494, Japan

Fixed Field Alternating Gradient (FFAG) elements are usually designed in a circular shape, but straight sections can also be imagined. A demonstration using the scaling condition is first shown. Combining different scaling FFAG sections is then discussed and opens new possibilities for scaling FFAGs. As an example, an application with a new lattice proposal for the PRISM project is finally presented in this paper.

Keywords: Scaling FFAG; transport line; insertion; dispersion suppressor; PRISM.

PACS number: 29.20.dk

1. Introduction

The concept of scaling FFAG is usually applied to circular machines, where each cell is designed to provide the same total bending angle. However, scaling FFAG cells can also be imagined and designed to guide particles which have no net overall bend.[1] In this case, the scaling condition leads to a different field law than in circular ring elements. This is demonstrated in the first section. Then, insertions in scaling FFAG rings and dispersion suppressor principle are discussed. Finally, an example of application is presented with a new lattice proposal for the PRISM project.

2. Scaling Law

The scaling condition entails two hypotheses:

- geometrical similarity of closed orbits as a function of momentum, which leads to
- constant number of the betatron oscillations, implying zero-chromaticity for the system.

To deal with the betatron oscillations, we use the linearized equations of motion around the closed orbit for a given momentum:

$$\begin{cases} \dfrac{d^2x}{ds^2} + \dfrac{1-n}{\rho^2}x = 0 \\ \dfrac{d^2z}{ds^2} + \dfrac{n}{\rho^2}z = 0 \end{cases}, \tag{1}$$

with ρ the curvature radius, s the curvilinear abscissa, x and z the perpendicular displacement off the closed orbit respectively in horizontal and in vertical and n the field index defined as

$$n = -\frac{\rho}{B}\left(\frac{\partial B}{\partial x}\right)_{z=0}. \tag{2}$$

To satisfy the scaling condition, Eq. (1) has then to be independent of momentum.

In circular elements, we start with a set of closed orbits for each momentum lying in the median plane. In this case, similarity of the closed orbits means that each of them is a photographic enlargement of preceeding orbits. The general form of the vertical component of the magnetic field B in the mid-plane is[2,3]

$$B = B_0\left(\frac{r}{r_0}\right)^k \mathcal{F}(\theta), \tag{3}$$

with r and θ the polar coordinates, B_0 the magnetic field at the radius r_0, $\mathcal{F}$ an arbitrary periodic function, and k the geometrical field index.

While in circular elements, the concept of closed orbit is obvious, the corresponding notion of a reference trajectory in a "straight" cell or insertion has first to be defined. The reference trajectory of a straight cell is defined as a trajectory followed by a particle whose coordinates (i.e. angle and position) are the same at the entrance and at the exit of the cell.

As in the circular case, we start with a set of reference trajectories for each momentum in the median plane. In this case, similarity of the reference trajectories means that each of them is a translation of each other. Each reference trajectory is specified by its average abscissa X over one cell.

The number of betatron oscillations is invariant in momentum if Eq. (1) is the same for every momentum, and since s is independent of momentum, the condition to have invariant betatron oscillations is

$$\begin{cases} \dfrac{\partial}{\partial p}\left(\dfrac{1}{\rho^2}\right) = 0 \\ \dfrac{\partial}{\partial p}\left(\dfrac{n}{\rho^2}\right) = 0 \end{cases}. \tag{4}$$

The similarity condition of the reference trajectories validates the first equation of the system (4), since the curvature radius depends only on s, and so is independent of momentum. We now focus on the second equation of the system (4).

If we differentiate the equation $p = qB\rho$, for a particle of momentum p and charge q, with respect to x, we have:

$$B\frac{\partial \rho}{\partial x} + \rho\frac{\partial B}{\partial x} = \frac{1}{q}\frac{dp}{dx}\,. \tag{5}$$

If we introduce the field index n in Eq. (5), we have:

$$n = \frac{\partial \rho}{\partial x} - \frac{\rho}{p}\frac{dp}{dx}. \tag{6}$$

To express Eq. (6) in the coordinates (X, s), we now introduce the parameters η and ϵ that link dx with ds:

$$\eta = dx/dX, \tag{7}$$

$$\epsilon = ds/dX. \tag{8}$$

Then, rewriting Eq. (6) with η and ϵ, we get

$$n = -\frac{1}{\eta}\left(m\rho + \epsilon\frac{d\rho}{ds}\right), \tag{9}$$

with m a parameter given by

$$m = \frac{1}{p}\frac{dp}{dX}. \tag{10}$$

Rewriting m with the magnetic field B, we get:

$$m = \frac{1}{B}\frac{dB}{dX}. \tag{11}$$

In consequence, we have

$$\frac{n}{\rho^2} = -\frac{1}{\eta\rho}\left(m + \frac{\epsilon}{\rho}\frac{d\rho}{ds}\right). \tag{12}$$

The similarity condition gives that ρ, η and ϵ depend only on s, therefore they are independent of momentum. So, starting from the similarity of the reference orbits, The reference betatron oscillations are independent of momentum if and only if m is independent of momentum. In this case, we can integrate Eq. (11) and with the initial condition $B(X_{_0}) = B_0$, we obtain the scaling law:

$$B = B_0 e^{m(X - X_{_0})}\mathcal{F}(s), \tag{13}$$

where $\mathcal{F}$ is an arbitrary periodic function.

As a remark, in the linear approximation, the field index n can be written in the circular section as

$$n = \frac{\rho}{r_0}k, \tag{14}$$

and in the straight section as

$$n = m\rho. \tag{15}$$

3. Insertions and Dispersion Suppressor Principle

3.1. *Matching of reference trajectories*

FFAG straight sections could be used with circular FFAG sections, but since field laws in each section are different, there will occur a discontinuity of reference trajectories at the border between these two sections. Before combining them together, it is useful to consider them separately. In scaling FFAG, the periodic dispersion function D of a cell for a given momentum p_0 is defined as

$$D_{circ.}(p_0) = p_0 \left(\frac{\partial r}{\partial p}\right)_{p_0} = \frac{r}{k+1} \tag{16}$$

in circular elements, with r the radius of the closed orbit, and k the geometrical field index of the cell, and

$$D_{str.}(p_0) = p_0 \left(\frac{\partial a}{\partial p}\right)_{p_0} = \frac{1}{m} \tag{17}$$

in straight elements, with a the abscissa of the reference trajectory and m the factor in the exponential law we discussed in Sec. 2.

In consequence, to combine a straight section and a circular section, after matching a special momentum p_0, dispersion can be matched with

$$m = \frac{k+1}{R_0}, \tag{18}$$

with R_0 the radius of the closed orbit for the momentum p_0 at the border of the cell in the circular section. But this matching is done only to the first order in $\frac{R-R_0}{R_0}$, with R the radius of the closed orbit for a momentum p at the border of the cell in the circular section. Higher orders effects create a reference trajectory mismatch for momenta other than p_0.[1] By a proper choice of p_0, the mismatch could be minimized for the considered momentum range. An example has been computed by simulating the insertion of straight sections in the 150 MeV FFAG ring of KURRI, for kinetic energies between 20 MeV and 150 MeV. The mismatch x as a function of kinetic energy is presented in Fig. 1. This maximum mismatch is around one cm for this case. It would be smaller for larger rings.

In the same way, it is possible to match two circular FFAG sections with different radii r_1 and r_2. The dispersion matching condition is kept by adjusting the geometrical field index:

$$\frac{k_1+1}{r_1} = \frac{k_2+1}{r_2}. \tag{19}$$

3.2. *Matching of linear parameters*

Once the reference trajectories are matched, the periodic beta-functions of the cells have also to be matched to limit the amplitude of the betatron oscillations. If a correct matching is not achievable, then an insertion with a phase advance

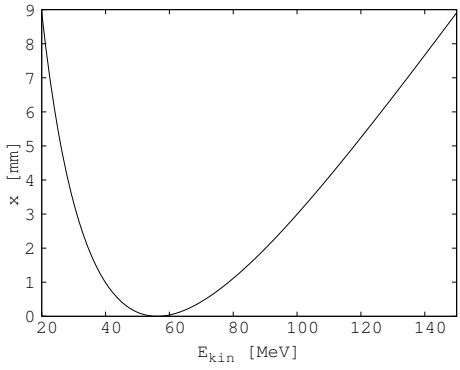

Fig. 1. Mismatch of reference trajectories between circular cells and straight cells in 150 MeV FFAG ring example.

multiple of 180° can be done for one of the two different types of cells. To lowest order, this insertion becomes transparent (-I transformation), thereby minimizing the magnitude of the betatron mistmatch induced in the ring lattice.

3.3. *Dispersion Suppressor*

In FFAGs, dispersion suppressors can be useful at the end of a transport line, or to reduce excursion where rf cavities are set in FFAG rings. The effect of a dispersion suppressor would be to decrease the excursion, i.e. to bring closer the reference trajectories around a matched one. This excursion reduction can even be a complete suppression (see Fig. 2).

A principle of a dispersion suppressor in scaling FFAGs is presented in Fig. 2. The components of this scheme are three types of scaling FFAG cells, straight or circular. The area 1 contains FFAG cells with a dispersion D_1 at the border, the area 2, constituting the dispersion suppressor itself, contains FFAG cells with a dispersion D_2 at the borders, and the area 3 contains FFAG cells with a dispersion D_3 at the border. The conditions to have a dispersion suppressor are a phase advance of 18° for the cells of the area 2 and the dispersion D_2 has to satisfy

$$D_2 = \frac{D_1 + D_3}{2}. \tag{20}$$

This principle is based on the linear theory, so is valid as long as the effect of non-linearities is negligible.

4. PRISM Case

The PRISM (Phase Rotated Intense Slow Muon beam) project aims to realize a low-energy muon beam with a high-intensity, narrow energy spread and high purity. For this purpose, a scaling FFAG ring has been proposed.[4] Requirements for the FFAG ring include a large transverse and longitudinal acceptance. The original design of

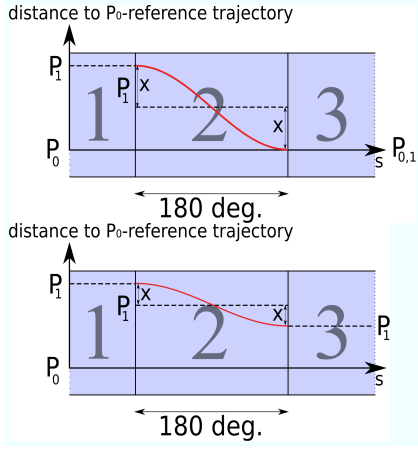

Fig. 2. Principle of a dispersion suppressor with scaling FFAG cells. The upper scheme shows the case of a complete suppression of the dispersion, the lower one—the case of a remaining dispersion after the dispersion suppressor.

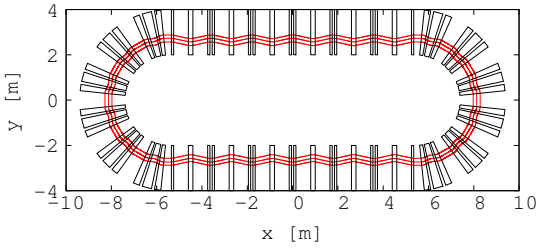

Fig. 3. Closed orbits of 55 MeV/c, 68 MeV/c and 82 MeV/c muons μ^- in the lattice with straight sections.

the FFAG ring for PRISM is based on 10 identical DFD triplets. If this design fulfills the requirements of acceptance, the problem of injection and extraction still remains. To solve this problem, we consider the use of straight cells in the lattice and a new design is proposed (see Fig. 3). Parameters are summarized in table 1.

Particle tracking is done with Runge-Kutta integration in soft edge fields with linear fringe field falloffs. Components of the field off the mid-plane are obtained from a first order Taylor expansion, satisfying the Maxwell equations.

The original PRISM design has a very large dispersion function ($\sim$ 1.2 m) that makes difficult the injection and the extraction. The new proposal starts then from a smaller one ($\sim$ 0.8 m). As discussed in Sec. 3.2, a better matching of the periodic beta-functions of the different cells gives a less modulated beta-function, and helps to have a larger acceptance. The first step is thus to minimize the mismatch of the beta-functions, then the bending part of the ring is made transparent to limit the effect of the remaining mismatch on the amplitude of the betatron oscillations.

Table 1. Parameters of the new lattice.

Circular section: FDF triplet scaling FFAG cell	
k	2.55
Mean radius (at 68 MeV/c)	2.7 m
Horizontal phase advance	60 deg.
Vertical phase advance	90 deg.
Number of cells in the ring	12
Straight section: FDF triplet scaling FFAG cell	
m	1.3 m^{-1}
Length	1.8 m
Horizontal phase advance	27 deg.
Vertical phase advance	97 deg.
Number of cells in the ring	12

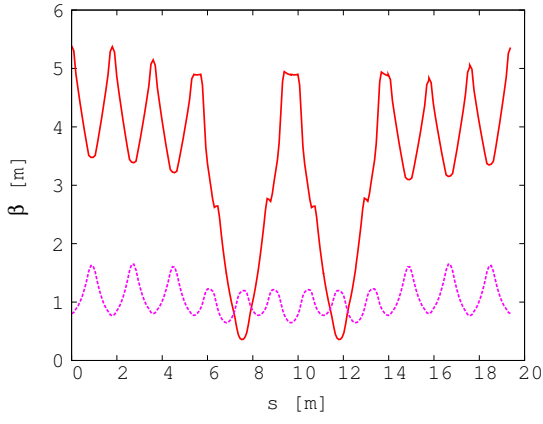

Fig. 4. Horizontal (plain red) and vertical (dotted purple) beta-functions for half of the ring.

The resulting beta-functions for a momentum of 68 MeV/c, obtained with a small amplitude motion off the closed orbit, are presented in Fig. 4. The following step is to choose the working point in the tune diagram so that it is far from the structural normal resonances. The present working point is presented in Fig. 5.

The transverse acceptance in both planes is studied by tracking over 30 turns a particle with a displacement off the closed orbit and a small deviation in the other transverse direction (1 mm). Collimators ($\pm$ 1 m in horizontal, $\pm$ 30 cm in vertical) are used to identify the lost particles. The regions drawn by the particle with the largest initial stable amplitude in the horizontal and vertical phase spaces are respectively presented in Fig. 6 and 7. Horizontal ($\sim$ 24000 π.mm.mrad) and vertical ($\sim$ 6000 π.mm.mrad) acceptances are then measured by the area of the biggest ellipse included in this region.

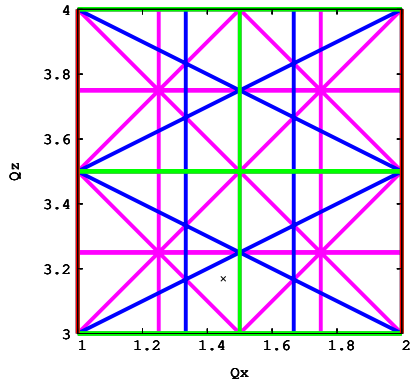

Fig. 5. Working point of the super-cell (half of the ring) in the tune diagram. Integer (red), quadrupole (green), sextupole (blue) and octupole (purple) normal resonances are plotted.

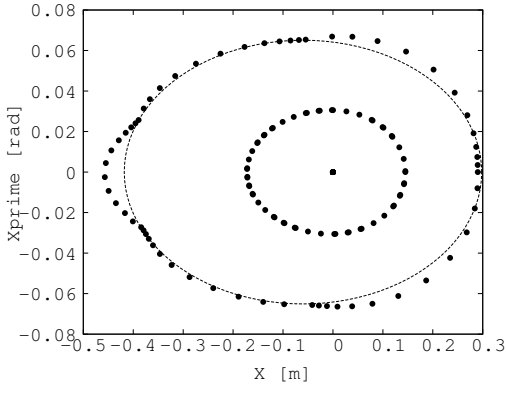

Fig. 6. Horizontal phase space. Two particles with an initial displacement of 15 cm and 29 cm are tracked over 30 turns. The dotted ellipse is the one used to measure the acceptance.

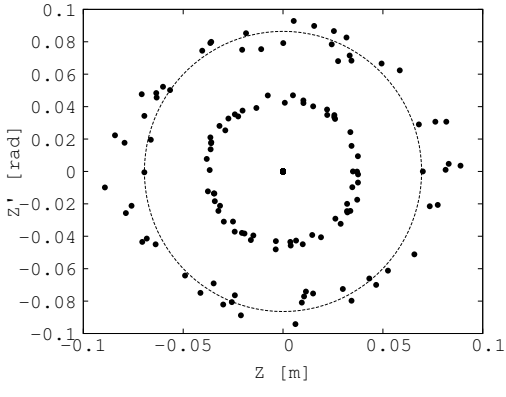

Fig. 7. Vertical phase space. Two particles with an initial displacement of 3.5 cm and 7 cm are tracked over 30 turns. The dotted ellipse is the one used to measure the acceptance.

5. Summary

The scaling condition in straight sections leads to an exponential field law in the horizontal direction. Combining different scaling FFAG cells opens new possibilities in terms of shape for rings and transport lines, and also to create dispersion suppressors. Applying this concept to the PRISM case, a new lattice is proposed.

References

1. JB. Lagrange *et al*, Straight section in scaling FFAG accelerator, in *Proc. of PAC*, (2009).
2. K. R. Symon *et al.*, *Phys. Rev.* **103**, 1840-1842 (1956).
3. A. A. Kolomensky and A. N. Lebedev, *Theory of Cyclic Accelerators*, (North-Holland, Amsterdam, 1966).
4. The PRISM Project—A Muon Source of the World-Highest Brightness by Phase Rotation, *LOI for Nuclear and Particle Physics Experiments at the J-PARC* 217 (2003).

International Journal of Modern Physics A
Vol. 26, Nos. 10 & 11 (2011) 1794–1806

DOI: 10.1142/S0217751X11053195

World Scientific
www.worldscientific.com

S-CODE FOR FIXED FIELD ALTERNATING GRADIENT ACCELERATOR DESIGN AND PARTICLE TRACKING

SHINJI MACHIDA

ASTeC, STFC Rutherford Appleton Laboratory,
Harwell Science and Innovation Campus,
Didcot, Oxfordshire, OX11 0QX, UK
shinji.machida@stfc.ac.uk

The constant field nature of a fixed field alternating gradient (FFAG) accelerator requires a modeling which separates the layout of accelerator elements from the geometry of beam orbits. A new code, named s-code, is made to design an FFAG accelerator and to track a beam in it. We will describe the model of accelerator elements and the way to integrate the equation of motion of a particle.

Keywords: Fixed field alternating gradient (FFAG); particle tracking code; kick and drift.

PACS numbers: 29.27.-a, 41.85.-p

1. Introduction

A design code for a synchrotron assumes an ideal orbit which goes through the center of focusing magnets. As the strength of all the magnetic elements synchronizes with the beam momentum, the orbit and the focal length become independent of beam momentum. Therefore, the curvature ρ and the normalized field gradient $K = \frac{B'L}{B\rho}$, where B' is the field gradient, L is the length and $B\rho$ is the magnetic rigidity, are used to calculate beam orbit and optics instead of the absolute bending field and field gradient. One does not have to know the exact momentum range to design a synchrotron at the beginning.

A fixed field alternating gradient (FFAG) accelerator, on the other hand, uses a constant field independent of beam momentum so that orbits move radially and focal length is not constant when a beam is accelerated.[1–2] In fact, the transverse tune still becomes independent of momentum by using a magnet whose field profile has a form of r^k, where r is the radial coordinate and $k = \frac{r}{B}\frac{dB}{dr}$ is a constant called field index, and whose entrance and exit face sit along a radial line. This type of FFAG is called a scaling FFAG, where all the orbits become isomorphic and the focal length becomes proportional to the average radius. In this type of FFAG, once we calculate orbit and optics at a certain momentum, they can be scaled for an off momentum beam.

This is not the case in a recently proposed linear nonscaling FFAG accelerator.[3–5] It consists of dipoles and quadrupoles. The closed orbit shape is no longer isomorphic as momentum changes although the orbit shift is minimized by an extremely small dispersion function. The phase advance per cell moves from just below 180 degree at the lowest momentum to 10 to 20 degree at the highest one.

In either a scaling or a nonscaling FFAG, a layout of magnets does not specify a geometry of beam orbits. A closed orbit should be found only after tracking a particle with various initial conditions. The optics is then calculated taking into account the magnetic gradient along the closed orbit. It follows that the design approach is different from that for a synchrotron.

In order to realize this new approach in practice, a design code for a synchrotron is not useful. Although it is still possible to model a nonscaling FFAG with a synchrotron design code such as MAD,[6] the results are not accurate for the whole momentum range.[7] The only exceptions are Zgoubi[8] and PTC.[9] Both can be used to design a synchrotron as well as a FFAG accelerator because the separation of the layout of magnets from the geometry of beam orbits is implemented. PTC, however, does not support an option of magnetic element whose field profile is r^k.

We made a new design and particle tracking code specifically for an FFAG accelerator named s-code. It has models of all the magnetic elements needed to design a variety of FFAG accelerators. Using a kick and drift integration method, a particle is tracked through the lattice elements. After a closed orbit is found iteratively, optics parameters are extracted from a particle tracking. A single particle tracking as well as a multi particle tracking with some distributions can be performed. In this paper, we first explain the code structure. We will then show a couple of commands to design an FFAG accelerator and to track a particle or a beam. Some examples using the code will be demonstrated.

2. Code Structure

2.1. *Coordinate system*

First, all the accelerator elements are positioned in a plane. At this point, we do not know where the beam orbit is although it should be around each element. The coordinate system is defined such that the center of the first element should be positioned at the origin of the Cartesian coordinate system and a beam moves roughly toward the x direction. The center position of the second element is specified relative to the first element by the distance and the angle with respect to the x axis. The center position of the third element is also specified relative to the second element by the distance and the angle, where the angle is with respect to the line between the first and second elements. If it is a ring accelerator, the position of the last element, usually it is a marker, coincides with that of the first element. The coordinate system in which the center of each element is defined is named global coordinates.

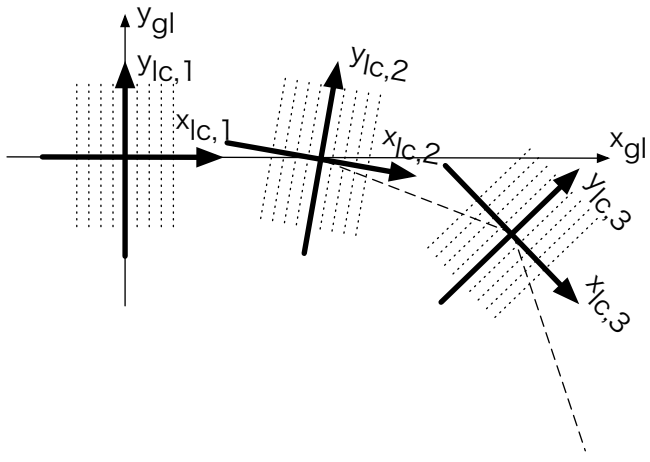

Fig. 1. Global and local coordinate systems. Global coordinates (x_{gl}, y_{gl}) specify the center of each element. Each element has its own local coordinates ($x_{lc,n}$, $y_{lc,n}$).

With respect to the center position of each element, it is convenient to define another coordinate system in which properties of an element like field strength as a function of position are defined. This is known as the local coordinate system. Depending on the physical shape of an element and the way element properties are defined, local coordinate system is either Cartesian or cylindrical. In each local coordinate system attached to an element, the y axis of the Cartesian system or the r axis of the cylindrical system becomes the horizontal direction, the z axis of the Cartesian or cylindrical system becomes the vertical direction and the x axis of the Cartesian system or the θ axis of the cylindrical system becomes the longitudinal direction. As a default, local coordinates are rotated with respect to the z axis such that the entrance angle and the exit angle become equal as shown in Fig. 1.

Shift and rotation of an element as well as that due to alignment errors can be included as shift and rotation of local coordinates with respect to the points in global coordinates where the origin of local coordinates is initially defined.

2.2. *Description of elements*

An element is defined in local coordinates and the equation of motion of a particle is integrated. The following elements are currently supported: rectangular shaped quadrupole, wedge shaped scaling FFAG magnet with and without multipole expansion, rectangular shaped scaling FFAG magnet with and without multipole expansion, rf cavity, beam position monitor and marker. The local coordinate system includes the fringe region of an element as well as the body region as shown in Fig. 2.

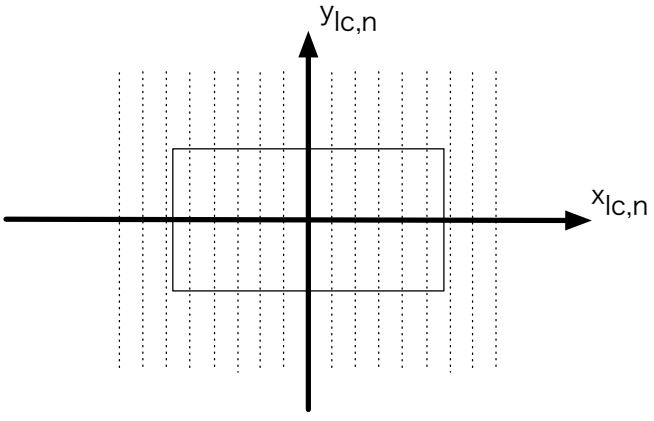

Fig. 2. A lattice element indicated by the rectangular shape. Properties of the element are defined at the dashed line in the local coordinate system, so that the fringe field region is also included.

2.2.1. *Quadrupole*

The magnetic field of an m^{th} multipole is derived from the scalar potential in cylindrical coordinates[10]

$$P_m(r,\theta,z) = \frac{r^m \sin m\theta}{m!} G_m(r,z),$$

where

$$G_m(r,z) = \sum_{p=0}^{\infty} G_{m,2p}(z) r^{2p}$$

and

$$G_{m,2p(p>0)}(z) = (-1)^p \frac{m!}{4^p (m+p)! p!} \frac{d^{2p} G_{m,0}}{dz^{2p}}.$$

In this cylindrical coordinate system, (r,θ) is the transverse direction and z is the longitudinal one.

For a quadrupole ($m = 2$)

$$P_2(r,\theta,z) = \frac{r^2 \sin 2\theta}{2} [G_{2,0}(z) + G_{2,2}(z) r^2 + \ldots],$$

where

$$G_{2,2p}(z) = (-1)^p \frac{2}{4^p (2+p)! p!} \frac{d^{2p} G_{2,0}(z)}{dz^{2p}}. \tag{1}$$

The three magnetic field components in cylindrical coordinates are

$$B_r(r,\theta,z) = \frac{\partial P_2}{\partial r} = \sin 2\theta \left[G_{2,0}(z)r + G_{2,2}(z)r^3 + \ldots\right],$$
$$B_\theta(r,\theta,z) = \frac{1}{r}\frac{\partial P_2}{\partial \theta} = \cos 2\theta \left[G_{2,0}(z)r + G_{2,2}(z)r^3 + \ldots\right],$$
$$B_z(r,\theta,z) = \frac{\partial P_2}{\partial z} = \frac{\sin 2\theta}{2}\left[\frac{\partial G_{2,0}}{\partial z}r^2 + \frac{\partial G_{2,2}}{\partial z}r^4 + \ldots\right].$$

From the cylindrical components, the ones in Cartesian local coordinates are simply obtained:

$$B_x = B_z,$$
$$B_y = B_r\cos\theta - B_\theta \sin\theta,$$
$$B_z = B_r\sin\theta + B_\theta\cos\theta.$$

As $G_{2,0}(z)$ we take the Enge function[11]

$$G_{2,0}(z) = \frac{G_0}{1+\exp\left[\sum_{i=0}^{5} C_i(s/g)^i\right]},$$

where G_0 is the strength of a quadrupole, $s = z - z_0$ is the distance from the hard edge boundary z_0; g is the scaling parameter of the order of the gap, and C_i are the Enge coefficients which are $C_0 = 0.1455$, $C_1 = 2.267$, $C_2 = -0.6395$, $C_3 = 1.1558$ and $C_4 = C_5 = 0$. The code at the moment takes the term up to $G_{2,1}$ as a default, but the higher order terms calculated in Eq. (1) can be included as an option.

2.2.2. *Rectangular shaped scaling FFAG magnet*

Another way to describe magnetic fields is to expand the fields in terms of the distance from the median plane. In Cartesian coordinates,

$$B_x = B_{x0}(x,y) + B_{x1}(x,y)z + B_{x2}(x,y)z^2 + \ldots,$$
$$B_y = B_{y0}(x,y) + B_{y1}(x,y)z + B_{y2}(x,y)z^2 + \ldots,$$
$$B_z = B_{z0}(x,y) + B_{z1}(x,y)z + B_{z2}(x,y)z^2 + \ldots.$$

To satisfy Maxwell equations

$$\mathrm{div}\mathbf{B} = \frac{\partial B_x}{\partial x} + \frac{\partial B_y}{\partial y} + \frac{\partial B_z}{\partial z} = 0,$$
$$\mathrm{rot}\mathbf{B} = \left(\frac{\partial B_z}{\partial y} - \frac{\partial B_y}{\partial z}, \frac{\partial B_x}{\partial z} - \frac{\partial B_z}{\partial x}, \frac{\partial B_y}{\partial x} - \frac{\partial B_x}{\partial y}\right) = 0,$$

with the boundary conditions

$$B_{x0}(x,y) = 0,$$
$$B_{y0}(x,y) = 0,$$
$$B_{z0}(x,y) = B_0\left(\frac{y}{y_0}\right)^k G(x),$$

where $G(x)$ is the Enge function defined similarly to $G_{2,0}(z)$:

$$G(x) = \frac{G_0}{1 + \exp\left[\sum_{i=0}^{5} C_i((x - x_0)/g)^i\right]},$$

B_{x0}, B_{y0}, B_{z0}, B_{x1}, B_{y1}, B_{z1}, B_{x2}, B_{y2}, $B_{z2}, \ldots$ are obtained iteratively. It is easy to see that $B_{x2n} = B_{y2n} = B_{z(2n+1)} = 0$, where n is an integer.

To model a rectangular shaped scaling FFAG magnet with multipole expansion, the boundary conditions are slightly altered

$$\begin{aligned}
&B_{x0}(x, y) = 0,\\
&B_{y0}(x, y) = 0,\\
&B_{z0}(x, y) = B_0 \left(1 + \sum_{m=1}^{m_{max}} \frac{k(k-1)\ldots(k-m+1)}{m! y_0^m}(y - y_0)^m\right) G(x).
\end{aligned}$$

2.2.3. *Wedge shaped scaling FFAG magnet*

Magnetic fields of a wedge shaped scaling FFAG magnet are calculated in the similar way in cylindrical coordinates,

$$\begin{aligned}
B_r &= B_{r0}(r, \theta) + B_{r1}(r, \theta)z + B_{r2}(r, \theta)z^2 + \ldots,\\
B_\theta &= B_{\theta 0}(r, \theta) + B_{\theta 1}(r, \theta)z + B_{\theta 2}(r, \theta)z^2 + \ldots,\\
B_z &= B_{z0}(r, \theta) + B_{z1}(r, \theta)z + B_{z2}(r, \theta)z^2 + \ldots.
\end{aligned}$$

To satisfy Maxwell equations

$$\begin{aligned}
\mathrm{div}\mathbf{B} &= \frac{1}{r}\frac{\partial(rB_r)}{\partial r} + \frac{1}{r}\frac{\partial B_\theta}{\partial \theta} + \frac{\partial B_z}{\partial z} = 0,\\
\mathrm{rot}\mathbf{B} &= \left(\frac{1}{r}\frac{\partial B_z}{\partial \theta} - \frac{\partial B_\theta}{\partial z}, \frac{\partial B_r}{\partial z} - \frac{\partial B_z}{\partial r}, \frac{1}{r}\left[\frac{\partial(rB_\theta)}{\partial r} - \frac{\partial B_r}{\partial \theta}\right]\right) = 0
\end{aligned}$$

with boundary conditions

$$\begin{aligned}
&B_{r0}(r, \theta) = 0,\\
&B_{\theta 0}(r, \theta) = 0,\\
&B_{z0}(r, \theta) = B_0 \left(\frac{r}{r_0}\right)^k G(\theta),
\end{aligned}$$

B_{r0}, $B_{\theta 0}$, B_{z0}, B_{r1}, $B_{\theta 1}$, B_{z1}, B_{r2}, $B_{\theta 2}$, $B_{z2}, \ldots$ are iteratively obtained. It is easy to see that $B_{r2n} = B_{\theta 2n} = B_{z(2n+1)} = 0$, where n is an integer.

It is not always the case that the extent of the fringe field is parameterized only by θ. In a scaling FFAG whose magnetic field profile is created by gap shaping, for example, the extent of the fringe field is shorter as radius increases. The extent can be a function of radius as well.

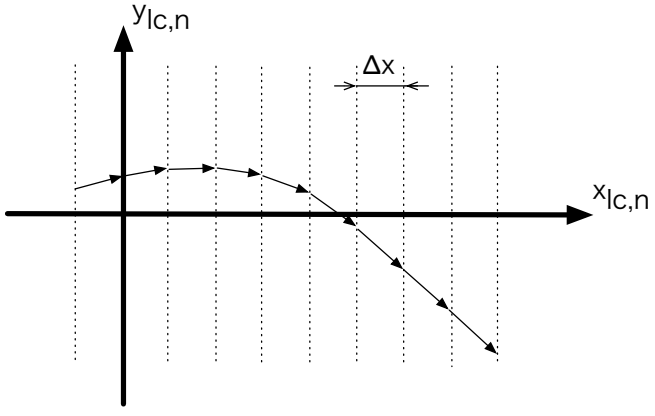

Fig. 3. At each slice, a particle gets a momentum kick. Between slices, a particle goes straight.

2.2.4. *Rf cavity*

At the moment, an rf cavity is modeled in a simple way. It gives a longitudinal energy gain or loss depending on the rf phase. There is an option which gives constant energy gain or loss to simulate acceleration by induction units.

2.3. *Integration of motion*

Once we know the electric and magnetic fields of the elements, we can integrate the equation of motion. Each element has its own local coordinates and the integration is done on that space. There is no overlap with the neighboring local coordinates. At the beginning of a particle tracking, the 6-D particle positions (three positions and three momenta) of a beam generated in the global coordinates are converted to the 6-D positions in the first local coordinates. After integration of motion with the non-zero electric and magnetic field in local coordinates, the 6-D positions are converted back to global coordinates.

The integration is done by a kick and drift method as shown in Fig. 3. We prepare many slices perpendicular to the x axis in Cartesian coordinates or to the θ axis in cylindrical coordinates.

When a particle goes through the slices where the magnetic field is not zero, its momenta are updated as

$$
\begin{aligned}
p_{y,new} &= p_{y,old} + e(\frac{p_{z,old}}{p_{x,old}} B_x - B_z)\Delta x, \\
p_{z,new} &= p_{z,old} + e(B_y - \frac{p_{y,old}}{p_{x,old}} B_x)\Delta x, \\
p_{x,new} &= \sqrt{p_{x,old}^2 + p_{y,old}^2 + p_{z,old}^2 - p_{y,new}^2 - p_{z,new}^2},
\end{aligned}
$$

where Δx is the distance between the slices.

When a particle goes through the slices where the electric field is not zero, its momenta are updated as

$$\begin{aligned} p_{y,new} &= p_{y,old}, \\ p_{z,new} &= p_{z,old}, \\ p_{x,new} &= \sqrt{p_{x,old}^2 + E_{new}^2 - E_{old}^2}, \end{aligned}$$

where E_{old} and $E_{new} = E_{old} + \Delta E$ is the total energy before and after the element with an energy gain of ΔE. We assume that the electric field only gives an energy gain in the x (longitudinal) direction.

A motion between the slices draws a straight line so that the coordinates are updated as

$$\begin{aligned} y_{new} &= y_{old} + \frac{p_y}{p_x}\Delta x, \\ z_{new} &= z_{old} + \frac{p_z}{p_x}\Delta x, \\ x_{new} &= x_{old} + \Delta x. \end{aligned}$$

The independent variable is time in the code. Depending on its velocity, a particle reaches some position between slices. At each time step, particle coordinates of a beam are distributed in longitudinal as well as transverse direction which makes a snapshot picture.

The number of slices for each element is normally about 1000 or more to ensure that the integration results do not depend on the number of slices.

3. Commands

The code has several commands to design a lattice and to track a particle. More specifically, defining initial particle distribution, finding a closed orbit, calculating Twiss parameters, tracking many particles, etc, are available as commands.

3.1. *Twiss*

Twiss command finds a closed orbit if there is a periodic boundary condition or an orbit starting with the initial coordinates if not. After finding a closed orbit, the command finds lattice functions (Twiss parameters) and a dispersion function which satisfy a periodic boundary condition. There is an option which propagates lattice functions from the initial values if there is no periodic condition.

A closed orbit is found iteratively. Starting with an initial guess, the code tracks a single particle for the specified section. The distance between the initial coordinates and the final one in the 4-D transverse space is calculated and the initial coordinates are reset to minimize the difference. This process is repeated until the distance is below an user specified value.

The lattice and dispersion functions are calculated by a particle tracking as well. A set of particles which have small amplitude in each direction from the closed orbit

are tracked. With the initial and final coordinates, all the elements of the transfer matrix which describes the specified section are derived. The lattice and dispersion functions everywhere are calculated by propagating them from a point where the transfer matrix is obtained.

3.2. *Track*

Either a single particle or a bunch of particle (a beam) can be tracked. Two typical examples are dynamic aperture survey and a study of emittance growth. For dynamic aperture survey, a particle whose 6-D initial particle positions are specified is tracked through a section or a ring many times. If the particle's transverse amplitude becomes larger than the criterion one specifies, say 1 m, one regards the particle as lost. A particle with smaller initial amplitude is tracked again to check whether it goes through. On the other hand, if the particle goes through to the end, a particle with larger initial amplitude is tracked.

Another type of tracking is a tracking of a beam. The rms emittance, particle distribution and the number of particles are specified. With a random number generator, 6-D initial particle positions of those particles are calculated. The initial particle distribution can be a Gaussian, Waterbag, or KV distribution in the transverse 4-D space. In this type of tracking, we are interested in the evolution of statistical values such as the center of particle distribution, rms emittance and momentum spread. The fraction of beam loss is recorded during a tracking.

4. Examples

As examples of the application of the code, design and particle tracking of a linear nonscaling FFAG, a scaling FFAG and an FFAG beam transport line will be shown.

4.1. *Linear nonscaling FFAG*

A linear nonscaling FFAG is designed as the main muon accelerator of a neutrino factory. It accelerates a muon from 12.5 GeV to 25 GeV in about 10 turns. In order to accept the huge muon emittance, 30π mm rad normalized, the lattice magnets do not have any nonlinear components. As a result, orbit shape as well as an average orbit radius change when a beam is accelerated as shown in Fig. 4. The transverse cell tune just below 0.4 at injection becomes around 0.1 after acceleration as shown in Fig. 5. The whole ring consists of many simple triplet focusing cells, which should eliminates resonance crossing of integer and half-integer systematic resonances. Since there is no time to modulate rf frequency, the so-called serpentine acceleration which uses a path outside of rf bucket in longitudinal phase space is employed as shown in Fig. 6.

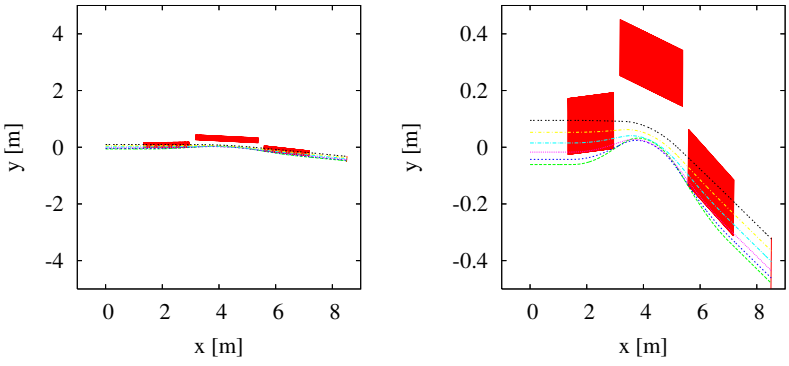

Fig. 4. Element and orbits in a unit cell. Three red rectangular shape shows triplet focusing magnets including fringe field area. Orbits are drawn every 2.5 GeV from 12.5 GeV to 25.0 GeV. (left) properly scaled view and (right) magnified view in horizontal direction.

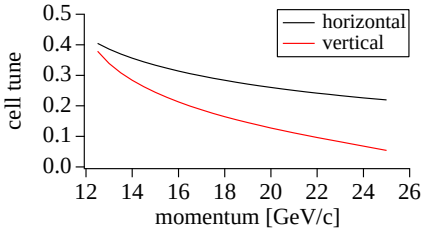

Fig. 5. Transverse cell tune during acceleration.

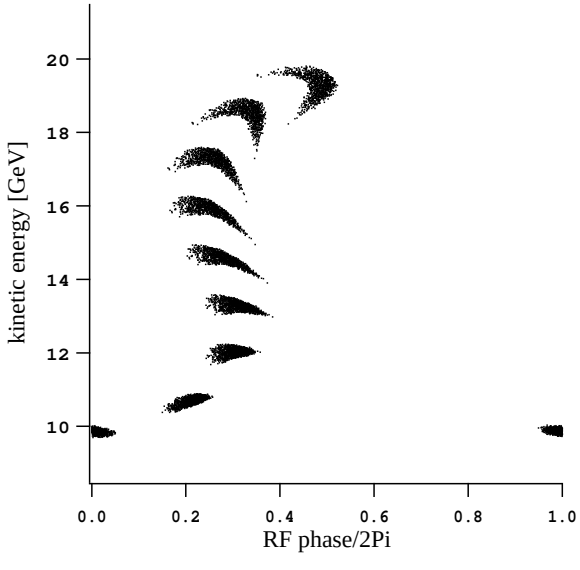

Fig. 6. Bunch shape in longitudinal phase space by serpentine acceleration. This is a result based on a previous baseline lattice where a muon is accelerated from 10 GeV to 20 GeV. See Ref. 12.

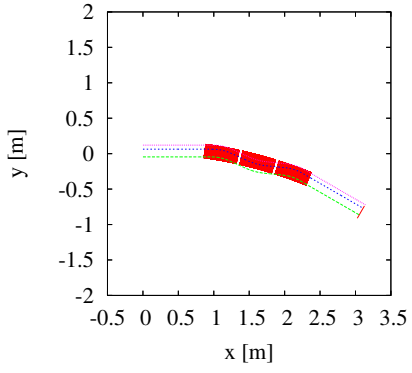

Fig. 7. Three red wedge shape shows triplet focusing magnets including fringe field area. Three orbit lines correspond to 0.243, 0.5, 0.729 GeV/c from inside.

4.2. *Scaling FFAG*

The repetition rate of an FFAG accelerator is only determined by the available rf voltage. As proton and carbon accelerator for particle therapy, a FFAG has the potential of 1 kHz operation which enables the spot scanning. Although a nonscaling FFAG has shorter orbit shift during acceleration and therefore a smaller lattice magnet, it will inevitably have emittance growth and beam loss when the acceleration takes more than 100 turns due to a resonance crossing.[13] A scaling FFAG or a nonlinear nonscaling FFAG[14] is a reasonable choice for a particle therapy accelerator. Figure 7 shows the triplet focusing magnets and orbits for a 250 MeV proton scaling FFAG. In this design, the operation point in the second stability region as shown in Fig. 8 is used so that the orbit shift from 31 MeV to 250 MeV is about five times smaller than an ordinary scaling FFAG.

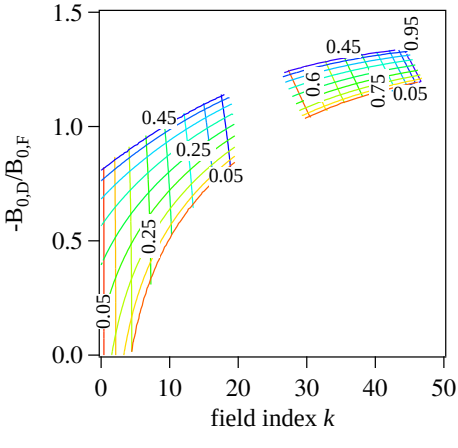

Fig. 8. From Ref. 15. Stability diagram shows two stability regions. Upright numbers indicate vertical cell tune and vertically aligned numbers indicate horizontal cell tune. Line are drawn with 0.05 step. We use the region on the right.

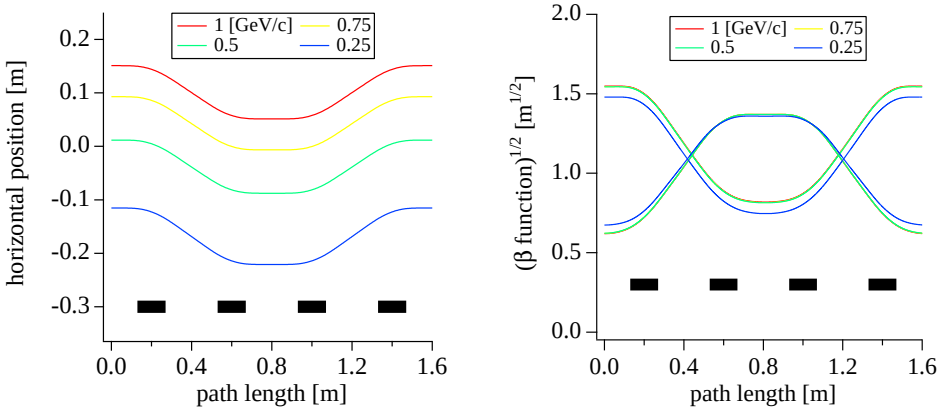

Fig. 9. From Ref. 17. (left) Different momentum orbits in a unit cell which satisfy the periodic boundary condition. Rectangles at the bottom show the position of FDDF magnets. (right) Beta functions with different momenta in a unit cell.

4.3. *FFAG beam transport line*

A concept of FFAG optics can be applied to a beam transport line as well as a ring accelerator. In particular, it is useful as a beam transport line between an FFAG accelerator for particle therapy and gantry where a beam momentum may change pulse by pulse with as much as 1 kHz repetition. Adjustment of magnetic strength for different momentum is not possible. An FFAG beam transport line can be designed as the limit of large curvature of a ring. In the limit,[16] the magnetic field profile is represented more appropriately by $\exp(kr/\rho)$ instead of r^k. Figure 9 shows a layout of FDDF focusing unit with orbits of different momentum. With cells of doubled k and phase advance of 180 degrees, the dispersion suppressor can be designed as shown in Fig. 10.

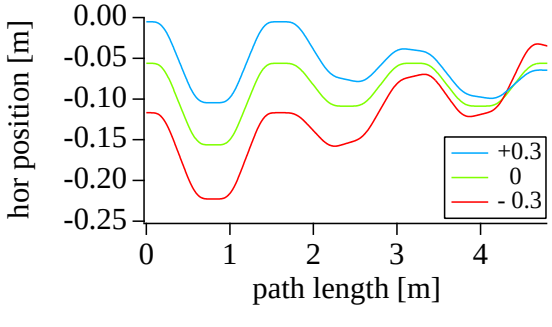

Fig. 10. From Ref. 17. Different momentum orbits in a normal cell and the dispersion suppressor. Numbers in legend show the momentum deviation from the reference momentum. Normal cell is from 0 to 1.6 m and dispersion suppressor section from 1.6 to 4.8 m.

5. Summary

A design and particle tracking code specifically for an FFAG accelerator has been written. The separation of layout of accelerator elements and geometry of beam orbits is essential feature to model an FFAG. Accelerator elements are positioned in the global coordinates and an equation of motion is integrated in the local coordinates which are attached to each element. Dipole and quadrupole magnets are included to design a linear nonscaling FFAG. Wedge shaped and rectangular shaped magnets which has a field profile of r^k or a truncated expansion of the scaling field are included to design a scaling and a nonlinear nonscaling FFAG. The same tools are used to design an FFAG beam transport line including the dispersion suppressor at the end. A simple model of rf cavity makes it possible to simulate acceleration. The integration of motion adopts a kick and drift method. A closed orbit as well as lattice functions are calculated by the particle tracking. Some examples using the code are demonstrated.

Acknowledgments

The work is supported by the UK Neutrino Factory/Particle Physics and Astronomy Research Council (PPARC) under Contract No. 2054. We would like to thank Drs. C. R. Prior, G. H. Rees, Y. Mori, S. Ohnuma, S. J. Brooks and D. J. Kelliher for their fruitful discussions and continuous encouragement.

References

1. K. R. Symon, D. W. Kerst, L. W. Jones, L. J. Laslett and K. M. Terwillinger, *Phys. Rev.* **103**, 1837 (1956).
2. A. A. Kolomensky and A. N. Lebedev, *Theory of Cyclic Accelerators* (North-Holland, Amsterdam, 1966), p. 337.
3. C. Johnstone, W. Wan and A. Garren, in *Proc. of the 1999 Particle Accelerator Conference* (IEEE, New York, 1999), p. 3068.
4. E. Keil and A. M. Sessler, *Nucl. Instrum. Methods Phys. Res.* Sect. A **538**, 159 (2005).
5. D. Trbojevic, E. D. Courant and M. Blaskiewicz, *Phys. Rev. ST Accel. Beams* **8**, 050101 (2005).
6. MAD-X Home Page, http://mad.web.cern.ch/mad/.
7. E. D. Courant, S. J. Berg and D. Trbojevic, in *Proc. of the 2003 Particle Accelerator Conference* (IEEE, Portland, 2003), p. 3485.
8. F. Meot, *Nucl. Instrum. Methods Phys. Res.* Sect. A **427**, 353 (1999).
9. E. Forest, F. Schmidt and E. Mcintosh, KEK Report 2002-3, July 2002.
10. M. Bassetti and C. Biscari, *Particle Accelerators*, **52**, 221 (1996).
11. H. A. Enge, *Focusing of Charged Particles*, vol. 2, ed. by A. Spetier (Academic Press, New York, 1967), p. 203.
12. S. Machida, *Phys. Rev. ST Accel. Beams* **9**, 104002 (2006).
13. S. Machida, *Phys. Rev. ST Accel. Beams* **11**, 094003 (2008).
14. S. L. Sheehy, K. J. Peach, H. Witte, D. J. Kelliher and S. Machida, to appear in *Phys. Rev. ST Accel. Beams.*
15. S. Machida, *Phys. Rev. Lett.* **103**, 164801 (2009).
16. Y. Mori, T. Uesugi, T. Planche and J. B. Lagrange, *private communications.*
17. S. Machida, to appear in *Phys. Rev. ST Accel. Beams.*

International Journal of Modern Physics A
Vol. 26, Nos. 10 & 11 (2011) 1807–1821

DOI: 10.1142/S0217751X11053201

World Scientific
www.worldscientific.com

HIGH-ORDER OUT-OF-PLANE EXPANSION FOR 3D FIELDS

K. MAKINO* and M. BERZ
Department of Physics and Astronomy, Michigan State University, East Lansing, MI 48824, USA
**makino@msu.edu*

C. JOHNSTONE
Fermilab, Batavia, IL 60510, USA

The precise determination of the dynamics in accelerators with complicated field arrangements such as Fixed Field Alternating Gradient accelerators (FFAG) depends critically on the ability to describe the appearing magnetic fields in full 3D. However, frequently measurements or models of FFAG fields postulate their behavior in the midplane only, and rely on the fact that this midplane field and its derivatives determine the field in all of space. The detailed knowledge of the resulting out-of-plane fields is critical for a careful assessment of the vertical dynamics.

We describe a method based on the differential algebraic (DA) approach to obtain the resulting out-of-plane expansions to any order in an order-independent, straightforward fashion. In particular, the resulting fields satisfy Maxwell's equations to the order of the expansion up to machine precision errors, and without any inaccuracies that can arise from conventional divided difference or finite element schemes for the computation of out-of-plane fields.

The method relies on re-writing the underlying PDE as a fixed point problem involving DA operations, and in particular the differential algebraic integration operator. We illustrate the performance of the method for a variety of practical examples, and obtain estimates for the orders necessary to describe the fields to a prescribed accuracy.

1. Introduction

The differential algebraic (DA) methods[1,2] allow the efficient computation and manipulation of high-order Taylor transfer maps. When integrating transfer maps through electromagnetic fields, the full 3D fields are computed as part of each integration time step using DA PDE (partial differential equation) solvers. First, we address the mechanism of the method of DA fixed point PDE solvers, and as will be seen, the method is very compact and fast, and only requires an analytic representation of the field in the midplane.

Compared to multipole electromagnetic elements such as dipoles, quadrupoles and so forth, the fringe fields in FFAGs and related accelerators are dominating and extend for relatively long distance. After developing the theoretical background, we study the practical performance of the method to illustrate the quality of the

out-of-plane expansions for various examples, including a model of a dipole field with known 3D field, as well as models of FFAG fringe fields based on Enge function field falloff as implemented in the FFAG simulation tool FACT Particularly because of this long extension of the fringe fields, in practice it is important to be able to efficiently combine the fields of all poles together, and then hand the total midplane field to the DA PDE solvers.

2. High-Order Derivatives of Fields

The idea of differential algebraic (DA) methods[1–3] is based on the observation that it is possible to extract more information about a function than its mere values on computers. One can introduce an operation T denoting the extraction of the Taylor coefficients of a pre-specified order n of the function $f \in C^n(R^v)$. In mathematical terms, T is an equivalence relation, and the application of T corresponds to the transition from the function f to the equivalence class $[f]$ comprising all those functions with identical Taylor expansion in v variables to order n; the classes are apparently characterized by the collection of Taylor coefficients. Since Taylor coefficients of order n for sums and products of functions as well as scalar products with reals can be computed from those of the summands and factors, the set of equivalence classes of functions can be endowed with well-defined operations, leading to the so-called Truncated Power Series Algebra (TPSA).[4,5] More advanced tools address the composition of functions, their inversion, solutions of implicit equations, and the introduction of common elementary functions.[1] For treatment of ODEs and PDEs, the power of TPSA can be enhanced by the introduction of derivations ∂ and their inverses ∂^{-1}, corresponding to the differentiation and integration on the space of functions, resulting in the Differential Algebra ${}_nD_v$. This structure allows the direct treatment of many questions connected with differentiation and integration of functions, including the solution of the ODEs $d\vec{x}/dt = \vec{f}(\vec{x}, t)$ describing the motion and PDEs describing the fields,[6–8] and will be the key ingredient for the computation of out-of-plane fields as discussed in the next section.

High-order out-of-plane expansions can be done via recursion formulas (see Refs. 1, 9–11 and references therein) and require the higher derivatives of the field falloff. One of the simplest applications of the DA method is to compute these derivatives accurately. To illustrate the behavior of the method of computing derivatives of very high orders, we show the results of the computation of one-dimensional derivatives of a common ingredient in the analytic description of the falloff of midplane fields in the vicinity of the edge of the magnet, the so-called Enge function

$$E(s) = \frac{1}{1 + \exp(a_0 + a_1(s/d) + ... + a_k(s/d)^k}, \tag{1}$$

where s is the distance to the magnet, the coefficients a_0 to a_k describe the shape of the falloff, and the d is a scaling factor describing the half gap of the magnet

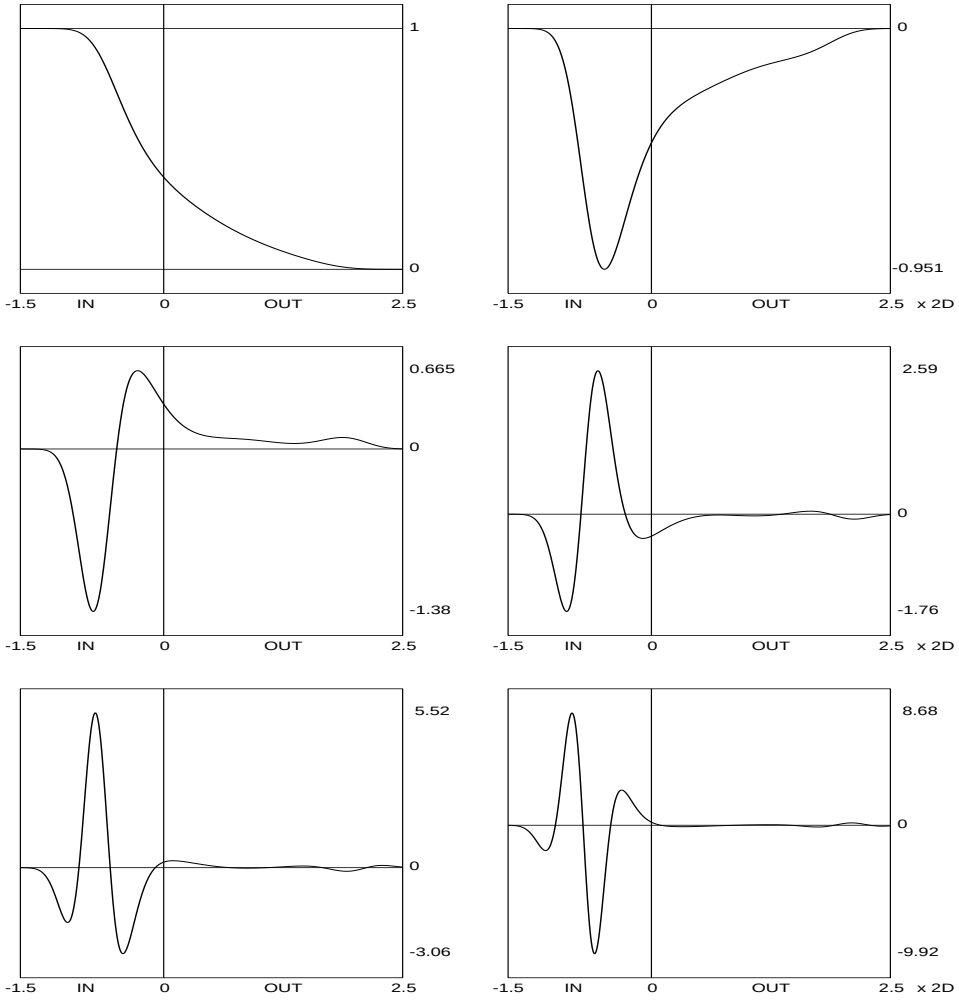

Fig. 1. Fringe field falloff profile of the COSY default model for magnetic dipoles, and derivatives 1 through 5.

at the edge. The code COSY INFINITY contains a library of default coefficients for common particle optical elements,[12] but for specific devices, it is important to determine the most suitable values of the coefficients.

In order to determine the high-order derivatives of the Enge function necessary for the out-of-plane expansion discussed later, it is merely required to evaluate the expression of the Enge function (1) using DA arithmetic with the variable s being one of the DA variables. To illustrate this feature, we show the field falloff profile of the default model for magnetic quadrupoles in COSY INFINITY, and their derivatives up to order five in Fig. 1, and to show that the orders do not represent a limitation, orders 10, 20, and 30 in Fig. 2.

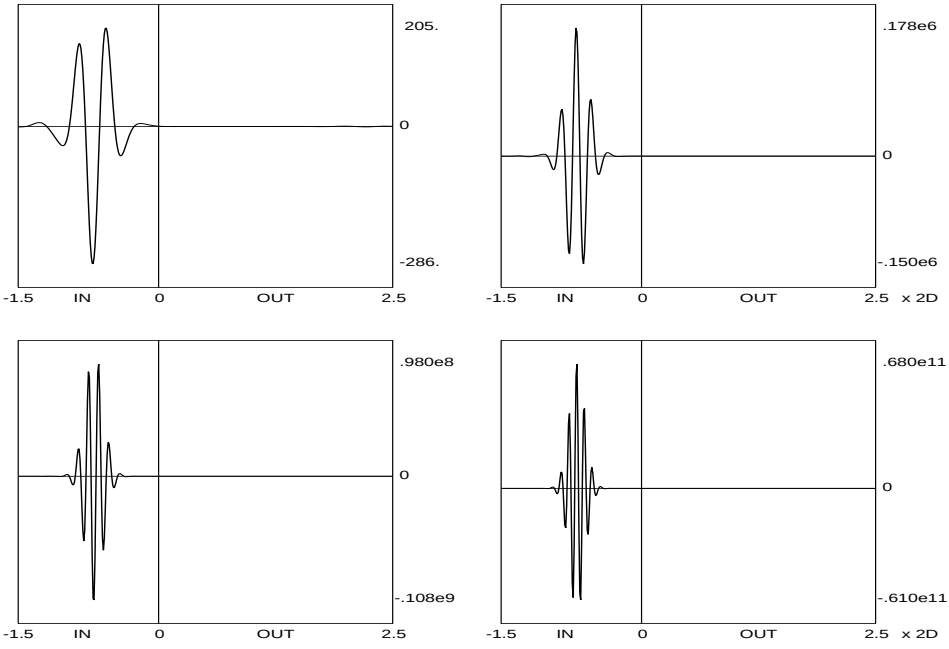

Fig. 2. Fringe field falloff of the COSY default model for magnetic dipoles, derivatives 10, 20, 30, and 40.

The figures illustrate the ease with which it is possible to obtain derivatives to very high orders using DA methods. Furthermore, different from conventional numerical differentiation schemes, the values are accurate to mere round-off error and are close to machine precision, which manifests itself in the absence of any apparent noise in the representation of the higher derivatives.

3. DA Fixed Point PDE Solvers

As discussed in the previous section, for the treatment of ODEs and PDEs, the power of TPSA can benefits from the introduction of derivations ∂ and their inverses ∂^{-1}, corresponding to the differentiation and integration on the space of functions, resulting in the Differential Algebra ${}_nD_v$. This structure allows the direct treatment of many questions connected with differentiation and integration of functions, including the solution of the ODEs $d\vec{x}/dt = \vec{f}(\vec{x}, t)$ describing the motion and PDEs describing the fields.[3]

For any element $[f] \in {}_nD_v$ we define the depth $\lambda([f])$ as

$$\lambda([f]) = \begin{cases} \text{Order of the first nonvanishing derivative of } f & \text{if } [f] \neq 0 \\ n+1 & \text{if } [f] = 0 \end{cases}.$$

In particular, any function f that does not vanish at the origin has $\lambda([f]) = 0$.

Let $\mathcal{O}$ be an operator on the set $M \subset {}_nD_v^m$, where ${}_nD_v^m$ is the set describing vector functions $\vec{f} = (f_1, ..., f_m)$ from R^v to R^m. Then we say that $\mathcal{O}$ is contracting on M if for any $\vec{a}$, $\vec{b} \in M$ with $\vec{a} \neq \vec{b}$,

$$\lambda(\mathcal{O}(\vec{a}) - \mathcal{O}(\vec{b})) > \lambda(\vec{a} - \vec{b}).$$

In practical terms this means that after application of $\mathcal{O}$, the derivatives in $\vec{a}$ and $\vec{b}$ agree to a higher order than before application of $\mathcal{O}$. For example, the anti-derivation ∂_k^{-1} is a contracting operator. Contracting operators satisfy a fixed point theorem:

Theorem 3.1. *(DA Fixed Point Theorem) Let $\mathcal{O}$ be a contracting operator on $M \subset {}_nD_v$ that maps M into M. Then $\mathcal{O}$ has a unique fixed point $a \in M$ that satisfies the fixed point problem $a = \mathcal{O}(a)$. Moreover, let a_0 be any element in M. Then the sequence $a_k = \mathcal{O}(a_{k-1})$ for $k = 1, 2, ...$ converges in finitely many steps (in fact, at most $(n + 1)$ steps) to the fixed point a.*

The fixed point theorem is of great practical usefulness since it assures the existence of a solution, and moreover allows its exact determination in a very simple way in finitely many steps. The proof of the theorem can be found in.[1] The DA fixed point theorem has many useful applications, in particular a rather straightforward solution of ODEs and PDEs.[3]

The direct availability of the derivation ∂ and its inverse ∂^{-1} allows to devise efficient numerical PDE solvers of any order. The DA fixed point theorem allows one to solve PDEs iteratively in finitely many steps by rephrasing them in terms of a fixed point problem. The details depend on the PDE at hand, but the key idea is to eliminate differentiation with respect to one variable and replace it by integration. As an example, consider a rather general PDE

$$a_1 \frac{\partial}{\partial x}\left(a_2 \frac{\partial}{\partial x} V\right) + b_1 \frac{\partial}{\partial y}\left(b_2 \frac{\partial}{\partial y} V\right) + c_1 \frac{\partial}{\partial z}\left(c_2 \frac{\partial}{\partial z} V\right) = 0,$$

where a_1, a_2, b_1, b_2, c_1 c_2 are functions of x, y, z. The PDE is re-written as

$$V = V|_{y=0} + \int_0^y \frac{1}{b_2}\left\{\left(b_2 \frac{\partial V}{\partial y}\right)\Big|_{y=0} - \int_0^y \left[\frac{a_1}{b_1}\frac{\partial}{\partial x}\left(a_2 \frac{\partial V}{\partial x}\right) + \frac{c_1}{b_1}\frac{\partial}{\partial z}\left(c_2 \frac{\partial V}{\partial z}\right)\right] dy\right\} dy\,.$$

The equation is now in fixed point form. Now assume the derivatives of V and $\partial V/\partial y$ with respect to x and z are known in the plane $y = 0$. If the right hand side is contracting with respect to y, the various orders in y can be calculated by mere iteration.

As a particularly important example, consider the Laplace equation. It can be represented in general curvilinear coordinates.[6,8] In the special case of a curvilinear coordinate system, the Laplace equation is obtained as[6,8]

$$\triangle V = \frac{1}{1+hx}\frac{\partial}{\partial x}\left[(1+hx)\frac{\partial V}{\partial x}\right] + \frac{\partial^2 V}{\partial y^2} + \frac{1}{1+hx}\frac{\partial}{\partial s}\left(\frac{1}{1+hx}\frac{\partial V}{\partial s}\right) = 0.$$

In the case of a straight section, where $h = 0$, it reduces to nothing but the Cartesian Laplace equation. The fixed point form of the Laplace equation in the planar curvilinear coordinates is

$$V = V|_{y=0} + \int_0^y \left(\frac{\partial V}{\partial y}\right)\Big|_{y=0} dy - \int_0^y \int_0^y \left\{ \frac{1}{1+hx} \frac{\partial}{\partial x} \left[(1+hx) \frac{\partial V}{\partial x} \right] + \frac{1}{1+hx} \frac{\partial}{\partial s} \left(\frac{1}{1+hx} \frac{\partial V}{\partial s} \right) \right\} dy dy \,.$$

In this form, the right hand side has the interesting property that, regardless of what function V is inserted, the parts not depending on y are reproduced exactly, since all integrals introduce y dependence. Because of the integral operation, for a given choice of x and s and considering only the y dependence, the right hand side is contracting. In COSY INFINITY,[13] the planar curvilinear Laplace equation is solved by the following very compact code:

```
POLD := P ;

HF := 1+H{*}DA(IX) ; HI := 1/HF ;

LOOP I 2 NOC+2 2 ;

P := POLD - INTEG(IY,INTEG(IY, HI{*}( DER(IX,HF{*}DER(IX,P))

+ DER(IS,HI{*}DER(IS,P)) ) )) ;

ENDLOOP ;
```

Here the boundary condition $V|_{y=0} + \int_0^y (\partial V/\partial y)|_{y=0}\, dy$ is provided through the incoming form of `P`, which is obtained using the DA expression in COSY. The DA fixed point iteration converges to the solution potential `P` in finitely many steps. `DA(IX)` represents the identity for x, `NOC` is the current transfer map computation order, and `DER(I,...)` and `INTEG(I,...)` correspond to the DA derivative and the DA anti-derivative operations with respect to the variable specified by the first argument `I`, namely "∂_{x_I}" and "$\int_0^{x_I} dx_I$". The full 3D field is derived from the solution potential `P`, using the elementary DA derivations ∂_x, ∂_y and ∂_s. In coded form, we have

```
BX := DER(IX,P) ; BY := DER(IY,P) ; BZ := DER(IS,P);
```

The advantages of the method are:

- only the field in the midplane is needed;
- the resulting field will always satisfy the stationary Maxwell equations;
- the method works to any order.

Although this is not of primary interest for the computation of fields of FFAGs, we briefly also discuss another important coordinate system, the cylindrical coordinates, in which the Laplace equation takes the simple form

$$\triangle V = \frac{1}{r}\frac{\partial}{\partial r}\left(r\frac{\partial V}{\partial r}\right) + \frac{1}{r^2}\frac{\partial^2 V}{\partial \phi^2} + \frac{\partial^2 V}{\partial s^2} = 0.$$

If V does not depend on ϕ, namely V is rotationally symmetric, as in solenoid magnets, the fixed point form of the Laplace equation is simplified to

$$V = V|_{r=0} - \int_0^r \frac{1}{r}\int_0^r r\,\frac{\partial^2 V}{\partial s^2} dr dr,$$

and the right hand side is contracting with respect to r. Since we are only interested in cases in which $V(s,r)$ is expressed in DA, if $\partial^2 V/\partial s^2$ is nonzero, the integral $\int_0^r r\,\partial^2 V/\partial s^2 dr$ contains r to a positive power. Thus, the factor $1/r$ in the outer integral simply lowers the power of r by one, and the right hand side of the fixed point form can be evaluated in DA without posing trouble. To perform the DA fixed point iteration for the purpose of obtaining the full potential $V(s,r)$, one only needs to prepare the on-axis potential expression $V(s,r)|_{r=0}$ as the boundary condition.

4. Behavior of the Out-of-Plane Expansion for an Analytical Model

In order to assess the ability to utilize the high-order derivatives of the fields in the midplane within the above framework for an out-of-plane expansion, we study a representative example for which an analytical field representation in 3D exists. Specifically, we consider the magnetic field of an arrangement of two rectangular uniformly magnetized iron bars. The bars extend to infinity from the inner surfaces characterized by $y = \pm d$ parallel to the midplane, which is located at $y = 0$. We denote by $x_{1,2}$ and $z_{1,2}$ the horizontal coordinates of the four corners of the magnet, so that the magnetized material of the bars is located inside $x_1 \le x \le x_2$ and $z_1 \le z \le z_2$.

For this bar magnet one can obtain an analytic solution for the magnetic field $\vec{B}\,(x,y,z)$, see for example Refs. 14–16. The fields are given by

$$\begin{aligned}
B_y\,(x,y,z) &= \frac{B_0}{4\pi}\sum_{i,j}(-1)^{i+j}\left[\arctan\left(\frac{X_i\cdot Z_j}{Y_+\cdot R_{ij}^+}\right) + \arctan\left(\frac{X_i\cdot Z_j}{Y_-\cdot R_{ij}^-}\right)\right] \\
B_x\,(x,y,z) &= \frac{B_0}{4\pi}\sum_{i,j}(-1)^{i+j}\left[\ln\left(\frac{Z_j + R_{ij}^-}{Z_j + R_{ij}^+}\right)\right] \\
B_z\,(x,y,z) &= \frac{B_0}{4\pi}\sum_{i,j}(-1)^{i+j}\left[\ln\left(\frac{X_i + R_{ij}^-}{X_i + R_{ij}^+}\right)\right],
\end{aligned} \tag{2}$$

where $X_i = x - x_i$, $Y_\pm = d \pm y$, $Z_i = z - z_i$, and $R_{ij}^\pm = \left(X_i^2 + Z_j^2 + Y_\pm^2\right)^{\frac{1}{2}}$. The geometric layout and midplane field of such a magnet is shown in Fig. 3.

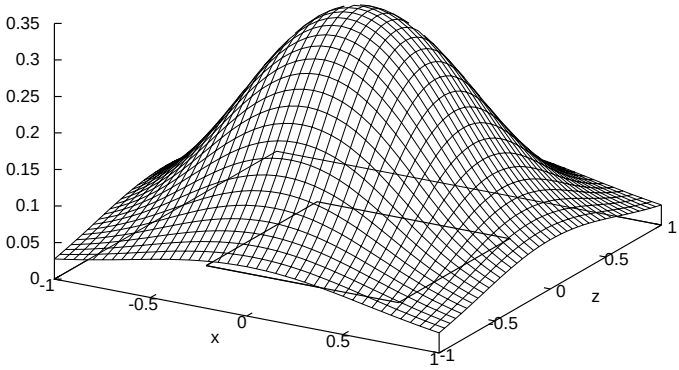

Fig. 3. The midplane field distribution of the bar magnets. The rectangular cross-section of the bars $[-0.5, 0.5] \times [-0.5, 0.5]$ is clearly marked on the graph.

This particular field arrangement can serve as useful test case for assessing the performance of computational methods. By itself, it represents a special case of the field of a magnetic dipole. But moreover, because the out-of-plane expansion schemes above are linear in the fields, it is also very indicative of the general behavior of any such methods, since most more complicated fields such as those in FFAGs are merely made by superimposing dipole-type fields of various apertures.

We next utilize the DA-based out-of-plane expansion method to determine the predicted field in space. Figure 4 shows the predicted fields at 25%, 50% and 75% of the aperture d. The left picture shows the vertical component B_y of the field, the middle picture shows B_x. The field component B_z is not shown directly since it is merely symmetric to B_x. The right picture shows the B_x and B_z components of the field as vectors for better clarity. The out-of-plane expansions were carried out to order 21.

It is quite apparent that the resulting field distributions are very smooth, suggesting the absence of major computational errors and inaccuracies. We now quantitatively analyze the quality of the out-of-plane expansion by a direct comparison with the true values of the field given by Eq. (2) and focus our attention to the dependence of the error on the expansion order that is being utilized. Furthermore, since the out-of-plane expansion is expected to lose accuracy with larger distance, we also study the quality of the expansion for distances to the midplane of $0.25d$, $0.5d$, and $0.75d$. For each computation order and distance from the plane, we evaluate the errors over a rectangular grid of 41×41 points for x and z in $[-1, +1]$.

We calculate both the average error of the representation as out-of-plane expansion, as well as its maximum. We record results for out-of-plane expansions of orders 3, 5, ..., 21 of the fields, corresponding to orders 4, 6, ..., 22 in the scalar potential. Since the field B_y is symmetric with respect to y, odd orders do not appear in its expansion with respect to y. Similarly, since the B_x and B_z fields are antisymmetric with respect to y, these fields do not exhibit even orders. So in order to show the trend of the accuracy with order, it is convenient to increase the orders by two in

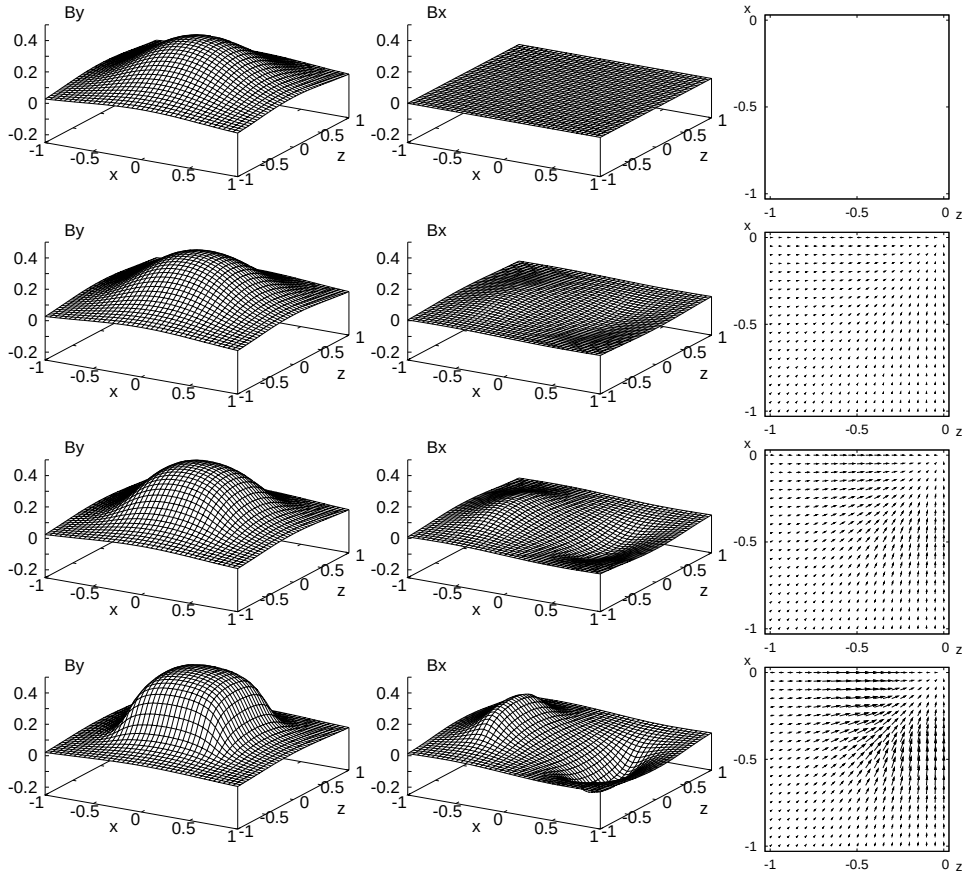

Fig. 4. Field distribution of the bar magnet in the x and y planes at $y = 0\%$ (midplane), 25%, 50%, and 75% of the half aperture d. The distributions of B_y and B_x are shown in 3D plots, and the B_x–B_z behavior is shown by vectors.

each step, and by choosing these orders to be odd, the actual highest appearing order of the B_y field is one order lower, while the highest appearing order for the B_x and B_z fields responsible for focusing effects is of the order shown.

Figure 5 shows a logarithmic plot for the resulting computational accuracies for the field component B_y. The other components are not shown since their behavior for each data point is within a few percent of those of B_y and thus lead to nearly indistinguishable plots. It can be seen that at the lowest order of 3 for B_x and B_z, the accuracies only range from about 10^{-3} to 10^{-1}, while at order 11 they reach 10^{-10} to 10^{-2}, and at order 21 they achieve 10^{-16} to 10^{-4}.

5. Out-of-Plane Expansion in Realistic FFAG Models

We now turn our attention to actual fields as they would appear in FFAG magnets. We utilize a field model based on superposition of individual combined function

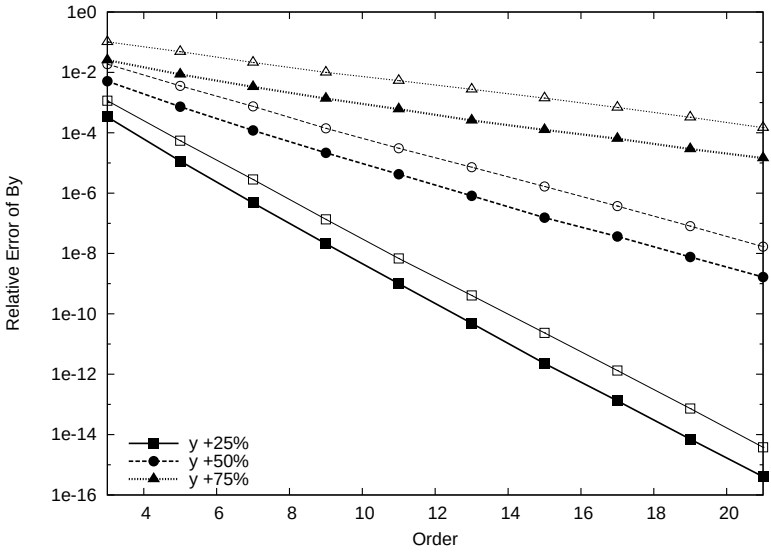

Fig. 5. Relative error of B_y of the bar magnet field depending on the out-of-plane expansion order at $y = 25\%$, 50%, 75% of the half aperture d as a function of the out-of-plane expansion order of the fields; the corresponding order of the potentials is higher by 1. The average error value (black markers) and the maximum error value (transparent markers) are plotted. Relative errors of B_x and B_z behave essentially the same way.

dipole fields as discussed in Ref. 17. Figure 6 shows the typical layout of such a FFAG ring, here made of nine individual cells, each of which contains two halves of a bending magnet (green) and a smaller magnet (red) bending in the opposite direction, both with a half aperture of 1 cm. The edges are carefully chosen so as to maintain horizontal and vertical tune stability.[18–20]

The fields are modeled utilizing an Enge falloff from the edges shown in the models, where the coefficients of the Enge function have been carefully adjusted to represent the situation of a permanent magnet, which constitutes one of the contemplated methods of constructing the magnet. Figure 7 shows the falloff of the resulting magnet on the right, and COSY's default fringe field falloff for dipoles on the left. Note that the FFAG falloff is steeper, leading to larger derivatives, and thus larger azimuthal out-of-plane field components.

As a result of the fringe fields thus imposed, the midplane field profile for B_y turns from the hard edge model shown in the leftmost picture of Fig. 8 to that shown in the rightmost one. For comparison, the softer falloff based on standard COSY dipoles is shown in the middle.

We now turn our attention to the performance of the DA-based out-of-plane expansion method described above and used in the code COSY. Figure 9 shows the predicted fields at 25%, 50% and 75% of the aperture d. The left picture shows the vertical component B_y of the field, the middle picture shows B_x. The right picture shows the B_x and B_z components of the field as vectors for better clarity.

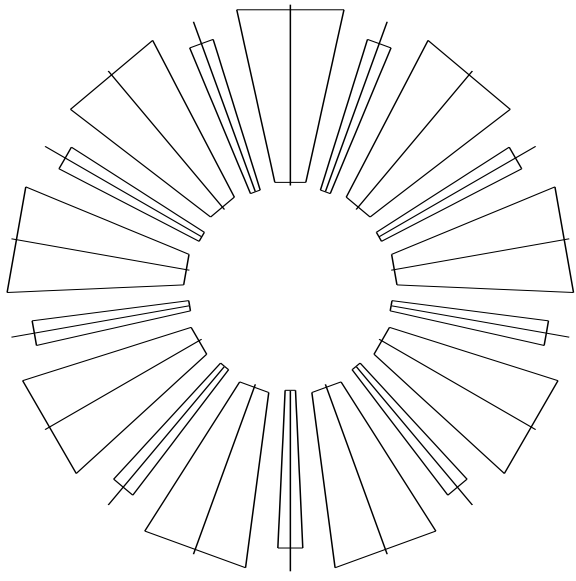

Fig. 6. Layout of a 9 cell model of non-scaling FFAG.

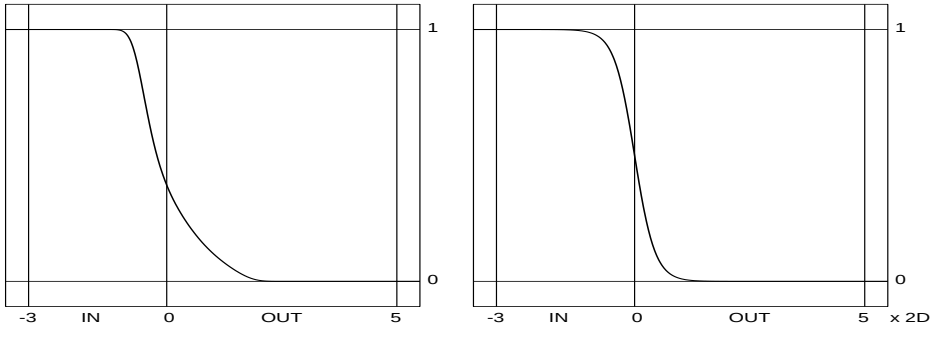

Fig. 7. Fringe field falloff profile based on Enge models. Left: default COSY dipole model, and right: model based on a permanent magnet, deemed more realistic for FFAG models.

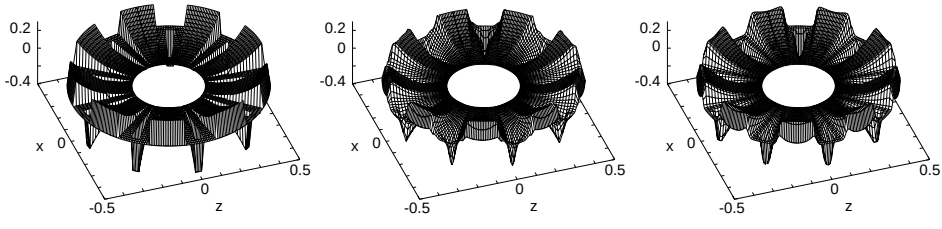

Fig. 8. Midplane field distribution of three FFAG models: A hard edge model, with fringe fields based on COSY default DI model, and with fringe field based on the field of permanent magnets as in the bar model.

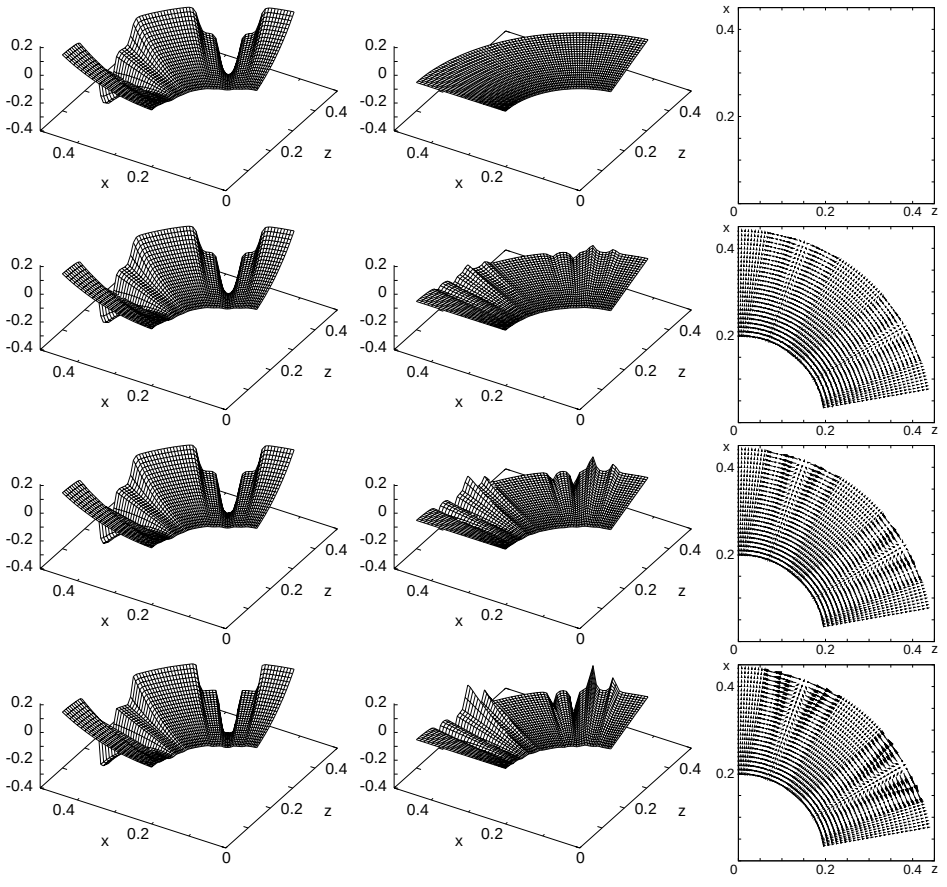

Fig. 9. Field distribution of a 80° section in the x and y planes—in the midplane and at $y =$ 2.5 mm, 5 mm, 7.5 mm planes. The distributions of B_y and B_θ are shown in 3D plots, and the B_r–B_θ behavior is shown by vectors. $0.20 \leq r \leq 0.44$ mm.

The out-of-plane expansions were carried out to order 21. It is apparent that the complexity of the resulting fields increases with larger distance to the midplane, and a rich amount of structure develops especially in the B_x field responsible for focusing.

We now quantitatively analyze the quality of the out-of-plane expansion. Different from the case of the bar magnet studied in the previous section, the exact value of the field is not known. So we perform our comparisons of accuracy of lower-order expansion by a comparison to an expansion of order 25 and assume that the differences with expansions of lower orders are meaningful estimates for the errors of these expansions. Again, since the out-of-plane expansion is expected to lose accuracy with larger distance, we also study the quality of the expansion for distances to the midplane of $0.25d$, $0.5d$, and $0.75d$. For each computation order and distance

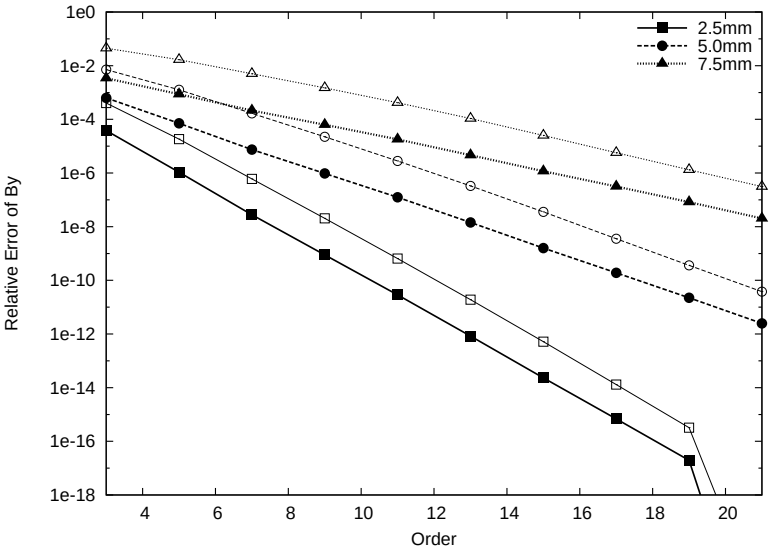

Fig. 10. Relative error of B_y depending on the out-of-plane expansion order at $y = 2.5$ mm, 5 mm, 7.5 mm planes. Shown are average error (black markers) and maximum error (transparent markers). The relative error of B_θ behaves almost identical, and the relative error of B_r is slightly lower but with the same overall behavior.

from the plane, we evaluate the errors over a grid in polar coordinates of 25×81 points in radius and azimuthal angle.

As before, we calculate both the average error of the representation as out-of-plane expansion, as well as its maximum. We record results for out-of-plane expansions of orders 3, 5, ..., 21 of the fields, corresponding to orders 4, 6, ..., 22 in the scalar potential. Since the field B_y is symmetric with respect to y, again odd orders do not appear in its expansion with respect to y, and likewise in B_x and B_z even orders do not appear.

Figure 10 shows a logarithmic plot for the resulting computational accuracies for the field component B_y. As before, the other components are not shown since their behavior for each data point is within a few percent of those of B_y and thus lead to nearly indistinguishable plots. It can be seen that at the lowest order of 3 for B_x and B_z, the accuracies only range from about 10^{-4} to 10^{-1}, while at order 11 they reach 10^{-11} to 10^{-3}, and at order 21 they achieve 10^{-16} to 10^{-6}.

To conclude, we see that for high-accuracy simulations, especially far away from the midplane, it is necessary to utilize rather high orders in the field expansions. While computations of tunes and related quantities require information only near the midplane, the study of detailed dynamics such as the computation of dynamic aperture limits requires careful consideration of all nonlinear effects including representations of high order.[17] Of particular consequence is the violation of the symplectic symmetry inherent in the dynamics in FFAGs, which arises whenever erroneous field representations are chosen.

Acknowledgments

The work was supported by the US Department of Energy and the National Science Foundation.

References

1. M. Berz. *Modern Map Methods in Particle Beam Physics*. Academic Press, San Diego, 1999. Also available at http://bt.pa.msu.edu/pub.
2. M. Berz. Differential algebraic description of beam dynamics to very high orders. *Particle Accelerators*, 24:109, 1989.
3. K. Makino, M. Berz, D. Errede, and C. J. Johnstone. High order map treatment of superimposed cavities, absorbers, and magnetic multipole and solenoid fields. *Nuclear Instruments and Methods A*, 519:162–174, 2004.
4. M. Berz. The new method of TPSA algebra for the description of beam dynamics to high orders. Technical Report AT-6:ATN-86-16, Los Alamos National Laboratory, 1986.
5. M. Berz. The method of power series tracking for the mathematical description of beam dynamics. *Nuclear Instruments and Methods*, A258:431–437, 1987.
6. K. Makino. *Rigorous Analysis of Nonlinear Motion in Particle Accelerators*. PhD thesis, Michigan State University, East Lansing, Michigan, USA, 1998. Also MSUCL-1093.
7. M. Berz and H. Wollnik. The program HAMILTON for the analytic solution of the equations of motion in particle optical systems through fifth order. *Nuclear Instruments and Methods*, A258:364–373, 1987.
8. K. Makino and M. Berz. Perturbative equations of motion and differential operators in nonplanar curvilinear coordinates. *International Journal of Applied Mathematics*, 3,4:421–440, 2000.
9. K. L. Brown, R. Belbeoch, and P. Bounin. First- and second- order magnetic optics matrix equations for the midplane of uniform-field wedge magnets. *Review of Scientific Instruments*, 35:481, 1964.
10. K. L. Brown. The ion optical program TRANSPORT. Technical Report 91, SLAC, 1979.
11. K. L. Brown. A first- and second-order matrix theory for the design of beam transport systems and charged particle spectrometers. Technical Report 75, SLAC, 1982.
12. M. Berz and K. Makino. COSY INFINITY Version 9.0 beam physics manual. Technical Report MSUHEP-060804, Department of Physics and Astronomy, Michigan State University, East Lansing, MI 48824, 2007. See also http://cosyinfinity.org.
13. M. Berz and K. Makino. COSY INFINITY Version 8.1 - user's guide and reference manual. Technical Report MSUHEP-20704, Department of Physics and Astronomy, Michigan State University, East Lansing, MI 48824, 2002. see also http://cosy.pa.msu.edu.
14. R. Degenhardt and M. Berz. High accuracy description of the fringe fields of particle spectrographs. In *Proceedings 1993 Particle Accelerator Conference*, Washington, DC, 1993.
15. R. Degenhardt and M. Berz. High accuracy description of the fringe field in particle spectrographs. *Nuclear Instruments and Methods*, A427:151–156, 1999.
16. S. L. Manikonda and M. Berz. An accurate high-order method to solve the Helmholtz boundary value problem for the 3D Laplace equation. *International Journal of Pure and Applied Mathematics*, 23,3:365–378, 2005.

17. K. Makino, M. Berz, P. Snopok, and C. Johnstone. High-order description of the dynamics in FFAGs and related accelerators. *International Journal Modern Physics A*, 24, 5:908–922, 2009.
18. Carol Johnstone and S. Koscielniak. *DPB Newsletter*, chapter The New Generation of FFAG Accelerators, pages 12–14. American Physical Society, 2008.
19. C. Johnstone, M. Berz, K. Makino, and P. Snopok. Innovations in fixed-field accelerators: Design and simulation. In *Proceedings, 19th International Conference on Cyclotrons and their Applications*, in print.
20. C. Johnstone, M. Berz, K. Makino, and P. Snopok. Isochronous (CW) non-scaling FFAGs: Design and simulation. In *Proceedings, 2010 Advanced Accelerator Concepts Workshop*, in print.

International Journal of Modern Physics A
Vol. 26, Nos. 10 & 11 (2011) 1822–1832

DOI: 10.1142/S0217751X11053213

World Scientific
www.worldscientific.com

UPGRADING EMMA TO USE LOW-FREQUENCY RF CAVITIES

CHIHIRO OHMORI
KEK, 1-1 Oho, Tsukuba, Ibaraki 305-0801, Japan

J. SCOTT BERG
Brookhaven National Laboratory, Building 901A,
PO Box 5000, Upton NY 11973-5000, USA

EMMA is an experiment to study beam dynamics in fixed field alternating gradient accelerators (FFAGs). It accelerates the beam in about 10 turns using 1.3 GHz cavities in a mode like that used for muon accelerators. Many applications of FFAGs prefer to have slower acceleration, typically thousands of turns. To do so in EMMA would require the RF system to be replaced with a low-frequency, high-gradient system. This paper describes the motivation for studying slow acceleration in EMMA and the required parameters for an RF system to do that. It then describes the technology needed for the RF system.

Keywords: Magnetic alloy RF cavity; fixed field alternating gradient accelerator.

PACS numbers: 29.20.D-, 84.40.-x, 29.27.Bd, 75.50.Kj

1. Low Frequency RF in EMMA

The Electron Model for Many Applications (EMMA)[1] is an experiment to study beam dynamics in linear non-scaling fixed field alternating gradient accelerators (FFAGs). It uses a 1.3 GHz RF system[2] to accelerate the beam in around 10 turns. This mode of acceleration is typically employed for muon acceleration,[3,4] where such rapid acceleration is essential and high RF frequencies are necessary.

However, most applications of FFAGs[5–15] FFAGs require comparatively slow acceleration, mostly in the low thousands of turns. The fixed-frequency 1.3 GHz RF system accelerating in the serpentine mode in EMMA will not permit arbitrarily slow acceleration (strictly speaking it will, but nearly all the time will be spent near two specific energies, and the required RF voltage will approach a constant nonzero value as the number of turns goes to infinity).[16,17] A low- and possibly variable-frequency RF system is therefore required to significantly reduce the acceleration rate in EMMA.

Due to its usage of linear magnets, a linear non-scaling FFAG such as EMMA crosses a number of linear imperfection resonances, nonlinear resonances, and space charge resonances. Authors have pointed out that when accelerating slowly in a linear non-scaling FFAG, the crossing of these resonances can lead to emittance

growth and beam loss.[18,19] Ref. 18 demonstrates that there is a relationship between the tolerable acceleration rate and the space charge tune shift for a given lattice, and that there is a relationship between the acceleration rate, emittance growth, and lattice errors. In all cases, if one could accelerate rapidly enough, the machine performance would be acceptable. Similarly, Ref. 19 shows that the emittance growth and dynamic aperture are related to the magnet errors and the acceleration rate. In particular, for parameters of the EMMA lattice, one has very good dynamic aperture in the presence of reasonable alignment errors when accelerating in 100 turns, while if acceleration takes 1000 turns, the dynamic aperture is significantly worse and highly sensitive to the alignment errors.

We would therefore like to study slow acceleration using the EMMA ring. The goal would be to study beam loss and emittance growth over the entire acceleration cycle as a function of the acceleration rate, lattice errors (which could be intentionally introduced), and bunch intensity. A low- and variable-frequency cavity would allow the acceleration rate to be varied. Since the EMMA magnets are on horizontal sliders, horizontal displacement errors are easily introduced. Quadrupole errors could be simulated by placing shunts across individual magnets. ALICE (formerly ERLP),[20,21] the injector to EMMA, is in principle capable of creating a beam that has a significant space charge tune shift in EMMA.[22]

Slow acceleration would also permit the study of the crossing of individual resonances. EMMA has the ability to inject the beam at any energy within its acceleration range, and thus we could inject at an energy just below any resonance and accelerate through it.

We want the lowest frequency possible so as to be able to vary the RF frequency and to be able to make more turns while accelerating before the RF phase deviates too much. In EMMA, this is about 18 MHz (harmonic 1). We would like to be able to accelerate by 10 MeV in 100 turns, leading to an RF voltage requirement of 100 kV. In general one would expect to start studies with the RF voltage at its maximum value, then reduce the voltage to look for increased emittance growth and beam loss at the lower acceleration rates. The cavity must fit in the existing EMMA drifts, meaning that it should be at most about 10 cm long.

1.1. *Acceleration mode*

There are three different acceleration modes one could imagine using. The simplest is to keep the RF frequency fixed, and use a serpentine acceleration mode as in the existing EMMA ring. Since the RF frequency would be 72 times lower, one would expect acceleration times 72 times longer, and therefore approaching 1000 turns. To prevent significant bunch lengthening due to the time of flight dependence on energy, it would likely be desirable to prepare the initial bunch distribution with the appropriate energy-time correlation, which could be done in ALICE.

One could instead vary the RF frequency to match the time of flight at the beam's current energy. This would allow an arbitrarily long time to be spent

accelerating. If one accelerated with a high RF voltage but far off crest, one could have some modest number of synchrotron oscillations during the acceleration cycle. One would have to quickly switch the RF phase near transition (see the time of flight plots in Ref. 23) to maintain the synchrotron oscillations. Doing anything else could lead to significant bunch lengthening. This mode of acceleration requires approximately an 0.3% variation in the RF frequency.

Another mode of operation is to modify the lattice so that the minimum of the time of flight is well outside the energy range of the machine. This will significantly increase the closed orbit excursion in the machine, but since this experiment would study beams with much smaller emittances than what the main EMMA ring is designed to accept, there should be plenty of horizontal space in the vacuum chamber to accommodate this larger excursion.[23] This mode of operation has longitudinal dynamics which would be similar to what one expects in the machines we are trying to study (where the time of flight dependence on energy is almost completely determined by the velocity variation with energy). Synchrotron oscillations would be stronger than in the previous mode of operation, and one would not have to make a rapid phase change to cross the transition energy. It has yet to be demonstrated that the lattice can be modified in this fashion. This mode of operation would require an RF frequency variation of approximately 3%. While being more challenging to implement than the other modes, this acceleration mode is probably the preferred one.

2. The Low-Frequency RF Cavity

For each of the three different acceleration modes using the low-frequency RF cavity, we would need more than 100 kV to finish the acceleration in 100 turns. The maximum frequency variation is 97.2 GHz/s, requiring a very rapid frequency sweep. The basic shape of driving current can be found by modeling the cavity as a parallel RLC circuit. As the voltage across each circuit element is the same, the total current for the frequency sweep is the sum of the currents in the elements,

$$I(t) = \frac{V(t)}{R} + \frac{1}{L}\int_0^t V(t')dt' + C\frac{dV(t)}{dt}. \tag{1}$$

When the frequency is swept, the RF voltage is

$$V(t) = V_0 \sin(\omega(t)t). \tag{2}$$

Equation (1) suggests that the inductance of the cavity, ωL, is much smaller than the shunt impedance, R, in the case of a high-Q system. Therefore, for the high-Q case, the driving current will be complicated and increasing.

Assuming the frequency is linear function of time, $\omega(t) = \omega_0 + \delta t$, a $Q = 100$ resonantor with a tuning loop requiress a driving current that is 10 times larger than what would be required for a slow frequency sweep because of this transient effect. For a low-Q system, the current would be similar to that for slow sweep case. In case of the Q=9 system, the required current is twice what is needed for a slow

sweep system. To reduce the transient effects, a magnetic alloy-loaded cavity with a relatively low Q ($Q \simeq 9$) will be used.

2.1. *Magnetic alloy-loaded RF cavity*

A magnetic alloy RF cavity was developed for MIMAS at Saclay laboratory in the 1980's.[24] It used a biasing circuit to tune the resonant frequency and the field gradient was limited. An intensive R&D program for a high intensity proton accelerator was started in KEK in 1995, and a high field gradient cavity was developed using a different type of magnetic alloy. This type of cavity has since been used for many different accelerators. For high intensity beam acceleration, it is used for the KEK PS-booster[25] and the J-PARC RCS (Rapid Cycling Synchrotron) and MR (Main Ring) synchrotrons.[26] It is also being used in medical applications due to its ease of tunability and good stability. For low-energy heavy ion acceleration, which requires a very wide frequency sweep, it is used at the Low Energy Ion Ring (LEIR) at CERN.[27] In many scaling FFAG's, it is also used because of its very fast frequency sweep.[28] Another application is the PRISM bunch rotation cavity which requires a very high field gradient at low frequency.[29]

2.2. *Magnetic alloy*

Magnetic alloy has two unique characteristics at high frequency. One is that the Q value of the resonator is below 1, and it is therefore suitable for a wideband system like that used in medical applications and ion synchrotrons. The Q value is controllable by two established techniques: a cut core configuration and a hybrid system with an external inductor.[30] Cut cores are used for the J-PARC MR cavities and the hybrid systems are used for RCS ones. Generally speaking, the hybrid system is suitable for Q values of 2-3 and a cut core is suitable for high Q systems.

The other advantage of magnetic alloy is that it is stable at high RF fields. Ferrite cavities have been used for many accelerators. Ferrites show degradation in their properties at RF magnetic fields of around 10 mT because their saturation fields are around 0.1-0.2 T. The saturation field of magnetic alloy is 1-2 T. It is still stable at the very high RF field magnetic fields of 0.2 T. Figure 1 shows the product $\mu'_p Qf$, which indicates the characteristics of the magnetic material for RF flux. $\mu'_p Qf$ is given by

$$R_p = \mu_0(\mu'_p Qf)t \ln \frac{\text{O.D.}}{\text{I.D.}}, \tag{3}$$

where O.D., I.D., and t are the outer diameter, inner diameter, and thickness of toroidal core. The product $\mu'_p Qf$ is independent of the size and shape of the magnetic core. It is used to evaluate the characteristics of the magnetic materials. The RF magnetic field B_{RF} is written as $B_{RF} = \frac{V_{RF}}{\omega S}$.

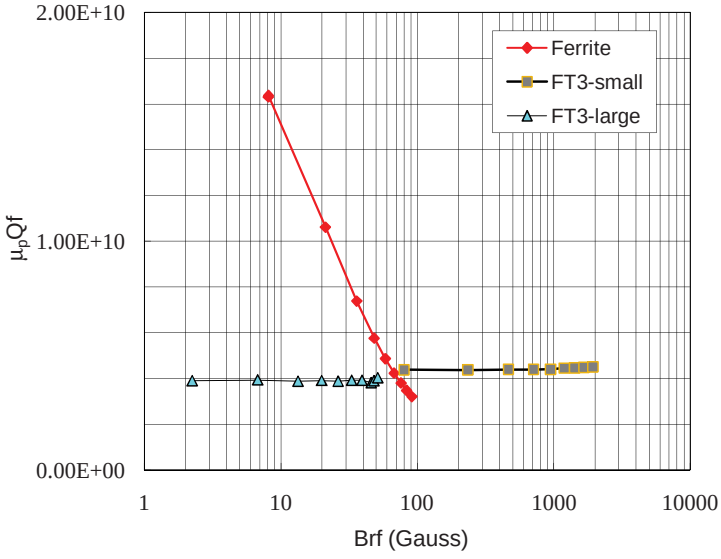

Fig. 1. Characteristics of magnetic material. FT means a magnetic alloy. Characteristics of MA cores are stable for RF magnetic field. Others are ferrite materials. In case of ferrite materials, degradations occur at a large field.

2.3. *New magnetic alloy*

Magnetic alloy is produced by starting with amorphous ribbon, winding the ribbon to a large size for accelerator use, and annealing at high temperature. For an amorphous core, the annealing temperature is relatively low, a few hundred degrees celcius. For a magnetic alloy with a fine crystallized structure, it is several hundred degrees celcius.

Recently it was found that the characteristics of the magnetic alloy can be improved by reducing the thickness of the ribbon and applying a magnetic field while annealing.[31] Figure 2 shows a comparison of MA cores. The material FT3M, which is annealed without magnetic field, and which has a ribbon thickness of 18 μm, is used for many MA cavities: in J-PARC, LEIR, medical applications, and FFAGs. Figure 2 shows that the μQf product was improved by 10–20% when the ribbon thickness was reduced to 13 μm. When the magnetic field is applied during the annealing process, the material is called "FT3L," and μQf is improved by 10-20% over FT3M as well. In addition, the combination of both improves the characteristics significantly. The mechanism of this effect is under study[31] using a μSR technique.

Using this new MA material, an upgrade scenario of the J-PARC MR was proposed in Ref. 32. The high field gradient obtainable by using FT3M gave a significant improvement for the accelerator design at J-PARC. The available field gradient became 2.5 times larger than that available from ferrite cavities with large

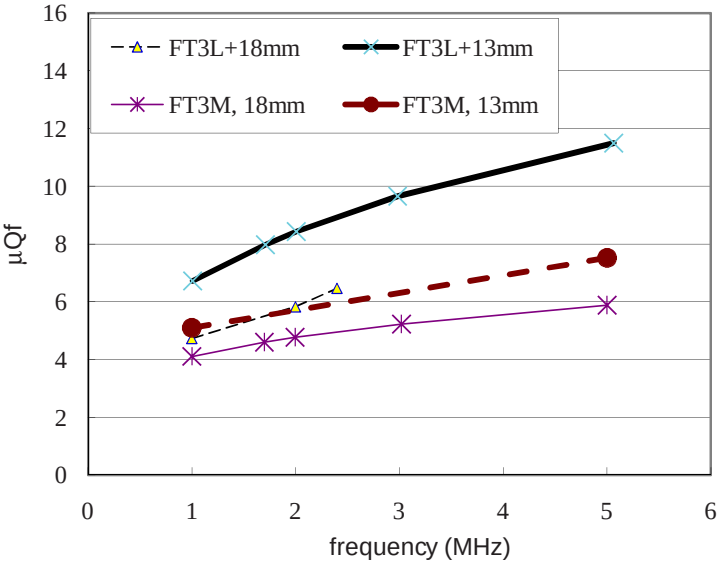

Fig. 2. Comparison of magnetic alloys.

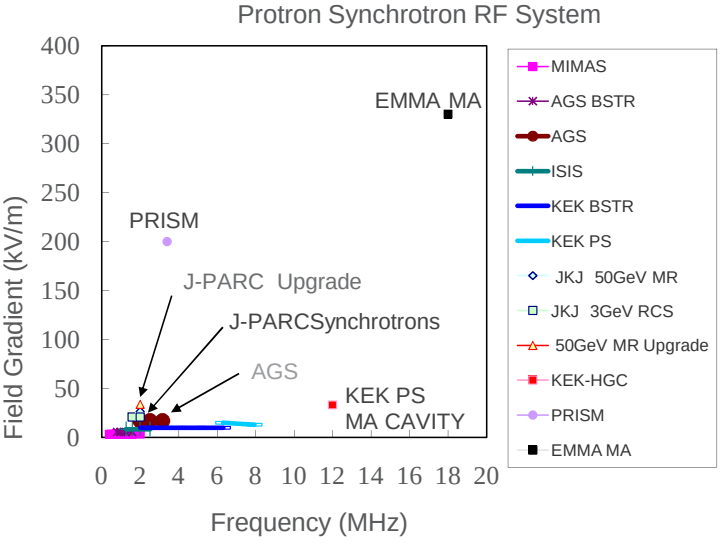

Fig. 3. Field gradient of RF cavities. In the case of low-duty pulsed operation (PRISM and EMMA MA), much higher gradients become available than for high duty oprations in other synchrotrons.

beam pipe size (see Fig. 3), and therefore the circumference of the J-PARC RCS could be made more compact (354 m). It would then become possible to increase the repetition rate of the acceleration cycle, and thus supply more power to the neutrino beam users.

2.4. *MA cavity*

When a cavity system is designed for an accelerator, RF frequency, RF voltage, and duty factor are the most important parameters. In case of an MA cavity, the RF frequency range determines the required cavity Q, and therefore determines whether to use an un-cut core, hybrid, or cut core system. When the bandwidth is wide, careful design is required to reduce floating capacitance of the whole system to enable the efficient use of an un-cut core.

The RF voltage and the duty cycle determine the choice for the cooling scheme of the MA cores. Several different schemes have been tested and used. When one has a low duty factor[33] and low voltage, air cooling is adopted. A forced-air cooling system was used for the high voltage and high duty factor RF system at the KEK PS booster,[25] the MA cavity used as a beam chopper and buncher between the ion source and accelerator, and the RIKEN buncher that was operated in the range of 18–45 MHz.[34] A direct cooling scheme which is used for ferrite cavities is also applied in medical accelerators[35] and the J-PARC R&D cavity.[36] Another method of direct water cooling is used for the J-PARC[37] and LEIR[27] cavities. Direct water cooling gives the best cooling effieciency, but is not applicable for frequencies higher than several MHz because the large dielectric constant of water causes impedance reduction. Direct cooling is still applicable if another coolant is used in the 12 MHz system described in Ref. 38. The field gradients of the MA and ferrite cavities described here are shown in Fig. 3.

2.5. *Pulsed operation*

In case of high duty factor operation, the field gradient is mainly limited by the cooling efficiency. If the duty factor is low, the MA cavity can be operated at a very high field gradient.[29] In particular, low duty factor operation enables air cooling. Because the frequency range of the cavity is affected by the coolant and cavity structure, air cooling is the most suitable option for a frequency higher than several MHz.

Another advantage of a low duty factor is the operation of the final stage amplifier. In the frequency range from below 1 MHz to several tens of MHz, vacuum tubes are used. The output power is limited by the anode dissipation in the vacuum tube in high duty factor operation. In the case of pulsed operation, the maximum voltage is given by an operation curve of the vacuum tube since the average power dissipation is negligible. This means that a small vacuum tube can be used to obtain a large output power for a short time. For the PRISM RF system, 100 kW tubes are used yet the output power is more than 1 MW. As the average power for pulsed operation is small, the anode power supply for the tube amplifier can be much smaller than that for high duty factor operation. For a synchrotron RF system, the cost of the anode power supply is the most expensive part; that cost can be reduced for low duty factor operation.

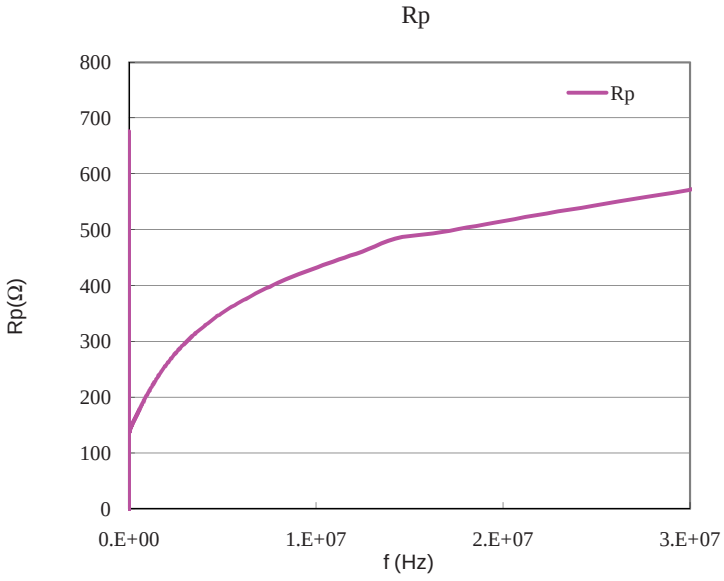

Fig. 4. Impedance of a MA core for EMMA application.

3. EMMA Low Frequency RF system

The main parameters of the low frequency cavity are summarized in Table 1. Because the EMMA latice has 27-fold symmetry, three RF cavities will be installed at symmetric points. The magnetic alloy FT3L with 13 μm thickness will be used to obtain voltage above 33 kV for each cavity to form the RF bucket. A preliminary test production of the FT3L cores already shows a high impedance of about 500 Ω at 18 MHz as shown in Fig. 4. The outer diameter of the cores is 27 cm, which is suitable for the EMMA cavities.

Table 1. Main Parameter of EMMA low frequency RF.

frequency	18 MHz
frequency sweep	3 %
total RF voltage	100 kV
Number of RF stations	3
Voltage per station	33.3 kV
Length of cavity	10 cm
Number of MA cores	2 per cavity
Size of MA core	27 cm O.D., 10 cm I.D. x 2.5 cm
Cut/un-cut	Cut core
Material	FT3L (13 μm thickness)
Q-value	about 9
Cavity impedance	1 kΩ

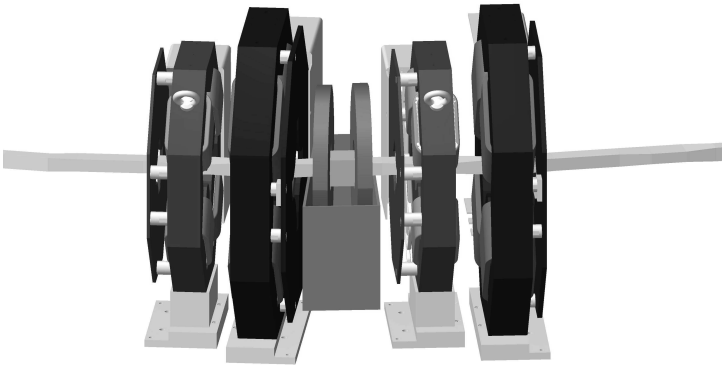

Fig. 5. EMMA low frequency cavity.

In the cavity, two FT3L cores are installed as shown in Fig. 5. The cavity is driven by a push-pull amplifier using two tetrode 4CW100K tubes. This tube has been used for the PRISM RF system and it has already been confirmed that it can generate about a 60 A RF current.[29] Assuming that the floating capacitance in the amplifier and cavity is 80 pF,[27] a cut core configuration is necessary to reduce the core inductance and to resonate at 18 MHz. The expected Q value will be 9. For a slow frequency sweep, the driving current to generate 33 kV would be 33 A (= 33 kV/1 kΩ). Because of the transient effect of the very fast frequency sweep, an RF current about two times larger is necessary. With the RF current available from the 4CW100K vacuum tubes, 33 kV can still be achieved.

4. Conclusion

Adding a low-frequency cavity to EMMA would, for a relatively modest cost, enable EMMA to study slow acceleration in FFAGs. This would greatly expand our understanding of under what circumstances particular types of FFAG designs are good choices. Construction and operation of the RF system would be an advance in and of itself. Furthermore, EMMA provides a unique environment for operating such a cavity since the EMMA repetition rate can be made as low as necessary, permitting air cooling and a smaller power supply for the cavity at this early R&D stage.

Acknowledgment

This work is supported by the U. S. Department of Energy, contract No. DC-AC02-98CH10886.

References

1. R. Edgecock *et al.*, EMMA—THE WORLD'S FIRST NON-SCALING FFAG, in *Proceedings of EPAC08, Genoa, Italy* (European Physical Society Accelerator Group, 2008), p. 3380.

2. C. D. Beard *et al.*, RF SYSTEM DESIGN FOR THE EMMA FFAG, in *Proceedings of EPAC08, Genoa, Italy* (European Physical Society Accelerator Group, 2008), p. 3377.
3. J. S. Berg and C. Johnstone, DESIGN OF FFAGS BASED ON A FODO LATTICE, in *Proceedings of the 2003 Particle Accelerator Conference*, eds. J. Chew, P. Lucas, and S. Webber (IEEE, Piscataway, NJ, 2003), p. 2216.
4. J. S. Berg *et al.*, *Phys. Rev. ST Accel. Beams* **9**, 011001 (2006).
5. A. G. Ruggiero *et al.*, 1.5-GEV FFAG ACCELERATOR AS INJECTOR TO THE BNL-AGS, in *Proceedings of EPAC 2004, Lucerne, Switzerland*, (European Physical Society Accelerator Group, 2004), p. 159.
6. D. Trbojevic *et al.*, ELECTRON ACCELERATION FOR E-RHIC WITH NON-SCALING FFAG, in *Proceedings of EPAC 2004, Lucerne, Switzerland*, (European Physical Society Accelerator Group, 2004), p. 932.
7. M. Tanigaki *et al.*, CONSTRUCTION OF FFAG ACCELERATORS IN KURRI FOR ADS STUDY, in *Proceedings of EPAC 2004, Lucerne, Switzerland*, (European Physical Society Accelerator Group, 2004), p. 2673.
8. T. Misu *et al.*, *Phys. Rev. ST Accel. Beams* **7**, 094701 (2004).
9. A. G. Ruggiero, FFAG-Based High-Intensity Proton Drivers, in *High Intensity and High Brightness Hadron Beams*, eds. I. Hofmann, J.-M. Lagniel, and R. W. Hasse (American Institute of Physics, 2005), p. 324.
10. G. H. Rees, *Nucl. Phys. B (Proc. Suppl.)* **155**, 301 (2006).
11. A. G. Ruggiero, *Nucl. Phys. B (Proc. Suppl.)* **155**, 315 (2006).
12. E. Keil, A. M. Sessler, and D. Trbojevic, *Phys. Rev. ST Accel. Beams* **10**, 054701 (2007).
13. A. G. Ruggiero *et al.*, HEAVY ION DRIVER WITH NON-SCALING FFAG, in *Proceedings of PAC07, Albuquerque, New Mexico, USA* (IEEE, Piscataway, NJ, 2007), p. 1880.
14. K. Peach *et al.*, PAMELA - A MODEL FOR AN FFAG BASED HADRON THERAPY MACHINE, in *Proceedings of PAC07, Albuquerque, New Mexico, USA* (IEEE, Piscataway, NJ, 2007), p. 2880.
15. T. Yokoi *et al.*, PAMELA: DEVELOPMENT OF THE RF SYSTEM FOR A NON-RELATIVISTIC NON-SCALING FFAG to appear in *Proceedings of PAC09, Vancouver, BC, Canada* (2009).
16. J. S. Berg, Longitudinal Reference Particle Motion in Nearly Isochronous FFAG Recirculating Accelerators, in *Proceedings of Snowmass 2001*, ed. N. Graf (SLAC, 2001), T503.
17. J. S. Berg, *Phys. Rev. ST Accel. Beams* **9**, 034001 (2006).
18. S. Y. Lee *et al.*, *New J. Phys.* **8**, 291 (2006).
19. S. Machida, *Phys. Rev. ST Accel. Beams* **11**, 094003 (2008).
20. S. L. Smith *et al.*, THE STATUS OF THE DARESBURY ENERGY RECOVERY LINAC PROTOTYPE, in *Proceedings of PAC07, Albuquerque, New Mexico, USA* (IEEE, Piscataway, NJ, 2007), p. 1106.
21. C. Beard *et al.*, THE CURRENT STATUS OF THE ALICE (ACCELERATORS AND LASERS IN COMBINED EXPERIMENTS) FACILITY, in *Proceedings of FEL2009, Liverpool, UK*, p. 333.
22. Y. M. Saveliev, D. J. Holder, B. D. Muratori, and S. L. Smith, RESULTS FROM ALICE (ERLP) DC PHOTOINJECTOR GUN COMMISSIONING, in *Proceedings of EPAC08, Genoa, Italy* (European Physical Society Accelerator Group, 2008), p. 208.
23. J. S. Berg, *Nucl. Instrum. Methods A* **596**, 276 (2008).

24. C. Fougeron *et al.*, VERY WIDE RANGE AND SHORT ACCELERATING CAVITY FOR MIMAS, in *Proceedings of the 1993 Particle Accelerator Conference* (IEEE, Piscataway, NJ, 1993), p. 858.
25. S. Ninomiya *et al.*, NON-RESONANT ACCELERATING SYSTEM AT THE KEK-PS BOOSTER, in *Proceedings of EPAC 2004, Lucerne, Switzerland*, (European Physical Society Accelerator Group, 2004), p. 1027.
26. M. Yoshii *et al.*, PROTON BEAM ACCELERATION WITH MA LOADED RF SYSTEMS IN J-PARC RCS AND MR SYNCHROTRONS, to appear in *Proceedings of PAC09, Vancouver, BC Canada* (2009).
27. R. Garoby *et al.*, THE LEIR RF SYSTEM, in *Proceedings of the 2005 Particle Accelerator Conference*, ed. C. Horak (IEEE, Piscataway, NJ, 2005), p. 1619.
28. Y. Yonemura *et al.*, *Nucl. Instrum. Methods A* **576**, 294 (2008).
29. C. Ohmori *et al.*, *Nucl. Phys. B (Proc. Suppl.)* **149**, 280 (2005).
30. A. Schnase *et al.*, MA CAVITIES FOR J-PARC WITH CONTROLLED Q-VALUE BY EXTERNAL INDUCTOR, in in *Proceedings of PAC07, Albuquerque, New Mexico, USA* (IEEE, Piscataway, NJ, 2007), p. 2131.
31. C. Ohmori *et al.*, DESIGN OF A NEW J-PARC RF CAVITY FOR MUON SHORT BUNCH, to appear in *Proceedings of PAC09, Vancouver, BC Canada* (2009).
32. C. Ohmori *et al.*, POSSIBLE UPGRADE SCENARIO FOR J-PARC RF, in *Proceedings of EPAC08, Genoa, Italy* (European Physical Society Accelerator Group, 2008), p. 799.
33. M. Fujieda *et al.*, *Phys. Rev. ST Accel. Beams* **2**, 122001 (1999).
34. T. Koseki *et al.*, DEVELOPMENT OF BUNCHER CAVITY USING MA CORES, in *Proceedings of the 2nd Annual Meeting of Particle Accelerator Society of Japan and the 30th Linear Accelerator Meeting in Japan (July 20–22, 2005, Tosu Japan* (2005), p. 329.
35. M. Kanazawa *et al.*, RF CAVITY WITH CO-BASED AMORPHOUS CORE, in *Proceedings of EPAC 2004, Lucerne, Switzerland* (European Physical Society Accelerator Group, 2004), p. 983.
36. C. Ohmori *et al.*, HIGH FIELD GRADIENT CAVITY FOR JAERI-KEK JOINT PROJECT, in *Proceedings of EPAC 2002, Paris, France* (European Physical Society Interdivisional Group on Accelerators and CERN, Geneva, Switzerland, 2002), p. 257.
37. M. Yamamoto *et al.*, HIGH POWER TEST OF MA CAVITY FOR J-PARC RCS, in *Proceedings of EPAC 2006, Edinburgh, Scotland* (European Physical Society Accelerator Group, 2006), p. 1322.
38. M. Yoshii *et al.*, MA RF CAVITY FOR THE KEK 12 GEV PS, in *Proceedings of EPAC 2000, Vienna, Austria* (2000), p. 984.

International Journal of Modern Physics A
Vol. 26, Nos. 10 & 11 (2011) 1833–1841

DOI: 10.1142/S0217751X11053225

World Scientific
www.worldscientific.com

HARMONIC NUMBER JUMP ACCELERATION OF MUON BEAMS IN SCALING FFAG RINGS

T. PLANCHE

Graduate School of Engineering, Kyoto University, Katsura Nishikyo-ku, Kyoto, 615-8530, Japan
tplanche@post3.rri.kyoto-u.ac.jp

J.-B. LAGRANGE

Graduate School of Engineering, Kyoto University, Katsura Nishikyo-ku, Kyoto, 615-8530, Japan

Y. MORI

Kyoto University Research Reactor Institute, Asashiro-Nishi, Kumatori-cho, Sennan-gun, Osaka, 590-0494, Japan

The harmonic number jump acceleration in scaling FFAG rings is considered in this paper. Constraints fixed by the acceleration scheme on the lattice design are detailed. An example of a 3.6 to 12.6 GeV muon lattice which satisfy these constraints is presented.

Keywords: Harmonic number jump acceleration; scaling FFAG; muon acceleration; dispersion suppressor; reduced excursion insertions; two-beam lattice.

PACS number: 29.20.dk

1. Introduction

As part of the international effort to design future neutrino factories and muon colliders, the development of accelerating structures using fixed guide fields and constant rf frequencies is required.[1–3] In such structures, the repetition rate is not limited by magnet ramping and rf frequency variation issues. Muon beams can thus be accelerated rapidly, which is essential to limit the number of muons lost by decay. Another constraint on the required acceleration scheme comes from the large longitudinal and transverse emittance of the beams to handle.

One feature of the scaling type of fixed field alternating gradient (FFAG) rings is, in addition to their static guide field, that their chromaticity is null. On the one hand, it implies that with a proper choice of the working point one can thus avoid the neighborhood of any harmful resonance and obtain a huge dynamical aperture for the whole energy range. On the other hand, the lowest order dependence of the time of flight on the transverse amplitude disappears.[4] Scaling FFAGs are then

less affected by the longitudinal amplitude growth for large transverse amplitude observed in the non-scaling type of FFAG.[5] This makes all the more large the 6D acceptance of scaling FFAG rings.

One of the main drawbacks of scaling FFAGs is that the variation of the time of flight with energy cannot be tuned once the value of the geometrical field index k is chosen. However two ways to use constant rf frequency acceleration in scaling FFAG lattices have been proposed.[6,7] One of these, the Harmonic Number Jump (HNJ) acceleration, where the period of revolution changes by a number of full rf periods every turn[8,9] is discussed in this paper.

2. General Considerations about Harmonic Number Jump Acceleration

The principle of the HNJ acceleration is to keep the synchronization between the revolution period T_{rev} of a reference particle and the rf period T_{rf}:

$$T_{rev} = h \cdot T_{rf} \qquad h \in \mathbb{N}, \tag{1}$$

by changing the harmonic number h by an integer value every turn. To that end, one must give the right energy gain to change the revolution period of an integer number of rf period every turn. The main feature of this scheme is to allow constant rf frequency acceleration in non-isochronous rings.

2.1. *Required energy gain per turn*

We examine the simple case of a ring with a single rf kick given at the beginning of each turn. Linearizing the variation of the time of flight around the energy E_i of the particle at the beginning of the turn number i, the required energy gain to jump an integer number Δh of harmonic(s) during the turn $i+1$ is given by:[10]

$$E_{i+1} - E_i = \frac{T_{rf}\Delta h}{\frac{\partial T_{rev}}{\partial E}\Big|_{E_i}}. \tag{2}$$

2.2. *Simultaneous acceleration of particles and their antiparticles*

We consider to use HNJ acceleration in a ring with N constant frequency rf cavities uniformly distributed around (see Fig. 1). To keep accelerating particle after the end of the first turn, all cavities must not be working at the same frequency.[11] For instance, in the particular case of a harmonic number increased by a constant value Δh each turn, assuming that this harmonic number h is always large and much larger than its variation between injection and extraction, the frequency of each cavity must follow:[10]

$$f_k \approx f_0 \left(1 - \frac{\Delta h}{h} \cdot \frac{k}{N}\right), \qquad k = \{0..N-1\}, \tag{3}$$

with f_0 the frequency of the cavity number $k = 0$.

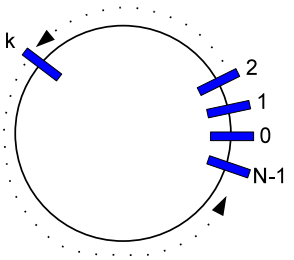

Fig. 1. N cavities (numbered 0 to N-1) uniformly distributed around a circular ring.

Since the frequency of each cavity is a monotonic function of its position k around the ring, acceleration is only possible in one direction of rotation when $N > 2$. If one wants to accelerate particles and their antiparticles simultaneously in the same ring, they must all circulate in the same direction.

2.3. *Issue of excursion in case of ultra-relativistic particles*

When HNJ is used to accelerate ultra-relativistic particles, the required variation of time of flight only comes from the variation of path length between each turn. In case of an acceleration cycle done over a number of turns N_t, with exactly one harmonic jump each turn, the average excursion from injection to extraction, defined as the variation of closed orbit circumference divided by 2π, is then given by:[10]

$$\text{average orbit excursion} = \frac{N_t}{2\pi} \cdot \lambda_{rf}, \tag{4}$$

where $\lambda_{rf} = \dfrac{c}{f_{rf}}$ is the rf wavelength.

If the number of turns is larger than 6, the average excursion becomes larger than the rf wavelength; rf cavity design issues could thus drastically limit the achievable number of turns. To avoid this problem, we need to vary the excursion along the ring, introducing reduced excursion insertions (REIs) in which cavities can be installed.

3. Design of Scaling FFAG Lattices for HNJ Acceleration of Muon Beams

In this section we consider the design of a muon ring only made of scaling FFAG cells, in which μ^+ and μ^- beams are accelerated simultaneously using the HNJ scheme. Regarding the constraints fixed in the previous section, this ring must have reduced excursion insertions, and must also be designed so that μ^+ and μ^- can circulate in the same direction.

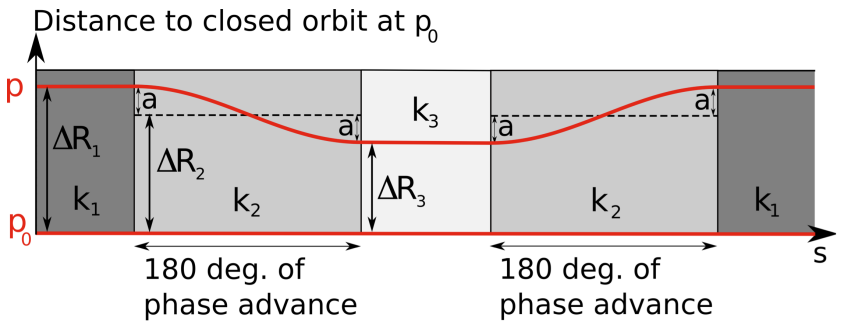

Fig. 2. Schematic view of a reduced excursion insertion (REI) made of scaling FFAG cells.

3.1. *Reduced excursion insertions*

To design a ring with REI we use different types of scaling FFAG cells. Before looking at the ring with insertions as a whole, it is useful to consider each type of cell separately. For a given momentum p, we thus define the "reference orbit" of each cell as the orbit followed by a particle which enters and exits the cell with the same transverse coordinates (r,z) and angles (r',z') with respect to the azimuthal vector.

We consider then to reduce the excursion by introducing, in a scaling FFAG ring made of cells with a field index k_1, two types of scaling FFAG cells with field indices k_2 and k_3 respectively. A schematic view of such an insertion is presented in Fig. 2. In this figure each gray shade represents an area filled with a different type of scaling FFAG cell, each cell consisting of several FFAG magnets.

Reference orbits of these three types of cells are matched at a given momentum p_0. The field indices k_1, k_2, and k_3 are chosen so that, for any momentum p:

$$\Delta R_1 - \Delta R_3 = 2 \cdot a = 2 \cdot (\Delta R_1 - \Delta R_2), \tag{5}$$

with a, ΔR_1, ΔR_2, and ΔR_3 as defined in Fig. 2. Now we consider the exact relation in scaling FFAG cells:

$$p = p_0 \cdot \left(\frac{R_i + \Delta R_i}{R_i} \right)^{k_i+1}, \qquad i = \{1,2,3\}. \tag{6}$$

with R_i the reference orbit radius for the given momentum p_0 in the section made of cells with field index k_i. Expanding it to first order in $\frac{\Delta R_i}{R_i}$ and using Eq. (5), one gets the relation between k_1, k_2, and k_3:

$$\frac{R_1}{k_1+1} + \frac{R_3}{k_3+1} = \frac{2 \cdot R_2}{k_2+1}. \tag{7}$$

The first order expansion in $\frac{\Delta R_i}{R_i}$ implies that this approach is valid as long as the maximum excursion is much smaller than the machine radius. In our case, since we are dealing with large rings for which the machine radius is much larger than

the orbit excursion, this condition is always valid. Thus, since ΔR_i is proportional to $\frac{1}{k_i+1}$, the dispersion is reduced by a factor of $\frac{k_3+1}{k_1+1}$.

For a momentum different from the reference momentum p_0, a mismatch appears in the positions of the reference orbits between the different types of cells. This mismatch induces a perturbation of the closed orbit shape, which can be seen as a coherent betatron oscillation around the reference orbit of the k_2 cells. Using a linear approach to describe the motion around this reference orbit one notices that, if the section made of k_2 cells has a horizontal phase advance of 180 degree, the closed orbit deformation is in the form of a half betatron oscillation. This way, the resulting closed orbit merges with the reference orbits in the sections made of k_1 and k_3 cells.

The fact that the reference radii R_i can be chosen different allows the design of non-circular rings. A large reference radius can be used in these reduced excursion area to increase the length of drift space allowing cavities to be installed without increasing the required magnetic field.

The principle of such an excursion suppressor relies on a strictly linear description of the motion around the reference orbit of the section made of k_2 cells. This principle is valid for any momentum, as long as the effect of non-linear field components is negligible.

3.2. *Several dispersion suppressors in cascade*

To reduce the excursion further, it can also be useful to use several dispersion suppressors in cascade. For an arbitrary number n of types of cells in cascade, following a similar approach to Sec. 3.1, one gets:

$$\frac{R_1}{k_1+1} + (-1)^{n-1}\frac{R_n}{k_n+1} = 2\sum_{i=2}^{n-1}(-1)^i\frac{R_i}{k_i+1}, \tag{8}$$

which is a generalized expression of Eq. (7).

3.3. *Two-Beam scaling FFAG lattices*

It is possible to circulate μ^+ and μ^- beams in the same direction simultaneously using the two-beam type of scaling FFAG doublet lattice proposed in Ref. 13. In order to improve the matching between different types of cells of a two-beam FFAG ring, we propose to use a two-beam lattice made of quadruplet cells, instead of doublets. The quadruplet type of cell has two main advantages compared to doublet:

(i) closed orbits of μ^+ and μ^- beams can overlap perfectly in the drift space, as shown in Fig. 3, which simplifies the closed obit matching between different types of cells;
(ii) values of the Twiss parameters are the same for μ^+ and μ^- beams at the matching point (middle of the long drift). The symmetrical behavior of both beams is thus conserved.

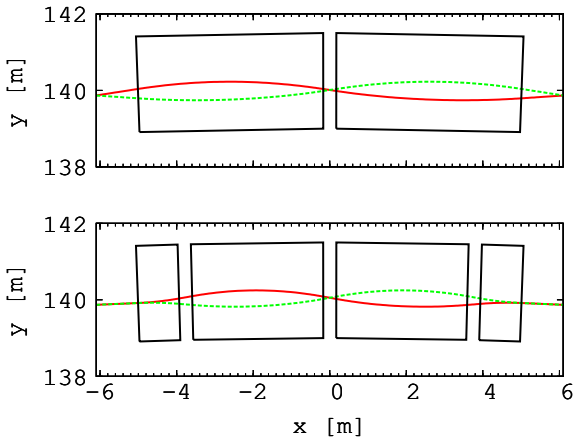

Fig. 3. Closed orbits of μ^+ (solid red lines) and μ^- (dotted green lines) circulating in the same direction in two-beam scaling FFAG doublet (upper part) and quadruplet (lower part) lattices. Closed obits are obtained from particle tracking in geometrical field model. Position of the magnet effective field boundaries are shown (black solid lines). Closed orbits for other energies are photographic enlargements of these ones.

Table 1. Ring Cells Parameters.

	Ring main part	Reduced excursion section	First dispersion suppressor	Second dispersion suppressor
Cell opening angle [deg.]	5	2.5	4.3	3.2
Reference orbit radius [m]	140	295	178	240
Field index k	130	508.5	186.4	339.6
Horizontal phase adv./cell [deg.]	87.4	85.8	90.0	90.0
Vertical phase adv./cell [deg.]	50.7	30.1	42.4	31.4
Number of these cells in the ring	8×4	8×4	4×4	4×4

3.4. *Example of lattice parameters*

We consider the example of a 3.6 to 12.6 GeV ring, only made of two-beam scaling FFAG quadruplet cells, with parameters given in Table 1. It is assumed to use scaling FFAG magnets with a maximum field below 4 T. It is a reasonable assumption once superconducting magnets with left-right asymmetrical coil distribution[14] are employed to realize the scaling field law. A schematic view of the ring is shown in Fig. 4. In this ring there are four insertions in which the excursion is reduced by almost a factor two.

We use stepwise particle tracking in geometrical field model to determine the lattice linear parameters and study the beam dynamics. Tracking simulations are conducted using a code based on Runge-Kutta integration developed at Kyoto University. The field distribution in the magnet mid-plane follows the form:

$$B_z(r,\theta) = B_{z0}\,\mathcal{R}(r)\,\mathcal{F}(\theta), \tag{9}$$

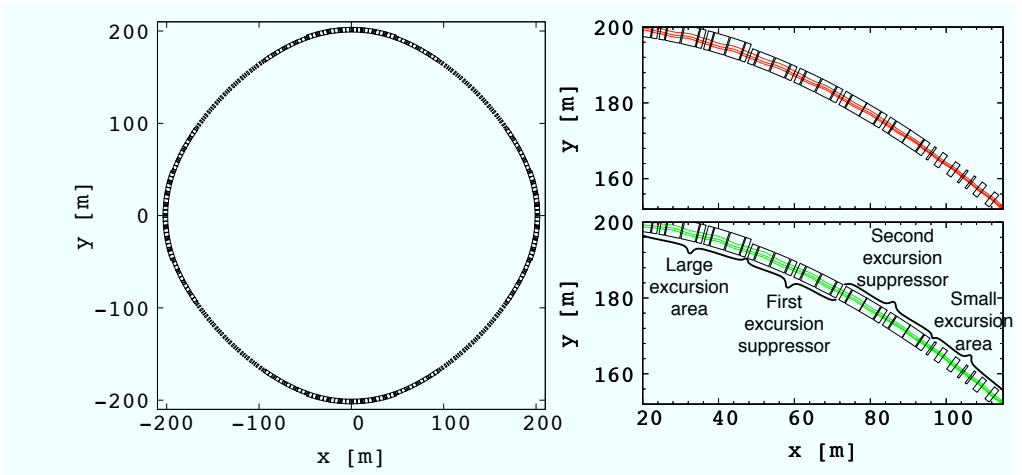

Fig. 4. Schematic view of the 3.6 to 12.6 muon ring. The four regions with the largest average radius are the reduced excursion areas. A zoom on the dispersion suppressors is presented in the right part of the figure. Closed orbits of μ^+ (upper-right part) and μ^- (lower-right part) circulating in the same direction are plotted at 3.6, 6 and 12.6 GeV.

with r the distance from the machine center and θ the azimuthal coordinate. The radial field law $\mathcal{R}(r)$ is proportional to r^k. The azimuthal field distribution $\mathcal{F}(\theta)$ is softened using Enge type of field fall-off.[15] Coefficient of the Enge distribution have been determined from a fit of the field fall-off of the RACCAM prototype magnet model.[16] Components of the field off the mid-plane are obtained, satisfying the Maxwell's equations, from a 4^{th} order Taylor expansion.

The phase advances given in Table 1 and the beta functions presented in Fig. 5 are obtained from stepwise tracking with small amplitude motion. The variation of betatron tunes between 3.6 and 12.6 GeV are shown in Fig. 6. Variations are identical for μ^+ and μ^- circulating in the same direction.

4. Summary and Discussions

We developed a lattice which has the unique features of:

(i) being only made of scaling FFAG type of cells,
(ii) including reduced excursion insertion and,
(iii) allowing μ^+ and μ^- beams to be accelerated in the same direction.

The tune variation over the whole energy range is limited to about 0.1. 6D tracking simulations results will be addressed in future work.

Moreover, with the two-beam quadruplet type of lattice presented in this paper, closed orbits of a particle and its antiparticle can overlap in drift space. This particular feature could open a way to low energy particle-antiparticle in-flight interaction experiments.

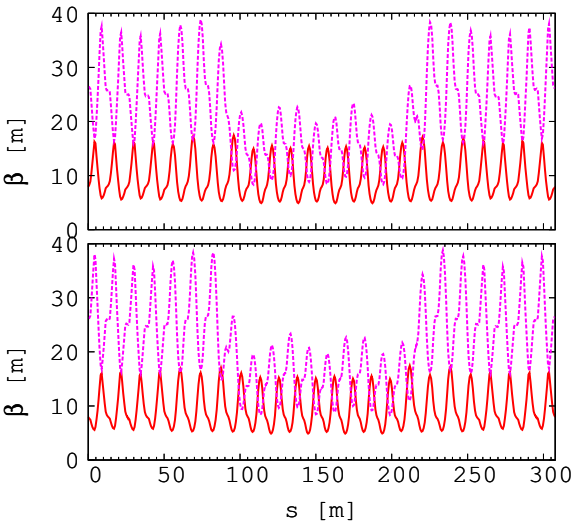

Fig. 5. Horizontal (red solid line) and vertical (dotted purple line) beta functions in the case of 6 GeV μ^+ (upper part) and μ^- (lower part) circulating in the same direction. One quarter is presented, with the larger excursion area placed in the central part of the plot.

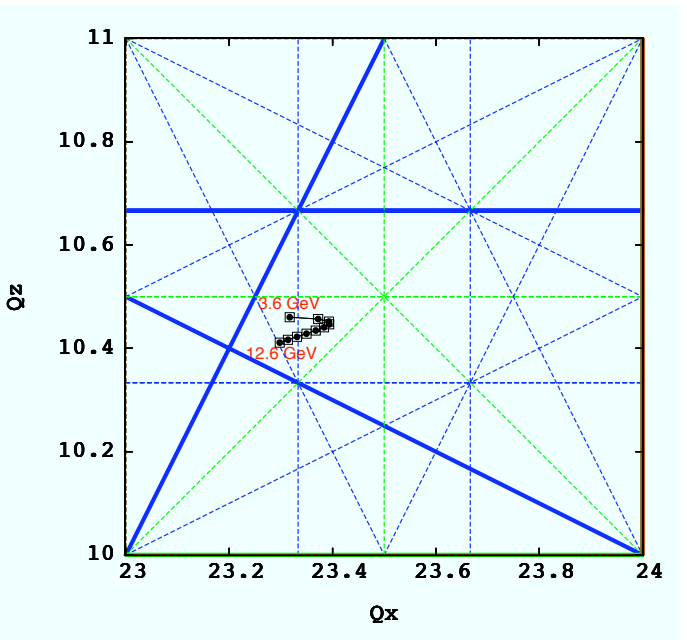

Fig. 6. Tune variation from 3.6 to 12.6 GeV, plotted every 1 GeV in the tune diagram. Result obtained for μ^+ are shown with squares. Results obtained with μ^- circulating in the same direction are show with dots. Both results are very similar. Structure resonance lines are shown with solid bold lines, while non-structure resonance lines are shown with dotted lines.

References

1. Y. Kuno *et al.*, A feasibility study of a neutrino factory in Japan, *KEK report*, (2001).
2. S. Ozaki *et al.*, Feasibility study-II of a muon-based neutrino source, *BNL report* **52623**, (2001).
3. The ISS Accelerator Working Group *et al.*, Accelerator design concept for future neutrino facilities, JINST 4 P07001, (2009).
4. J.S. Berg, *Nucl. Instr. and Meth. A* **570** ,15, (2007).
5. S. Machida, *Phys. Rev. ST Accel. Beams* **9**, 104002 (2006).
6. Y. Mori, FFAG accelerators and their applications, in *Proceedings of EPAC'06 conference*, (UK, Edinburgh, 2006), p. 950.
7. Y. Mori et al, Muon acceleration by scaling FFAG with harmonic number jump, in *presentation at ISS Machine WG 2628*, (USA, Princeton, 2006). `http://www.cap.bnl.gov/mumu/project/ISS/060726/`.
8. A. A. Kolomenskii, *Sov. Phys. Tech. Phys.* **5**,1278 (1961).
9. A. G. Ruggiero, *Phys. Rev. ST Accel. Beams* **9**, 100101 (2006).
10. T. Planche and Y. Mori, Harmonic number jump acceleration in scaling FFAG ring, to appear in *Proceedings of PAC'09 Conf.*, (Canada, Vancouver, 2009).
11. J. S. Berg, Harmonic number jump in a ring with cavities distributed everywhere, in *Proceeding of FFAG'06 Conf.* (Japan, Osaka, 2006), p. 69.
12. T. Planche and Y. Mori, Scaling FFAG lattices for muon acceleration, to appear in *Proceedings of NuFact09 Conf.*, (USA, Chicago, 2009).
13. T. Ohkawa, *Rev. Sci. Inst.* **29-2**, 108, (1958).
14. T. Nakamoto *et al.*, Design of Superconducting Combined Function Magnets for the 50 GeV Proton Beam Line for the J-PARC Neutrino Experiment, in *Proceedings of IEEE Int. Conf. Magnet Technology No18*, (Japan, Morioka City, 2004), p. 616.
15. H. A. Enge, Deecting Magnets, in *Focusing of Charged Particles*, Vol. 2, (A. Septier Academic Press, 1967), p. 203.
16. T. Planche *et al.*, *Nucl. Instr. and Meth. A* **604**, 435 (2009).

International Journal of Modern Physics A
Vol. 26, Nos. 10 & 11 (2011) 1842–1851

DOI: 10.1142/S0217751X11053237

World Scientific
www.worldscientific.com

EFFECTS OF ALIGNMENT ERRORS IN PROTON NON-SCALING FFAG ACCELERATORS

SUZANNE L. SHEEHY

John Adams Institute for Accelerator Science, University of Oxford, Denys Wilkinson Building, Keble Rd, Oxford, Oxfordshire, OX13RH, UK
s.sheehy1@physics.ox.ac.uk

DAVID J. KELLIHER

ASTeC, STFC Rutherford Appleton Laboratory, Chilton, Didcot, Oxfordshire, OX11 0QX, UK
david.kelliher@stfc.ac.uk

Non-scaling FFAGs have gained interest in the past decade for their potential application to charged particle therapy using proton and ion beams. However, linear ns-FFAGs naturally cross betatron resonances throughout acceleration. With an acceleration cycle of thousands rather than tens of turns, we find that resonance crossing produces severe orbit distortion in a linear proton/ion ns-FFAG in the presence of alignment errors. To overcome this, the PAMELA (Particle Accelerator for MEdicaL Applications) lattice design avoids resonance crossing with a non-linear ns-FFAG design. This design is outlined and a comparative analysis of alignment tolerances presented.

Keywords: FFAG; charged particle therapy; resonance crossing; hadron therapy; PAMELA.

PACS numbers: 11.25.Hf, 123.1K

1. Introduction

Non-scaling FFAG accelerators are being considered as an option for charged particle therapy (CPT) in place of existing technologies such as synchrotrons and cyclotrons, specifically as part of the PAMELA (Particle Accelerator for MEdicaL Applications) project.[1–3] The fixed magnetic field of the ns-FFAG allows 1kHz repetition rates, much higher than a synchrotron, while allowing for variable energy extraction, a property which cannot easily be provided by a cyclotron. The ns-FFAG can also be compact in size compared to a synchrotron and avoids complications of synchronizing magnetic field ramping with RF variation. The price paid for these advantages in the linear ns-FFAG is that the optical functions, specifically the betatron tunes, vary throughout the acceleration cycle, crossing potentially harmful resonances.

The main resonances of concern here are integer total tune resonances where Q_{horiz} or Q_{vert} = n. While previous studies such as Refs. 4, 5 studying muon or electron ns-FFAGs have suggested that the crossing of resonances is not harmful if the acceleration rate is sufficiently fast, a proton/ion accelerator for medical applications such as PAMELA will naturally have a much slower acceleration rate than a muon ns-FFAG. With this slower acceleration rate, for the design to be feasible it must be shown that resonance crossing does not lead to significant beam blow-up when realistic magnet alignment errors are taken into account.

For this purpose, three different proposed lattice designs are presented here and are systematically studied with the introduction of random alignment errors in order to determine the feasibility of each design once realistic errors are included. Two of the lattice designs are linear ns-FFAGs, these are the Keil, Sessler, Trbojevic (KST) lattice as in Refs. 6, 7 and 8 and a recent version of D. Trbojevic's lattice as in Ref. 9. The third is a novel ns-FFAG employing higher order multipoles to constrain the tune excursion of the whole ring to within half an integer throughout acceleration as in Refs. 10, 11.

2. Linear and non-linear ns-FFAG designs

Clinical considerations require that a proton/carbon CPT facility provides protons from 70 to 250 MeV and Carbon (C^{6+}) from 68 to 400 MeV/u. To achieve this, usually two or more accelerating rings are required. The lattice designs considered here all accelerate protons from 31 to 250 MeV and carbon ions from 8 to 68 MeV/u.

The ray-tracing code ZGOUBI[12] version 5.0.0 is used for the magnet descriptions and simulations as it allows for complex magnet geometry, highly accurate particle tracking and acceleration simultaneously.

2.1. *Lattice 1: KST lattice*

This lattice is the 2nd ring of the Keil, Sessler, Trbojevic (KST) 3-ring linear non-scaling FFAG complex for CPT. The lattice comprises 48 FD doublet cells, in which the quadrupoles provide both focusing and bending components due to a radial offset between the F and D.

For simulation purposes the lattice is modeled as quadrupole magnets with the radial offset described by a dipole field component. Lattice parameters are outlined in Table 1 and the cell layout shown in Fig. 1.

The magnets are rectangular in shape, and magnetic fringe fields are described using the Enge model, given in Eq. (1), where $F(R, \theta)$ is the fringe field coefficient. F is dependent on the radial coordinate and the azimuthal angle θ within the magnet, as the ZGOUBI magnet description is in polar coordinates. In this instance we use a half-gap height $g_0 = 0.03$m with coefficients: $C_0 = 0.1455, C_1 = 2.2670, C_2 = -0.6395, C_3 = 1.1558, C_4 = C_5 = 0$.

$$F(R, \theta) = \frac{1}{1 + \exp P(d)}. \tag{1}$$

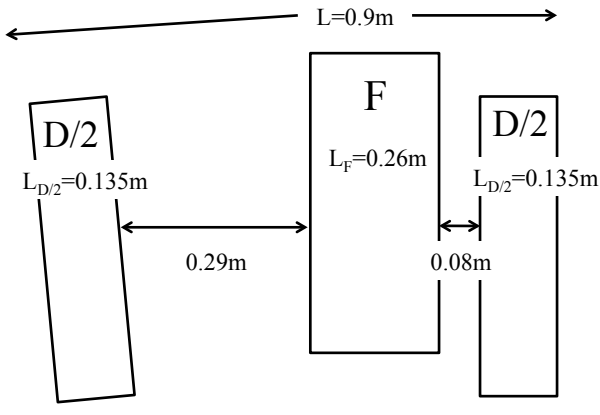

Fig. 1. Layout of one cell of the KST lattice from centre to centre of the D magnets in two adjacent cells.

Table 1. Parameters for KST lattice.

Parameter	Inj.	Ref.	Extr.
Proton Kin. Energy [MeV]	30.95	118.38	250
C^{6+} Kin. Energy [MeV/u]	7.84	30.98	68.36
Bρ [Tm]	0.81071	1.62142	2.43213
Cells	48		
r_0 [m]	6.875		
Magnet length (F/D) [m]	0.26 / 0.27		
Bend angle (F/D) [rad]	-0.1149 / 0.2458		
Quad. strength K (F/D) [m^{-2}]	9.56 / -10.74		
Half gap height [m]	0.03		
Long drift [m]	0.29		
Short drift [m]	0.08		
Orbit excursion [m]	0.065		

$P(d)$ is given in Eq. (2), where d is the distance to the edge of the magnet description and depends on (R, θ). Further details of this description can be found in Ref. 13.

$$P(d) = C_0 + C_1\frac{d}{g} + C_2\frac{d}{g}^2 + C_3\frac{d}{g}^3 + C_4\frac{d}{g}^4 + C_5\frac{d}{g}^5 \quad (2)$$

2.2. *Lattice 2: D.Trbojevic lattice*

This design is a linear non-scaling FFAG with 24 doublet focusing cells in a DF configuration. In this design the magnets are sector shaped, the details of which are given with the other lattice parameters in Table 2. For clarity, one cell with relevant parameters is shown in Fig. 2. As in Lattice 1 the Enge fringe field model is employed here with the same coefficients, with a half-gap height $g_0 = 0.03$m.

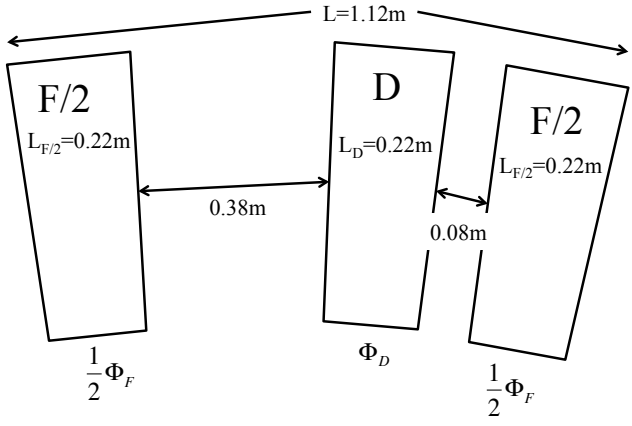

Fig. 2. Layout of one cell of the Trbojevic lattice from centre to centre of the F magnets in two adjacent cells.

Table 2. Parameters for D.Trbojevic lattice.

Parameter	Inj.	Ref.	Extr.
Proton Kin. Energy [MeV]	30.95	118.38	250
C^{6+} Kin. Energy [MeV/u]	7.84	30.98	68.36
Bρ [Tm]	0.81071	1.62142	2.43213
Cells	24		
r_0 [m]	4.278		
Magnet length (F/D) [m]	0.44 / 0.22		
Quad. gradient (F/D) [T/m]	8.73 / -14.30		
Sector angle (F/D) [rad]	0.153/0.109		
Half gap height [m]	0.03		
B_{max} (F/D) [T]	1.794 / 1.496		
Long drift [m]	0.38		
Short drift [m]	0.08		
Orbit excursion [m]	0.24		

2.3. *Lattice 3: PAMELA lattice*

This lattice was designed to overcome the high sensitivity of linear ns-FFAG lattices to alignment errors by avoiding resonance crossing. To avoid major integer and half-integer structural resonances it is necessary to constrain the total betatron tune to within half an integer throughout acceleration.

To achieve this, the lattice design begins with the concept of a radial-sector FDF triplet scaling FFAG. In a true scaling FFAG, the magnetic guide field strictly follows the scaling law $B = B_0(r/r_0)^k$, where r is the radial coordinate, k is the field index defined as $k = (r/B_y)(dB_y/dr)$ and y is the vertical direction. This results in a constant tune throughout acceleration.

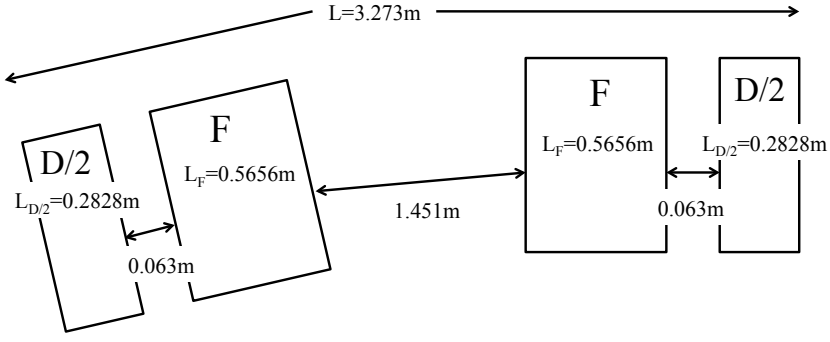

Fig. 3. Layout of one cell of the PAMELA lattice from centre to centre of the D magnets in two adjacent cells.

Table 3. Parameters for PAMELA lattice.

Parameter	Inj.	Ref.	Extr.
Proton Kin. Energy [MeV]	30.95	118.38	250
C^{6+} Kin. Energy [MeV/u]	7.84	30.98	68.36
Bρ [Tm]	0.81071	1.62142	2.43213
Cells	12		
r_0 [m]	6.251		
Magnet length (F/D) [m]	0.3144 / 0.3144		
Bending angle inj. (F/D) [deg]			
Bending angle extr. (F/D) [deg]			
Field index, k	38		
Long drift [m]	1.702		
Short drift [m]	0.3144		
Orbit excursion [m]	0.176		

To reduce the large orbit excursion characteristic of scaling FFAGs, this design employs a field index which is in the second stability region of Hill's equation. The PAMELA lattice design, as in Fig. 3, then makes a number of changes and simplifications which make the machine non-scaling.[10]

Firstly, the magnetic field is expanded in terms of its multipole components and only the dipole and first few multipoles are retained. This allows each multipole field to be introduced independently and removes the need for iron-cored magnets with complicated pole shaping used in a scaling FFAG. To ease cost, construction and alignment issues, the magnets are made rectangular rather than sector-shaped and are aligned along a straight line in each cell rather than along an arc, further violating the scaling law. The lattice design parameters for PAMELA are outlined in Table 3, and the betatron tunes throughout acceleration are shown in Fig 4. For all following studies the magnetic field expansion includes multipoles up to and including the decapole. The cell tunes at injection are $\nu_x = 0.732$, $\nu_y = 0.293$.

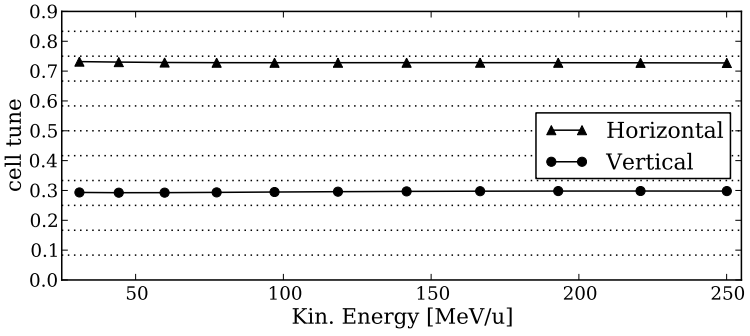

Fig. 4. Betatron cell tunes throughout acceleration for PAMELA lattice design with multipoles up to decapole. Dashed lines correspond to integer and half-integer total tune resonances.

3. Sensitivity to alignment errors

3.1. *Method*

For each of the designs, Gaussian distributed patterns of random horizontal alignment errors were introduced to each magnet in the lattice, using 10 different values of the standard deviation σ from 0 to 100 μm in steps of 10 μm. The gaussian distributions are cut-off at 3σ, which removes very large errors which could have a dominating effect on the dynamics.

For each value of σ, a different random value is applied to each of the lattice magnets and a single particle is tracked over 1000 turns. This is repeated 10 times for each σ value and the mean and RMS values of the orbit distortion are obtained.

To ascertain the sensitivity of each design to alignment errors, the same acceleration rate is used in each lattice. In each case acceleration is achieved in 1000 turns with an energy gain of 183.85 kV/turn. Whilst this does not quite cover the full energy range of each lattice, it is suitable as a point of comparison. Synchrotron motion is neglected as only the transverse dynamics are of interest here. The 'cavities' are represented as zero-length elements providing a simple energy gain and in each case are evenly spaced throughout the lattice.

The orbit distortion is defined as the maximum deviation of the tracked particle from the closed orbit of the error-free lattice. The distortion is quantified by an 'amplification factor' A:

$$A = \frac{\langle \text{Orbit distortion [mm]} \rangle}{\langle 1\sigma \text{ Alignment Error [mm]} \rangle}. \tag{3}$$

3.2. *Results*

The results of the orbit distortion study with horizontal alignment errors are shown in Fig. 5. For each σ value, the mean orbit distortion is plotted along with error bars corresponding to the RMS values. This distribution is presented with a linear

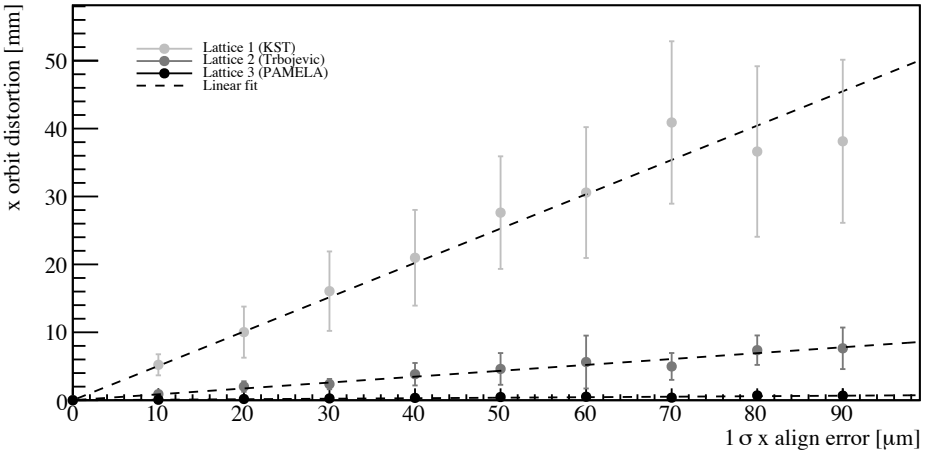

Fig. 5. Comparative orbit distortion of each lattice as a function of alignment error.

Table 4. Amplification factors.

Lattice	Horizontal amplification factor, A
1 (KST)	505.4 ± 54.7
2 (Trbojevic)	86.7 ± 10.5
3 (PAMELA)	7.4 ± 1.2

fit, the gradient of which corresponds to the amplification factor obtained for the relevant lattice design. The amplification factors are given in Table 4.

3.3. *Discussion*

The best alignment tolerances achieved in reality are around 50 μm. In Lattice 1, where the amplification factor is found to be 505.4 ± 54.7, this magnitude of error would result in an orbit distortion of around 25 mm. In Lattice 2 a similar error would result in orbit distortion of around 4.3 mm, which is a significant improvement. However, taking into account additional sources of error including vertical and rotational alignment errors and a realistic magnetic field quality, in a real machine a more severe orbit distortion is expected than that observed here. Both of these lattices appear to require alignment tolerances which are extremely severe and not achievable with current alignment techniques.

Orbit correction may be possible in the linear ns-FFAG lattices. An example of this is Ref. 14, where the level of reduction in orbit distortion was $\approx 25\%$ by optimizing the injection phase space parameters, with small further reductions achieved by using a so-called overall correction method. While these reductions are advantageous, they would be insufficient in the case of the linear proton ns-FFAGs, where a reduction in orbit distortion of around an order of magnitude or more is required.

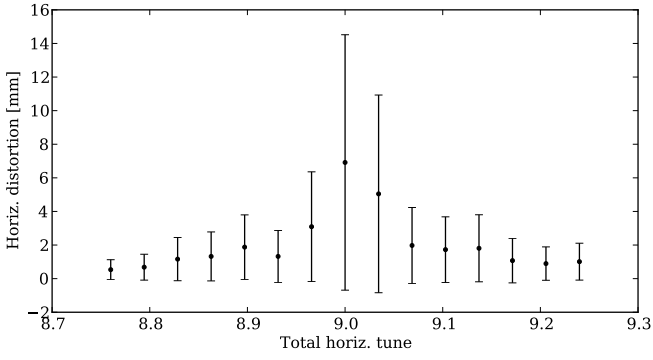

Fig. 6. Orbit distortion of Lattice 3 for 50 μm horizontal alignment errors for varying total horizontal tune.

The difference between the results of Lattice 1 and Lattice 2 is assumed to arise from the number of major resonances crossed during the acceleration cycle in each machine and the crossing speed of these resonances. For Lattice 1, around 12 integer machine tune resonances are crossed in the horizontal plane, compared with just 3 in the horizontal plane for Lattice 2. The effect of resonance crossing also depends on the speed of the crossing. According to Baartman[15] amplitude growth should be proportional to $Q_t^{-1/2}$ where Q_t is the change in tune per turn. Since the same number of turns is used in each case, the ratio of the lattice average crossing speeds should also be 1:4 and thus the amplitude growth should be 2:1 for Lattice 1 and Lattice 2, respectively. Within error, these two effects can account for the observed differences.

By comparison, the results for Lattice 3 indicate that by avoiding crossing major resonances, the alignment tolerances become much less severe. The orbit distortion from 50 μm errors in this case is just 0.4 mm. To check if distortion also arises in this lattice when the total horizontal tune is near to an integer, the varying distortion with total horizontal tune was studied. Lattice configurations were used varying the field index, k and ratio between the D and F magnets to achieve total horizontal tunes between 8.7 and 9.3 at the injection energy. For each configuration a random Gaussian distribution of horizontal alignment errors was applied to the lattice magnets, with a standard distribution of 50 μm. A single particle was tracked through 10 turns without acceleration at each tune value and the maximum distortion calculated as before. This is done 10 times for each tune value and the resulting mean is shown with error bars representing the RMS of the 10 trials. There is a clear increase in the distortion when the tune nears the integer, as shown in Fig. 6. This shows that the tune in this lattice must be kept away from an integer in order to avoid unnecessary orbit distortion.

It should be noted that the introduction of non-linear field components has the effect of reducing the dynamic aperture of this type of ns-FFAG when compared to its linear counterpart. However, the dynamic aperture of this lattice design has

previously been found to be more than 30π mm mrad normalized in both the horizontal and vertical plane[11] and is not expected to degrade substantially with the inclusion of alignment errors, as discussed in Ref. 10. This dynamic aperture is sufficient for the CPT application.

4. Summary

Non-scaling FFAGs remain an attractive option for CPT. However, the two linear ns-FFAG designs studied here are highly sensitive to alignment errors when acceleration is achieved in 1000 turns. The density of the linear ns-FFAG lattices may also make injection and extraction extremely challenging. The non-linear ns-FFAG design for PAMELA employs a lattice which successfully constrains horizontal and vertical betatron tunes to within half an integer, avoiding resonance crossing, while providing long straight sections to enable injection and extraction. Avoiding resonance crossing dramatically reduces the sensitivity to alignment errors and indicates that the design is feasible in terms of alignment tolerances. The variable energy extraction system for the PAMELA design requires the orbits on each turn to be separated by 30 mm.[16] The small amount of orbit distortion in the PAMELA lattice is significantly smaller than this and should not affect variable energy extraction.

Acknowledgment

This work is supported by EPSRC grant EP/E032869/1.

References

1. K. Peach et al., in *Proc. Particle Accelerator Conference*, (Albuquerque, 2007), p. 2880.
2. K. Peach et al., in *Proc. Particle Accelerator Conference*, (Vancouver, 2009).
3. R. Barlow et al., in *Proc. Particle Accelerator Conference*, (Albuquerque, 2007), p. 2886.
4. S. Machida and D. J. Kelliher, *Phys. Rev. ST Accel. Beams* **10**, 114001 (2007).
5. S.Machida, *Phys. Rev. ST Accel. Beams* **11**, 094003 (2008).
6. E. Keil, A. M. Sessler and D. Trbojevic, *Phys. Rev. ST Accel. Beams* **10**, 054701 (2007).
7. E. Keil, A. M. Sessler and D. Trbojevic, in *Proc. European Particle Accelerator Conference*, (Edinburgh, 2006), p. 1681.
8. E. Keil, A. M. Sessler and D. Trbojevic, in *Proc. International Workshop on FFAG Accelerators*, (2007).
9. D. Trbojevic, Small proton therapy accelerator by non-scaling FFAG, presented at *International Workshop on FFAG Accelerators*, (Manchester, 2008).
10. S. Machida, FFAGs for proton acceleration, presented at *International Workshop on FFAG Accelerators*, (Manchester, 2008).
11. S. L. Sheehy, H. Witte, K. Peach, D. Kelliher, S. Machida, Fixed field alternating gradient accelerator with small orbit shift and tune excursion, *Phys. Rev. ST Accel. Beams* **13**, 040101 (2010).
12. F. Méot, *Nucl. Instr. Meth. A* **427**, p. 353 (1999).

13. F. Méot, S. Valeri, ZGOUBI users' guide, *CEA DSM DAPNIA* **02**, 395 (2002), p.86.
14. D. Kelliher, S. Machida, Orbit distortion and its correction in a non-scaling FFAG, in *Proc. European Particle Accelerator Conference*, (Genoa, 2008), p. 3383.
15. R. Baartman, Fast crossing of betatron resonances, in *Proc. International Workshop on FFAG Accelerators*, (2004).
16. T. Yokoi et al., in *Proc. International Particle Accelerator Conference*, (Kyoto, 2010), p. 567.

International Journal of Modern Physics A
Vol. 26, Nos. 10 & 11 (2011) 1852–1864

DOI: 10.1142/S0217751X11053249

World Scientific
www.worldscientific.com

CROSSING RESONANCES IN A NON-SCALING FFAG

D. TRBOJEVIC,* M. BLASKIEWICZ and E. FOREST
Brookhaven National Laboratory, Upton, New York, USA
**dejan@bnl.gov*

There are many possible applications for the non-scaling Fixed Field Alternating Gradient (NS-FFAG): accelerating non-relativistic ions, ion cancer therapy, proton drivers, accelerator driven subcritical reactors, heavy radioactive ions, recirculating linacs, and etc. They are confronted with two significant challenges: first is crossing integer resonances as the tunes vary with energy, and that the required fast acceleration has not yet been achieved in practice. An example of a small 30–250 MeV NS-FFAG proton accelerator is used to study both problems. After an introduction, the second chapter shows theoretical predictions for the emittance blow up from crossing the integer resonances. In the third part, the lattice of the ring is briefly described. The fourth chapter describes the "phase jump" a method for fast proton acceleration, while in the chapter five a six dimensional simulations of acceleration is described, ending with conclusions.

1. Introduction

The scaling Fixed Field Alternating Gradient (FFAG) accelerators revival during the last decade is very prominent.[1] There are already built and commissioned machines, mostly in Japan, with clear possibilities for more applications. A fast acceleration of the short lifetime muons is very difficult by varying the magnetic field if the linac solution is considered too expensive. The NS-FFAG came out from trying to solve a problem of accelerating muons very fast due their short decay time. The fixed magnetic field and acceleration at the fixed frequency at the top of the RF wave with several turns has been considered a valuable solution. For the relativistic particles, the time of flight dependence on energy might be within acceptable range to allow the "serpentine" acceleration, where particles arrive after every turn close enough to the top of the sine RF voltage. The NS-FFAG came as an alternative method trying to reduce the relative large required aperture of the scaling FFAG's at the expense of losing isochronicity and constant tune with zero chromaticity. Other possible applications of the NS-FFAG in accelerating non-relativistic ions could be in proton/carbon cancer therapy accelerators, for a proton driver, for a accelerator driven subcritical nuclear reactor, acceleration of radioactive heavy ions, recirculating linacs for muon or electron acceleration, etc. Tune and chromaticity variation with energy present a very serious problem as hundreds of turns are required due to the limits of how fast can the RF frequency or phase

can change during a short time. The non-relativistic acceleration of the proton or light ions with the NS-FFAG has to be fast enough to avoid emittance or beam amplitude blowup due to crossing integer resonances. The amplitude growth during the resonance crossings depends on errors in the magnetic field and on the speed of the resonance crossing. Results of few simulation studies[7–9] have shown very good agreement with analytical predictions by R. Bartmaan.[10] Details of the analytical predictions and simulation are presented in the next chapter.

2. Resonance Crossing During Acceleration

The resonance occurs when m$\nu = n = fN_p$ where ν is the tune of the ring, m is the order of the resonance driving term, n corresponds to the n^{th} harmonic Fourier component of the $(m-1)^{th}$ derivative of the magnetic field, f is an integer, and N_p is the number of lattice periods. The intrinsic or systematic resonances of an accelerator depend on the number of lattice periods N_p through the resonance condition: $m\nu = N_p$. The betatron amplitude is defined as $A = \sqrt{2J/\nu}$ with a resonance condition $m\nu = n$, while the resonance strength parameter $b_{n,m}$ is such that

$$nb_{n,m+1} = \frac{\overline{R}}{\overline{B}} \frac{1}{m!} \frac{\partial^m B_n}{\partial x^m}, \tag{1}$$

where the average magnetic field $\overline{B} = B\rho/R$. One of the most important parameters in resonance crossing is the speed of tune variation $\nu_\tau = \Delta\nu/N_0$, where the $\Delta\nu$ is the tune change and N_0 is the number of turns during acceleration. The action variables J and ψ, with $x = A\cos(n\theta + \phi) = A\cos\psi$, where θ is the azimuth around the ring. Resonance crossing through the integer $(m = 1)$, half-integer $(m = 2)$, and the third of an integer $(m = 3)$ are shown in this order:

1. The first order $m = 1$: For $m = 1$ and $\nu = n$ the amplitude growth for integer resonance crossing is:

$$\Delta A = \pi \frac{b_{n,1}}{\sqrt{\nu_\tau}} = \frac{\pi}{\sqrt{\nu_\tau}} \frac{\overline{R}}{\overline{B}} \frac{B_n}{\nu} = \frac{1}{2\nu} \frac{C}{\sqrt{\nu_\tau}} \frac{B_n}{\overline{B}}. \tag{2}$$

2. The half integer $m = 2$: For the half integer resonance crossing $m = 2$ and $n = 2\nu$, the resonance coefficient $b_{n,2}$ is:

$$b_{n,2} = \frac{\overline{R}}{n\overline{B}} \frac{\partial B_n}{\partial x}, \tag{3}$$

with the ratio of the final to the initial amplitude is given by:

$$\log \frac{A_f}{A_i} = \frac{\pi}{\sqrt{2}} \frac{b_{n,2}}{\sqrt{\nu_\tau}}. \tag{4}$$

3. Third order $m = 3$: The higher order resonances are less of a problem but the third integer resonance crossing could be a serious problem if the cell tunes cross a value 1/3, as any systematic sextupole fields in the ring also excite the intrinsic resonance $3\nu = N_p$, making the emittance growth such that

$$\Delta\frac{1}{\sqrt{\varepsilon}} = \frac{\pi}{4\sqrt{3}}\frac{1}{\sqrt{\nu_\tau}}\frac{R}{B\rho}\left|\beta^{3/2}\frac{\partial^2 B_z}{\partial x^2}\right|_{n=3\nu}, \tag{5}$$

where R is the radius of the ring, $\partial^2 B_z/\partial x^2$ is the second derivative of the magnetic field, and β_x the transverse betatron amplitude.

Faster acceleration in the NS-FFAG is preferable not only due to better resonance crossings without significant amplitude growth, but also for the higher ion delivery rate reducing the time of patient treatment. To accelerate non relativistic ions with the NS-FFAG implies a large range of speeds, and some small orbit length change, and thus requires fast and large frequency variation or fast RF phase jump variation after every turn. In crossing the one-fourth integer of the cell tune may be of concern if transverse space charge forces are at a significant level.

3. Non-Scaling FFAG Ring Lattice

The resonance crossing simulation in six dimensional phase space were performed on the small NS-FFAG ring, presented in Fig. 1. The ring is constructed of 24 cells. Each cell has two 44 cm and 30 cm long focusing and defocusing combined function magnets, respectively. The momentum acceptance for protons at the fixed magnetic field is $\delta p/p = \pm 50\%$ or, for the kinetic energy, 31–250 MeV. The diameter of the ring is 8.56 m with a circumference of $C = 26.88$ m. There are twelve cavities marked by the lines—thin lens approximations, and three injection/extraction kickers represented by rectangular boxes. The sector type combined function magnets are represented by trapezoidal shapes.

Two focusing and defocusing combined function magnets have positive bending for the central momentum, with the magnetic fields of $B_f = 0.563$ T and $B_d = 0.804$ T, respectively. The magnetic fields at focusing and defocusing combined function magnets are at the maximum orbit offsets: $B_{f-max} = 1.79$ T at $x_{max} = 14.1$ cm with the gradient of $G_f = 8.73$ T/m, and $B_{d-max} = 1.7$ T at $x_{max} = -6.3$ cm with the gradient of $G_d = -14.3$ T/m, respectively. The magnets of the one cell and orbit offsets are shown in Fig. 2.

The variation of the tunes with momentum (energy) is shown in Fig. 3. The magnet gradients were retuned to avoid $\nu_x = 0.333$ crossing the third order per cell after the results of the acceleration simulation.

The variation of the betatron amplitude functions in the cell due to momentum is shown in Fig. 4.

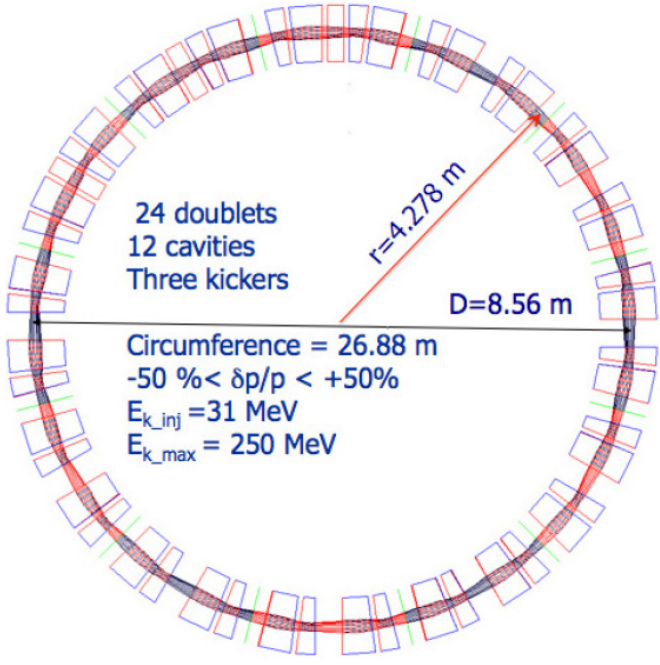

Fig. 1. NS-FFAG ring for accelerating protons from 31–250 MeV. A circumference is 26.88 m, 12 cavities (lines), 3 injection/extraction kickers (rectangular boxes), doublets—combined function magnets (trapezoidal shapes).

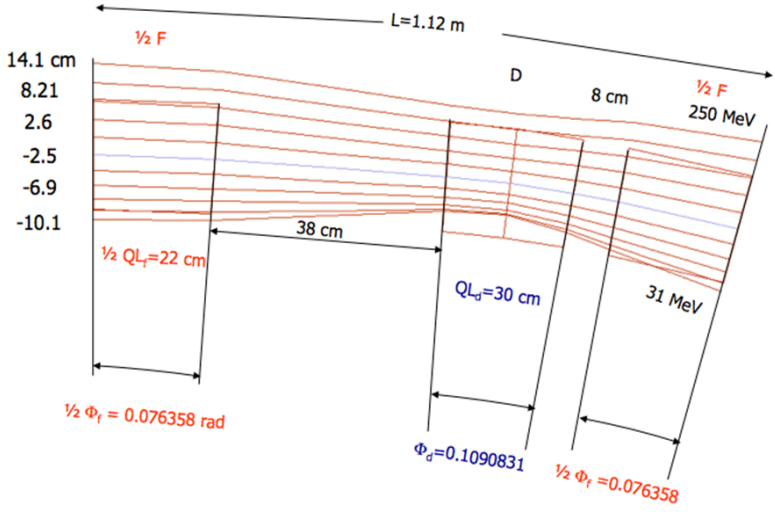

Fig. 2. The basic cell with magnets and drifts dimensions with orbit offsets variation with energy. The 38 cm drifts are for cavities and injection/extraction kickers.

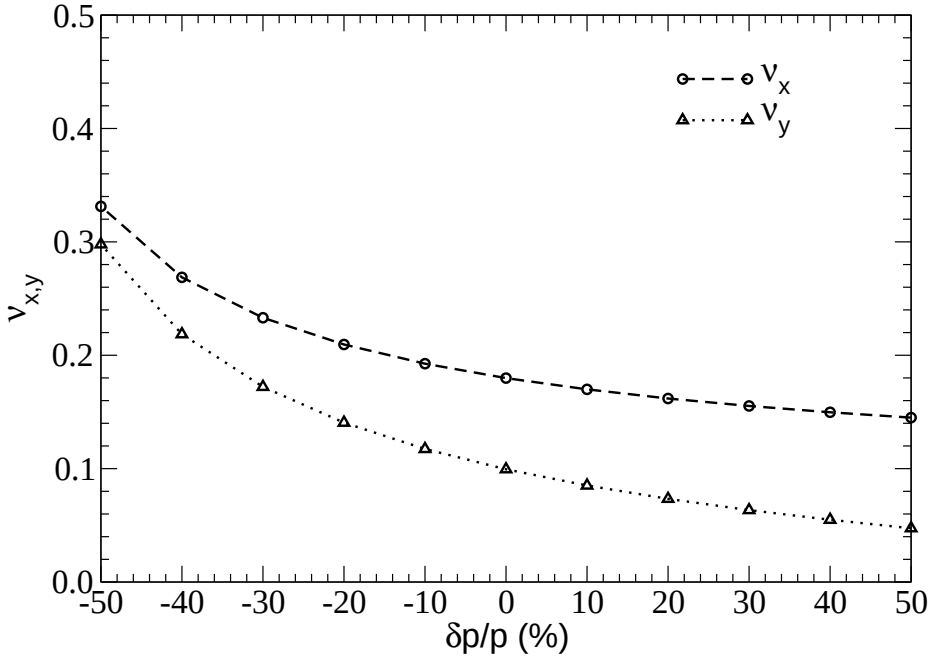

Fig. 3. Tune dependence on momentum in the basic cell of the NS-FFAG.

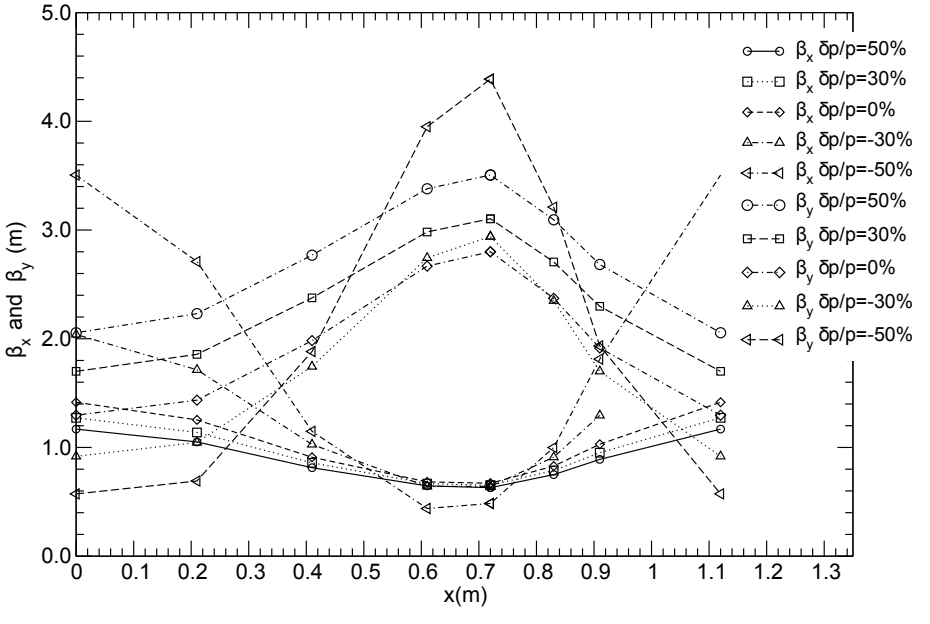

Fig. 4. Betatron functions variation with energy in the basic NS-FFAG cell.

4. Acceleration Method—Phase Jump

The acceleration is performed by adjusting the RF phase each turn. The phase jump during acceleration with a fixed frequency has previously been shown at CERN[14] and recently re-examined by M. Blaskiewicz[15] from BNL. The RF frequency needs to be in a high range, $\sim$370 MHz, because of the required large number of RF cycles between the passages of bunches, in order to achieve higher values of Q. The basic idea is to accelerate a train of bunches with a gap. During the gap the RF phase is adjusted so that when the bunch train next arrives the phase is correct for acceleration. The challenge is find a low level RF drive signal, which causes the cavity voltage to reach a certain target value during the gap. We will find that power is an issue, so let the output RF amplitude of the klystron be related to the low level drive by,

$$\tau_k \frac{d\hat{I}}{dt} + \hat{I} = gV_L, \tag{6}$$

where $I(t) = Re(\hat{I}(t)\exp(j\omega_0 t))$ is the klystron output current and ω_0 is the angular resonant frequency of the RF cavity. The amplitude of the cavity voltage satisfies:

$$\tau_c \frac{d\hat{V}}{dt} + \hat{V} = 2R\hat{I}, \tag{7}$$

where R is the cavity shunt impedance, $\omega_0\tau_c = Q$ and the resonant frequency of the cavity and klystron are the same. For a step input $V_L(t) = H(t)V_0$ with H the Heaviside function the klystron current is:

$$\hat{I}(t) = H(t)gV_0[1 - \exp(-t/\tau_k)]. \tag{8}$$

The cavity voltage amplitude has a simple solution for $\tau_c = \tau_k = \tau$ which is

$$\hat{V}(t) = H(t)2gV_0R[1 - (1 + t/\tau)\exp(-t/\tau)]. \tag{9}$$

This equation does not go to a finite value in fixed time. However consider $V_T(t) = \hat{V}(t) + a\hat{V}(t-T) + b\hat{V}(t-2T)$ where a and b are constants and T is some characteristic time. By choosing a and b correctly one can make $V_T(t)$ constant for $t > 2T$. The solution is shown in Fig. 5. Fig. 6 shows the necessary drive to shift the phase by 180°, the worst case. For other phases one would drive the out of phase part of the drive, i.e. the imaginary part of $V_L(t)$ would be non-zero. For the 190° jump the peak klystron output current is about 2.5 times larger than the steady state value. This means that the installed RF voltage, when running steady state, must be able to generate 2.5 times more voltage than the beam needs. The total gap in the bunch train is $2T = Q/\omega_0$ and provides the tightest constraint at top energy since the revolution period decreases but the length of the bunch train, in time, remains fixed. We have modeled an RF cavity for proton acceleration to 250 MeV, the β value changes from injection 0.251 to 0.614 and the cavity impedance varies by a factor of three. At top energy $R/Q = 30\Omega$ throughout the cycle $Q = 50$ and $f = 374$ MHz, and the exponential decay time for the field is 43 ns.

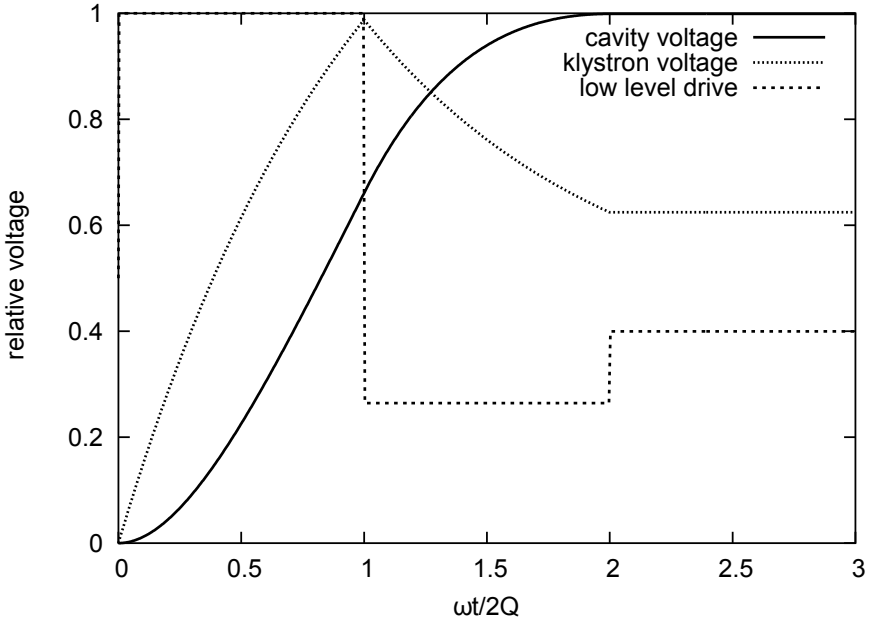

Fig. 5. Cavity voltage during the phase jump acceleration. The klystron voltage in shown using a dotted line, while the low level RF drive is shown using a dashed line.

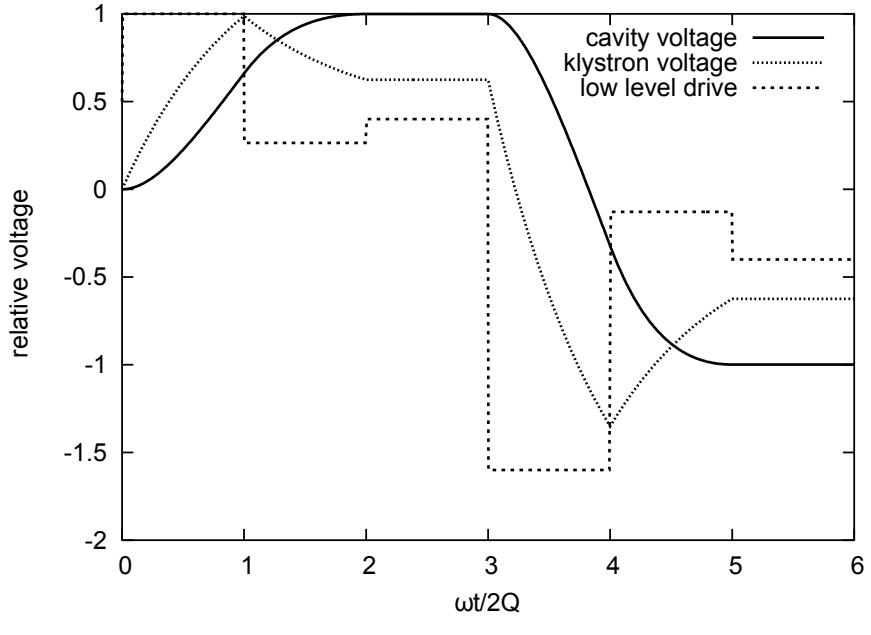

Fig. 6. The full cycle with the cavity voltage (firm line) during the phase jump acceleration. The klystron voltage in shown using a dotted line, while the low level RF drive is shown using a dashed line.

With a 100 kW klystron the steady state cavity voltage is $\hat{V} = \sqrt{8PR} = 35$ kV. Dividing by 2.5 yields an operating voltage of 14 kV at top energy and, correcting for transit time, 5 kV at injection energy.

For the simulations, we took 19 kV per cavity so the number of proton revolutions required is 1200. Assuming the use of 12 cavities, the total RF power involved is 1.2 MW and this is a consequence of the rapid acceleration. Faster resonance crossing would involve even more power.

5. Crossing Resonances in the NS-FFAG—Six Dimensional Simulation

The six-dimensional phase space simulation of acceleration in the NS-FFAG was performed by using the Polymorphic Tracking Code (PTC) by E. Forest.[13] The initial transverse emittance of $0.5 \cdot 10^{-6}$ m·rad is used with initial of $N_{init} = 1100$ particles distributed in the six dimensional phase space with Gaussian distributions in the transverse phase space. The average beam size σ was defined from the emittance ε_N as $\sigma = \sqrt{\varepsilon_N \beta_{twiss}/6\pi\beta\gamma}$, where β_{twiss} is the amplitude-betatron function, $\beta\gamma$ are relativistic factors. In the longitudinal phase space, a line of charges started the acceleration to become a bucket after going through the twelve RF cavities in few turns. A logical flag was set and each lost particle was accounted for. The NS-FFAG has linear dependence of the magnetic field along the radial axis. The tune shift does not depend on amplitude unless we introduce the magnetic field errors $\Delta B/B_n$ or misalignment errors. Most of the NS-FFAG designs include a horizontal tune of 1/3 in the range of allowed tune variation (0.4–0.1) per single cell. The resonance crossing of the third integer, $m = 3$, when the cell tune includes tunes of 1/3, can become very difficult if there is a slight systematic sextupole component in the magnetic field.[10] The third integer resonance occurs when $3\nu = n$. The strength of the resonance $b_{n,3}$ (Eq. 5) becomes large when $n = N_p$, a condition for the intrinsic or structural resonance. In the first acceleration simulation study, the random magnetic field errors were absent and no emittance growth was observed.

1. The cell tune $\nu_{x,y} = 1/3$ included, $\Delta B/\overline{B}_n = 10^{-3}$, and $N_{turns} = 6000$.
   The random error of the magnetic field $\Delta B/\overline{B}_n = 10^{-3}$ was introduced. The range of the tunes variation per cell was $0.4 \leq \nu_{x,y} \leq 0.1$ (or $9.6 \leq \nu_{x,y} \leq 2.4$ for the whole ring) included the horizontal tune per cell of $\nu_x = 1/3$. The acceleration speed $\nu_\tau = \Delta\nu/N_0$ was $\nu_\tau = 1.2{\cdot}10^{-3}$ for a total number of turns $N_0 \sim 6000$. The horizontal tune in the ring crosses the integer value of $\nu_x = 8.00$ at the beginning of the acceleration cycle (the horizontal tune in the cell was $\nu_{x\_cell} = 1/3$). This represents a problem as $3\nu_x = 24$ with $n = 24$. The slower acceleration rate of 6000 turns has shown very large amplitude growth with a significant beam loss of $N_{lost} = 609$ of $N_{init} = 1100$ protons, as presented in Fig. 7. Details of the $x - x_p$ phase space during the third resonance crossing are shown in Fig. 8. The emittance blow-up due to the third integer crossing provided by Eq. 5 with

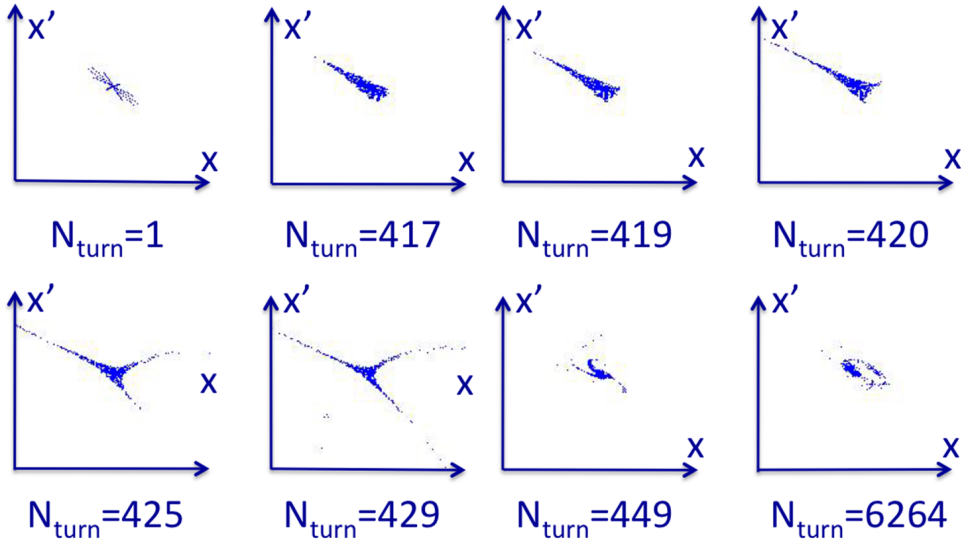

Fig. 7. Slow proton acceleration from 31–250 MeV in the NS-FFAG, with a total number of turns of $N_0 \sim 6000$. When the turn number reached $N_{turn} = 428$, the horizontal betatron tune in the 24 period ring was equal to $\nu_x = 8.00$.

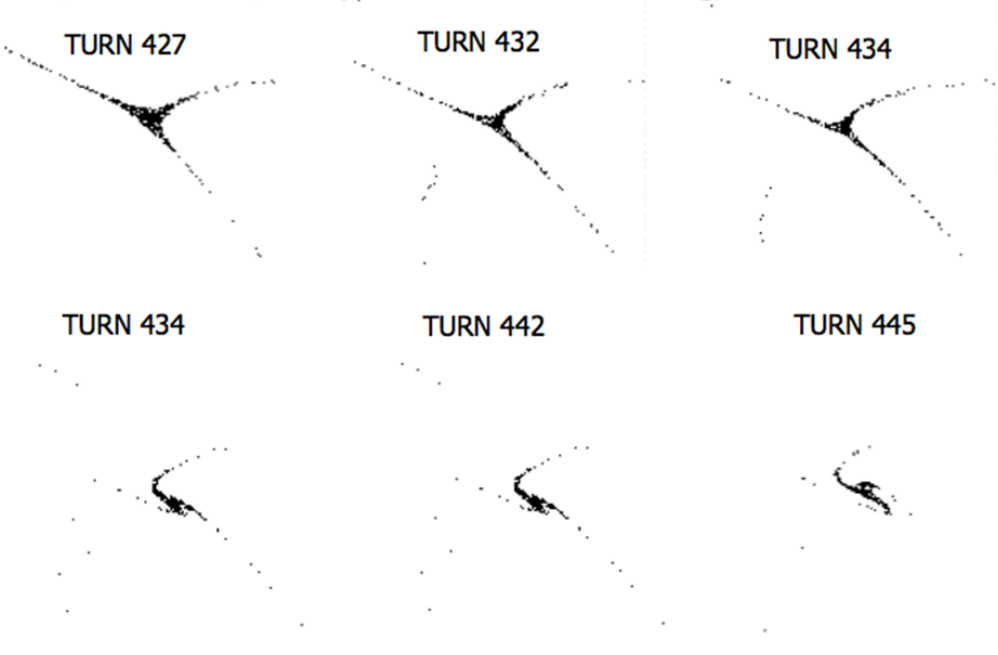

Fig. 8. Details of the slow (∼6000 turns) resonance crossing of the $\nu_{x_{cell}} = 1/3$ per cell in the NS-FFAG during the proton acceleration.

$\beta = 0.6$ m, $C = 26.88$ m and $B\rho = 0.818$ Tm is:

$$\Delta\left(\frac{1}{\sqrt{\varepsilon}}\right) = 1.102\frac{\partial^2 B_z}{\partial x^2}\frac{1}{\sqrt{\nu_\tau}} \text{ or for } \varepsilon = 0.5\cdot 10^{-6} \text{ mrad:}$$
$$\frac{\Delta\varepsilon}{\varepsilon} = 1.56\cdot 10^{-3}\frac{\partial^2 B_z}{\partial x^2}\frac{1}{\sqrt{\nu_\tau}}. \tag{10}$$

The sextupole component of the magnetic field in the Taylor expansion could be estimated as $B''x^2/2! = 2\cdot 10^{-3}\cdot B_0$, $B'' \sim 6.2$ T/m^2. The emittance blow-up, with an average sextupole component of $2{\cdot}10^{-3}$ for 6000 turns is $\Delta\varepsilon/\varepsilon_{6000} \sim 0.28$.

2. The cell tune $\nu_x = 1/3$ included, $\Delta B/\overline{B}_n = 10^{-3}$, and $N_{turns} = 1300$.
The simulation of the proton acceleration with a rate of $\nu_\tau = 5.54\cdot 10^{-3}$, and a total number of $N_0 = 1300$ turns is presented in Fig. 9. The crossing of the third order resonance per cell did not produce a dramatic amplitude growth and the beam loss was reduced to $N_{lost} = 98$ protons, with initial number of $N_{init} = 1100$. Eq. 10 predicts $\Delta\varepsilon/\varepsilon = 0.129$ for the emittance blow-up with the same assumptions as with 6000 turns acceleration. The third order shape in the $x - x'$ phase space was still noticeable at the end of acceleration. With the magnetic field error of $\Delta B/\overline{B}_n = 10^{-3}$, the horizontal and vertical amplitude blowup at the end of acceleration were, respectively, $\Delta A_x/A_x \sim 1.3$ and $\Delta A_y/A_y \sim 1.9$ times, as shown in Fig. 9.

3.1. The cell tune $\nu_x = 1/3$ avoided, $\Delta B/\overline{B}_n = 10^{-4}$, and $N_{turns} = 1300$.
The next study used a lattice where both horizontal and vertical tunes avoided crossing the value of 1/3 in the cell is shown in Fig. 10. This has been accomplished by adjustments of the quadrupole gradients of the combined function magnets. The random variation of magnetic field was set to $\Delta B/\overline{B}_n = 10^{-4}$.
It is noticeable that the horizontal phase space $x - x_p$ shows no change of the emittance The vertical phase space crossing the resonance $\nu_y = 2.0$ (corresponds to $\nu_y = 0.083333$ per cell) at the turn 688 shows an amplitude increase of $y_{final}/y_{initial} = 1.14$ A number of lost particles is $N_{lost} = 101$ with respect to the initial number of $N_{init} = 1100$.

3.2. The cell tune $\nu_{x,y} = 1/3$ avoided with $\Delta B/\overline{B}_n = 10^{-3}$, and $N_{turns} = 1300$.
The simulations study with an input of $N_{init} = 1100$ protons included the random magnetic field error of $\Delta B/\overline{B}_n = 10^{-3}$. The amplitude blow up during acceleration was $\Delta A_x/A_x \sim 1.3$ and $\Delta A_y/A_y \sim 1.9$ times, as shown in Fig. 11. A recorded number of the lost particles was $N_{lost} = 184$ with initial number of $N_{initial} = 1100$. Ranges of the horizontal and vertical tunes $\nu_{x,y}$ in the ring were 7.82–3.41 and 7.2–1.01, respectively. The horizontal and the vertical emittance blows up due to crossing of many intrinsic resonances $m\nu = N_p$ with $3 \le m \le 8$ during acceleration. The equations (1), (2), and (3) provide estimates for the blowup as: $\Delta A = \Delta B/\overline{B}_n \cdot C(2\nu_m\sqrt{\nu_\tau}) = \Delta A \quad 2\cdot\nu_m\sqrt{5.54\cdot 10^{-3}/26.88}$. For a random error in the magnetic field of $\Delta B/\overline{B}_n = 10^{-3}$ the horizontal amplitude increase ΔA_x for integers 7, 6, 5, 4, and 3 is: $\Delta A_x(\nu_x = 7) \sim 0.025$, $\Delta A_x(\nu_x = 6) \sim 0.03$, $\Delta A_x(\nu_x = 5) \sim 0.036$, $\Delta A_x(\nu_x = 4) \sim 0.045$, and

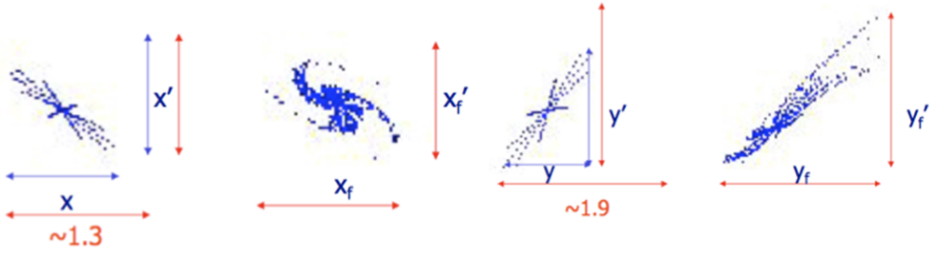

Fig. 9. Amplitude blow-up in the $x - x_p$ and $y - y_p$ phase space during proton acceleration with the 1300 turns in the NS-FFAG. In the horizontal phase space $x - x_p$ amplitude blow-up was $x_{final}/x_{initial} \sim 1.3$, while in the vertical phase space $y - y_p$ amplitude blow-up was $y_{final}/y_{initial} \sim 1.9$.

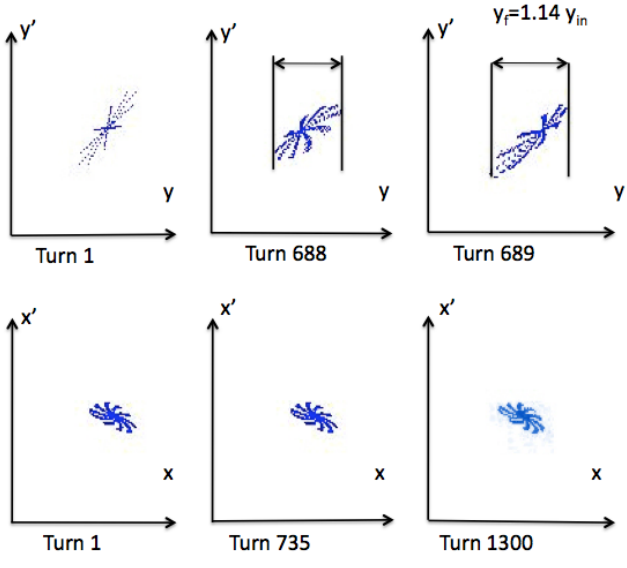

Fig. 10. Vertical and horizontal phase space during acceleration with random magnetic field error of $\Delta B/\overline{B}_n = 10^{-4}$.

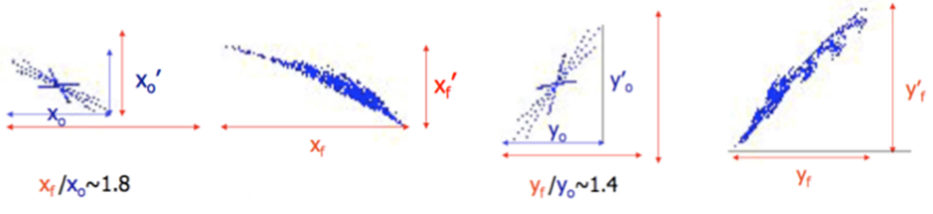

Fig. 11. Amplitude blow-up during 1300 turn acceleration in the NS-FFAG, the resonance crossing of the $\nu_x = 1/3$ per cell is avoided. The amplitude in the horizontal and vertical plane were magnified $x_{final}/x_{initial} \sim 1.8$ and $y_{final}/y_{initial} \sim 1.4$, respectively.

$\Delta A_x(\nu_x = 3) \sim 0.06$, respectively. For the vertical amplitude the increase ΔA_y for integers 7, 6, 5, 4, 3, 2 and 1 is: $\Delta A_y(\nu_y = 7) \sim 0.025$, $\Delta A_y(\nu_y = 6) \sim 0.03$, $\Delta A_y(\nu_y = 5) \sim 0.036$, $\Delta A_y(\nu_y = 4) \sim 0.045$, $\Delta A_y(\nu_y = 3) \sim 0.06$, $\Delta A_y(\nu_y = 2) \sim 0.09$, and $\Delta A_y(\nu_y = 1) \sim 0.18y$.

The $\Delta B/\overline{B}_n = 5{\cdot}10^{-3}$ field errors should be easily achievable for short magnets, so the results should not indicate a significant problem.

6. Conclusions

The non-scaling FFAG are fixed magnetic field accelerators or beam line in the case of gantries or beam transfer with relatively small aperture. This makes them advantageous with respect to the scaling FFAG, as they require relatively large aperture magnets. Unfortunately in the case of NS-FFAG many advantages of the scaling FFAGs like fixed tunes, zero chromaticity, isochronous condition—the same path length for all energies are not present any more. For the relativistic particles, the NS-FFAG application for acceleration is an easier challenge as the parabolic function dependence of the path length to the energy changes allows use of the "gutter acceleration" using the top of the RF sinusoidal wave. This non-linear part of the sine function allows acceleration within small number of turns $\sim$10.[16] Tune variations with energy present an additional problem due to resonance crossing. The muon acceleration or electron re-circulating linacs could be achieved by NS-FFAG as the resonance crossing is very fast and the emittance growth is very small. Other applications like the cancer therapy machines, proton drivers for the muon production, proton driven sub-critical reactors, radioactive heavy ion acceleration, etc. have to accelerate particles in a non-relativistic regime. There are few significant concerns: the RF wave has to follow a very large variation of the speed of particles, the relativistic factor β gets more than twice larger during acceleration, and the more turns required for acceleration the more difficult is passing through the integer resonances. The first problem of the fast frequency change or fast RF phase adjustment every turn for NS-FFAG's is very similar to the problem of upgrading the synchrotrons for faster acceleration. Advantage of the scaling and NS-FFAGs with respect to the synchrotron is the fixed magnetic field during acceleration especially in the case of proton driven systems, where it looks like the FFAG might be the only choice for required large intensity 1 GeV protons. The six dimensional simulations of the NS-FFAG acceleration presented in this report show that crossing resonances for $\sim$1300 turns represents a problem as there is an emittance growth. In addition if the tune of 1/3 in the basic cell is not avoided the third order resonance crossing becomes a serious problem for very slow the acceleration. The second problem of the RF acceleration under non-synchronous condition—time of flight dependence on energy—was solved by using the RF phase adjustment each turn. This solution requires very large RF power and more R&D is required to raise the level of the RF voltage and allow faster acceleration with smaller number of turns.

Acknowledgment

This work is supported by the US Department of Energy under contract No. DE-AC02-98CH10886.

References

1. U. Enrich, Proc. EPAC'06 [Edinburgh, UK, 2006], 964.
2. M. Craddock, CERN Courier 44 (#6), p.23 (2004).
3. T. Ohkawa, Proceedings of annual meeting of JPS (1953).
4. K. R. Symon, Phys. Rev. **100**, pp. 1247(1955).
5. K. R. Symon, D. W. Kerst, L. W. Jones, L. J. Laslett, and K. M. Terwillinger, Fixed-Field Alternating-Gradient Particle Accelerators, Phys. Rev. **103**, pp. 1837-1859 (1956).
6. A. Kolomensky et al., Zh. Eksp. Teor. Fiz. **33**, pp. 298(1957).
7. S. Machida, Phys. Rev. S.T. Accel. Beams 11 094003 (2008).
8. T. Yokoi, J. Cobb, K. Peach and S. Sheehy, Beam acceleration studies of proton NS-FFAG, in Proc. EPAC'08 (Genoa, Italy, 2008), THPP011.
9. S. Sheehy, Dynamics of the Machida lattice, Presented at FFAG Workshop at the University of Manchester, United Kingdom, September 1–5, 2008). `http://www.cockcroft.ac.uk/events/FFAG08`
10. R. Baartman, Resonance crossing topics. Presented at FFAG Workshop (Vancouver, Canada, 2004). `http://legacyweb.triumf.ca/ffag2004`
11. D. Trbojevic, B. Parker, E. Keil and A. M. Sessler, *Phys. Rev. S.T. Accel. Beams* **10**, 053503 (2007).
12. D. Trbojevic, Innovative gantry design with non-scaling FFAG. Workshop on Hadron Beam Therapy of Cancer (Erice, Sicily, Italy; Apr. 24–May 1, 2009). `http://erice2009.na.infn.it/programme.htm`
13. E. Forest, E. McIntosh and F. Schmidt. KEK Report 2002–3, CERN-SL-2002-044 (AP) 44, 3 (2002).
14. D. Boussard, RF for p$\overline{p}$(PARTIII). CERN/SPS/B4-2 ARF (Geneva, Jan. 1984), pp. 1–31.
15. M. Blaskiewicz, private communication.
16. D. Trbojevic, E. D. Courant, and M. Blaskiewicz, Phys. Rev. S.T. Accel. Beams 8, 050101 (2005).

International Journal of Modern Physics A
Vol. 26, Nos. 10 & 11 (2011) 1865–1872

DOI: 10.1142/S0217751X11053250

World Scientific
www.worldscientific.com

STATIONARY BUCKET ACCELERATION IN THE SCALING FFAG ACCELERATOR

E. YAMAKAWA

Graduate School of Engineering, Kyoto University,
Katsura Nishikyo-ku Kyoto, 615-8530, Japan
yamakawa@post3.rri.kyoto-u.ac.jp

T. UESUGI

Kyoto University Research Reactor Institute,
Asashiro-Nishi, Kumatori-cho, Sennan-gun, Osaka, 590-0458, Japan

Y. MORI

Kyoto University Research Reactor Institute,
Asashiro-Nishi, Kumatori-cho, Sennan-gun, Osaka, 590-0458, Japan

Stationary bucket acceleration in the scaling type of fixed field alternating gradient (FFAG) accelerator is examined in this paper.

Keywords: Scaling FFAG; stationary bucket acceleration; serpentine acceleration; proton driver; muon accelerator.

PACS number: 29.20.dk

1. Introduction

Recently, particle accelerators have been widely used not only for particle physics[1] but also for many applications such as cancer therapy,[2–3] nuclear power engineering,[4] etc. Requests for high beam power proton drivers to produce intense secondary particle beams, in particular, are increasing. Fixed-field alternating-gradient (FFAG) accelerators[5] are one of the possible candidates for such proton drivers. In the FFAG accelerator, the guiding magnetic field is static. Because of that, the acceleration repetition rate only depends on the capability of rf system.

Various methods of beam acceleration using rf cavities have been proposed for FFAG accelerators. One is an ordinary method where the beam acceleration is realized with frequency modulation of the rf system. With this acceleration scheme, the acceleration repetition rate is limited by the capabilities of the rf system such as its changing speed of rf frequency and rf voltage. Another scheme is the stationary bucket acceleration[6] where rf frequency is fixed. Since cw operations become possible in stationary bucket acceleration, a larger current beam can be obtained. In

stationary bucket acceleration, however, the total acceleration energy gain is limited by the bucket height. In order to increase the energy gain in beam acceleration, a new so-called serpentine acceleration[7] scheme has been proposed. In serpentine acceleration, the injected beam is accelerated between stationary buckets. Serpentine acceleration has been considered for the non-scaling type of FFAG so far. If serpentine acceleration is also used for the scaling type of FFAG, higher energy beam acceleration can be realized.

In this paper, the longitudinal hamiltonian for the stationary bucket acceleration in the scaling FFAG is derived analytically, and the features of serpentine acceleration and two applications based on serpentine acceleration in the scaling FFAG are also presented.

2. The Longitudinal Hamiltonian in the Scaling FFAG Accelerator

In cylindrical coordinates, the magnetic field in scaling FFAG accelerator has the form:

$$B_z(r, z = 0) = B_0\left(\frac{r}{r_0}\right)^k,$$

where r is the radial coordinate with respect to the center of the ring, B_0 is the magnetic field at r_0, k is the geometric field index, and z is the vertical coordinate. The closed orbits for different momenta (P) are given by

$$r = r_0\left(\frac{P}{P_0}\right)^{\frac{1}{k+1}}, \tag{1}$$

where r_0 is the radius of the closed orbit at the momentum of P_0.

In longitudinal particle dynamics with constant rf frequency acceleration in the scaling FFAG accelerator, the phase discrepancy per revolution $\Delta\phi$ is written by

$$\Delta\phi = 2\pi(f_{rf} \cdot T - h), \tag{2}$$

where h is the harmonic number, f_{rf} is the rf frequency and T is the revolution period of a non-synchronous particle. Eq. (2) becomes

$$\frac{\Delta\phi}{2\pi} = \frac{hT}{T_s} - h, \tag{3}$$

where T_s is the revolution period of a synchronous particle. The Eq. (3) is also expressed with another description based on Eq. (1) as follows;

$$\begin{aligned}\frac{T}{T_s} &= \left(\frac{r}{r_s}\right) \Big/ \frac{P/E}{P_s/E_s} \\ &= P_s^{1-\alpha}\frac{E}{E_s}P^{\alpha-1},\end{aligned} \tag{4}$$

where r_s is the reference radius, α is the momentum compaction factor and E_s is the reference energy at the reference radius. Below the transition energy, there is the stationary energy E_s. As the particle energy increases across the transition

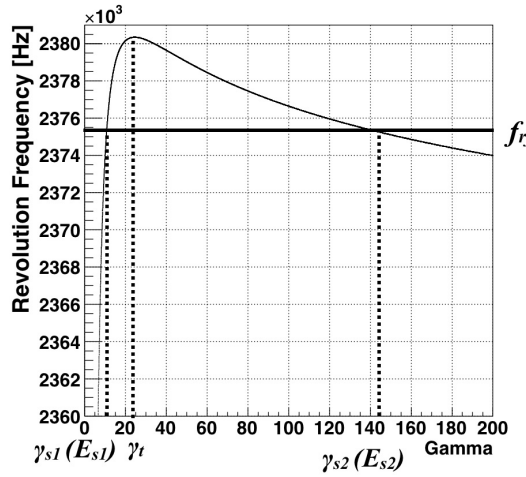

Fig. 1. Relation between revolution frequency and energy for particles, where γ_t is the transition energy and γ_{s1} and γ_{s2} are correspond to E_{s1} and E_{s2}, respectively. E_{s1} is the stationary energy below the transition energy. E_{s2} is the stationary energy above the transition energy.

energy, there is the other stationary energy E_{s2}, as shown in Fig. 1. Combining Eq. (3) and Eq. (4), the phase difference becomes

$$\Delta\phi = 2\pi h\Big(\frac{P_s^{1-\alpha}}{E_s} E P^{\alpha-1} - 1\Big).$$

Now we exchange $\Delta\phi/2\pi$ and $d\phi/d\theta$ to derive the phase and energy equation of longitudinal motion,

$$\frac{d\phi}{d\theta} = h\Big(\frac{P_s^{1-\alpha}}{E_s} E P^{\alpha-1} - 1\Big), \tag{5}$$

$$\frac{dE}{d\theta} = \frac{eV_{rf}}{2\pi} \sin\phi, \tag{6}$$

where V_{rf} is the rf voltage par turn and θ is an azimuthal angle in the machine. We introduce the energy variable E canonically conjugate to the coordinate variable ϕ. Eq. (5) and (6) derive the longitudinal hamiltonian:

$$H(E, \phi; \theta) = h\Big(\frac{1}{\alpha+1} \frac{P^{\alpha+1}}{E_s P_s^{\alpha-1}} - E\Big) + \frac{eV_{rf}}{2\pi} \cos\phi. \tag{7}$$

3. Serpentine Acceleration in the Scaling FFAG Ring

In this section, the features of serpentine acceleration are studied. First the behavior in longitudinal phase space near the transition energy and the idea of serpentine acceleration are discussed. The effect of using serpentine acceleration is also studied. Second, the minimum rf voltage which is necessary to obtain serpentine acceleration

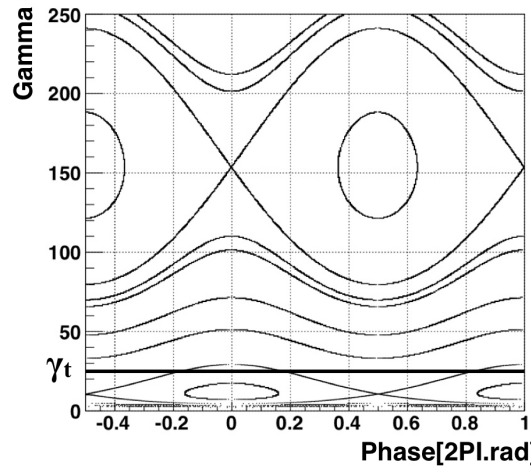

Fig. 2. Longitudinal phase space. Two stationary buckets are separated from each other.

is derived from calculations based on Eq. (7). Finally the behavior of the beam shape during acceleration is shown in longitudinal phase space.

3.1. *Longitudinal phase space*

When E_{s1} and E_{s2} are far from each other, two stationary buckets are separated as shown in Fig. 2. When the two stationary energies approach each other, a channel between two stationary buckets appears as shown in Fig. 3. If particles can be accelerated using this channel, then the total energy gain through the acceleration shown in Fig. 3 as ΔE_{acc}, becomes large.

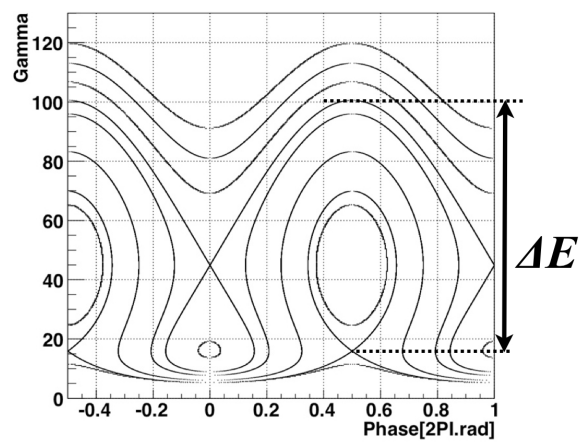

Fig. 3. Longitudinal phase space near the transition energy. There are two stationary buckets which are close to each other.

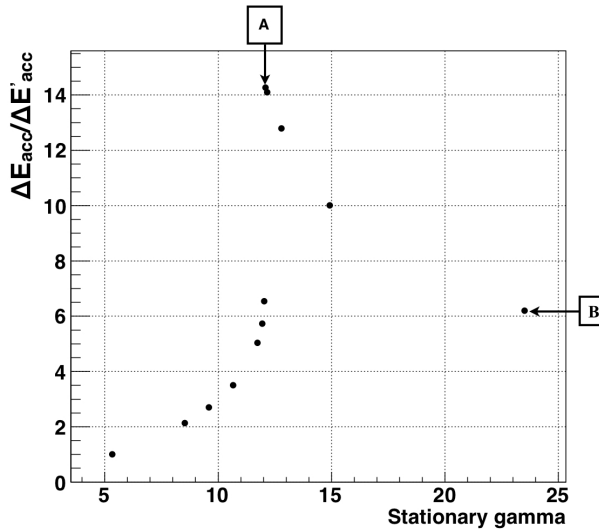

Fig. 4. Relation between stationary energy and energy gain, where stationary gamma is derived from stationary energy, ΔE_{acc} is energy gain at each E_{s1} and $\Delta E'_{acc}$ is the minimum value of ΔE_{acc} which is around 5. The vertical axis shows the ΔE_{acc} which is normalized by $\Delta E'_{acc}$.

In order to show the effect of using serpentine acceleration, ΔE_{acc} is examined by changing E_{s1}. As E_{s1}, ΔE_{acc} becomes large as shown in Fig. 4. The largest ΔE_{acc} is at the point **A** in Fig. 4, and Fig. 5 shows longitudinal phase space at this time. Increasing E_{s1} additionally, however, ΔE_{acc} decreases to the point **B** shown in Fig. 4 where E_{s1} equals the transition energy. If particles can be accelerated using serpentine acceleration, total energy gain through the acceleration becomes larger than the total energy gain within a stationary bucket.

3.2. *Minimum rf voltage to make the serpentine acceleration channels*

The minimum rf voltage to make the acceleration channels is derived from Eq. (7). As shown by Fig. 5, the limiting serpentine path goes through two unstable fixed points where $H(E_{s1}, \pi)$ equals $H(E_{s2}, 0)$.

$$H(E_{s1}, \pi) = H(E_{s2}, 0). \tag{8}$$

From Eq. (8) and the relation between E_{s1} and E_{s2},

$$E_{s1} P_{s1}^{\alpha-1} = E_{s2} P_{s2}^{\alpha-1},$$

the minimum rf voltage is derived;

$$V_{rf} = \pi h \left[\frac{1}{\alpha + 1} \left(\frac{P_{s1}^2}{E_{s1}} - \frac{P_{s2}^2}{E_{s2}} \right) + (E_{s2} - E_{s1}) \right]. \tag{9}$$

Eq. (9) shows that once the k value and the stationary energy are given, the minimum rf voltage to achieve channel acceleration can be calculated.

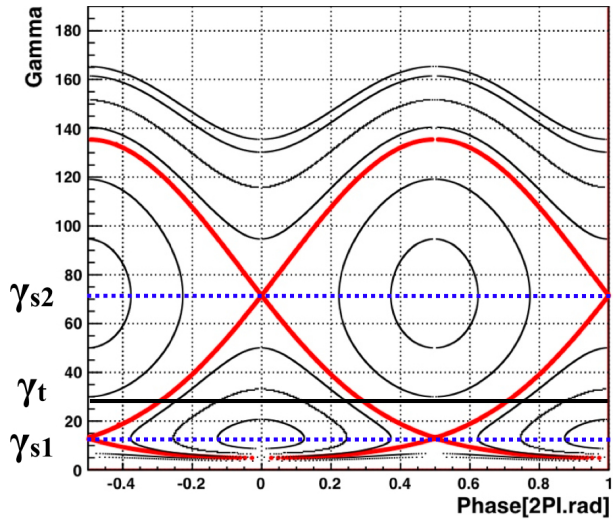

Fig. 5. Two stationary buckets are close to each other, where γ_{s1} corresponds to E_{s1} and γ_{s2} corresponds to E_{s2}.

Table 1. Parameters of proton accelerator.

Stationary Kinetic Energy	650 MeV
Mean Radius @γ_s	10 m
k value	3
rf voltage / turn	50 MV
rf frequency	3.7 MHz

4. Applications for Serpentine Acceleration in the Scaling FFAG Accelerator

With serpentine acceleration, high current beam is generated by cw operations. And also, total energy gain is larger than only in the bucket. Furthermore, fast acceleration can be achieved. This is desirable for unstable particles such as muons. In this section, two examples of applications are shown; one is as a proton driver, the other is as a muon accelerator.

Parameters of proton driver are summarized in Table 1. The beam trajectories in the longitudinal phase space are shown in Fig. 6. As shown in Fig. 6, injection kinetic energy is 500 MeV±1%. Injection phase range is from 0.25 to 0.3 2πrad. Final kinetic energy is 2018 MeV±1.4%. The number of turn during acceleration is 35 turns. The ratio of injection to final momentum is 2.6.

Parameters of muon accelerator are summarized in Table 2. The beam trajectories in the longitudinal phase space are shown in Fig. 7. As shown in Fig. 7, injection kinetic energy is 45.5 MeV±1.1%. Injection phase range is from 0.35 to 0.4 2πrad.

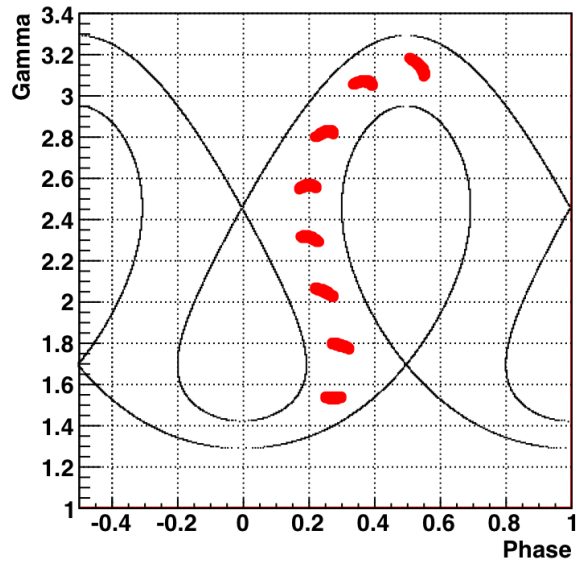

Fig. 6. Proton beam is plotted by every 5 turns in longitudinal phase space.

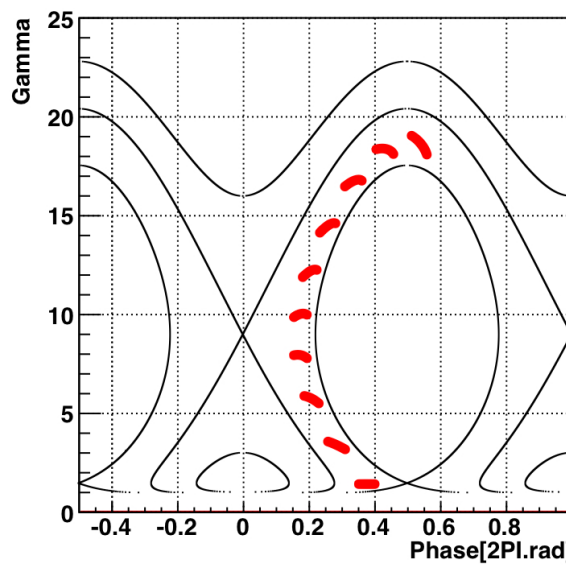

Fig. 7. Muon beam is plotted by every turn.

Final kinetic energy is 1855 MeV±5.4%. The number of turn during acceleration is 9 turns. The ratio of injection to final momentum is 18. In this scheme, a low energy muon beam can be accelerated to high energy within a few turns. It shows a good expectation for the neutrino factory or muon collider, in the future.

Table 2. Parameters of muon accelerator.

Stationary Kinetic Energy @under E_t	844.8 MeV
Mean Radius @γ_s	10 m
k value	6
rf voltage / turn	250 MV
rf frequency	4.7 MHz

Since serpentine acceleration is based on stationary bucket acceleration, the bunch is rotated during acceleration. Therefore, the injected beam shape is rotated during acceleration, and a narrow bunched beam can be obtained at extraction.

5. Summary

In order to obtain a high power beam with high repetition rate, serpentine acceleration with constant rf frequency has been proposed for the scaling FFAG accelerator. The longitudinal hamiltonian in the scaling FFAG accelerator has been obtained analytically. In order to design the high power proton driver with serpentine acceleration, further studies are needed.

References

1. Y. Kuno et al, *NufactJ Working Group*, 2001.
2. Y. Mori, *Nuclear Inst. and Methods in Physics Research, A*, Vol. 562, 2006.
3. H. Tanaka et al, *Nuclear Inst. and Methods in Physics Research, B*, 267, 2009.
4. Kaichiro Mishima et al, *Journal of Nuclear Science and Technology*, vol. 44, 2007, NO3 Special Issue on GLOBAL 2005, pp. 499–503.
5. C. Ohkawa, in *Proc. of JPS*, 1953.
6. Y. Mori, *International Workshop on FFAG Accelerators (FFAG2006)*, FNAL, Chicago, USA, 2006.
7. S. Machida, *Proc. of the International Workshop on FFAG Accelerators (FFAG05)*, KURRI, Osaka, Japan, 68, 2005.

International Journal of Modern Physics A
Vol. 26, Nos. 10 & 11 (2011) 1873–1886

DOI: 10.1142/S0217751X11053262

World Scientific
www.worldscientific.com

KICKER-LESS FFAG: AN APPROACH TO HIGH INTENSITY FFAG

TAKEICHIRO YOKOI
John Adams Institute for Accelerator Science, Oxford University, Oxford, UK
t.yokoi1@physics.ox.ac.uk

The most challenging issue to realize an accelerator for an Accelerator Driven Sub-critical Reactor system (ADSR) is the handling of high intensity beam—more than 1 mA. For such an application, FFAG is one of most promising candidates. To take advantage of the FFAG as a high intensity accelerator, efficient injection/extraction and acceleration schemes are crucially important. One approach to achieve a high intensity FFAG is to eliminate the kicker magnet from the injection and extraction process and also to implement multi-bunch acceleration.

1. Introduction

An indispensable element of the ADSR is a high intensity proton driver with a beam current of at least 1 mA and maximum beam energy of 250 MeV∼1 GeV. The FFAG is one promising candidate for such an application and the PAMELA project (Particle Accelerator for MEdicaL Application) is developing FFAG accelerators with a comparable energy range,[1] though the required beam intensity is much lower than that for ADSR. The major differences in the requirements of the accelerator between particle therapy and ADSR are summarised in Table 1. Investigating the applicability of technologies developed in PAMELA to ADSR accelerator is a natural extension of this project.

The primary challenges are realisation of ultra-high intensity medium energy accelerator combined with high reliability. Reliability is in some sense, a secondary

Table 1. Requirements for the application of particle therapy and ADSR.

	Particle therapy	ADSR
Beam current	10∼100 nA	>1 mA
Max energy	250 MeV (proton)/400 MeV/u (carbon)	250 MeV∼1000 MeV
Extraction Energy	Variable	Fixed
Extraction Energy spread	<1 MeV @ patient	O(MeV) is acceptable
Beam structure	Pulse/CW	CW is preferable
Operation cycle	150 day, 10 h/day	150day, 24 h/day
Maximum acceptable beam break	1 day	1 sec.

issue, since without a concrete scheme to achieve such a high power accelerator, failure analysis is not defined.

2. PAMELA

The primary goal of the PAMELA project is to design a particle therapy facility using a NS-FFAG.[1] The specification and details are given in Ref. 2. The remarkable features of the NS-FFAG as it is applied in PAMELA are (1) a flexible, tunable operating point using a fixed field accelerator and (2) a high repetition rate. Unlike the conventional scaling FFAGs which apply a scaling law to the magnetic field, PAMELA instead achieves a stable betatron tune using truncated multipole fields, which is expressed as Eq. (1), generated by double-helix multipole magnet.[5]

$$\left(\frac{B}{B_0}\right) = \left(\frac{R}{R_0}\right)^k \to 1 + \sum_{n=1} \alpha(k,n) \left(\frac{\Delta r}{R_0}\right)^n, \tag{1}$$

where Δr, $\alpha(k,n)$ are the deviation from magnet centre, $r - R_0$, expansion factor of the , respectively. The double helix scheme enables each multipole field components to be changed individually, and this powerful feature gives the PAMELA design the ability to tailor the tune footprint. Details of the tune tailoring are presented in Ref. 2. The main parameters of PAMELA ring are summarised in Table 2. In this paper, the proton ring of PAMELA was employed as a study model for an ADSR system.

Table 2. Main parameters of PAMELA.

	Ring 1 (proton, carbon)	Ring 2(carbon)
Energy	30∼250 MeV(p) 8∼68 MeV/u(c)	68∼400 MeV(c)
Diameter	12.5 m	18.4 m
k-value	38	41
Orbit excursion	18 cm	21 cm
Revolution frequency	1.94∼4.62 MHz(p) 0.98∼1.92 MHz(c)	1.94∼3.91 MHz(c)
Maximum field	3.6 T	3.5 T
Magnet	FDF Triplet Superconducting	FDF triplet Superconducting
Length	57 cm/magnet	113 cm/magnet
Aperture	25 cm	33 cm
Long drift	1.3 m	1.2 m
Packing factor	0.48	0.65

3. Space Charge Tune Shift

In a high intensity proton machine with a current in excess of 1mA, consideration of space charge effect cannot be avoided. To elucidate the ring requirements, space charge tune shift was evaluated using an analytical expression. Incoherent space charge tune shift, $\Delta\nu_u$ is evaluated using

$$\Delta\nu_u = -\frac{r_c N_{tot} \bar{R}}{2\pi\nu_0 B\beta^2\gamma^3} \frac{1}{\bar{\sigma_u}(\bar{\sigma_x} + \bar{\sigma_y})}, \tag{2}$$

where ν_0, r_c, N_{tot}, ν_0, β, γ, σ_u are betatron tune without space charge, classical electron radius, bunch intensity, relativistic β, γ, and beam size of u direction, respectively. Using the lattice parameters of the PAMELA proton ring and assuming that 1mA of protons with a 200π mm·mrad are accelerated at a repetition rate of 1 kHz, the estimated tune shifts are about -0.2 for horizontal, and -0.4 for vertical, respectively. These tune shifts almost reach the practical limit. Possible measures to mitigate the space-charge tune shift problem include (1) increase the ring size (2)increase the repetition rate and therefore the bunch charge,(3) increase the beam size, (4) increase injection energy, or a combination of these. In the most realistic scenario a combination of (1)$\sim$(4) with a optimized lattice is chosen. Even after the optimization, a repetition rate above 1 kHz is still a requirement for ADSR system considered here.

4. Improving Reliability

In order to realize an accelerator system with high reliability, three approaches can be considered. These are (1) redundancy, (2) derated operation and (3) reduction or elimination of pulsed elements. To introduce redundancy in an accelerator, the reliabilities of injection and extraction system are the key issue, since these two systems are difficult to be redundant. A 1 kHz repetition rate, for example, implies 1×10^6 excitation of pulsed elements occurs in only about 15 min. Although kicker power supplies today use semiconductor elements, such as IGBT, and the reliability of switching elements is greatly improved, the reliability of pulsed system as a whole is still a serious concern under such extreme operating conditions. In this sense, eliminating pulsed elements from the FFAG accelerator is a promising new option to improve the reliability of the accelerator.

To eliminate pulsed elements from FFAG ring, multi-turn extraction and charge exchange injection are a promising solution. However, at this time, no working FFAGs implement such injection and extraction schemes.

5. Multi-Turn Extraction

A remarkable feature of PAMELA lattice is the flexibility and tuneability of the operating point. The variability of individual multipole field strengths makes it possible to change not only the average betatron tune but also the tune footprint.

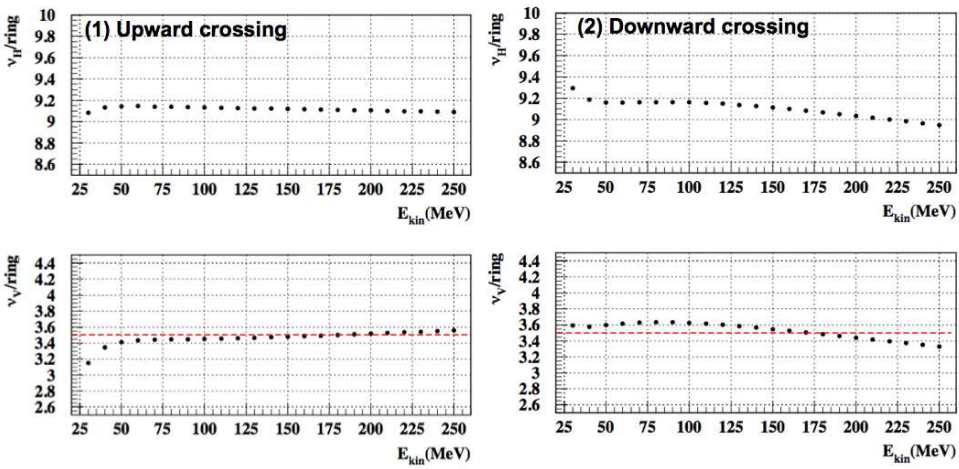

Fig. 1. Example of tune footprint adjustment in PAMELA proton ring: (1) upward half integer resonance crossing, (2) downward half integer resonance crossing.

First, in a scaling FFAG, vertical tune can be varied by changing F/D strength ratio, which is the field strength ratio of focusing magnet and defocusing magnet. In the PAMELA lattice, a 1% change of F/D ratio can change the vertical tune by at least 0.5.[8] Then, in a ring that supports a vertical tune change, as does PAMELA, between injection and extraction, the resonance energy can be changed through the F/D strength ratio. (The tune change in present lattice of PAMELA is controlled to within 0.5[8] over the entire energy range.) Variable energy extraction is possible in the PAMELA lattice using half-integer resonance crossing. Second, in PAMELA lattice, tune footprint can also be tailored by trimming the multipole field strength as shown in Fig. 1. Combining these characteristics, variable energy extraction is feasible using the PAMELA-type lattice. This feature makes for a versatile accelerator capable of both high intensity and variable energy.

In a scaling FFAG, due to the intrinsic nonlinear field components, betatron motion experiences an inevitable nonlinear detuning, which is a strong amplitude-dependent tune shift. Fig. 2 shows the vertical phase space (left) alongside a typical vertical detuning vs. amplitude (right) of the PAMELA lattice.[a] In the presence of such nonlinear detuning, the beam motion in phase space exhibits different behaviour and dynamics depending on the tune direction in which the beam crosses the resonance.[9] Fig. 3, and Fig. 4 show typical beam behaviour during half integer resonance crossing when beam crosses the resonance from a tune below (upward crossing) and then from a tune above (downward crossing) of the half integer, respectively. In exciting the half integer resonance, the driving term was introduced by perturbing the quadrupole field component to match the harmonics of $2\nu_V = 7$. Typical amplitude of the quadruple perturbation, $\Delta B_1/B_1$ is $\sim 10^{-3}$.

[a]All the beam simulations in the paper were carried out using ZGOUBI.[6]

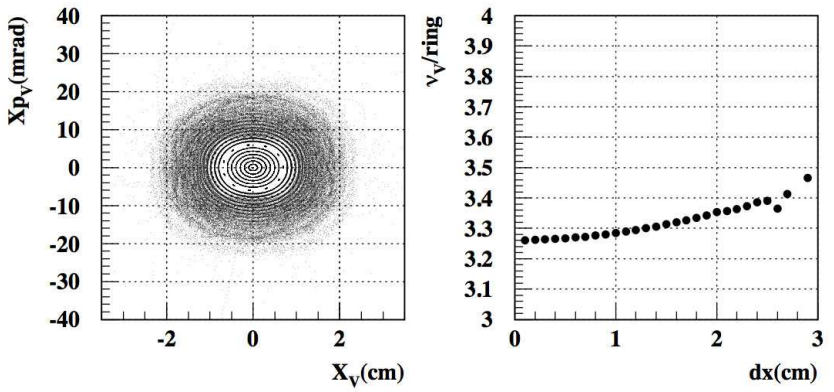

Fig. 2. Vertical detuning of PAMELA proton ring, left: vertical beam phase space, right: amplitude dependence of vertical tune.

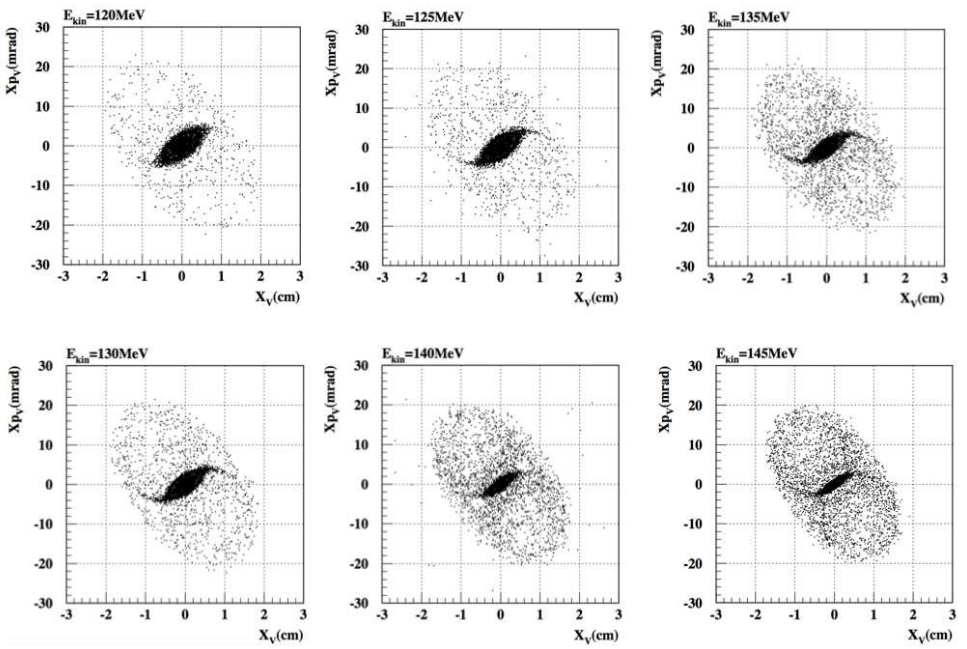

Fig. 3. Beam motion in upward half integer resonance crossing.

In crossing the resonance from below the half integer, the tune shift with amplitude causes outer particles in the distribution to cross the resonance first and therefore extraction progresses from high-amplitude particles towards the center of the distribution. Further, the energy at which a particle crosses the resonance is dictated by this tune shift, or amplitude—the higher the particle amplitude or the higher the strength of the quadrupole perturbation, the lower the energy of the half-

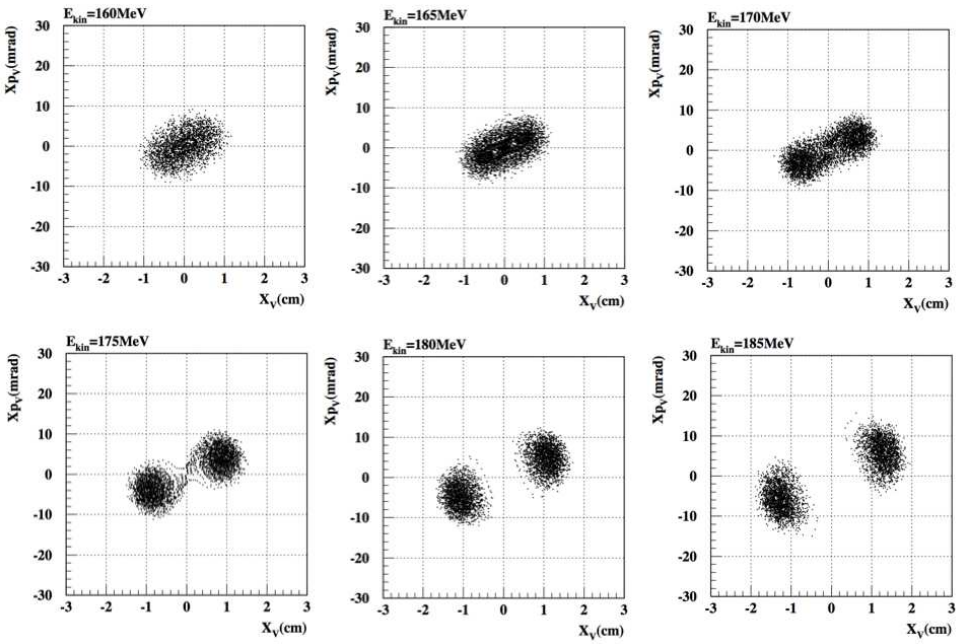

Fig. 4. Beam motion in downward half integer resonance crossing.

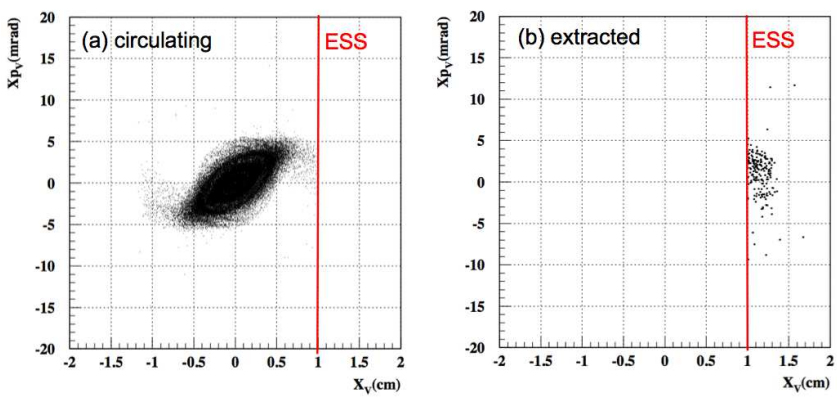

Fig. 5. Beam distribution of upward half integer resonance extraction, (a) circulating beam, (b) extracted beam.

integer resonance. As a result, the energy of extracted beam is strongly influenced by both the initial beam distribution and by the amplitude of the excitation. Extracted beam develops a pronounced energy dependence as a function of beam size (for a given quadrupole perturbation), but also as a function of the magnitude of the perturbation. Fig. 5 shows a typical phase space distribution for extracted beam. Sensitivity to the amplitude of the perturbation is shown in Fig. 6. Fig. 7 shows the

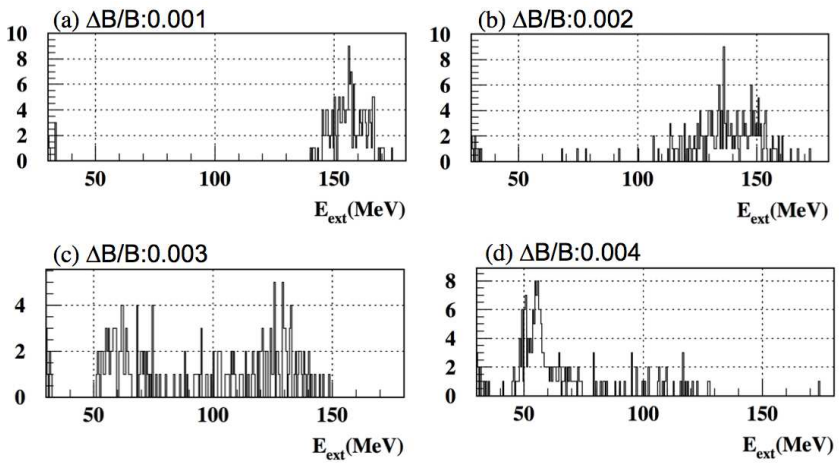

Fig. 6. Perturbation amplitude dependence of extracted beam energy spread in upward half integer resonance crossing.

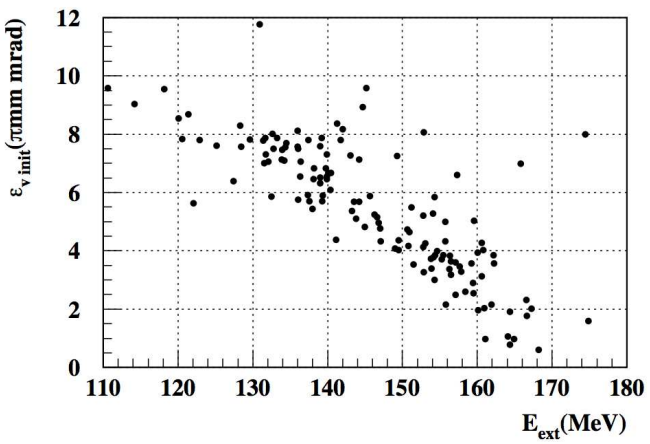

Fig. 7. Beam size dependence of extracted energy in upward half integer resonance crossing.

amplitude dependence on the energy of extracted beam. This unwanted dependence of the extracted beam energy on phase space and perturbation strength is not acceptable and eliminates resonant extraction from a lower tune in this type of FFAG.

In contrast, when crossing the half integer resonance from a higher tune, or downward crossing, the center particles in the beam experience the resonance first, and resonance excitation instead evolves from the center of the distribution outward. As a results, two islands are formed and move outward as a group (see Fig. 4). Therefore, the extraction process does not have a strong connection with the initial beam distribution. Fig. 8 shows a typical distribution of extracted beam from a downward crossing, and Fig. 9 shows the driving term dependence on the beam

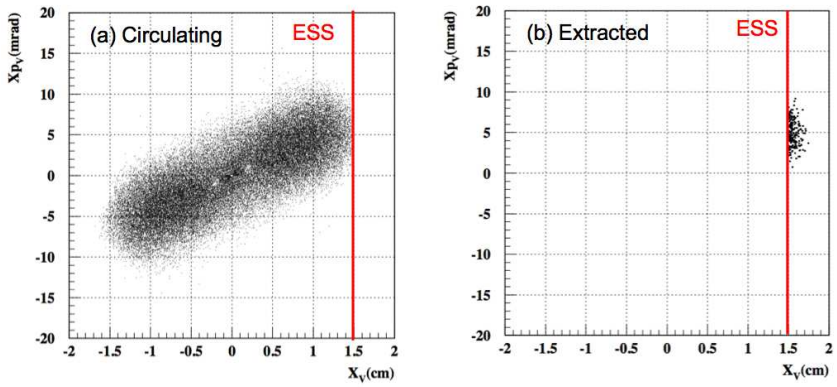

Fig. 8. Beam distribution of downward half integer resonance extraction (a) circulating beam, (b) extracted beam.

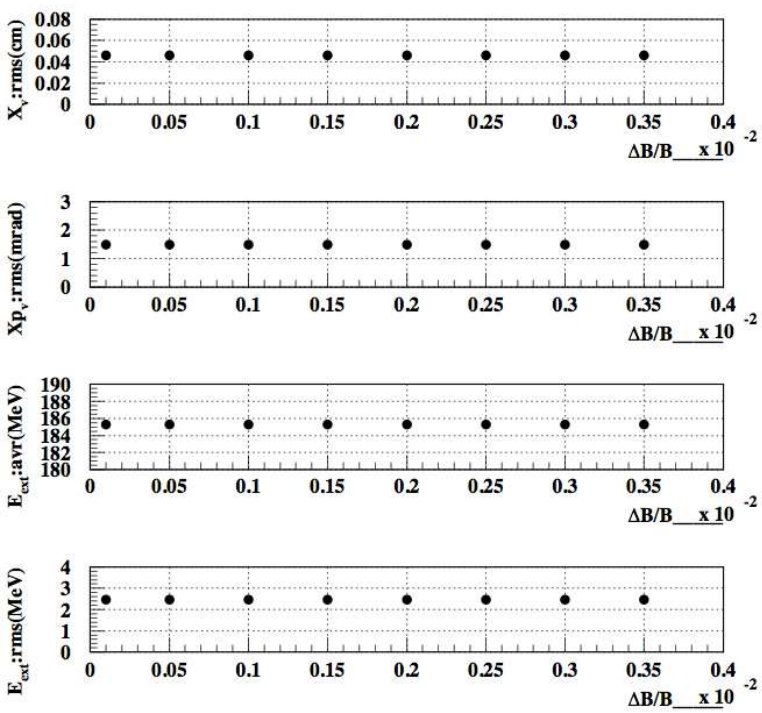

Fig. 9. Influence of driving term $\Delta B_1/B_1$ on the beam in downward half integer resonance crossing. From top to bottom: beam size, average extraction energy and extracted energy spread.

distribution. In this case, extracted beam properties are not particularly sensitive to factors such as beam distribution or perturbation strength, and, therefore, this extraction mode is suitable for the applications proposed. It should be mentioned, however, that due to the dynamics of extraction process, it is difficult to control the

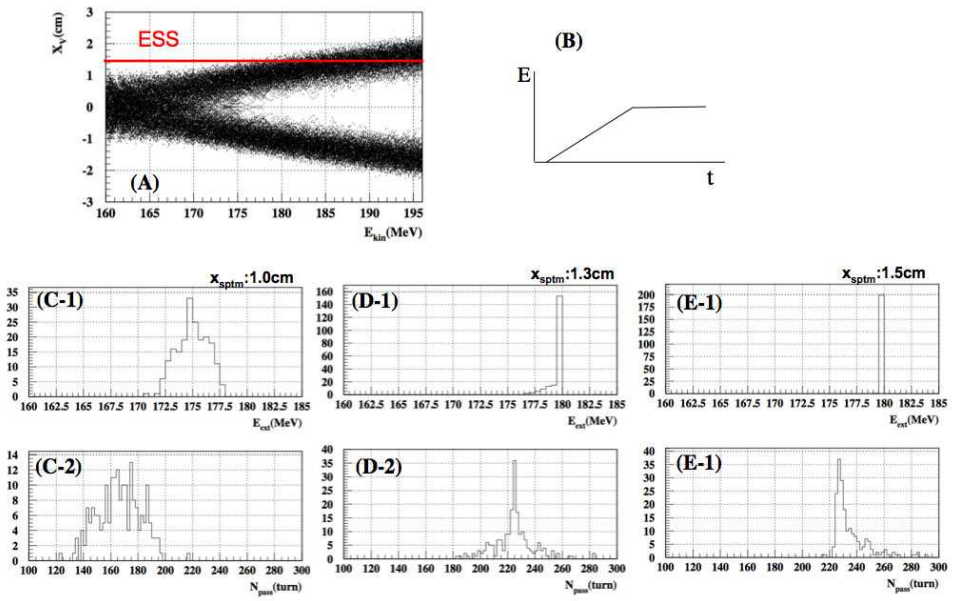

Fig. 10. Extracted energy and timing distribution in the downward half integer resonance extraction with a flattop, (a) correlation of horizontal beam position and beam energy, (b) flattop, (c-1) extracted beam energy distribution @ x_{ESS}=1.0 cm, (c-2) extracted timing resolution @ x_{ESS}=1.0 cm, (d) @ x_{ESS}=1.3 cm, (e) @ x_{ESS}=1.5 cm.

rate of extraction. In this sense, the resonance extraction proposed here is "multi-turn extraction", not the "slow extraction" characteristic of a synchrotron.

In downward-crossing extraction, another approach can be considered. By introducing a flattop, or coasting beam, in the acceleration cycle and simultaneously adjusting the tune, or resonance energy, the energy distribution can be minimized as shown in Fig. 10. This almost monochromatic resonance extraction has various applications. One, for example, is an alternative extraction method for the carbon ring of PAMELA, where an extraction kicker presents technical problems.

Modelling of resonant extraction in a FFAG using an ESS (Electro Static Septum) is complicated by the nonlinear detuning and requires extraction to be verified by an advanced tracking simulation, since the nonlinear detuning potentially deforms the beam distribution of extracted beam considerably. Fig. 12 shows a typical beam distribution after resonantly extracting beam through the ESS. In the simulation the electric field of the ESS is 7MV/m. Since, with existing technology, 20 MV/m is achievable, present technology permits scaling the ESS to accommodate a 1 GeV proton beam.

6. Charge Exchange Injection

Charge exchange injection is a powerful method to increase beam intensity without significantly increasing beam size (by painting, for example). However, for charge

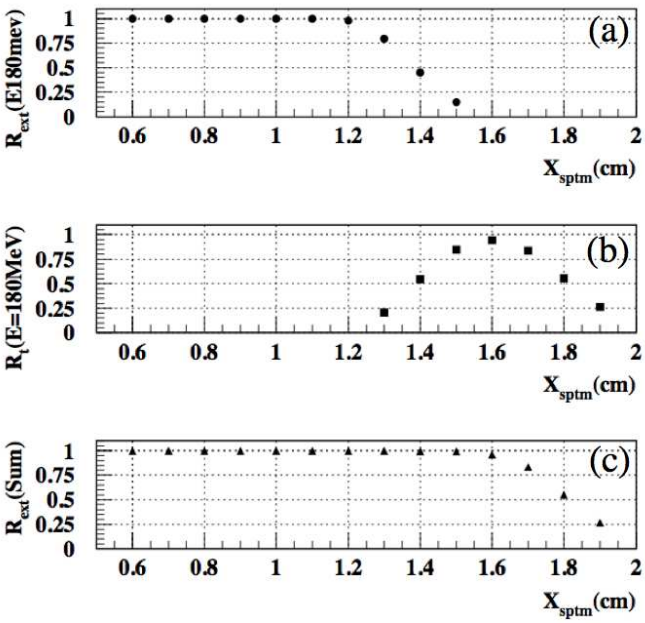

Fig. 11. Energy fraction as a function of septum position, (a) fraction of extracted beam below flattop energy to the circulating beam, (b) fraction of extracted beam with flattop energy to the circulating beam, (c) fraction of extracted beam to the circulating beam.

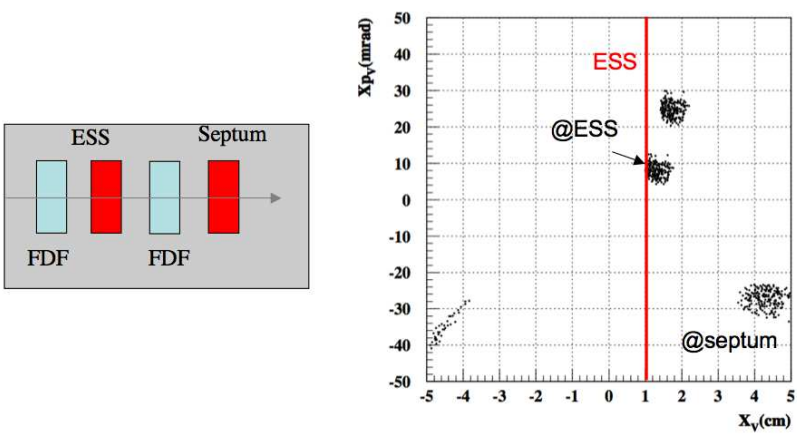

Fig. 12. Typical phase space motion of extracted beam after ESS.

exchange, such as in the case of the stripping foil, the optics of injection orbit need to be carefully designed. For example, in the design study for the Ibaraki particle therapy center, a stripping foil was planned for installation inside of a FFAG sector magnet. Such a scheme is hard, if even possible, to implement in the PAMELA base cell unit, since a single cryostat houses the superconducting triplet magnet.

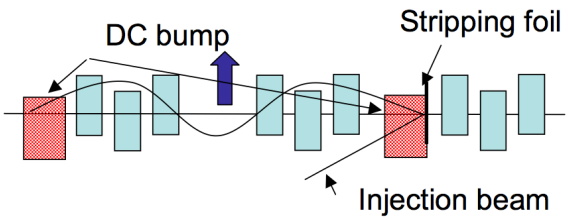

Fig. 13. Schematic diagram of Charge exchange injection using DC bump.

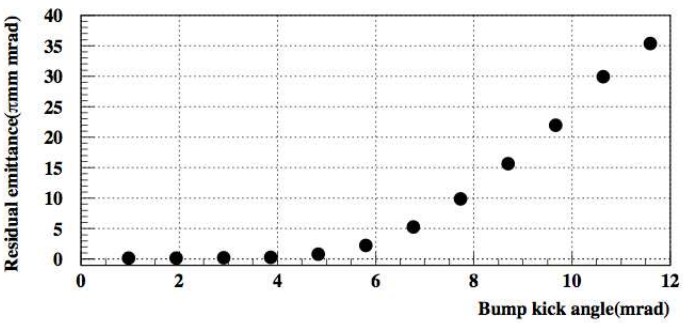

Fig. 14. Emittance blow up in bump orbit in PAMELA lattice (initial beam is zero emittance beam).

Considering the horizontal tune of PAMELA lattice, however, ∼0.75/cell, another approach can can be considered. A pair of "C" magnets (DC) can be installed in the PAMELA straight sections with an empty straight section in between the pairs. The first magnet bumps the circulating beam off the closed orbit at injection, making an angle equal and opposite to the incoming H^+ at the foil. The second magnet therefore is used to merge the orbit of H^+ and H^+. In FFAG, the closed orbit moves outward as the beam is accelerated. Thus, the pair of C magnets works as an orbit bump system as long as the phase advance between them is appropriate (see Fig. 13). Fig. 14 shows the bump orbit distortion as a function of bending angle. It shows that the bump orbit closes as long as the bending angle of bump magnet is small (less than 6 mrad). The intrinsic non-linear detuning of scaling FFAG causes the bump orbit to remain unclosed for a large bending angle. Whether, strictly speaking, non-closure is harmful in a FFAG where orbits move anyway requires further study, especially for high intensity applications from the viewpoint of space charge (where a larger beam size is desirable to minimize tune shift). In fact, a small, orbit offset can potentially be used for horizontal phase space painting.

However, from the standpoint of beam losses, a large dynamic aperture is always preferable and the present dynamic aperture of PAMELA($\sim 400\pi$ mm·mrad) may not be sufficient for "painting". Increasing the dynamic aperture of an FFAG for ADSR can be achieved using lower value for the scaling index, k.

7. Multi-Bunch Acceleration

In order to increase the duty cycle of a non-isochronous fixed field accelerator, two schemes have been considered. One is the single bunch acceleration and an increasing rf voltage. The other is multi-bunch acceleration combining different rf waveforms in order to accelerate bunches at different energies.[10] With multi-turn extraction and charge exchange injection, an FFAG can accommodate as many bunches as it can confine and accelerate in the ring. A low-Q cavity such as MA cavity does not need a biasing current to tune the resonance frequency. Thus, the low-Q cavity can generate a broad wave form as required for multi-bunch acceleration with a single cavity. Multi-bunch acceleration in a FFAG has been demonstrated using PoP FFAG.[11] The power consumption in a rf cavity can be written as

$$P = \int \frac{(\sum V)^2}{R} dt. \tag{3}$$

The superposition of different frequencies can be described as

$$(\sum V)^2 \equiv (\sum V_i \sin(f_i t))^2 \tag{4}$$

$$= \sum (V_i \sin(f_i t))^2 + \sum V_i \sin(f_i t) \cdot V_j \sin(f_j t). \tag{5}$$

In multi-bunch acceleration, the second term is a form of a beat wave and becomes negligible considering the time average. Therefore, although the power consumption of single bunch acceleration increases with the square of repetition rate, that of multi-bunch acceleration increases proportional to repetition rate as long as the accelerating voltage is equivalent to that of single beam acceleration. Thus, as long as rf system can generate such a broad rf waveform, increasing the number of simultaneously accelerated bunches is more efficient than increasing the repetition rate from a power consumption standpoint. To avoid interference between rf buckets, rf frequencies need to be separated from each other. Typically, the separation should be larger than $4 \times f_s$, where f_s means synchrotron frequency. In PAMELA lattice, synchrotron's frequency is typically less than 50 kHz. It means maximum 20 bunches can be accelerated simultaneously.

As discussed above, multi-bunch acceleration is expected to reduce the average power consumption. On the other hand, the required peak power is proportional to the number of simultaneously accelerated bunches, and therefore requires a larger initial cost. As the number of superimposed frequencies is increased (see Fig. 15), the amplitude is reduced drastically as shown in Fig. 16. For example, in the case of 20 superimposed frequencies, 97% of time, the amplitude is less than half that compared to the peak voltage. This degraded feature of multi-bunch acceleration is expected to help to increase the reliability of rf system. In addition, due to the smallness of the large amplitude fraction, it might be possible to reduce the peak voltage and allowing some deformation of the waveform caused by intermittent saturation. However, such a mode of operation is predicted to introduce higher harmonics, and could introduce instabilities. The dynamics of the beam should be

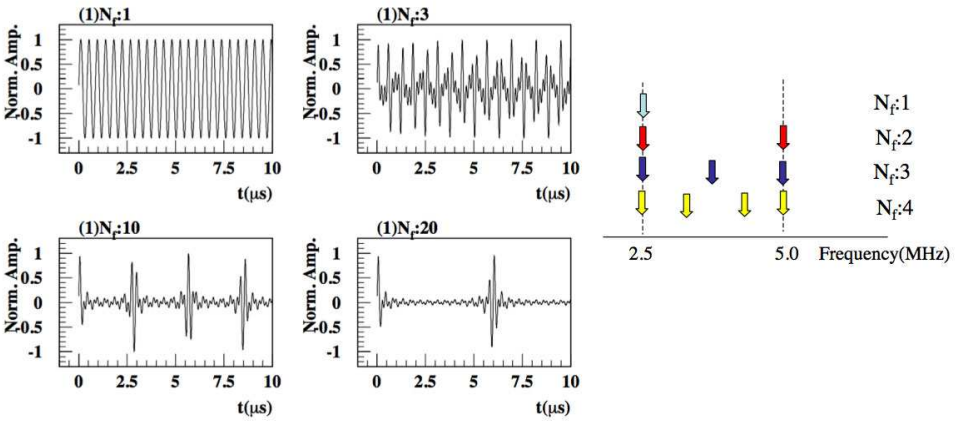

Fig. 15. Superposition of multi-frequency sine wave with constant frequency separation.

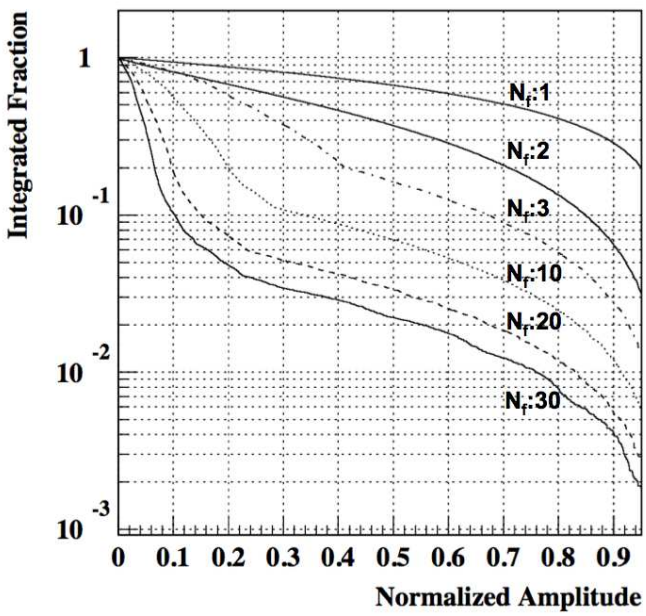

Fig. 16. Integrated fraction of amplitude in multi-frequency superposition.

carefully studied using tracking simulations to establish the feasibility of saturated operation. The issue remains for a the future study.

8. Summary

The applicability of the technology developed for PAMELA to a high intensity proton accelerator has been investigated. The flexible, tuneable operating point provides the potential for unique operation of a fixed field accelerator, especially

for resonant, multi-turn extraction capability. Combining resonant extraction with charge exchange injection, it is possible to eliminate the kicker magnet for injection and extraction, and, further, is anticipated to increase the reliability of accelerator. The fixed magnetic fields and a MA cavity can potentially accelerate multi-bunches. Further, this scheme is expected to be energy efficient and exhibit high reliability, particularly in regard to the rf system. The energy variability feature of resonant extraction supports a wide variety of applications, making the FFAG a versatile medium energy accelerator and not limited to a high intensity application for ADSR.

One open question to realize a FFAG proton driver for ADSR is injection. For 1mA beam current, the bunch intensity is about 10^{13} proton, even with a 1kHz repetition rate. To accumulate such a beam, assuming the 100 μs accumulation time at injection, the duty factor of the injector is 0.1, even in the multi-bunch acceleration case. Thus, an ion source of 10 mA peak power is required to achieve this intensity. In addition, the 1 GeV machine system must be a cascaded, or multi-accelerator system. Multi-turn extraction is no longer suitable for an upstream booster and means that practical implementation of a 1 GeV beam energy, requires a more complex approach.

References

1. K. Peach *et al.*, PAMELA—a model for an FFAG based hadron therapy machine, *Proceedings of PAC 07,* 2007, p. 2280.
2. T. Yokoi, Status of PAMELA, in this Proceedings.
3. T. Yokoi *et al.*, Beam acceleration studies of proton NS-FFAG, *Proceedings of EPAC 08,* 2008, p. 3398.
4. S. Machida, Scaling Fixed-Field Alternating Gradient accelerators with a small orbit excursion, *Phys. Rev. Lett.* 103(2009)164801.
5. H. Witte *et al.*, PAMELA magnet—Design and Performance, *Proceedings of PAC 09,* 2009.
6. F. Meot and S. Verelo, ZGOUBI user's manual, 2006.
7. J. E. Griffin and G. Nicholls, A review of some dynamics loss properties of Ni–Zn accelerator rf system ferrite, *IEEE Trans. for Nucl. Sci.* 26(1979) 3965.
8. T. Yokoi, *et al.*, PAMELA: Development of the rf system for a non-relativistic non-scaling FFAG, *Proceedings of PAC 09,* 2009.
9. G. Guignard., A General treatment of resonances in acceleration, *CERN report,* 78-11, 1978.
10. A. A. Kolomensky and A. N. Lebdev, Theory of cyclic accelerator, *John Wiley & Sons,* 1966, p. 352.
11. Y. Mori *et al.*, Multi-beam acceleration in FFAG synchrotron, *Proceedings of PAC 01,* 2001, p. 588.

International Journal of Modern Physics A
Vol. 26, Nos. 10 & 11 (2011) 1887–1902

DOI: 10.1142/S0217751X11053274

World Scientific
www.worldscientific.com

STATUS OF PAMELA: AN UK PARTICLE THERAPY FACILITY PROJECT USING NS-FFAG

TAKEICHIRO YOKOI
(on behalf of PAMELA Collaboration)
John Adams Institute for Accelerator Science, University of Oxford, Oxford, UK
t.yokoi1@physics.ox.ac.uk

PAMELA(Particle Accelerator for Medical Application) aims to design a particle therapy facility using NS-FFAG(Non-Scaling Fixed Field Alternating Gradient) accelerator. A newly proposed lattice design and the new type of combined function magnet provide the accelerator flexible tuneability of operating point and variability in operation modes. A remarkable features for a fixed field accelerator are its high repetition rate, about 1 kHz, and energy variable beam extraction. These features make the machine a promising candidate of versatile accelerator not restricted to medical applications.

Keywords: FFAG; proton; medical application.

1. Project Overview

The FFAG accelerator has been drawing growing attention as a promising candidate for the next generation accelerator due to its remarkable features such as ability for rapid acceleration of large emittance beam and design flexibility. The features open up possibilities for large varieties of applications from fundamental science to practical application such as particle therapy.

For the development of NS-FFAG, BASROC(British Accelerator Science and Radiation Oncology Consortium) has been supporting CONFORM(Construction Of NsFfag for Oncology, Radiation and Medicine),[1] which has two major R&D programs, EMMA[2] and PAMELA.[3]

The goal of PAMELA is to design a particle therapy facility with NS-FFAG acceleration which flexibly delivers proton and carbon beams for spot scanning irradiation.[3] To satisfy the requirements, the facility is required to employ a cascaded ring system due to the limitation of momentum range of FFAG ring. As for the injector, the dual beam needs a dual injector system, which contains a cyclotron for protons and an RFQ–Linac system for the carbon beam.[4] The extracted beam from the accelerator is a pulsed structure, and the target repetition rate was set as 1 kHz, which is one of the major challenges of the project. A schematic layout of PAMELA is shown in Fig. 1, and the main parameters of PAMELA are summarized in Table 1.

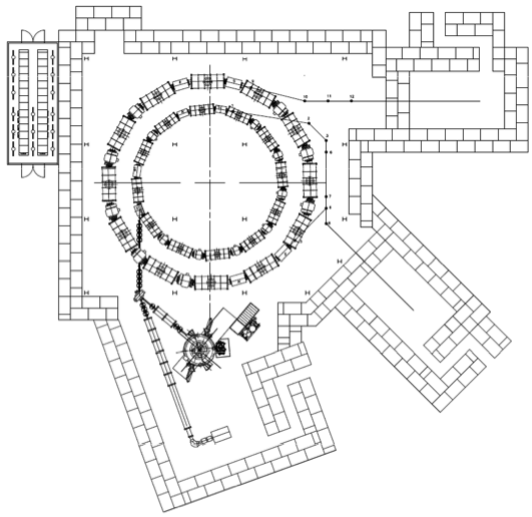

Fig. 1. Accelerator Layout of PAMELA.

Table 1. Main clinical requirements of PAMELA.

Particle	proton, carbon
Extraction energy: p	60∼240 MeV
Extraction energy: C	110∼450 MeV/u
Energy step	1∼5 MeV
Energy resolution	1.8∼3.5 MeV
Voxel size	$4 \times 4 \times 4 \sim 10 \times 10 \times 10$ mm
Dose field size	$100 \times 100 \sim 250 \times 250$ mm
Dose rate: p	2∼ 10 Gy/min
Dose rate: C	2∼ 10 Gy/min
Bunch charge: p	1.6∼16 pc
Bunch charge: C	300∼3000 fc
Repetition rate	0.5∼1 kHz

2. Medical Requirements

2.1. *Spot scanning*

Spot scanning irradiation is a next generation irradiation scheme of particle therapy. In the scheme, the target volume is subdivided into small voxels and each voxel is irradiated individually using a pencil beam. The advantages of the scheme are

(1) finer dose field formation, which can form a conformal dose field and minimize the unnecessary dose in healthy tissue,
(2) the ability of delicate dose control,
(3) the possibility to eliminate or minimize the use of collimator, which can minimize the unnecessary neutron dose caused by the material along the beam line.

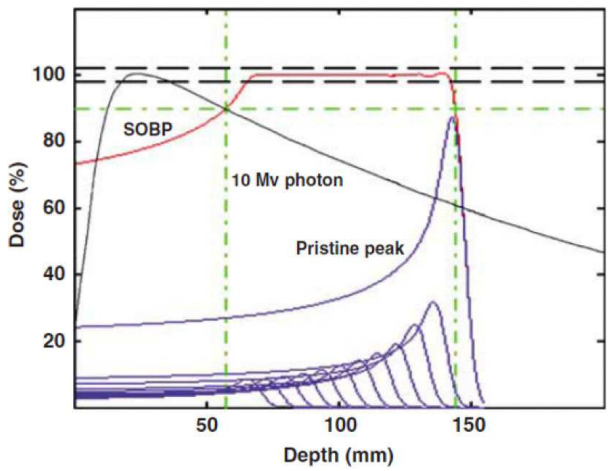

Fig. 2. The % energy depostion as a function of depth for protons and photons, showing the Bragg peak and the SOBP.[5]

Extracted beam from FFAG accelerators is usually in a pulsed structure. The beam structure combined with the high repetition rate is considered to suit the spot scanning well. In the spot scanning treatment, the typical voxel size is 4 mm $\times$ 4 mm $\sim$ 10 mm $\times$ 10 mm. PAMELA employs fast extraction as the extraction scheme. Thus, the extracted beam emittance is the same as that of the circulating beam. Assuming a typical β function on the surface of the patient of 1 m, the typical beam emittance at extraction is $\sim 10\pi$ mm·mrad.

2.2. *Dose control in pulsed beam accelerator*

Dose control is a crucially important issue in particle therapy. In the treatment, to achieve a good balance between therapeutic effect and the minimisation of unnecessary dose in healthy tissues, a SOBP(Spread-Out Bragg Peak) is usually formed over the target volume.[5] The 'uniformity' of dose field, which is defined as the local dose deviation from average dose, is required to be less than 2%, and the 'tolerance', which is defined as the deviation of average dose from the prescription, should be less than 5%.[a]

To form a uniform dose field in spot scanning, the beam intensity must be modulated depth-wise, ultimately in every voxel, which is called IMPT(Intensity Modulated Particle Therapy). In varying beam energy, the cyclotron uses energy degrader, which inevitably deteriorates the beam quality. To avoid the deterioration, PAMELA is required to flexibly change the beam energy at extraction stage.

To modulate the beam intensity, conventional particle therapy accelerators such as the cyclotron and synchrotron adjust the timing gate width of the extracted

[a]Actually, existing particle therapy facilities have already achieved tolerance below 2%.

beam, since their extracted beam can be macroscopically considered a DC beam. However, for a pulsed beam accelerator such as a FFAG, intensity modulation should be carried out at the injection stage. Therefore, a different approach from that for the conventional accelerators is required. Intensity modulation with pulsed beam can be obtained in two ways. One is 'direct intensity modulation', in which the beam intensity from the injector is modulated directly. The other way is 'multi-beam painting', in which an individual voxel is irradiated by multiple 'beamlets' until the accumulated dose reaches the prescription. While the advantage of direct intensity modulation is that low repetition rate can suffice, the realization will require a complicated control system for intensity control of the injector. Thus, uncertainty of precision still remains. The multi-beam painting requires a higher repetition rate, but dose control is expected to be easier and more reliable. Due to the present uncertainty of the tuneability of the ion source output, PAMELA employs multi-beam painting. The target repetition rate of 1 kHz comes from the medical requirement for multi-beam painting.[7]

2.3. *Stability and tuneability*

To satisfy the requirements of uniformity and tolerance using pulsed beam, two aspects of the injector beam intensity need careful consideration.

One is the stability. The other is the tuneability. As for the stability, the time scale should be taken into account. In the short time range, with a typical beam bunch interval in the multi-bunch painting scheme, several % of intensity fluctuation would be acceptable, because such a short term fluctuation is averaged out with multi-bunch painting. On the other hand, for the long time range, typically longer than the interval of voxel scanning, the requirement is less than 2%, since the long term stability directly affects the uniformity. Actually, the existing ion source has already achieved that level of long term stability.

The requirements of intensity tuneability come from the tolerance of the dose field. The output current must be tuned **easily** with a precision of 5%. In the study of quantized intensity modulation, the minimum 'beamlet' intensity for 1 Gy dose is about 10^6 proton/bunch. In the present rf scheme for PAMELA, with a capture length per bunch as 10 ns, the average current of injector beam is 20 μA. That means the precision of the output current should be less than 20 $\mu\text{A} \times 0.02 = 0.4$ μA. In addition, in clinical use the prescribed dose needs to be changed for an individual treatment. Thus, the intensity must be precisely and quickly changed with a transient time of typically less than 1 s.

Due to the nonlinearity of the plasma formation process in an ion source, the tuneability is still an open question in the present stage of design. However, ideally speaking, the dose control scheme should be implemented in a very early stage of accelerator system design, since in a pulsed beam accelerator such as FFAG, intensity is hard to control at the extraction stage. To implement the capability of IMPT in the system, intensity modulation is carried out with a multi-bunch painting scheme

in PAMELA. Another option for intensity modulation, direct intensity modulation, was discarded due to the uncertainty of the tuneability of the output current of the ion source.

However, there is another way to realize direct intensity modulation with fixed ion source current. By installing an active chopper, which consists of a pair of kicker magnets where the relative timing is controlled by a programmable delay generator, the bunch intensity can be controlled. For example, in the PAMELA proton ring, the circulation period at the injection energy is about 500 ns, Thus, more than 200 ns can be used for the injection beam using adiabatic capture. The existing commercial programmable delay generator can control the delay timing with an accuracy below 1 ns. Thus, the dynamic intensity modulation of more than one order of magnitude would be feasible. If the intensity control of the ion source becomes reliable, combining that with the active chopper, a further larger dynamic range becomes feasible. In this case, the transient time of the source current change might be a concern. In spot scanning, the changing of the beam energy is followed by the horizontal scanning. Therefore the transient overhead time due to the intensity change would be tolerable. With direct intensity modulation, the effective repetition rate can be drastically enhanced in IMPT. It is a significant improvement in terms of the treatment efficiency and eases the requirements on the system, especially the rf.

3. Ring Design

In general, a NS-FFAG has considerable tune drift to satisfy the specific operational requirements. The acceleration of the proton beam is a relatively slow process and resonance crossing of up to half integer resonances will result in serious beam distortion.[8,9] To avoid beam blow-up due to resonance crossings, tune stabilisation over the entire energy range is a crucially important issue from both aspects of beam quality and cost. The lattice of PAMELA aims to satisfy the following requirements at the same time. These are:

(1) stable betatron tune;
(2) small orbit excursion;
(3) simple lattice configuration;
(4) long straight section and
(5) operational flexibility.

PAMELA uses a simplification of a scaling FFAG as the lattice design strategy. The compact orbit excursion is realized by employing a high field gradient scaling FFAG lattice which uses the second stability region of Hill's equation.[10] Scaling field is described as $(B/B_0) = (R/R_0)^k$. In PAMELA, instead of explicitly implementing a scaling field, it is expanded about R_0 into a series of truncated multipole fields as

$$\frac{B}{B_0} = \left(\frac{r}{r_0}\right)^k \to 1 + \sum_{n=1} \alpha(k,n) \left(\frac{\Delta r}{R_0}\right)^n, \tag{1}$$

where $\Delta r = r - R_0$ and $\alpha(k, n)$ is expressed as

$$\alpha(k, n) = \frac{\Gamma(k+1)}{\Gamma(n+1)\Gamma(k-n+1)}, \tag{2}$$

where $\Gamma(z)$ is Gamma function. In the case that k is integer, $\alpha(k, n)$ is the binomial coefficient, ${}_kC_n$. Taking finite orders of multipole fields can approximate the scaling field with a sufficient accuracy around the centre of field expansion. In PAMELA, multipole fields up to decapole are implemented. The field is realized employing a new type of superconducting combined function magnet, which can separately vary each multipole field from the scaling "scaling baseline field" (see later section). The feature expands the range of tuneablity of the lattice from that of strictly scaling field.

It should be mentioned that R_0 in Eq. (1) should be the centre of orbit excursion at each magnet to assure symmetry of the expansion. Otherwise, considerable field error is introduced and results in larger tune variation.

In the present PAMELA lattice, a long straight section of more than 1.3 m is reserved. It helps in injection/extraction and acceleration. The cost of the long straight section is the requirement of a strong field of more than 3 T. It forces PAMELA to employ superconducting magnets to realize the lattice. With the field distribution given by Eq. (1), a linearly aligned cell structure, which consists of three rectangular magnets, was employed. The structure makes the magnet system simple and make the implementation of the superconducting magnets easier. The cell layout is shown in Fig. 3. Triplet magnets are installed in single cryostat, and they are arranged so that the centre of each magnet is located to the centre of orbit excursion. The ring parameters of the proton and carbon rings are summarized in Table 2. The long straight section and small orbit excursion are remarkable features of the lattice for a fixed field accelerator.

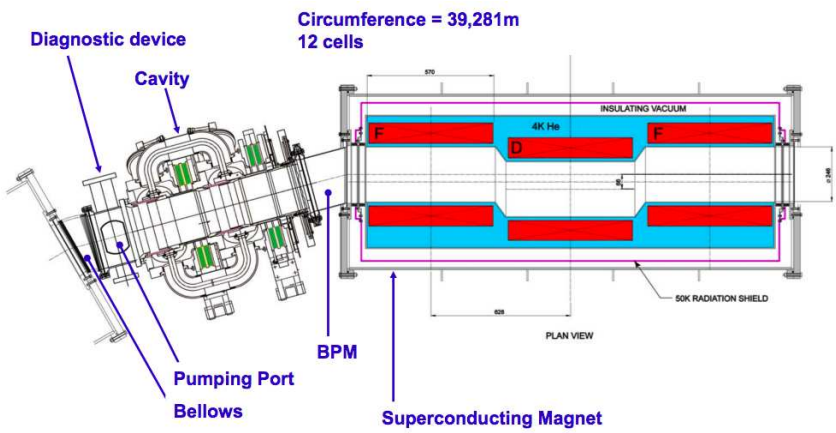

Fig. 3. Cell layout of the PAMELA proton ring (magnet module and rf cavity).

Table 2. Main parameters of PAMELA.

	Ring 1 (proton, carbon)	Ring 2(carbon)
Energy	30∼250 MeV(p) 8∼68 MeV/u(C)	68∼400 MeV(C)
Diameter	12.5 m	18.4 m
k value	38	41
Orbit excursion	18 cm	21 cm
Revolution frequency	1.94∼4.62 MHz(p) 0.98∼1.92 MHz(C)	1.94∼3.91MHz (C)
Maximum field	3.6 T	3.5 T
Magnet	FDF Triplet Superconducting	FDF triplet Superconducting
Length	57 cm/magnet	113 cm/magnet
Aperture	25 cm	33 cm
Long drift	1.3 m	1.2 m
Packing factor	0.48	0.65

4. Magnet

The magnet of PAMELA must generate multipole fields which contain up to decapole moments with a maximum field strength of more than 3 T. Generating such field in a magnet with large bore and short length makes it difficult to use conventional approaches, such as a $cos\theta$ type magnet. To tackle the challenge, the double-helix magnet scheme was adopted.[19] The scheme employs a pair of helical coils for each multipole.[13,14] The principle is shown in Fig. 4. Fig. 5 shows the coil configuration.

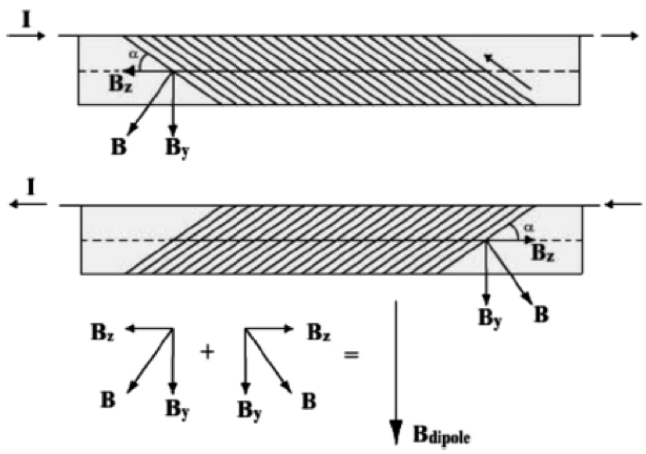

Fig. 4. Principle of the double-helix magnet.

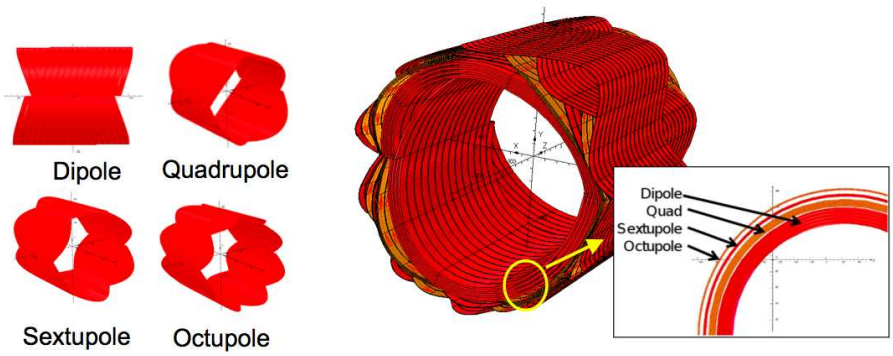

Fig. 5. Schematic view of a double helix combined function magnet.

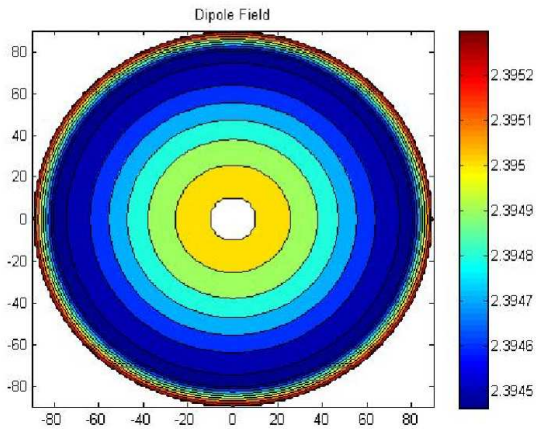

Fig. 6. Field quality of a PAMELA magnet.

The advantage of the scheme is the tuneability of individual multipole components, and ease of implementation for superconducting magnet.

Field calculation demands that the uniformity of each multipole field can be controlled within 10^{-3} or better.[19] Fig. 6 shows typical field quality for the horizontal plane.

5. Beam Dynamics

Employing truncated multipole fields, the lattice was modelled using ZGOUBI.[11] Fig. 7 shows the betatron tune of the PAMELA proton ring as a function of kinetic energy. A tune drift of less than 0.1 for the ring tune was achieved. This means that in PAMELA there is no large resonance crossing during acceleration.[b]

[b]In the tracking study, Enge fall-off was employed as the fringe field model, but the field distribution with the double helix multipole is different from that of the Enge model. Thus, 3D tracking study with realistic field distribution is indispensable in the design optimisation.

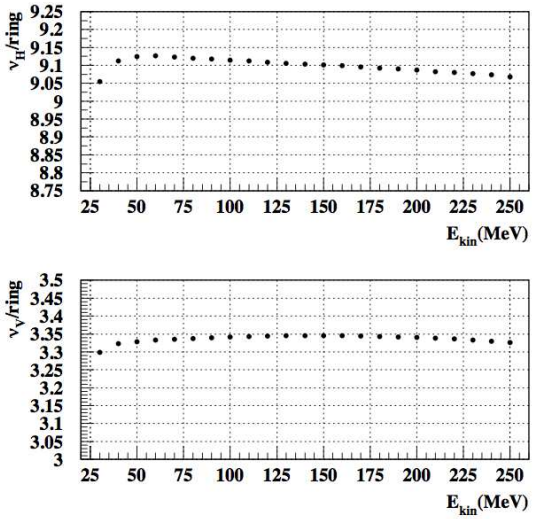

Fig. 7. Betatron tune of the PAMELA proton ring.

Table 3. Tuning knobs of the PAMELA lattice.

Horizontal tune	k-value
Vertical tune	F/D ratio
Curvature of Tune drift	Octupole
Gradient of Tune drift	Decapole

One significant advantage of the truncated multipole scheme is its flexibility. In ordinary fixed field accelerators, the field distributions are fixed at the design stage and there exists almost no room for adjustment after construction. The lack of tuning of the operation point sometimes causes problems in the commissioning and operation of fixed field accelerators. The combined magnet structure using the double-helix multipole magnet makes it possible to change each multipole component individually and provides PAMELA an ability to tune the operating point flexibly not only for the average tune but also the shape of the tune footprint itself. The tuning knobs are summarized in Table 3. The flexibility of operation place PAMELA in a unique position among fixed field accelerators. An application of the tune tailoring is discussed in Ref. 18.

Fig. 8 shows the k value dependence of horizontal tune and F/D ratio dependence of vertical tune, respectively. Field margins to change the average betatron tune over the range of 0.5 in both directions are 1%(dipole), 4%(quadrupole), 6%(sextupole), 9%(octupole), and 15%(decapole), respectively. They are within a feasible range from engineering viewpoint. Fig. 9 shows an example of changing the tune footprint. As shown in Fig. 10, the dynamic aperture is sufficiently large for a medical accelerator ($>400\pi$ mm mrad).

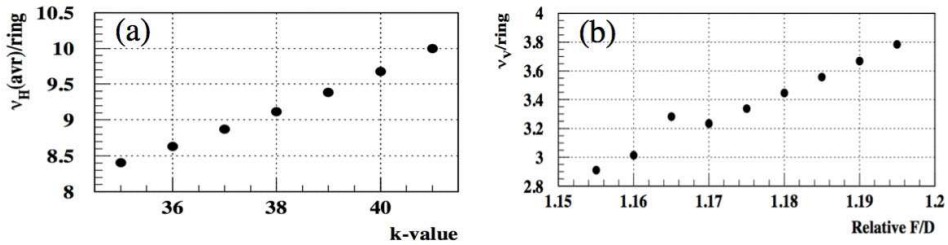

Fig. 8. k value dependence and F/D ratio of the betatron tunes of the PAMELA proton ring.

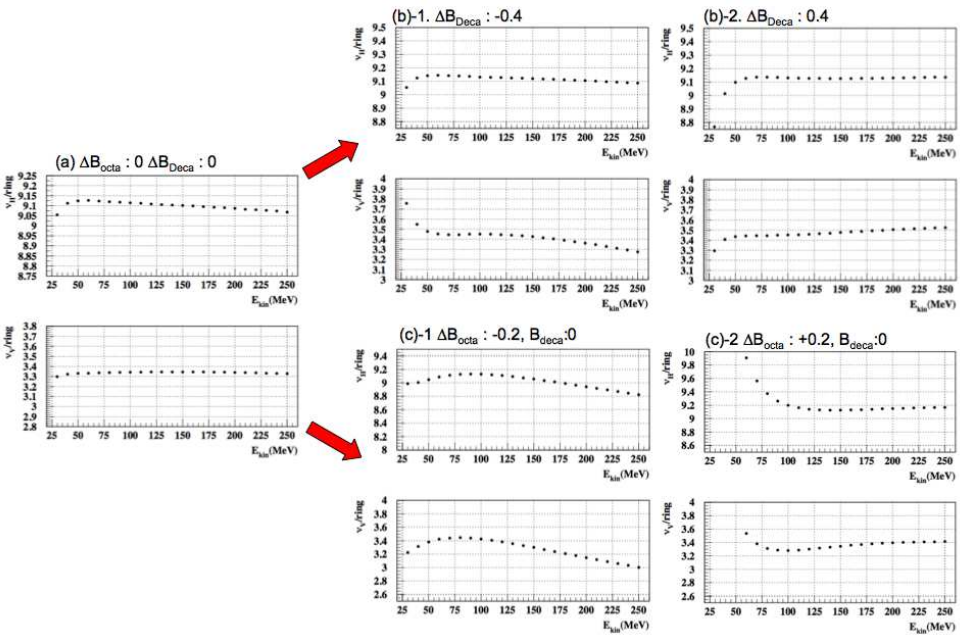

Fig. 9. Example of tune trimming: (a) reference tune; (b) decapole effect, 1: 40% reduction of decapole field, 2: 40% increase of decapole field; (c) octupole effect 1: 40% reduction of octupole field, 2: 40% increase of octupole field.

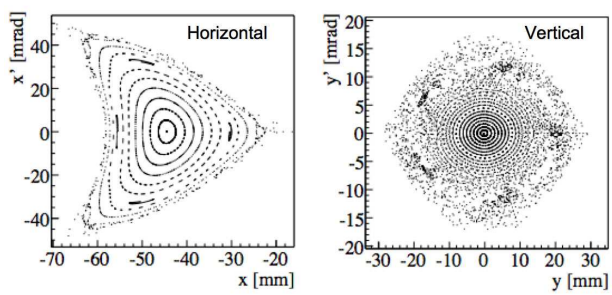

Fig. 10. Dynamic aperture at injection.[20]

Table 4. Specifications of the PAMELA proton ring kicker magnet.

Direction	Vertical
Aperture	3cm(V)×20cm(H)
Max field	0.6kgauss
Inductance	0.2μH(analytical)
	0.4μH(FEA)
PS HV	25kV(analytical)
	50kV(FEA+Circuit sim.)

6. Beam Extraction

A big challenge for beam extraction in PAMELA is the energy variability in a fixed field accelerator. In all the FFAGs ever built, beam was extracted horizontally. Variable energy horizontal extraction in a fixed field accelerator encounters three major difficulties. The first one is the large horizontal aperture of the extraction kicker, which leads to large inductance in the kicker magnet and results in severe requirements on the kicker power supply. The second is the orbit separation. In the PAMELA case, to extract 70 MeV proton beam horizontally, an orbit separation of more than 11 cm needs to be generated by the kicker system. Such a huge orbit separation is difficult to generate not only from the hardware aspect but also from the dynamics aspect, with the existence of nonlinear detuning in scaling FFAG. The third point is the matching of the transport line. In the horizontal extraction, the horizontal orbit excursion of scaling FFAG results in the large horizontal dispersion at septum. Thus, horizontal orbit matching must be made after extraction, and it is a non-trivial issue. Due to the reasons described above, vertical extraction was chosen in PAMELA.[c] In the vertical extraction, the problems listed above are circumvented. In addition, due to the cell-wise orbit symmetry of the FDF triplet, feasibility of direct beam extraction means the injection can be carried out in the same way with much less stringent engineering requirements. In addition, the extraction kicker can also be used as the injection kicker.

The kicker and septum are installed in the adjacent long straight sections. Table 4 summarizes specifications of extraction system and Fig. 11 shows a typical beam distribution in the extraction process.

In this scheme, the major R&D item is the kicker magnet. The large aspect ratio of the kicker introduces considerable uncertainty in inductance and field quality. In addition, the high repetition rate of ∼1 kHz enters into an unknown region of strong fast kicker operation in terms of system reliability, and requires careful design consideration. Therefore, the proposal for the development of a prototype kicker is in preparation.

[c]In RACAAM FFAG the difficulties are circumvented by varying the main field and injection beam energy.[12]

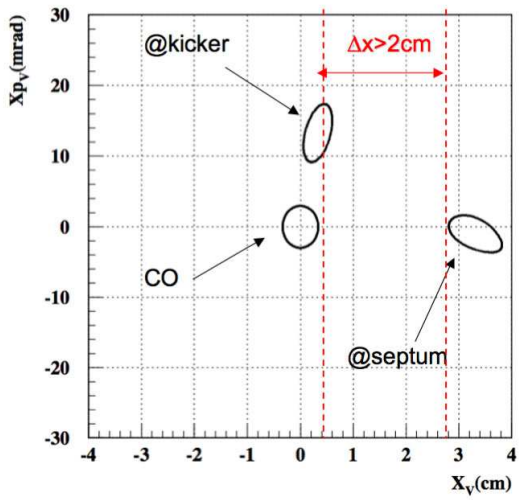

Fig. 11. Beam motion in vertical beam extraction ($E_{\rm kin} = 250$ MeV, $B_{\rm kicker} = 0.6$ kgauss).

7. RF System

To achieve a repetition rate of 1 KHz, the energy gains per turn are 100 keV for the proton and 300 keV for the carbon ring, respectively. Assuming the synchronous phase of 50°, the required peak voltage is 130 kV for proton and 420kV for carbon, respectively. At this stage of initial investigation, three options are considered. These are (1) a ferrite-loaded tuning cavity,[21] (2) a MA cavity,[22] and (3) an induction cavity.[23] The characteristics of the options are summarized in Table 5.

Table 5. Characteristics of rf system options for PAMELA.

	Merit	Demerit	Misc
Ferrite	Hi Q	Low max B_{rf} Tuning system	High loss effect Dynamic loss effect
MA	High μQf High saturation field Broadband (low Q)	High heat load (low Q)	Multi-bunch acceleration
Induction cavity	Long bunch train Arbitrary wave form	Complicated control Low efficiency	Not good for small ring

Among these options, the induction cavity was dropped due to complexity of control system, relatively low accelerating voltage compared to other options, and the fact that it is not suitable for small ring. The advantages of the MA cavity are high μQf value in high B_{rf} region, higher saturation field, compared to a conventional cavity,[22] and broadband characteristics. With these characteristics, a MA cavity can realize high field gradient with a simplified control system. In addition, broadband characteristics provides the option of multi-bunch acceleration

in a fixed field accelerator,[24] though the vertical beam extraction of PAMELA eliminates the multi-bunch acceleration. In the low B_{rf} region, conventional ferrite still provides higher μQf, and is expected to have lower power consumption. Due to the above reason, the ferrite-loaded cavity was employed as the primary option for PAMELA rf, although careful design and control of the B_{rf} is indispensable for the implementation.

7.1. *Ferrite-loaded cavity*

In the PAMELA rf system, the biggest challenge is the compatibility of a high duty cycle with rapid frequency modulation and high field gradient. Among them, handling of huge power dissipation, which is inevitable in the high duty proton acceleration, is the problem that has to be fixed first of all. The advantage of a ferrite-loaded cavity is its relatively high Q-value. It is expected to suppress the power dissipation to a tolerable level. In PAMELA proton ring, it is expected to be below 100 kW/cavity.[17] Another advantage is relative maturity of the ferrite-loaded cavity as an accelerator technology. In order to make the cavity length shorter to fit the straight section, higher harmonics (h=10) are used. The specifications of the rf cavity for PAMELA proton ring are summarized in Table 6 and a schematic drawing of a PAMELA rf cavity is shown in Fig. 12.

Table 6. Specifications of the PAMELA proton ring rf system.

Scheme	Ferrite-loaded tuning cavity
Number of cavities	8 (max)
Total energy gain	100 kV/turn
rf frequency (h=10)	19.4∼46.2 MHz
Length	1.1 m
Aperture	23 cm
Repetition rate	1 kHz
Power dissipation	∼100 kW/cavity

To use such a cavity in PAMELA, several unknown properties of ferrite should be determined. Evaluating the performance of the PAMELA rf cavity, it was assumed that the Q-value of 100 is constant over the operation frequency range. The basic ferrite property of the Q-value under biased condition should be measured for a realistic design. In addition, for the high field gradient and high frequency modulation rate operation, dynamic properties of ferrite such as high loss effect[16] and dynamics loss effect must be investigated. To clarify such unknown items, measurement of ferrite properties has started.

A proposal for the construction of a prototype cavity will be developed after the measurement and fixing the appropriate candidate of ferrite. In the cavity development, the ability for high-rate frequency modulation is an important requirement. A ferrite cavity requires bias current system for resonance frequency tuning, and

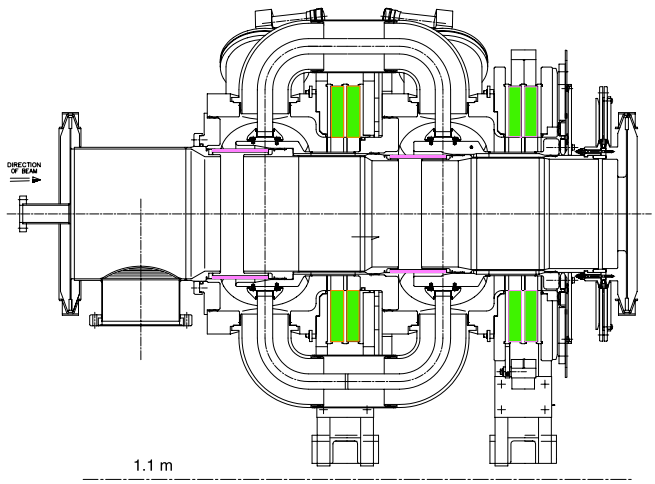

Fig. 12. Schematic drawing of a PAMELA rf cavity.

the bias field system requires large current. Therefore, rapid frequency modulation is also a technical challenge and needs a demonstration using a realistic system. Such an item is also an important research issue of the prototype rf cavity system.

8. Injector

PAMELA aims to deliver both proton and carbon beams flexibly. Therefore, it uses two injectors. One is a cyclotron for protons and the other is an RFQ for the carbon beam. The cyclotron would be a commercial one, but the RFQ is a dedicated design for PAMELA. The tracking study of RFQ is proceeding and the refinement of modelling shows the beam transmission is more the 99%.[4] The beam emittance from the injector is assumed to be 1π mm·mrad(unnormalized).

9. Beam Transport

The advantage of PAMELA is a flexible variability of extracted beam energy with high repetition rate. To fully exert this advantage, the beam transport downstream of extraction section must have the ability to accept a wide range of beam momenta. Such characteristics require a different approach to existing beam transport systems. One approach is to apply the FFAG principle to the beam transport line. A symmetric magnet configuration can make up a straight FFAG transport line. In the case of a straight configuration, the field distribution should be modified following:

$$\frac{B}{B_0} = \left(\frac{r}{r_0}\right)^k \rightarrow \frac{B}{B_0} = \left(\frac{y}{y_0}\right)^k, \tag{3}$$

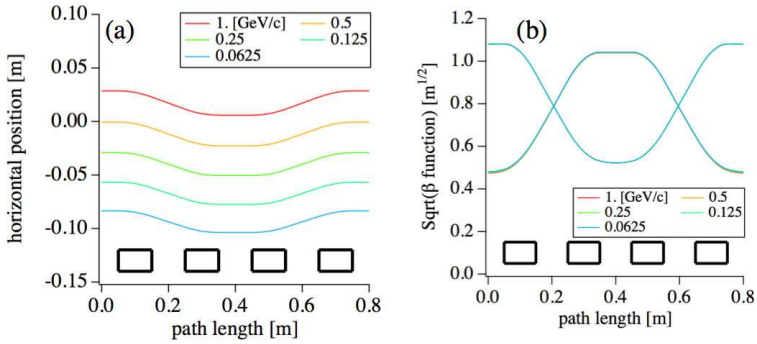

Fig. 13. (a) Horizontal orbit of FFAG transport, (b) beta function of FFAG transport.

where r and y are the distance from the machine centre and horizontal position in the magnet-centred coordinate system.

Fig. 13 shows the horizontal orbit in the transport and the beta function for different momenta. The beam transport has sufficiently large momentum acceptance and transverse acceptance. It should be mentioned the magnet used in the PAMELA ring can be used for FFAG transport as well.

10. R&D Schedule

PAMELA is a project with a length of 3.5 years, and 2010 is the final year of the project. It aims to finish the overall ring design by the end of fiscal year 2009, and a budget request will be developed after the completion of the design report. At the moment, three major hardware items are needed: a magnet, a kicker, and an rf system. After prototyping and establishing the engineering feasibility of these elements, the proposal for the construction of a full-size machine and facility will be made.

11. Summary

The PAMELA project aims to design a particle therapy facility using NS-FFAG. The accelerator developed for the project has unique features for a fixed field accelerator, such as energy variable beam extraction and tuneability of the operating point. Intense design study is underway, and hardware R&D has also started. The realization of the project will give a birth not only to a new particle therapy facility but also to a new versatile accelerator.

Acknowledgment

The project is supported by BASROC and is carried out by CONFORM collaboration under EPSRC grant number EP/E0332869/1.

References

1. R. J. Barlow *et. al.*, The CONFORM project: Construction of a Nonscaling FFAG and its application, *Proceedings of PAC07*, 2886 (2007).
2. R. Edgecock *et. al.*, EMMA—The World's first non-scaling FFAG, *Proceedings of EPAC08*, 3380 (2008).
3. K. Peach *et. al.*, PAMELA—a model for an FFAG based hadron therapy machine, *Proceedings of PAC07*, 2880 (2007).
4. M. J. Easton *et. al.*, Injection layout for PAMELA, *Proceedings of PAC09* (2009).
5. W. P. Levin *et. al.*, *British journal of Cancer* **93**, 849 (2005).
6. A. Lomax *et. al.*, *Med. Phys.* **28**, 317 (2001).
7. T. Yokoi *et. al.*, Beam injection issues of FFAG for particle therapy, *Proceedings of EPAC08*, 3401 (2008).
8. S. Machida, *Phys. Rev. St Accel. Beams* **11**, 094003 (2008).
9. T. Yokoi *et. al.*, Beam acceleration studies of proton NS-FFAG, *Proceedings of EPAC08*, 3398 (2008).
10. S. Machida, *Phys. Rev. Lett.* **103**, 164801 (2009).
11. F. Meot and S. Verelo, ZGOUBI user's manual, (2006).
12. F. Meot *et. al.*, Variable energy protontherapy FFAG accelerator, *Proceedings of EPAC06*, 2008 (2006).
13. D. I. Meyer, R. Flasck, *Nucl. Instr. and Meth* **80**, 339 (1970).
14. C. Goodzeit *et. al.*, Combined function magnets using double-helix coils, *Proceedings of PAC07*, 560 (2007).
15. S. Machida *et. al.*, to be published.
16. J. E. Griffin and G. Nicholls, *IEEE Trans. for Nucl. Sci.* **26**, 3965 (1979)
17. T. Yokoi *et. al.*, PAMELA: Development of the rf system for a non-relativistic non-scaling FFAG, *Proceedings of PAC09*, (2009).
18. T. Yokoi , Kicker-less FFAG: An approach to high intensity accelerator, *Proceedings of FFAG09*, (2010).
19. H. Witte *et. al.*, PAMELA magnet—Design and Performance, *Proceedings of PAC09*, (2009).
20. S. Sheehy *et. al.*, PAMELA Lattice Design and Performance,*Proceedings of PAC09*, (2009).
21. I. S K. Gardner, Ferrite dominated cavities, *CERN Acc. School, CERN 92-03*, Vol. II, 349.
22. Y. Mori *et. al.*, A new type of rf cavity for high intensity proton synchrotron using high permeability magnetic alloy, *Proceedings of EPAC98*, 299 (1998).
23. K. Torikai *et. al.*, Induction accelerating cavity for a circular ring accelerator, *Proceedings of EPAC04*, 704 (2004).
24. Y. Mori *et. al.*, Multi-beam acceleration in FFAG synchrotron, *Proceedings of PAC01*, 588 (2001).